Analyse morphologique quantitative des cendres des dépôts pyroclastiques d'origine hydrovolcanique et magmatique

Ersoy Orkun

Numéro d'Ordre: **1769**

UNIVERSITE BLAISE PASCAL-CLERMONT FERRAND II
(U.F.R. de Recherche Scientifique et Technique)

ECOLE DOCTORALE DES SCIENCES FONDAMENTALES

N° 540

THESE

Présentée pour obtenir le grade de

DOCTEUR D'UNIVERSITE

Spécialité : Volcanologie

Par

ERSOY Orkun

Master

ANALYSE MORPHOLOGIQUE QUANTITATIVE DES CENDRES DES DEPOTS PYROCLASTIQUES D'ORIGINE HYDROVOLCANIQUE ET MAGMATIQUE

Soutenue publiquement le 28 Septembre 2007, devant la commission d'examen.

President (Rapporteur)	**BOURDIER Jean-Louis**	Université d'Orléans
Rapporteur	**ÇİNER Attila**	Université d'Orléans
Examinateur	**LE PENNEC Jean-Luc**	IRD, Clermont-Ferrand
Examinateur	**TEZCAN Levent**	Université Hacettepe, Ankara
Directeur de thèse	**AYDAR Erkan**	Université Hacettepe, Ankara
Directeur de thèse	**GOURGAUD Alain**	Université Blaise Pascal Clermont II

" True glory consists in doing what deserves to be written; in writing what deserves to be read; and in so living as to make the world happier for our living in it "

G. Plinius Secundus

Résume

Les cendres volcaniques issues des différents mécanismes de fragmentation ont diverses textures et morphologies externes. Chaque particule de cendre peut donner des informations sur son propre environnement et sur des mécanismes de formation. On peut définir un régime de fragmentation, l'intensité de la fragmentation et la quantité d'eau qui participe au processus de fragmentation. Actuellement, les cendres volcaniques ont surtout fait l'objet d'approches qualitatives. En effet, la complexité et la variabilité des formes des particules volcaniques rendent l'approche quantitative difficile et la caractérisation numérique des textures de surface des cendres volcaniques, en raison de sa complexité, est encore mal définie. Des descriptions de surface simples et bien définies sont présentées dans cette étude. On se base sur le fait que la variation de niveau de gris est liée à la variation de rugosité de la surface. Ici, des valeurs de niveau de gris ont été employées sous une forme correspondant aux valeurs z vertical sur la surface. Les inconvénients et les avantages de la simplicité de la méthode sont discutés. Sept paramètres de rugosité (Rq, Ra, Rsk, Rku, Rv, Rp, Rt), trois paramètres de quadtree (nQT, mQT, sQT) et dimension de fractale sur des surfaces de cendres sont mesurés. Une analyse de gradient basée sur des opérateurs de Sobel a été exécutée et des parcelles de terrain polaires ont été produites, sur la base de la fréquence des gradients. Différents paramètres de forme, tels que le facteur de forme, la compacité, l'arrondi, l'allongement, la solidité, la convexité et les dimensions de fractale sont calculés sur les parcelles de terrain polaires. Des échantillons provenant de l'activité variée de cinq volcans ont été choisis pour l'analyse 2D: Nemrut, Erciyes (Turquie), Galunggung (Indonésie), Villarica (Chili) et Miyakejima (Japon). Cependant, des images tridimensionnelles permettent à différents dispositifs morphologiques d'être mieux interprétés et mesurés. En conséquence, des coupes de particules, la stéréoscopie et le meulage commandé ont été employés pour acquérir une reconstruction 3D. Des paramètres externes sont calculés sur les surfaces 3D des particules des cendres du volcan Villarica (Chili).
Les paramètres externes sont employés pour regrouper les différents types de particules selon leurs mécanismes de fragmentation et en particulier pour séparer les changements de styles en cours d'éruptions, liés au rapport eau/magma. Les paramètres de morphologie de surface optima ont été déterminés à l'aide des corrélations entre les paramètres de surfaces qualitatif, la porosité, l'abondance des xénolithes, les rapports de masse eau-magma (R) et des paramètres de surfaces quantitatifs. On admet que Ra et Rq sont les paramètres de rugosité sensibles à la micro-rugosité (par exemple la poussière fine) tandis que d'autres paramètres de rugosité, Rsk et Rku, mesurent la macro-rugosité liée aux cavités de surface (vésicules). En effet, le paramètre de quadtree nQT, la dimension de fractale des surfaces et la solidité des parcelles de terrain polaires ont également la même réponse à la micro-rugosité, semblable à Ra et Rq. En raison de l'intérêt croissant pour les propriétés externes de matériaux normaux, les paramètres des surfaces proposés dans cette étude peuvent être appliqués aux surfaces de divers matériaux normaux.

Mots Clés: cendre volcanique, microscopie électronique à balayage, phréatomagmatisme, rugosité, analyse de gradient, texture surface

Quantitative morphological analysis of ashes from pyroclastic deposits of hydrovolcanic and magmatic origin

Abstract

Volcanic ash particles from different fragmentation mechanisms have different surface textures and morphologies. Every single ash particle may convey information about its own formation environment and conditions. Certain features may give a hint about the fragmentation regime, the intensity of fragmentation and quantity of water that partakes in the fragmentation process. However, volcanic ash was characterized widely by qualitative set phrases up to date and the success in the discrimination of ash types depended on the experience of the person who dealt with characterization of particles. Furthermore, the complexity and variability of volcanic particle shapes make quantitative characterization difficult and numerical characterization of volcanic ash surface texture, because of its complexity, still remains largely unresolved. Simple and well-defined surface descriptors were presented in this study. It is based on assuming that the gray level variation is related to the roughness variation of the surface. Here, gray level values were used in a form corresponding to vertical z-values on the surface. The disadvantages and advantages of the simplicity of method have been discussed. Seven roughness descriptors (Rq, Ra, Rsk, Rku, Rv, Rp, Rt), three quadtree parameters (nQT, mQT, sQT) and fractal dimensions (FDs) on ash surfaces were measured. A gradient analysis based on Sobel operators was performed and polar plots were generated based on frequency of gradients. Different shape descriptors such as form factor, compactness, roundness, aspect ratio, solidity, convexity and the fractal dimensions (FD_PP) were calculated on polar plots. Samples from five volcanoes with different eruption styles were selected for 2D analysis (Nemrut, Erciyes (Turkey), Galunggung (Indonesia), Villarica (Chile) and Miyakejima (Japan)). However, three-dimensional images allow different morphological features to be correctly interpreted and definitively measured. Therefore, optically sectioned particles, stereoscopy and controlled grinding were used to acquire 3D datasets for reconstruction. Surface descriptors were calculated on 3D surfaces of ash particles from Villarica volcano (Chile).
The surface descriptors were used to cluster different type of particles according to their fragmentation mechanisms and designated the phase changes in eruptions associated with interacting water/magma ratios. The optimum distinctive surface descriptors were determined with the assistance of correlations between qualitative surface descriptions, vesicularity, xenolith abundance, calculated water/magma mass ratios (R) and quantitative surface descriptors. It is agreed that roughness parameters R_a and R_q are sensible to micro-roughness (eg. fine dust) while other roughness parameters R_{sk} and R_{ku} measure the macro-roughness associated with cavities on the surface (vesicles). Furthermore, quadtree parameter nQT, fractal dimension of surfaces and solidity of polar plots also have the same response to micro-roughness similar to R_a and R_q. Because of increasing interest in surface properties of natural materials, surface descriptors proposed in this study can be applied to surfaces of various natural materials.

Keywords: volcanic ash, scanning electron microscopy, phreatomagmatism, roughness, gradient analysis, surface texture

Dedication

For my wonderful parents Asya and Şeref Ersoy who have raised me to be the person I am today and my warm-hearted wife Hilal who motivated and supported me throughout the course of this thesis. In loving memory of my grandparents and my aunt's husband Nadir Yücel who always called me as "doctor".

Acknowledgements

Firstly, I would like to thank my supervisors, Erkan Aydar and Alain Gourgaud for their help, guidance and discussions on this study. I am indebted to my friends H. Evren Çubukçu, İnan Ulusoy and Erdal Şen for their assistance in field studies. Gary Chinga is thanked for providing most of the plugins used in this study and his first rate ideas and advices on progress of the method. Thanks to Jean-Marc Hénot for his help and patience during acquisition of SEM images in Laboratoire Magmas et Volcans. Thanks to Nobuo Geshi and Silke Lohmar for samples from Miyakejima and Villarica volcanoes, respectively. Thanks to Xavier Labouze (Attaché de coopération Universitaire), Tunçalp Özgen (rector of Hacettepe University), Albert Odouard (ex-rector of Blaise Pascal University) and Nadine Lavignotte (rector of Blaise Pascal University) for providing cooperation between universities.

1. Introduction

1.1. Why to study tephra

The term "tephra" comes from the Greek for ‘ash’ but refers to particles regardless of size that were erupted into the air and then fell back to the ground. The term was introduced by Thorarinsson (1944, 1954) to describe volcanic ash and coarser detritus that were projected through the air (Mullineaux, 1996). Hot magma rising through the earth's crust releases gases that expand and may come into contact with external water that vaporizes. The magma is then fragmented into an accelerating gas-particle/droplet mixture that is shot into the atmosphere, possibly in an overpressured state, where it may buoyantly rise up into the stratosphere as an ash plume, partially or totally collapse back to the surface, or rapidly expand sideways, or undergo a combination of these processes. Tephra is deposited on the Earth's surface by pyroclastic fall, flow or surge, or some hybrid mechanism. The combination of processes that operate from the degassing of magma to the emplacement of tephra makes an explosive volcanic eruption. A stylized explosive eruption system is depicted in Fig. 1. The explosive volcanic activity has always captured the public’s attention. Thus, understanding the dynamics of explosive eruptive events has been the primary goal of the volcanological community for many years.

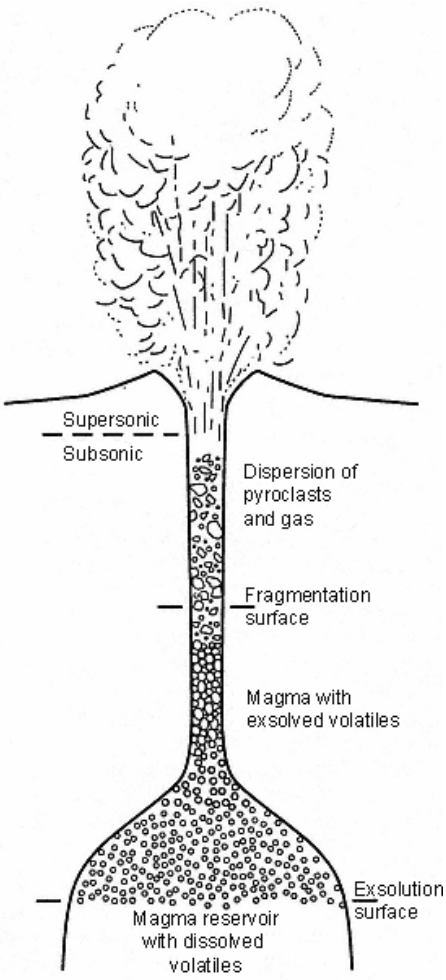

Figure 1: Schematic of an idealized volcanic eruptive system (Wilson et al., 1981 and Wohletz and Heiken, 1992)

Because the pyroclastics yield clues to interior, they provide a valuable aid in reconstructing dynamic aspects of earth evolution as well as predicting future volcanic hazards; understanding sedimentary basins containing petroleum and gas deposits; locating ore deposits in volcanic complexes and heat sources in geothermal prospecting; and facilitating stratigraphic analysis in complex volcanic terrains (Fisher and Schmincke, 1984). Pyroclastic particles are fundamental component of most volcanoes and their distribution extends far from the foot of the volcanoes themselves. The coarser (> 1 mm in diameter) pyroclastic material that is injected into the atmosphere by eruption falls out within an hour but remaining finer particles (< 10 μm) can stay suspended for days to months. These finer particles can be transported great distances and deposit irregularly and in unusually thick amounts far from the volcanic source (Riley et al., 2003 and references therein). Thus, volcanic ash has additional importance for volcanic hazard assessments and bears traces of not only the eruption environment but also the fragmentation mechanism (Zimanowski et al, 2003). Every single ash particle may convey information about its own formation environment and conditions. Certain features on particles may give a hint about the fragmentation regime, the intensity of fragmentation and quantity of water that partakes in the fragmentation process, etc. On this account, this study majored in the analysis on finer pyroclastic material, namely volcanic ash particles. Quantitative analyses on these particles provide insight into the energy release rate of volcanic explosions and associated hazards. The continuous observation on volcanic ash textures during an eruption phase may provide an opportunity to forecast the next behavior of the eruption, thus the violence of the disaster on people and habitat (Ersoy et al., 2007b-in section 4.3). Furthermore, analysis on volcanic ash particles can be used to understand problems associated with volcanic ash clouds such as deposition of ash, visibility, atmospheric dispersion, and aircraft engine damage.

1.2. Volcanic ash: What it is and how it forms

Tephra is a general term for all particles produced during volcanic eruptions by mechanical fragmentation of magma and/or country rock, and volcanic ashes are those particles with average diameters <2 mm (Fig. 2). Mechanical fragmentation of magma can be generally viewed as taking place in two fragmentation regimes, depending upon whether the characteristic deformation times are greater or less than the viscous relaxation time (Navon et al., 1998): (1) hydrodynamic fragmentation in the ductile regime (i.e. liquid like); and (2) brittle fragmentation in the brittle regime (i.e. solid-like). Hydrodynamic fragmentation (1) generally involves the rapid acceleration of magma by a pressurized fluid/gas. It is restricted to deformation of 2-D interfacial areas (boundaries between the melt and gas) and is most efficient in accelerated systems at low viscosities, low interfacial tension, and high-density contrast with the accelerating fluid and surrounding media. On the other hand, brittle fragmentation (2) is the result of 3-D crack growth caused by excess strain that exceeds the elastic properties of a medium (e.g. bulk modulus) (Zimanowski et al., 2003).
There are three main mechanisms of volcanic ash formation including the fragmentation regimes mentioned above: (1) the release of gases due to decompression within the magma ascending to the surface (magmatic eruptions), (2) chilling and explosive fragmentation of magma during contact with ground and surface water or ice and snow (phreatomagmatic eruptions), and (3) the comminution and ejection of particles from vent walls or crater debris during eruptions of steam and hot water (phreatic eruptions). Volcanic ash can be produced by one or more of these mechanisms (Heiken and Wohletz, 1985).
Scientists who are interested in volcanic ash have a glorious reference book thanks to Heiken and Wohletz (1985) who extensively described characteristics of volcanic ash from many

well-studied eruptions. This study was greatly benefited from the book named above and personal communications with an author of this book, Ken Wohletz.

Figure 2: Volcanic ash collected in Randle, Washington, located about 40 km NNE of Mount St. Helens. Photograph by D.E. Wieprecht (http://volcanoes.usgs.gov).

1.2.1. Volcanic ash from magmatic eruptions

In early models, the coalescence of bubbles was considered to be the main mechanism of magma fragmentation and formation of pyroclastics (Verhoogen, 1951). However, McBirney and Murase (1970) and Sparks (1978) demonstrated that coalescence is unlikely to be the leading fragmentation mechanism for highly viscous magmas, although possibly applicable for eruptions of low viscosity magmas. McBirney and Murase (1970) suggested that fragmentation of highly viscous magma occurs when the gas pressure within vesicle exceeds the tensile strength of the magma. The high angularity of pyroclasts has been explained by the disruption of highly viscous, "semi-molten" or "nearly solid" vesicular magma by tensile stresses (Heiken, 1978; Heiken and Wohletz, 1985, 1991). The recent activity in the field of experimental fragmentation of magmas and analog materials by rapid depressurization using shock tube techniques has stimulated further considerations of the mechanisms responsible for magma fragmentation (Alidibirov, 1993; Mader et al., 1994, 1996; Sugioka and Bursik, 1995; Phillips et al., 1995; Alidibirov and Dingwell, 1996; Zhang et al., 1997; Alidibirov and Dingwell, 2000). In summary, magmatic pyroclastic rocks are formed by magma vesiculation and this process is dependent upon composition, temperature, and volatile content of the magma; these factors control viscosity and surface tension. Shapes of vitric ash particles from magmatic eruptions are mostly dependent on vesicle shapes and densities, which are dependent on the parameters listed above (Heiken and Wohletz, 1985).

Volcanic ash derived from basaltic explosions is typical according to the low-viscosity magma. For instance, Hawaiian eruptions consist of fountains of low-viscosity lavas that produce small- smooth-surfaced glass droplets (spheres, teardrop shapes), long threads of glass (Pele's hair), irregular cloths of glass, and scoria (Fig. 3).

Strombolian eruptions of slightly more viscous lava produce distinctive tephra that are considerably different than those formed in Hawaiian eruptions. Ash produced during Strombolian activity consists of a variety of pyroclasts, from irregular sideromelane droplets to blocky tachylite (black to dark brown microcrystalline pyroclasts) (Heiken and Wohletz, 1985). Sideromelane pyroclasts are smooth-skinned, vesicular droplets that form an irregular, partly open framework of vesicle walls (Fig. 4A). Angular, blocky tachylite pyroclasts range in shape from those with irregular, open-vesicle networks to nonvesicular blocky grains (Fig. 4B and C). The grain surfaces and vesicle walls of tachylite pyroclasts are not smooth, but

rough; they exhibit both fracture surfaces and diktytaxitic textures. In both sideromelane and tachylite pyroclasts, melt viscosities are not low enough to allow formation of the smooth-skinned spheres and ovoids that are typical of tephra produced Hawaiian eruptions. The variety of pyroclasts indicates the variety of conditions that may exist in a Strombolian eruption. Sideromelane pyroclasts exhibit the most pronounced deformation by surface tension and, thus, the lowest viscosities. They are produced by a higher temperature magma, which may be the case if lava flux from the conduit is high or if the vent is open and some jetting is possible (similar to characteristic Hawaiian activity). If the vent is clogged or lava flux is low, occasional bursts of cooler, les vesicular melt, which pools for a while, an "accidental" pyroclasts derived from slumps into the crater will produce an abundance of the blocky, tachylite pyroclasts (Heiken and Wohletz, 1985).

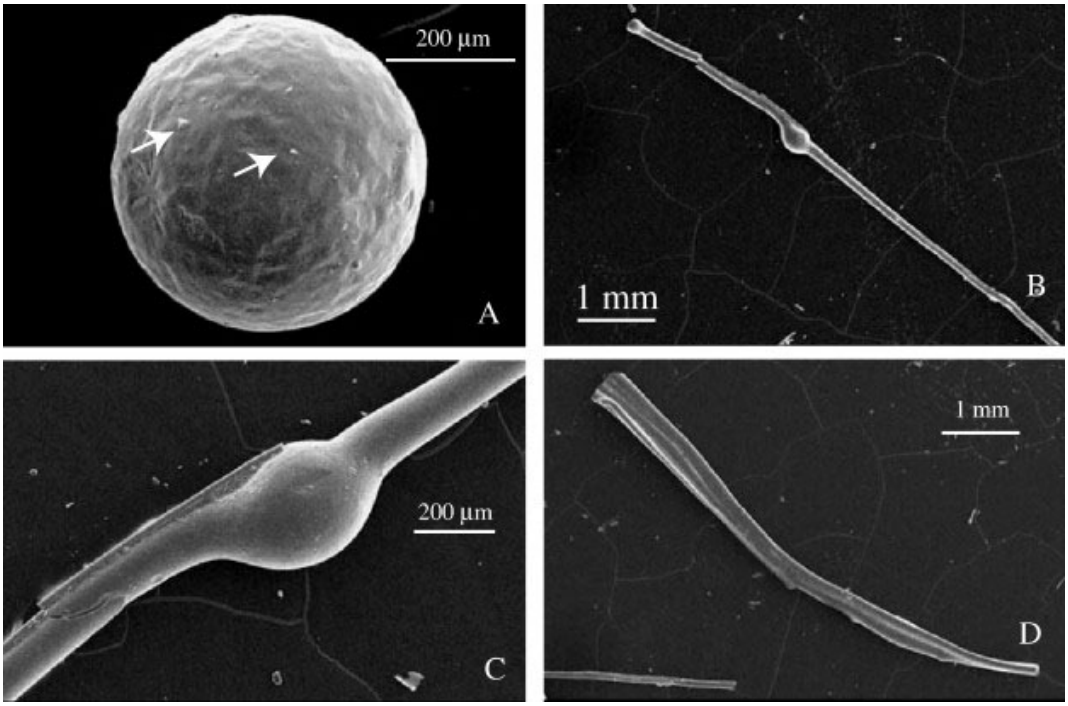

Figure 3: Morphologies of Pele's hair and tears from Masaya volcano (Nicaragua). (A) SEM image of a Pele's tear (spherical basalt pyroclast). (B) SEM image of a Pele's hair associated with a "knot" along the hair and a droplet, known as Pele's tear, at its end. (C) Enlargement of a Pele's hair exhibiting a "knot". (D) Pele's hairs with long vesicles parallel to stretching axis. Images and related explanations in figure caption are from Moune et al. (2007).

Petrologic and morphologic characteristics of intermediate and acidic pyroclasts are related to higher viscosities (10^3 to 10^6 poise) and the higher volatile contents of their source magmas. Viscosities of above 10^3 poise do not allow the formation of droplets by surface tension; pyroclast shapes are dependent upon the geometry of vesicles developed within the highly viscous magmas. Pyroclasts derived from such high viscosity magmas do not have smooth surfaces; exposed broken vesicle walls provide sharp, irregular surfaces (Fig. 5). Only the vesicle walls are smooth. The matter of substance if we envisage the "textural characterization of pyroclasts" is the heterogeneous vesicle development in acidic magmas. They consist of "pockets" of large, ovoid vesicles and thin, highly elongate vesicles. It is possible for vesicle growth to begin at depths of 2 or 3 km in rhyodacitic or rhyolitic melts with a water content of 3% or more (Sparks, 1978; Heiken and Wohletz, 1985). In this case, early vesicle growth begins at phenocryst surfaces, when those surfaces act as bubble nuclei. The larger pockets

with thin internal vesicle walls have a higher bulk viscosity than the surrounding melt and resist deformation by flow. However, as magma rise, vesiculation begins around the pockets. Closer to the surface, later stage vesicles are sheared into highly elongate, tube-like forms. At or near the surface, this heterogeneous, vesicular mass is fragmented, perhaps by a pressure wave passed down into the vent (Heiken an Wohletz, 1985). The complicated characterization of ash surfaces from different fragmentation mechanisms of acidic magmas due to heterogeneous vesiculation will be touched on later in Section 4.4.

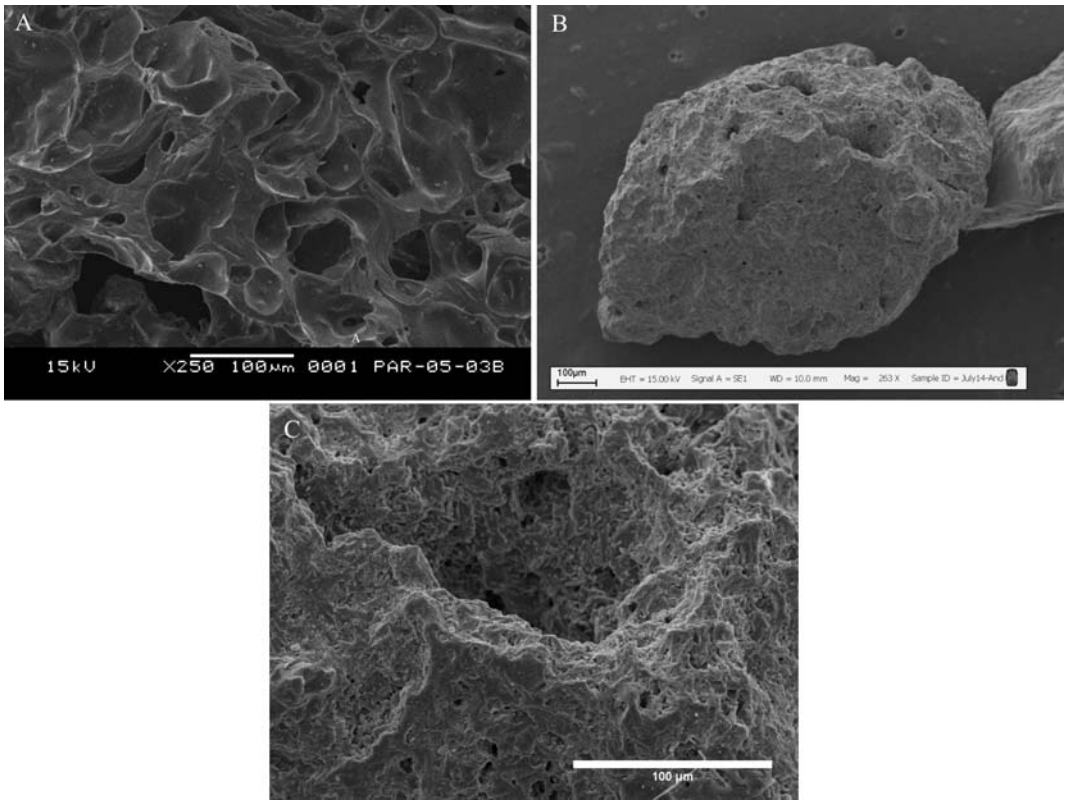

Figure 4: (A) Smooth-skinned vesicular pyroclast from the strombolian eruption phase of Puy Pariou (Massif central, France). (B) Blocky basaltic andesite pyroclast with diktytaxitic texture (C) with groundmass minerals having thin coating of glass (Miyakejima 2000 eruption, Japan).

1.2.2. Volcanic ash from phreatomagmatic (hydrovolcanic) eruptions

Phreatomagmatic (hydrovolcanic) eruptions typically produce fine ash deposits by a fragmentation mechanism involving vaporization of external water by the magmatic heat (Wohletz, 1983) (Fig. 6). In contrast with magmatic fragmentation, which has been studied from both theoretical approaches and experimental evidence, phreatomagmatic fragmentation has been investigated largely through field observation until Wohletz (1983). Recently, water/magma interaction is investigated by experimental facilities (e.g. Zimanowski et al., 1997; Kurszlaukis et al., 1998; Büttner et al., 1999; Suzuki et al., 2007; Trigila et al., 2007). The major consideration in understanding the hydrovolcanic eruptive mechanism is the energy of steam explosions. This quantity can be related to the size of pyroclasts produced, the mechanism of emplacement, and the amount of water that interacted with the magma (Wohletz, 1987). The explosive contact of water with melt begins with the formation and collapse of steam films on the melt surface (Fig. 7). This process is cyclic on a micro- or

millisecond time scale; it results in the generation of fluid instabilities at the contact, water jet penetration of the melt, thereby increasing surface area and heat-transfer rates. The effects of superheating and detonation waves are critical to the vaporization of water. Superheating is a process involving nonequilibrium heat transfer and homogeneous nucleation that causes instantaneous vaporization. It is still poorly understood, but it causes explosive efficiencies several orders of magnitude higher than in normal boiling processes. Detonation waves are shock waves that propagate through the melt to cause fragmentation and mixing with water by fluid instabilities and vapor film collapse. Consideration of the explosive mechanism and the presence of blocky, equant glass shapes have resulted in the general conclusion that phreatomagmatic ash is formed by thermal contraction and shattering of glass (Heiken and Wohletz, 1985).

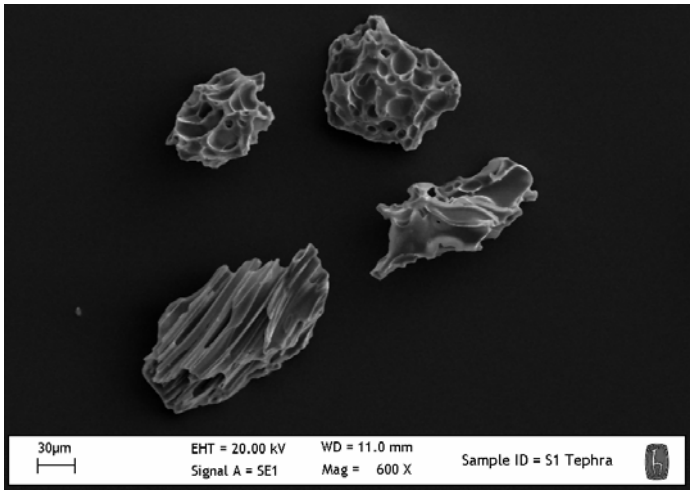

Figure 5: Highly vesicular volcanic ash particles (Sample# S1 Tephra) with irregular surfaces. Samples are related to sediment cores retrieved during Meteor cruise M51/3 in Eastern Mediterranean. The surface analyses of mentioned sample are still ongoing with a view to match its surface texture to those from eruptions of Anatolian origin.

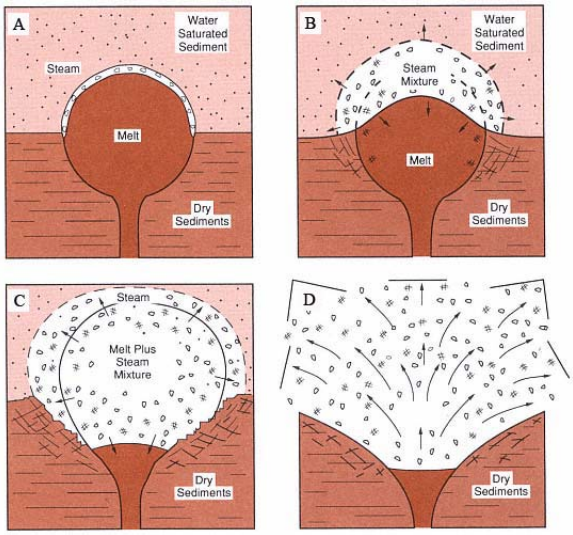

Figure 6: Hypothetical setting of subsurface hydrovolcanic activity, showing (A) initial contact of magma with water-saturated sediments, (B) vapor film growth, (C) mixing of magma with the sediments, and (D) expansion of the high-pressure steam in an explosion (Sheridan and Wohletz,1983 and Wohletz and Heiken, 1992).

Microscopic examination of grain shapes and textures also reveals hydrovolcanic features (Fig. 8). Quantitative analyses of these features can document the relative importance of hydrovolcanic (wet) and magmatic (dry) mechanisms in samples from deposits of mixed origins. Hydrovolcanic grain textures are also indicative of the type of water/magma interaction (for example, wet vs dry). Much of our qualitative and quantitative understanding of hydrovolcanic processes has developed from experimental and theoretical studies of the water/magma interaction mechanism (Wohletz and Heiken, 1992). Some of the characteristic grain shapes of experimental tephra shown in Figure 9, including blocky shapes, irregular and convoluted fluidal shapes, spheres, ribbons, and shell-like shards, can be used to interpret interaction and mixing mechanisms.

Fragment shapes produced during melt/water interactions reflect fragmentation by brittle failure during passage of stress waves and viscous melt/water mixing by fluid instabilities (Fig. 10). The most efficient explosive interactions appear to result in the latter of these two fragmentation mechanisms. Hence, the production of fine-grained debris with large surface areas and fluid shapes is predicted for highly explosive eruptions of fluid basalt. However, melt viscosity and strength strongly encourages development of instabilities. Therefore, for melts of intermediate and silicic composition, brittle fragmentation dominates. As mentioned above, complicated characterization of acidic pyroclasts due to heterogeneous vesicle types, chiefly for late stage water/magma interaction in already vesiculated magmas which prevents the occurrence of key features indicating phreatomagmatism will be discussed later in Section 4.4.

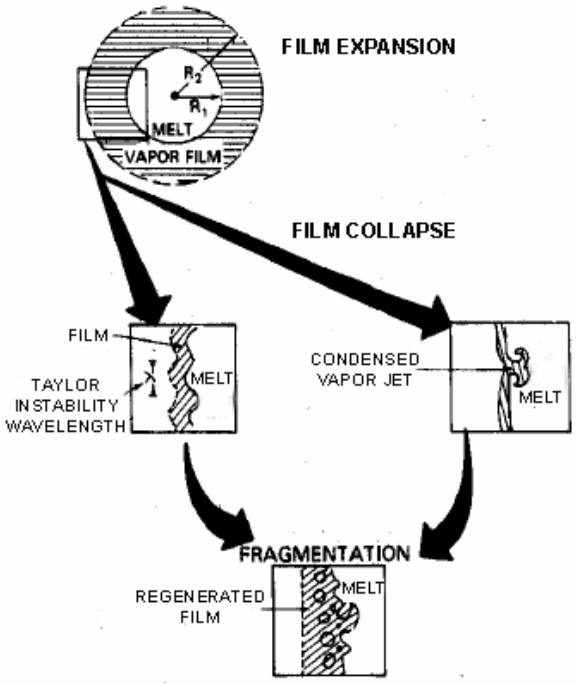

Figure 7: Diagrammatic illustration of the film collapse and fragmentation from Wohletz (1983)

1.2.3. Volcanic ash from phreatic eruptions

Hydrothermal activity at fumeroles and hot springs can become energetic enough to erupt explosively. The volcanic ash from this activity consists of fragments from vent walls and crater fill, and it contains no juvenile ash. In some instances phreatic explosions have preceded magmatic or phreatomagmatic eruptions. Tephra from active hydrothermal (steam) eruptions consist mainly of hydrothermally altered lithic and mineral fragments, commonly in a clay matrix. Included are subangular lithic ash (or lava) fragments in various states of alteration. Only relict textures remain to identify pyroclast types. Particle surfaces are often covered with aggregates of zeolite crystals or clay. Basaltic glass fragments may be rimmed with palagonite, a mixture of smectite clays and iron oxides. Ash particles are similar to the rock units exposed in vent walls and are broken from them by escaping steam; they are erupted to form a local low-volume pyroclastic deposit (Heiken and Wohletz, 1985). Due to absence of juvenile material, this type of pyroclasts is beside the point of this study.

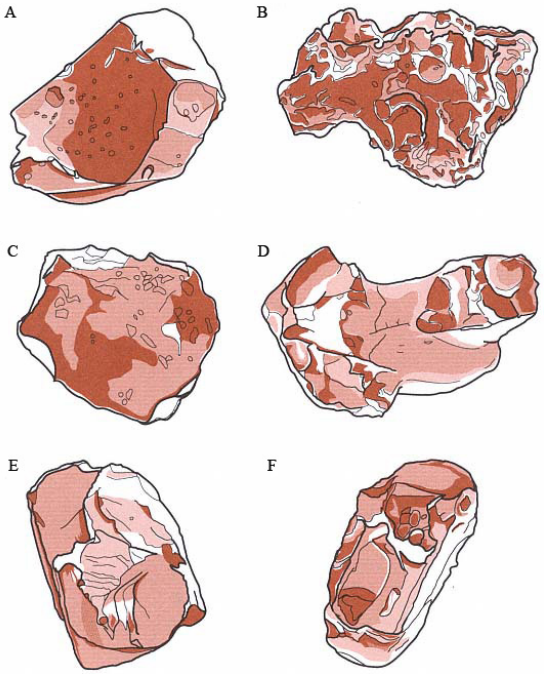

Figure 8: Sketches of pyroclast textures resulting from hydrovolcanism. These textures include (A) a characteristic blocky and equant glass shard, (B) a vesicular grain shard with cleaved vesicle surfaces, (C) a platy shard, (D) a drop-like or fused shard, (E) a blocky crystal with conchoidal fracture surfaces, and (F) a perfect crystal with layer of vesicular glass (Wohletz and Heiken, 1992).

1.3. Characterization of volcanic ash and the scanning electron microscope (SEM) for textural surface features

Ash particles are like snowflakes in that no two are alike. They present an infinite variety of morphological, chemical, and physical characteristics. In one sense, each ash grain is like a field area to be systematically mapped. On a statistical basis, the distinguishing characteristics of ash sample sets, consisting of thousand of grains, define a general relationship that is readily incorporated into the macroscopic world. The characterization of volcanic ash and its relationship to eruption phenomena have been of interest to scientists since the time of

Aristotle. Interest in this subject was renewed during the mid-1800s when European naturalists began studying volcanic fields in the Mediterranean, South America, and Indonesia. Three stages of ash development are considered (Wohletz and Krinsley, 1982): (1) formation by the eruptive process; (2) modification by transport abrasion; (3) alteration by post-emplacement processes. In this way, ash morphology and surface textures fit into a three-stage classification scheme: (1) morphologies indicative of ash formation; (2) textures related to transport abrasion; (3) types and amounts of alteration (Fig. 11).

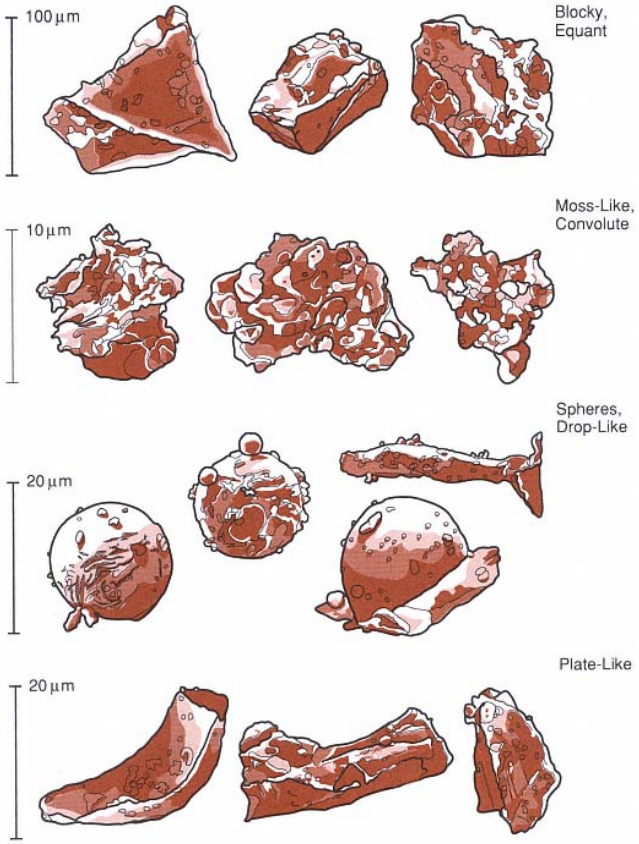

Figure 9: Sketches of four types of grain shapes observed during experiments in hydrovolcanism. Blocky and plate-like grains are thought to be produced by brittle failure of the melt when it is subjected to strong stress waves. Moss-like, drop-like, and spherical grains are likely produced by fluid instabilities at water/melt interfaces (Wohletz and Heiken, 1992).

Scanning electron microscopy (SEM) plays an increasing role in geology as a tool for understanding the nature of particulate matter and is useful in unraveling the histories of volcanic ash particles (Wohletz and Krinsley, 1982). SEM resolves surface structure down to the nanometer scale. Besides the development of morphological imaging, the SEM has been developed to detect signals, which are used to determine compositional information, such as X-rays, backscattered electrons, cathodoluminesce, Auger electrons, and specimen current. With the invention of the scanning electron microscope (SEM), a full range of pyroclast sizes could be investigated and chemical changes on grain surfaces measured. Used in conjunction with optical microscopy and the electron microprobe, the SEM has allowed beginning systematic characterization of volcanic ash (Heiken and Wohletz, 1985).
Early SEM studies of volcanic ash show that overall grain morphology is related to the mechanism of ash formation. Heiken (1972, 1974) and Walker and Croasdale (1972) studied

ash using the SEM and related ash morphology to magma composition and eruption type. Honnorez and Kirst (1975) combined SEM along optical microscopy to develop a system of morphometric quantification and to distinguish the morphometric parameters of hyaloclastites and hyalotuffs. They found that these ash types, products of submarine hydromagmatic volcanism can be distinguished by grain roundness measured by convexity, concavity, and planarity or by the relationship of the number of grain corners to grain planarity. Ash from hyaloclastites, tuffs occurring with pillow lavas extruded in deep water, has morphology similar to that of glass artificially granulated by quick chilling. There are more planar surfaces than on ashes of hyalotuff, which results from near surface steam explosions, an observation similar to that of Walker and Croasdale (1972).

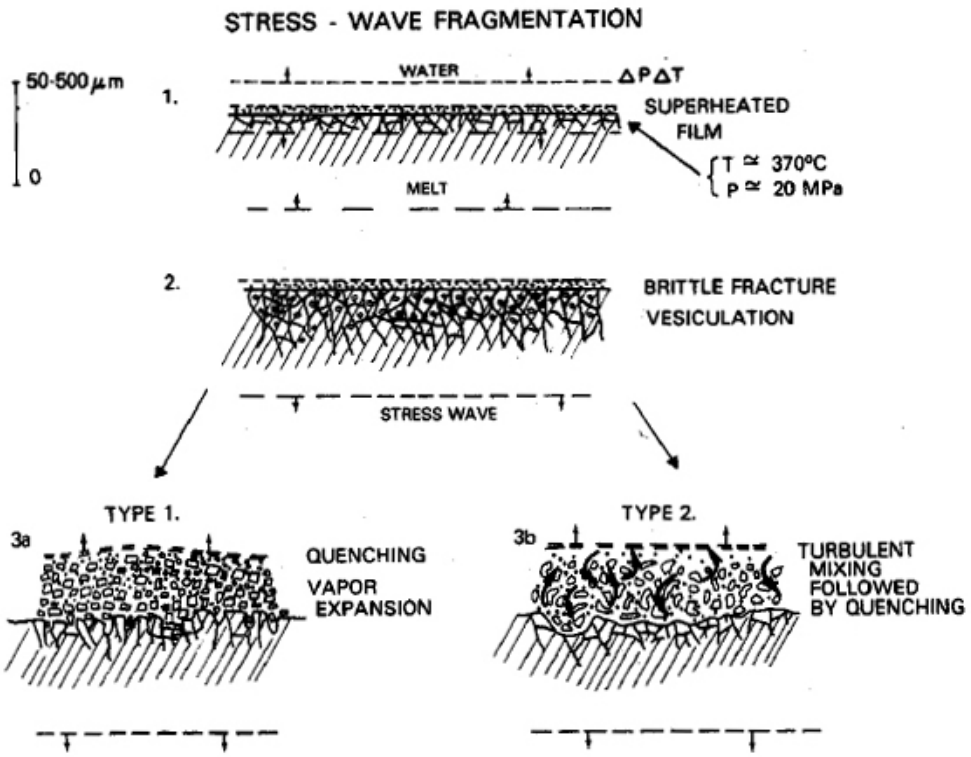

Figure 10: The collapse of a superheated vapor film or the explosive expansion of the film produces stress waves in the melt. If this exceeds the bulk modulus of the melt and it fractures brittly, blocky pyroclasts may form (Wohletz, 1983).

The fundamental observation of grain shape allows interpretation of the relative contribution of magmatic vesiculation and hydrovolcanic water interaction in production of pyroclasts. Magmatic eruptions produce ashes derived directly from a vesiculating magma that has not interacted with meteoric water. Their characteristics are related to the magma strength and viscosity and the thermodynamic behavior of gas phases within the magma (Heiken and Wohletz, 1985). Eruptive and transportation mechanisms of pyroclasts are inferred from the presence of certain "key" structures. For example, recurrence of "shards" and/or an abundance of vesicles are considered indicative of fragmentation processes due to the exsolution of magmatic gases (Dellino and La Volpe, 1996). Plate-like shapes observed in fine fraction may represent pieces of bubble walls or fracture of brittle, foliated lava (Heiken and Wohletz, 1985). The presence of hydration cracks, "mossy" irregular or blocky shapes and/or spherical to fluidal forms, is considered a sufficient condition to refer glassy particles

to hydromagmatic fragmentation processes (Dellino and La Volpe, 1996). Molds of crystals torn from enclosing glass are also typical of hydrovolcanic eruptions. Mossy (or moss-like) shapes (see Figure 9) demonstrate a high surface area to diameter ratio and are common in highly explosive magma-water interactions. High surface area is a necessary condition for highly efficient, conductive heat transfer from the magma to the water (Wohletz, 1987). Blocky grains (see Figure 9) with planar and curviplanar surfaces that may cut vesicle walls are most characteristic of hydrovolcanic fragmentation. This fragmentation mechanism appears to involve a form of brittle fracture and is likely caused by stress waves from the vapor explosions propagating through the melt.

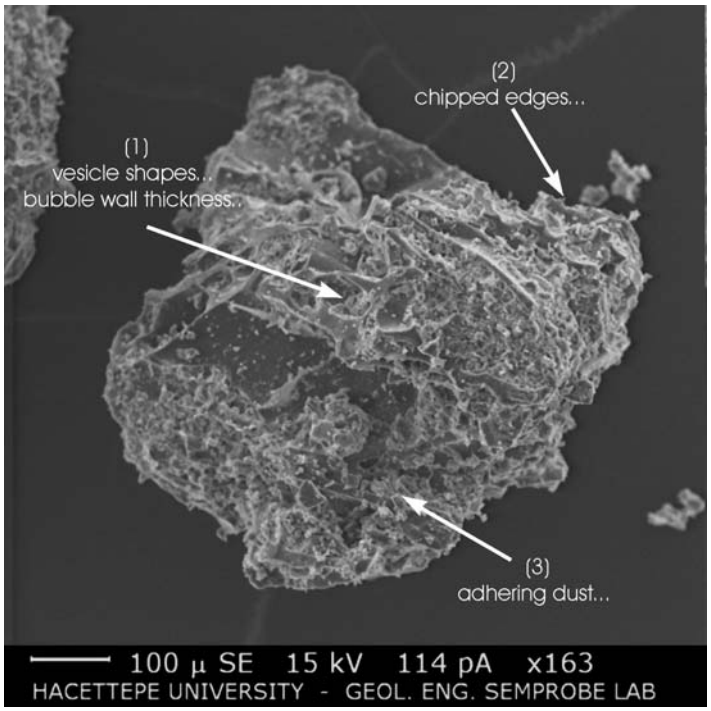

Figure 11: (1) morphologies indicative of ash formation; (2) textures related to transport abrasion; (3) types and amounts of alteration.

All pyroclasts undergo strong attrition in the vent but clasts in pyroclastic flows undergo a second major phase of abrasion during high-energy near-vent flow (Freundt and Schmincke, 1992). Abrasion due to transport may modify the overall grain morphology. Especially the surge ashes have edges that are smoothed and rounded by laminar and turbulent transport where grain collisions are abundant. The typical shapes of grain modification during transport abrasion are chipped edges and dish-shaped fracture surfaces. Fracture surfaces characterized by circular, or nearly circular, concave areas that are the result of conchoidal fracture of glassy material may form due to grain modification during transport abrasion (Heiken and Wohletz, 1985). Recent quantitative studies on outlines of ash particles proved their achievement in characterizing modes of volcanic transport/deposition (Dellino and La Volpe, 1996; Dellino and Liotino, 2002, Riley et al, 2003; Maria and Carey, 2007).
Weathering complicate identification of volcanic ash to the effect that most pre-Tertiary ash deposits are not recognized and consequently are classified as sedimentary rocks or lava flows. Strong alteration may completely obscure primary grain morphology and care must be taken to distinguish between primary and alteration morphologies (Wohletz, 1983). The process of hydration and palagonitization involve chemical and physical changes that are intermediate between those of weathering (diagenesis) and metamorphism. Hydration of glass

occurs when silicic pyroclasts or lavas are altered by water or steam and may be compared with the gradual alteration of basaltic glass during the process of palagonitization (Heiken and Wohletz, 1985). Three sources of water for post-depositional alteration are hydrothermal, groundwater and steam trapped within the deposits. Presence and quantity of the third source of water (steam), determines whether initially fresh deposits are wet and cohesive, or dry (Wohletz, 1983). Steam produced in the eruption may be cool enough to condense on particles as vesicle fillings of alteration material. Hence, the amount of water present in the environment during eruption affects the degree of chemical alteration as well as the energy of explosions (Sheridan and Wohletz, 1981). The first stage of glass alteration is the formation of a skin or rind on grain surfaces. These rinds are usually broken by straight or slightly curved cracks (Fig. 12). These cracks strongly resemble desiccation cracks in mud but are distinguishable from those formed by eruptive fragmentation and grain collisions during transport; both of the latter crack types tend to project through the grain. In the second stage of glass alteration, microcrystalline material forms, initially in vesicle hollows and then over the entire grain surface. In addition to the more common aspects of alteration (hydration-palagonitization-crystallization), solution and precipitation often affect glassy pyroclasts (Heiken and Wohletz, 1985 and references therein). Resulting textures include pitted or scalloped surfaces on a micron scale, rounding of upturned plates or other sharp features, and development of a frosted, light diffused surface as compared to the vitreous surface of fresh glass (Wohletz and Krinsley, 1982).

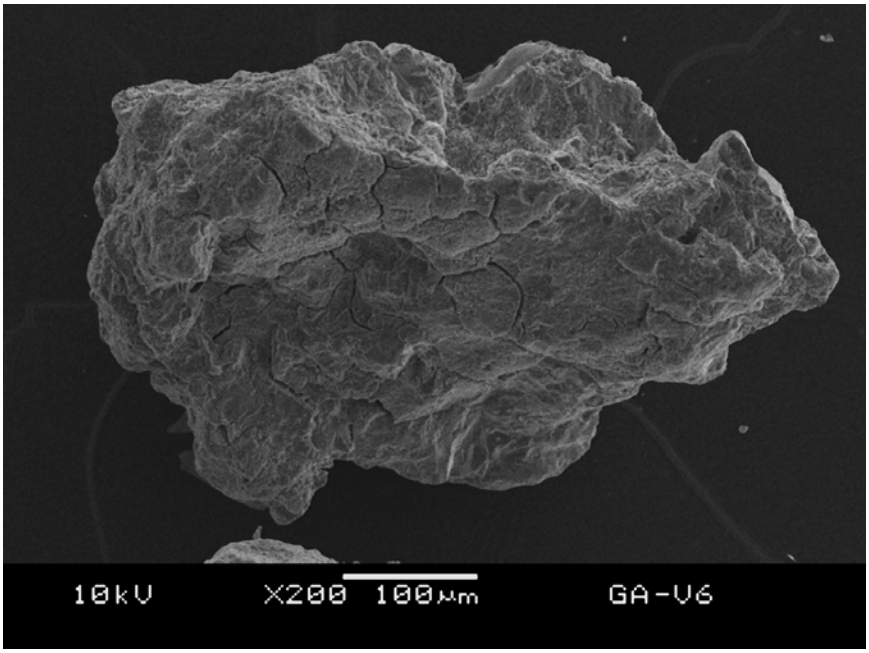

Figure 12: Volcanic ash particle from 1982 eruption of Galunggung (Indonesia). The surface involves hydration cracks formed in the first stage of glass alteration.

Most grains of hydromagmatic origin have surfaces in covered by adhering rounded particles of ash. The particles range in size from 1 to 20 µm and either lightly attached or partially fused to the surface of the larger grains. The abundant, fine, µm-sized material adhering to larger fragments is evidence of origin from strong explosions. These particles of ash represent the micron and smaller size-fraction of ash produced during eruption and are scavenged from the eruption cloud by the larger particles. During volcanic transport, small particles may agglutinate to larger ones due to cohesiveness of wet surfaces or electrostatic charging due to breakage (Wohletz and Krinsley, 1982 and references therein). However, µm-sized adhered

particles are encountered also in magmatic eruptions, even in plinian eruptions. Beside the alteration products, fine-grained broken vesicle wall fragments (shards) may cling to coarser pyroclast surfaces or fill vesicle hollows. The abundance of such angular fine juvenile particles on surfaces and vesicles may provide information on fragmentation mechanisms that are the energetic and related to the high explosive energy release (Zimanowski et al., 2003). Possible reasons for such fine dust on magmatic ash surface are discussed in Section 4.4.

A study of explosive fragmentation dynamics by examination of the morphological features of natural and experimental ash particles has demonstrated the significance of morphological micro-features on ash grains (Wohletz 1983) (see Figures 8 and 9). Hence, the lack of analogue particles produced by scaled experiments at that time however, allowed only a qualitative assessment. Although study of natural pyroclastic sequences combined with scaled laboratory experiments identified the different fragmentation mechanisms related to the water/magma mass ratios during their interaction (e.g. Büttner et al., 1999), the surface features of the ash were not quantified. Bayhurst et al. (1994) developed an automated program for the characterization of volcanic ash particles of Redoubt Volcano (Alaska) based on size, density, shape and mineralogy using a SEM with an energy dispersive X-ray detector (EDS). However, classification of volcanic ash surfaces is still limited to descriptive terms. Qualitative data describing volcanic ash also need to be expressed quantitatively, which requires supplementary methods including e.g. statistical analysis and artificial intelligence. In addition to developable side of quantitative methods with the assistance of supplementary ones, quantitative analyses are methodical and automated whereas qualitative analyses are time consuming and may be affected by the human operator. A test was conducted on seven volcanologists and atmospheric scientists by Sheridan and Marshall (1983) to determine if the operator is a significant variable in the interpretation of SEM micrographs of pyroclasts. Participants were asked to distinguish between fall, flow and base-surge material and to assess certain characteristics of each sample. The performances of operators were closely linked with their experience of correlating surface features with the mode of emplacement. The clast forms of volcanogenic particles are often complex due to morphologies indicative of ash formation, transport abrasion and post-emplacement alteration, whereupon Marshall (1987) states: “This is one reason why the analysis of volcanic clast shape has remained qualitative”. It is clear that quantification of grain shapes would facilitate sample characterization and identification.

2. Image processing and quantitative analysis on ash surfaces

Image analysis is widely used on geological particles in order to assess the shape, orientation and distribution of natural objects (e.g. Capaccioni and Sarocchi, 1996; Dellino and La Volpe, 1996; Capaccioni et al., 1997; Verrecchia, 2003; Maria and Carey, 2007). However, quantitative analysis on natural objects, chiefly on volcanic ash particles largely remained limited with shape measurements on outlines of two-dimensional surfaces (Dellino and La Volpe, 1996; Dellino and Liotino, 2002, Riley et al, 2003; Maria and Carey, 2007). Numerical characterization of particle surface texture, because of its complexity, still remains largely unresolved. This is not a case only for volcanic ash but also for many particles and is the subject of intense research (Stachowiak, 1998). Recently, Horwell et al. (2003) and Durant et al. (2004) measured the surface area of volcanic ash particles to measure the production of radicals on the surfaces and to investigate the ice nucleating ability, respectively. Riley et al (2003) and Kueppers et al. (2005) measured surface areas on ash surfaces by BET (Brunauer, Emmett, and Teller) method in order to assess shape-terminal velocity relation and fragmentation efficiency, respectively. Delmelle et al. (2007) announced the latest progress on quantification of ash surfaces and demonstrated the gas/aerosol-ash interaction in volcanic eruption plumes. Within the context of this study, several quantitative surface descriptors were calculated on two- and three-dimensional volcanic ash surfaces and these simple and well-defined descriptors have been presented in volcanology. Acceptance of quantitative surface descriptors in volcanology community is believed to be a progress in quantitative characterization of volcanic ash surfaces.

Image processing and analysis were performed using the ImageJ program (Rasband, 2004). ImageJ is a public-domain image-processing program based on Java and was designed with an open architecture that provides extensibility via Java plugins (available at http://rsb.info.nih.gov/ij/). The plugins used in the context of this study are freely available and their codes are in the public domain. However, some plugins, chiefly those are belonging to Gary Chinga were modified in accordance with the objects of this study.

2.1. Suitability of gradient analysis for surface structure quantification of volcanic ash

Gradient analysis is one of the most important approaches for characterizing surfaces. Several gradient definitions have been proposed to detect intensity and orientation of surface structures (Chinga et al., 2007). In vector calculus, the gradient of a scalar field is a vector field which points in the direction of the greatest rate of increase of the scalar field, and whose magnitude is the greatest rate of change. To explain the gradient in a macro world, let's consider a hill whose height above sea level at a point (x,y) is $H(x,y)$. The gradient of H at a point is a vector pointing in the direction of the steepest slope or grade at that point. The steepness of the slope at that point is given by the magnitude of the gradient vector.

The orientation of a gradient can be described by the direction of the outward surface normal vector, $\hat{n}$.

In polar coordinates (Fig. 13), $\hat{n}$ is given in terms of the polar angle, θ, and the azimuthal angle, ϕ, by

$$\hat{n} = n_x\hat{x} + n_y\hat{y} + n_z\hat{z} = (\hat{x}\cos\phi + \hat{y}\sin\phi)\sin\theta + \hat{z}\cos\theta \qquad (1)$$

Here, $\hat{x}$, $\hat{y}$ and $\hat{z}$ are unit vectors. $\hat{z}$ is a unit vector in the height direction.

Suppose the topographical image is regarded as a sampled version of the continuous height function z(x, y). Consider a point (x_0, y_0, z_0) on the surface. Approximating the height function by two terms in a Taylor series expansion gives:

$$z - z_0 \approx z(x,y) - z(x_0,y_0) = (x - x_0)\frac{\partial z}{\partial x} + (y - y_0)\frac{\partial z}{\partial y} \tag{2}$$

Alternatively, the equation for the plane tangent to the surface is

$$(x - x_0)n_x + (y - y_0)n_y + (z - z_0)n_z = 0\,. \tag{3}$$

Eliminating for $z - z_0$ between Eq. (2) and Eq. (3) and using Eq. (1) gives:

$$\phi = \arctan\left(\frac{\frac{\partial z}{\partial y}}{\frac{\partial z}{\partial x}}\right),\ \theta = \arctan\sqrt{\left(\frac{\partial z}{\partial x}\right)^2 + \left(\frac{\partial z}{\partial y}\right)^2} \tag{4}$$

These formulas show how the angles are related to the gradients of the height data in the topographical image. The gradients can be estimated by standard image processing techniques (Chinga et al., 2007), as described below.

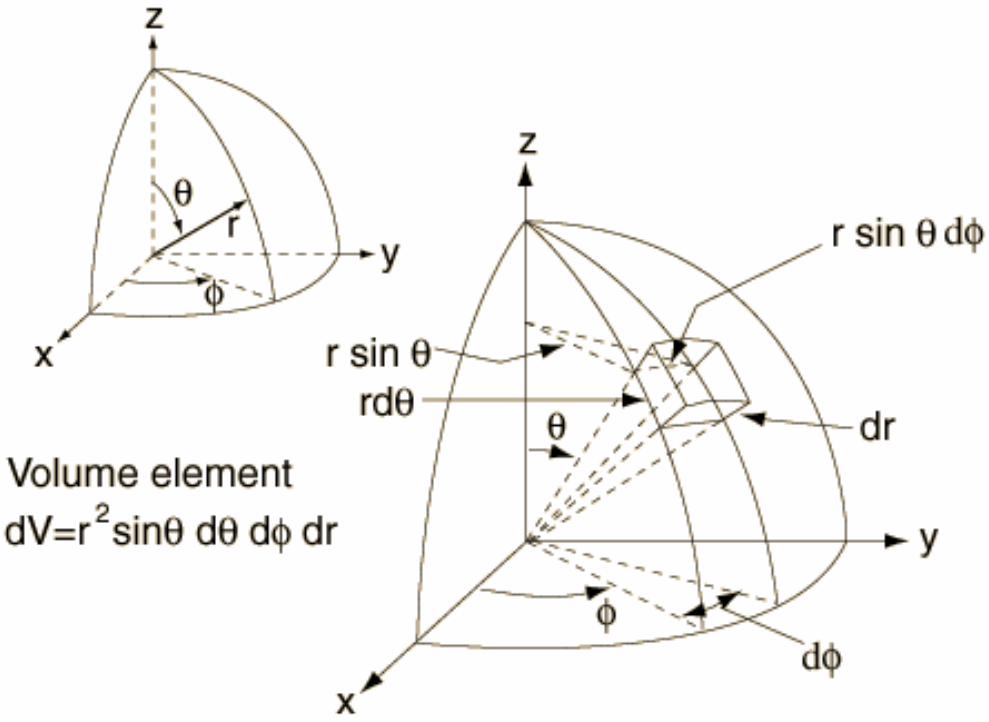

Figure 13: Spherical coordinates, also called spherical polar coordinates (Weisstein, Eric W. "Spherical Coordinates" From MathWorld-A Wolfram Web Resource. http://mathworld.wolfram.com/SphericalCoordinates.html)

Suppose the topographical image gives the height points at the points

$$(x_i, y_j) = (ih_x, jh_y) \quad i = 0,.....,N_x - 1,\ j = 0,.....,N_y - 1\,. \tag{5}$$

Application of the centered finite difference approximation for the partial derivative with respect to x gives

$$\left.\frac{\partial z}{\partial x}\right|_{(x_i,y_i)} \approx \frac{z\left(x_{i+1},y_j - x_{i-1},y_j\right)}{2h_i} \tag{6}$$

In image processing notation, this operation can be applied at every grid point by convolving the image with the 3x3 kernel

$$\frac{1}{2h_x}\begin{bmatrix} 0 & 0 & 0 \\ -1 & 0 & 1 \\ 0 & 0 & 0 \end{bmatrix} \tag{7}$$

Traditionally, the x-derivative at (x_i, y_j) is approximated by averaging this formula at (x_i, y_{j-1}), (x_i, y_j) and (x_i, y_{j+1}), with the weight values of 1, 2, and 1, respectively. This results in a convolution kernel of

$$\frac{1}{8h_x}\begin{bmatrix} -1 & 0 & 1 \\ -2 & 0 & 2 \\ -1 & 0 & 1 \end{bmatrix} \tag{8}$$

for the x-derivative and analogous kernel for the y-derivative.
SurfCharJ plugin (Chinga et al., 2003, available at http://www.gcsca.net) was used for gradient analyses. The processing algorithm produces a polar image representing the magnitude of the gradients relative to the surface and an azimuthal image representing the orientation of the local gradients in the surface plane. The local gradient orientations can be plotted in polar coordinates for gradient intensity analysis (Fig. 14).
The polar plots were analyzed with the *Shape Descriptor* plugin (available at http://www.gcsca.net) and shape descriptors such as form factor, roundness, compactness, aspect ratio, solidity and convexity were calculated on polar plots according to Russ (1999) (Table 1). The fractal dimensions of polar plots were calculated with box counting method using *Fractal-Box-Counter* plugin (defaultly installed on ImageJ). The plugin calculates the so-called "capacity" fractal dimension. A full description of the fractal calculation technique can be found in Smith et al. (1996).

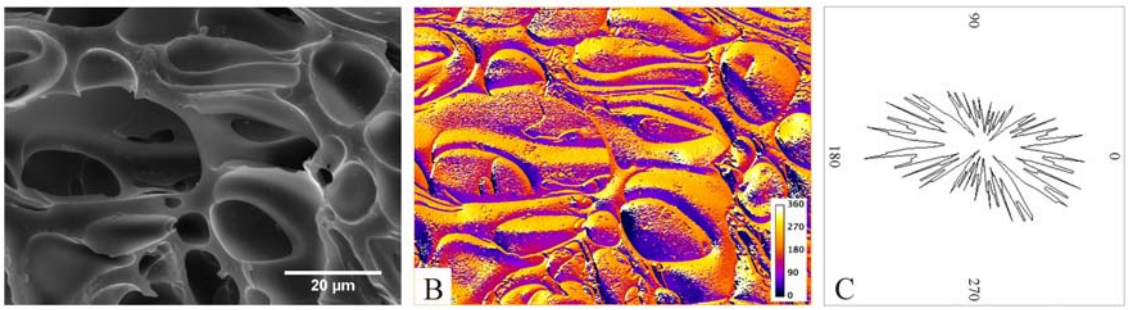

Figure 14: (A) SEM surface image of a volcanic ash (Sample# S1 Tephra). (B) Corresponding azimuthal image. (C) Corresponding polar plot based on frequency of gradients.

2.2. Quadtree decomposition approach for volcanic ash surface assessment

Hierarchical data structures are becoming increasingly important representation techniques in the domains of computer graphics, image processing, computational geometry, geographic information systems, and robotics. They are based on the principle of recursive decomposition. One such data structure is the quadtree (Samet, 1984). In the fields of image processing, computer graphics, and remote sensing two-dimensional point and region data are often indexed using quadtrees (Samet, 1990). Currently, quadtrees are used for point data, regions, curves, surfaces, and volumes.

Table 1 Calculated shape descriptors according to Russ (1999).

Shape descriptor	Formula
Form factor	$= \frac{4\pi \times Area}{Perimeter^2}$
Roundness	$= \frac{4 \times Area}{\pi \times Majoraxis^2}$
Compactness	$= \frac{\left(\left(4/\pi\right)Area\right)^2}{Majoraxis}$
Aspect ratio	$= Majoraxis / Minoraxis$

A quadtree is a representation of a regular partitioning of space where regions are split recursively until there is a constant amount of information contained in them (Wang and Armstrong, 2003). Each quadtree block (also referred to as a cell, or node) covers a portion of space that forms a hypercube in d-dimensions, usually with a side length that is a power of 2 (Hjaltason and Samet, 1999). Many different varieties of quadtrees have been defined, differing in the rules that govern node splitting, the type of data being indexed, and other details (Samet, 1984). Quadtree blocks may be further divided into 2^d sub-blocks of equal size; i.e., the sub-blocks of a block are obtained by halving the block along each coordinate axis, forming an adaptive grid (Fig. 15). A quadtree may be considered as an extended 2^d-ary tree, i.e., a tree in which every non-leaf node has 2^d children (Fig. 15). A quadtree is thus a tree, where the branch structure is based on space coverage (Hjaltason and Samet, 1999).
A quadtree decomposition routine interfaced to the ImageJ program was used for texture characterization (Chinga, 2006).The quadtree decomposition was performed by assessing the local grey value standard deviation (sGL).
The standard deviation is given by:

$$sGL = \left(\frac{1}{wh} \sum_{x=1}^{w} \sum_{y=1}^{h} (\bar{z} - z_{xy})^2 \right)^{1/2} \quad (9)$$

The minimum grey value standard deviation (sGL) of the stack including images was used for the decomposition as the threshold. If the image has a sGL value of threshold, the image is divided into four sub-images or blocks. Each sub-image is evaluated again using the same criteria. Each sub-image having a sGL value larger than the threshold is decomposed into four new sub-images (Fig. 16). This is done iteratively until the local area (sub-image) has a sGL value lower than the given threshold. Three quadtree variables; number of blocks (nQT), the

mean block size (mQT) and the standard deviation of block sizes (sQT) were calculated on volcanic ash surfaces.

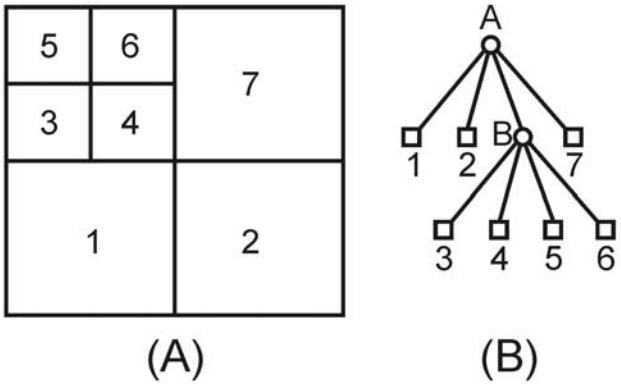

Figure 15: (A) Block decomposition; (B) tree structure of a simple quadtree, where leaf blocks are labeled with numbers and non-leaf blocks with letters (reproduced from Hijaltason and Samet, 1999).

2.3. Surface roughness assessment for volcanic ash

Surface roughness is the micro-geometrical deviation. The geometrical characterization of rough profiles or surfaces is a widespread problem in various geological examples such as erosion patterns, multiphase fluid percolation in porous rocks, fractures, or stylolites (Brouste et al., 2007 and references therein). The roughness parameters are estimated by the analyzing the topography scans of the sample's surface. Thus, everything that affects the "real" imaging of the topography will also affect the roughness estimation. Figure 17 depicts a schematic representation of a surface and the applied terms used to describe it. Surface profiles can be analyzed using normal distribution statistics, such as standard deviation, skewness and kurtosis (Nowicki, 1985). The roughness of a surface can be measured in different ways, which are classified into three basic categories: (1) Statistical descriptors that give average behavior of the surface height (e.g. average roughness Ra; the root mean square roughness Rq; the skewness R_{sk} and the kurtosis R_{ku}), (2) Extreme value descriptors that depend on isolated events (e.g. the maximum peak height Rp, the maximum valley height Rv, and the maximum peak to valley height Rt.), (3) Texture descriptors that describe variations of the surface based on multiple events.

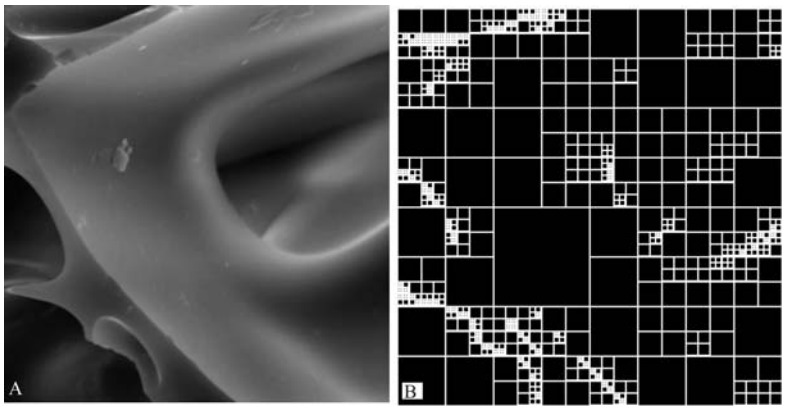

Figure 16: (A) SEM image of a vesicular ash surface (Sample # S1 tephra). (B) Quadtree decomposition of corresponding surface.

In engineering applications, the surface roughness is usually characterized using many statistical parameters defined in the ISO 4287 (2000) standards. A descriptive table including line profile calculations and their corresponding digital routine can be found in Table 2.

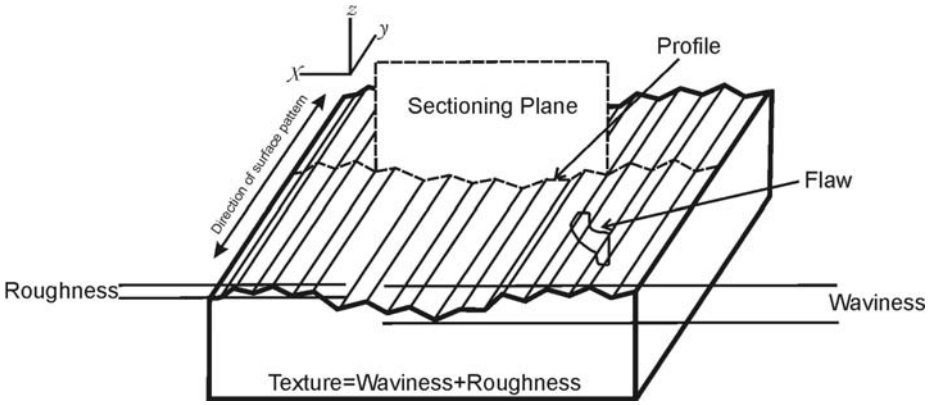

Figure 17: Surface profile (reproduced from TS 6956, 2004).

The average roughness (Ra) is the area between the roughness profile and its mean line or the integral of the absolute value of the roughness profile height over the evaluation length (Fig. 18A). Rq represents the standard deviation of the profile heights (equal to sGL mentioned above if roughness is measured on whole surface beside the profile line) and is used in computations of skew and kurtosis. Maximum profile peak height (Rp) and maximum profile valley depth (Rv) are the distances from the mean line (surface) to the highest and lowest point in the evaluation length/area, respectively (Fig. 18B). Skewness is a measure of the asymmetry of the profile about the mean line. Negative skew indicates a predominance of valleys, while positive skew is seen on surfaces with peaks (Fig. 19A). Kurtosis is a measure of the distribution of spikes above and below the mean line. For spiky surfaces, Rku > 3; for bumpy surfaces, Rku < 3; perfectly random surfaces have kurtosis 3 (Fig. 19B). The detailed explanation of surface characteristics can be found in relevant standards mentioned above. *SurfCharJ* plugin (Chinga et al., 2003, available at http://www.gcsca.net) was used for roughness analysis.

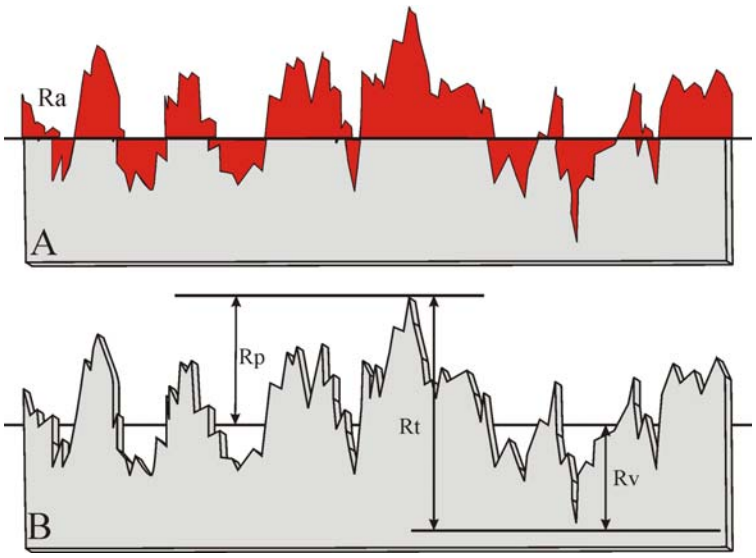

Figure 18: Graphically representation of Ra (A) and extreme value descriptors (B).

2.4. Fractal dimension approach for volcanic ash surfaces

The need for a rigorous, quantitative measure of "shape" has been a longstanding requirement in most sciences. Fractal geometry represents a major advance over previous methods for quantifying and simulating the complex patterns encountered in nature that were previously described only qualitatively. Fractals have been used more than two decades in geology for the description of outline and surfaces (Bérubé and Jébrak, 1999 and references therein). The fractal characterization of surface topography can improve conventional description of the irregularities of the profile. Moreover, close correlation between calculated areas based fractal dimension values and the measured roughness average values takes place (Grzesik and Brol, 2003).

Table 2 Profile parameters according to ISO 4287(2000). The corresponding digital routine is also given

R-parameter	Line Profile	Digital Routine	Description
Ra	$=\frac{1}{l}\int_0^L \lvert z(x)\rvert dx$	$=\frac{1}{mn}\sum_{i=1}^{m}\sum_{j=1}^{n}\lvert zij\rvert$	Arithmetical mean deviation
Rq	$=\sqrt{\frac{1}{l}\int_0^L z^2(x)dx}$	$=\left(\frac{1}{mn}\sum_{i=1}^{m}\sum_{j=1}^{n} zij^2\right)^{1/2}$	Root mean square deviation
Rsk	$=\frac{1}{Rq^3}\left[\frac{1}{l}\int_0^L z^3(x)dx\right]$	$=\frac{1}{Rq^3}\frac{1}{mn}\sum_{i=1}^{m}\sum_{j=1}^{n} zij^3$	Skewness of the assesed profile
Rku	$=\frac{1}{Rq^4}\left[\frac{1}{l}\int_0^L z^4(x)dx\right]$	$=\frac{1}{Rq^4}\frac{1}{mn}\sum_{i=1}^{m}\sum_{j=1}^{n} zij^4$	Kurtosis of the assesed profile
Rv			Largest profile valley depth
Rp			Largest profile peak height
Rt	$=Rv+Rp$		Sum of largest profile valley depth and peak height within the evaluation length

Note: Table data were taken from Chinga et al. (2003).

Fractals are a relatively new concept in science-about 40 years old (Mandelbrot, 1967). The general idea of a fractal has been introduced by Unwin (1989). There are several ways in which the general idea of fractals can be introduced. Usually this is as"space filling" geometry or by way of the "Steinhous Paradox" for "wiggly lines" (Whaley and Orford, 1989 and references therein). Practically, the idea of a fractal can be best seen in the coastline problem originally suggested by L.F. Richardson and discussed in Mandelbrot (1982). Fractal concepts now are being used in many areas of scientific enquiry and two complementary approaches can be identified. First, the description of irregularity in a formal framework has led to the application of fractals in many traditional areas of scientific measurement which are being informed by these ideas. Second, complementing description and measurement is the notion that fractals can be used to generate or simulate irregularity by building computer models of various natural and artificial forms (Longley and Batty, 1989).

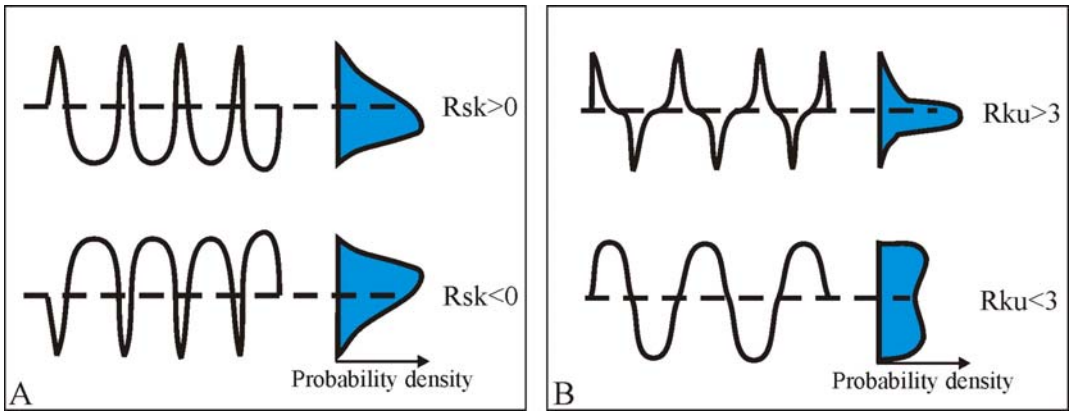

Figure 19: (A) Negative skew indicates a predominance of valleys, while positive skew is seen on surfaces with peaks. (B) For spiky surfaces, Rku > 3; for bumpy surfaces, Rku < 3; perfectly random surfaces have kurtosis 3

Fractals are self-similar sets of fractional dimensional. A pattern is self-similar if it composed of smaller-scale copies of itself. One should envision a fractal as an infinite regression of smaller and smaller images that constitute a whole that is similar to its parts. Because of self-similarity, fractals are also "scale invariant", or "scaling". Scale invariance means that they appear (mathematically, if not visually) to be the same at all scales of observation. The fundamental parameter of fractal sets is their fractal (or Hausdorff-Besicovitch) dimension, which, in fractals, is always a fraction, not an integer. Fractals form complex, irregular phenomena like those that predominate in nature. A fractal can be any kind of set: points, lines, surfaces, multi-dimensional data, or time series (Brown, 2001).
Almost any homogeneous power-law distribution is fractal because it is the only statistical distribution that does not possess a characteristic or inherent scale. Therefore, they are scale invariant and self-similar, which are the diagnostic qualities of fractals. Fractal, or power law, distributions take the general form

$$Y = aX^b \tag{10}$$

in which a is a constant and b is the parameter of interest. If one takes the logarithm of both sides of the equation, one obtains:

$$\ln Y = \ln a + b \ln X \tag{11}$$

This is a linear transformation. By plotting the logarithms of the variables, one can obtain an approximation of this linear relationship and thereby estimate the parameters of the power law (Brown, 2001 and references therein). Natural logarithms was used here, one can also use common (base 10) logarithms.
Traditionally, statistical functions and parameters, such as auto-correlation function, correlation length, auto-covariance function, structure function, etc., have been used to characterize the surface topography. The physical characteristics of some bodies are related to the fractal dimensions of their surfaces (Ortega et al., 2003). Recently, fractal methods have also been applied to describe the complexity of surface topography (Stachowiak, 1998, and references therein). The studies on fractal geometry of volcanic particles were limited with the boundary of a particle that results from an intersection with a plane, i.e. a thin section of a grain, contours obtained from SEM micrographs or photographs directly taken from drill cores or exposures (Carey et al., 2000; Dellino and Liotino, 2002; Barnett, 2004; Maria and Carey, 2007). The fractal dimensions of surfaces were calculated with the plugin of *Fractal Count for Maps 1.36* written by Per Christian Henden (available at:

http://www.pvv.org/~perchrh/imagej/fractal.html). Fractal Count for Maps estimates the fractal dimension of 2D greylevel images interpreted as topographic surface, i.e. images where the value of each coordinate specifies the height of that coordinate. The algorithm of the plugin is discussed in Wen-Shiung et al. (2003).

3. Supplementary analysis

3.1. Modeling of granulometric data and sequential fragmentation/transport theory

In order to better characterize the samples with respect to their size-distribution, and highlight possible changes in the fragmentation processes occurred during eruptions, the SFT (Sequential Fragmentation/Transport) theory (Wohletz et al., 1989) has been applied to tephra which was sufficient in amount to allow grain-size analysis. Bulk samples of tephra were sieved and segregated into several size classes at intervals of 1 phi (up to 4 phi), and the weight of each fraction was measured. The theory describes the size characteristics of a distribution of particles as they first undergo fragmentation and then attrition and size sorting during transport within a liquid or gaseous media (Fig. 20). It has been developed in order to find a particle size distribution based upon a physical, rather than empirical, basis that would provide a good fit to particle size distributions in pyroclastic deposits. The theory applies to a particle-mass distribution that undergoes a sequence of fragmentation and transport events starting from an initial parental mass: the population distribution resulting from each event is a function of the initial mass and of the nature of the fragmentation process, and is characterized by only one free parameter, γ (or dispersion; $\gamma \geq -1$). γ is -1 for an undefined distribution resulting from 0 events, and tends to become more positive as the number of fragmentation events that the population undergoes increases. Also, because of its physical basis, a range of γ values is predictable for a given fragmentation mechanism. Wohletz et al. (1989) demonstrated that in most pyroclastic deposits the sequential fragmentation/transport distribution provides a better fit than the more commonly used, empirical log-normal one; however, Brown and Wohletz (1995) show that the log-normal distribution can be mathematically derived from SFT.

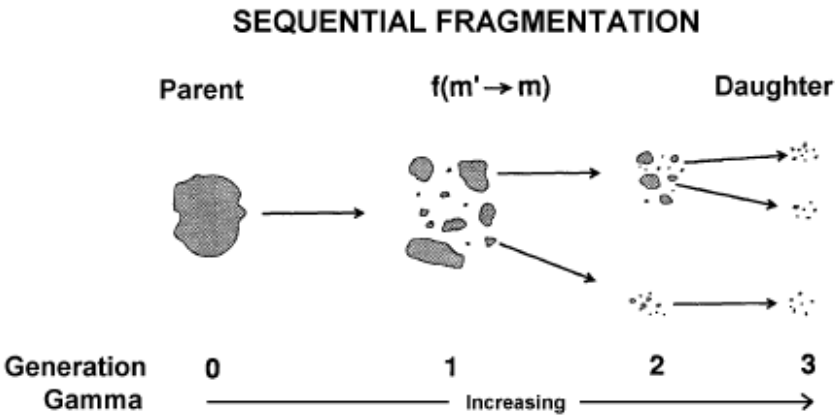

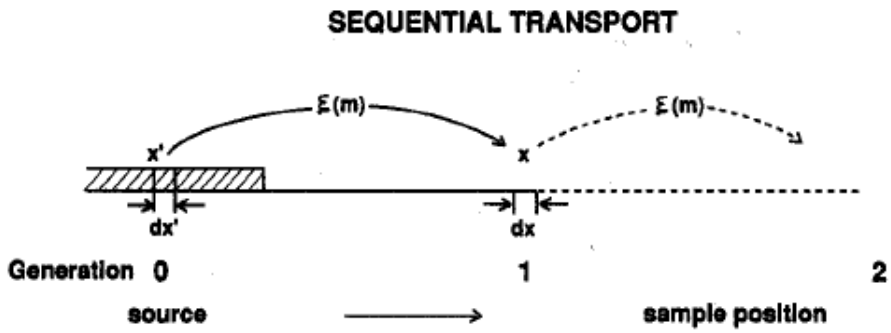

Figure 20: Schematic illustration of physical model for sequential fragmentation and transportation. Note that each generation is an ensemble of fragments that may range in size from the very finest particles to one that is nearly as large as its parent from the pervious generation. Such continued comminution produces a fragmentation cascade resembling a chain reaction (Wohletz et al, 1989).

The grain size distributions were analyzed using the Windows-based software SFT (a new version of SEQUEN from Wohletz et al., 1989), which allows user-interactive discrimination of the subpopulations present in the distribution, and their characterization in terms of three parameters: mode, dispersion and weight fraction.
The approaches for fragmentation and transportation of tephra using three parameters mentioned above are represented in concerning applications in sections ahead.

3.2. Artificial intelligence

Visualizing multi-dimensional data is critical to understanding complex relationships in natural systems; consequently, earth scientists are faced with increasingly large amounts of data. As the dimensionality of the data increases, the complexity of visualizing relationships also increases. To understand natural systems, data from diverse sources must be integrated in a manner that is comprehensible to human interpretation (Penn, 2005). Several approaches have been presented to convey high-dimensional data (e.g., Tukey, 1977; Levoy, 1988; Wegman and Solka, 2002). Methods, which preserve certain properties of the structure of the data set as faithfully as possible, are, called 'projection methods' (Ripley, 1996). A projection method that categorizes or groups similar data items is termed 'clustering'. Clustering methods can be divided into two basic types: hierarchical and partitional clustering (Kaski, 1997 and references therein). In this study, mostly data reduction method (linear projection method) factor analysis (principal component analysis) was performed on data to visualize different type volcanic ashes. The utility of factor analysis is plotting the singular samples on a factor diagram as factor scores ([Fr]). The most suitable parameters for differentiating between samples were determined by p-values well below 0,05 or 0,001 at a 95% confidence interval (C.I.) in analysis of variance (ANOVA). Furthermore, self-organizing maps (SOM) were used to cluster the different types of volcanic ash particles.
The self-organizing map (SOM) is a subtype of artificial neural networks (ANN) which are relatively crude electronic models based on the neural structure of the brain. ANN attempt to mirror the brain functions in a computerized way by resorting to the learning mechanism as the basis of human behaviour (Lipman, 1987; Anderson and McNeil, 1992; Hagan et al., 1996; Kartalopoulos, 1995). They are commonly composed of a large number of nodes, architecturally organised into layers, with connections between nodes in adjacent layers. The utility of ANN is that they can be used, through selection of an appropriate connection-weight

adjustment or training technique, to develop models of complex system behaviour (Aitkenhead et al., 2007 and references therein).
Inspired by the structure of the brain, a neural network consists of a set of highly interconnected entities, called *nodes* or *units*. Each unit is designed to mimic its biological counterpart, the neuron. Each accepts a weighted set of inputs and responds with an output (Skapura, 1996). Each unit has an input/output (I/O) characteristic and implements a local computation or function. The output of each unit is determined by its I/O characteristic, its interconnection to other units and (possibly) external inputs, and its internal function. The network usually develops an overall functionality through one or more forms of training. The fundamental unit or building block of the ANN is the artificial neuron (termed neuron from here on). The neuron has a set of inputs (X_i) weighted before reaching the main body of the processing element. In addition, it has a bias term, a threshold value that has to be reached or exceeded for the neuron to produce a signal, a non-linearity function (f_i) that acts on the produced signal (R_i), and an output (O_i) (Lipman, 1987; Haykin, 1994; Hagan et al., 1996; Kartalopoulos, 1995). The basic model of a neuron is illustrated in Figure 21.

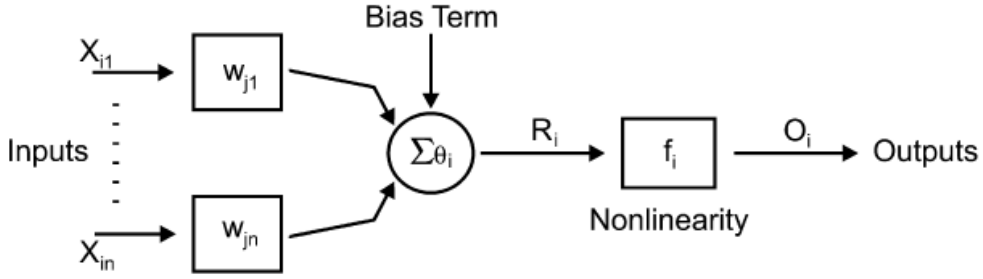

Figure 21: Basic model of artificial neuron.

Because all ANN are based on the concept of neurons, connections, and transfer functions, there is a similarity between the different structures or architectures of neural networks. The majority of the variations stem from the various learning rules and the way in which these rules modify a network's typical topology (Aleksander and Morton, 1990; Anderson and McNeil, 1992; Fausett, 1994; Schalkoff, 1997). Because of the advantages and accuracy of Kohonen self-organizing maps (SOM) for clustering problems of geological materials (Chang et al., 2002), SOM were used for the clustering problem of volcanic ash particles in the context of this thesis.

3.2.1. Kohonen self-organizing maps

Kohonen self-organizing maps (SOM) are unsupervised artificial neural networks developed by Kohonen (1982). They represent the result of a vector quantization algorithm that places a number of reference or codebook vectors into a high-dimensional input data space to approximate its data sets in an ordered fashion. When local-order relations are defined between the reference vectors, the relative values of the latter are made to depend on each other as if their neighboring values lie along an 'elastic surface'. By means of the self-organizing algorithm, this 'surface' becomes defined as a kind of nonlinear regression of the reference vectors through the data points. Mapping from a high-dimensional data space R^n onto, for example, a two-dimensional lattice of points, is thereby also defined. Such mapping can be used to effectively visualize metric ordering relations of input samples. In practice, mapping is obtained as an asymptotic state in a learning process (Kohonen et al., 1996).

4. Two-dimensional (2D) applications

4.1. Texture discrimination of volcanic ashes from different fragmentation mechanisms: A case study, Mount Nemrut stratovolcano, eastern Turkey

ELSEVIER

Computers & Geosciences 32 (2006) 936–946

COMPUTERS & GEOSCIENCES

www.elsevier.com/locate/cageo

Texture discrimination of volcanic ashes from different fragmentation mechanisms: A case study, Mount Nemrut stratovolcano, eastern Turkey

Orkun Ersoy[a,*], Gary Chinga[b], Erkan Aydar[a], Alain Gourgaud[c], H. Evren Cubukcu[a], Inan Ulusoy[a]

[a]*Department of Geological Engineering, Hacettepe University, 06532 Beytepe-Ankara, Turkey*
[b]*Paper and Fibre Research Institute (PFI), Høgskoleringen 6B, 7491 Trondheim, Norway*
[c]*Université Blaise Pascal, UMR-CNRS 6524, 5 rue Kessler, 63038 Clermont-Ferrand, France*

Received 3 May 2005; received in revised form 30 September 2005; accepted 21 October 2005

Abstract

Multicondition-driven mechanisms may produce pyroclastic deposits varying in fundamental properties such as dispersal, grain size, vesicularity and morphology of juvenile clasts, and the abundance of lithic or "wall rock" ejecta (xenoliths). Volcanic ash particles from different fragmentation mechanisms have different surface textures and morphologies. The analysis of the volcanic clast shape remained largely qualitative. A new method for ash particle characterization based on quadtree decomposition and surface gradient analysis is introduced. The approach is applied for assessing fragmentation mechanisms operating during eruptions. The surface descriptor variables like the number of quadtree blocks (nQT), the mean block size (mQT), the standard deviation of block sizes (sQT) and the surface descriptors derived from gradient analysis seem to be suitable for quantifying the structural changes of the ash surface due to variable explosion conditions. These parameters are presented in volcanology as distinctive key parameters for different eruption types. This may enrich our capabilities for effective prediction for the basis of planning to overcome the impending danger of eruptions.

Keywords: Nemrut; Volcanic ash; Hydrovolcanism; Quadtree decomposition; Gradient analysis

1. Introduction

1.1. Mount Nemrut

Mount Nemrut, an active stratovolcano in eastern Turkey, is a major danger for its vicinity. The volcano exhibits a summit caldera having a surface area of 8.5 km × 7 km. The eastern half of the caldera is filled by pyroclastic deposits related to maar-like explosion craters, lava domes and flows. The western half is filled by a freshwater lake covering a surface area of 5.3 km × 3 km and a small lake with hot springs. The fumarole activity is also present over a dome situated at the northern part of the caldera (Aydar et al., 2003). On the post-caldera stage of the volcano, related to the alternating

*Corresponding author. Tel.: +90 312 2977700; fax: +90 312 2992034.
E-mail address: oersoy@hacettepe.edu.tr (O. Ersoy).

0098-3004/$ - see front matter © 2005 Elsevier Ltd. All rights reserved.
doi:10.1016/j.cageo.2005.10.013

mass ratio of interacting water and magma, subplinian dispersal of pumice and air falls, base surge deposits with dune and anti-dune structures, cross-beddings, bread-crust bombs are observed.

1.2. Volcanic ash formation

Volcanic ashes are the particles with average diameters <2 mm those produced during volcanic eruptions by mechanical fragmentation of magma and/or country rock. There are three main mechanisms of volcanic ash formation: (1) the release of gases due to decompression within the magma ascending to the surface (magmatic eruptions), (2) chilling and explosive fragmentation of magma during contact with ground and surface water or ice and snow (phreatomagmatic eruptions), and (3) the comminution and ejection of particles from vent walls or crater debris during eruptions of steam and hot water (phreatic eruptions). Volcanic ash can be produced by one or more of these mechanisms (Heiken and Wohletz, 1985).

The term phreatomagmatic was introduced by Stearns and MacDonald (1946) in reference to explosions resulting from the conversion of groundwater to steam by ascending magma. A phreatomagmatic explosion refers to natural phenomena produced by the interaction of magma or magmatic heat with an external source of water, such as surface body or an aquifer (MacDonald, 1972; Sheridan and Wohletz, 1981). The products are water, steam, juvenile clasts and brecciated country-rocks (accessory and/or accidental xenoliths).

Accessory particles are fragmented co-magmatic volcanic rocks from previous eruptions of the same volcano. Accidental fragments are derived from the subvolcanic basement and therefore may be of any composition (Fisher and Schminke, 1984). Phreatomagmatic deposits are rich in xenoliths indicating the fragmentation of country rock with high energies due to abundant water (vapour).

Volcanic ash deposits produced during these eruptions are unique and their characteristics may be used to interpret eruptive mechanisms. The phreatomagmatic deposits contain grains that have been significantly affected by a variety of processes related to their formation, transport and alteration. The common shapes of glass pyroclasts can be ascribed to varying energies and modes of contact of water with magma, including blocky-equant, moss-like, plate-like and drop or spherical (Wohletz, 1983). Considering the explosive mechanisms and the presence of such glass shapes show that phreatomagmatic ash is formed by thermal contraction and shattering of glass which inhibits vesiculation. The very drastic increase in viscosity and the increase in solubility due to the decrease in temperature prevent volatiles from exsolution (Fisher and Schminke, 1984). The widely varying clast vesicularities reflect complex variations in the relative timing of vesiculation and water-induced fragmentation. Magma–water interaction at an early stage greatly reduces the vesicularity indices ($<40\%$) and broadens the ranges (as high as 80%), whereas late-stage interaction has only a minor effect on the index and broadens the range to a limited extent (Houghton and Wilson, 1989).

Deposits from phreatomagmatic eruptions are characteristically fine-grained, although coarse-grained lapilli- and tuff-breccias are common in some deposits (Fisher and Schminke, 1984). Walker (1973) shows that the median diameters is less than 1 mm in about 75% of the samples from phreatomagmatic explosions in Azores and Iceland. In any fragmentation mechanism the generated particles sizes reflect the kinetic energy available (i.e., the fragmentation energy density). Consequently, fine ash provides information on fragmentation mechanisms that are the most energetic and related to the highest explosive energy release (Zimanowski et al., 2002). With increasing water interaction, phreatomagmatism increases in explosivity. The abundance of fine ash (<63 μm) increases from 5 to over 30% as water interaction reaches an explosive maximum (Wohletz, 1983).

An important consideration is that both magmatic and phreatomagmatic fragmentation mechanisms may operate during an eruption. This situation was illustrated by Self and Sparks (1978) for phreatoplinian silicic eruptions in which magma is initially disrupted by exsolution and expansion of magmatic volatiles, producing relatively coarse-grained pyroclasts. Further fragmentation (fine-grained pyroclasts) is caused by explosive interaction with water. Theoretical consideration of experimental fragmentation mechanisms suggests that stress waves produced by high-pressure, vaporization of water at the magma/water interface may, in part, induce vesiculation in the melt (Heiken and Wohletz, 1985).

1.3. Classification of volcanic ash

Scanning electron microscopy (SEM) provides a method for classifying volcanic ash based upon

surface morphology and texture (Wohletz and Krinsley, 1982). Heiken (1972, 1974), Wohletz (1983) and Heiken and Wohletz (1985) presented the most extensive SEM studies of pyroclast shapes and found a marked difference in grain morphology between magmatic and phreatomagmatic ashes. While some forms of glassy particles refer to phreatomagmatic or magmatic fragmentation, the lack of clear "key" structures prevents the classification (Dellino and La Volpe, 1996). The success in the discrimination depends on the experience of microscopist (Sheridan and Marshall, 1983). Thus the analysis of the volcanic clast shape remained largely qualitative (Marshall, 1987).

Dellino and La Volpe (1996) introduced new methods using particle outline parameters such as elongation, roundness, compactness and rectangularity to define the particle forms from Monte Pilato-Rocche Rosse. The outline parameters are influenced by transportation mechanisms (Dellino and La Volpe, 1996) and the effects of transportation abrasion may be misinterpreted as fragmentation features or vice versa.

1.4. Texture characterization

Several texture descriptors have been developed to characterize the detailed surface structure of, e.g. aluminium (Lee et al., 1998), aggregate (Rao et al., 2003), wear particles (Stachowiak, 1998) and paper surfaces (Chinga et al., 2003; Chinga, 2004). Fractal dimension, autocorrelation, gradient analysis, bandpass filtering, wavelet analysis, roughness statistics and quadtree decomposition have been applied to assess complex surface structures (Panozzo Heilbronner, 1992; Costa, 2000; Chinga et al., 2003; Chinga, 2005). In this respect, quadtree decomposition seems to be an easy, intuitive and powerful technique for characterizing the horizontal and vertical variation of surfaces (Chinga, 2005).

Hierarchical data structures are becoming increasingly important representation techniques in the domains of computer graphics, image processing, computational geometry, geographic information systems, and robotics. They are based on the principle of recursive decomposition. One such data structure is the quadtree (Samet, 1984). In the fields of image processing, computer graphics, and remote sensing two-dimensional point and region data are often indexed using quadtrees (Samet, 1990). Currently, quadtrees are used for point data, regions, curves, surfaces, and volumes. In this paper, the quadtree representation of data is concerned with the representation of region data. A region quadtree is a representation of a regular partitioning of space where regions are split recursively until there is a constant amount of information contained in them (Wang and Armstrong, 2003). Each quadtree block (also referred as a cell, or node) covers a portion of space that forms a hypercube in d-dimensions, usually with a side length that is a power of 2. Quadtree blocks may be further divided into 2^d sub-blocks of equal size; i.e., the sub-blocks of a block are obtained by halving the block along each coordinate axis, forming an adaptive grid (Fig. 1A). A quadtree may be considered as an extended 2^d-ary tree, i.e., a tree in which every non-leaf node has 2^d children (Fig. 1B). A quadtree is thus a tree, where the branch structure is based on space coverage (Hjaltason and Samet, 1999).

Gradient analysis is also suitable for describing texture orientation. Similar methods have been used to detect the orientation of short-fibre composites (Gadala-Maria and Parsi, 1993) and actin fibres in cytoskeletal structures (Yoshigi et al., 2003). This may be valuable information for differentiating between textures having the same greylevel variation. The gradient analysis is based on Sobel operators as described by Gonzalez and Woods (1993) and implemented by Chinga et al. (2003).

This study introduces a new method for ash particle characterization based on a quadtree decomposition approach and gradient analysis. The approach is applied for assessing fragmentation mechanisms operating during eruptions. The calculated quadtree variables like the number of blocks

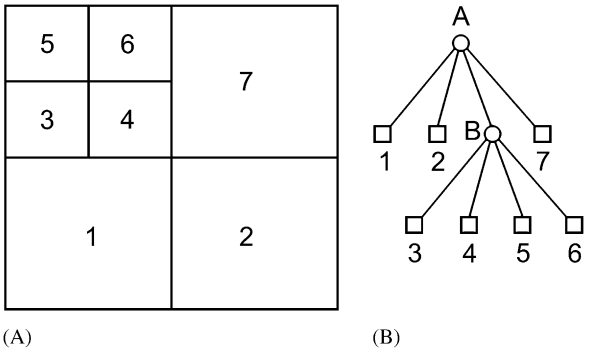

Fig. 1. (A) Block decomposition; (B) tree structure of a simple quadtree, where leaf blocks are labeled with numbers and non-leaf blocks with letters (reproduced from Hjaltason and Samet, 1999).

(nQT), the mean block size (mQT) and the standard deviation of block sizes (sQT), as well as surface descriptors derived from gradient analysis seem to be suitable for quantifying the structural changes of the ash surface due to variable explosion conditions. These parameters are presented in volcanology as distinctive key parameters for different eruption types.

2. Materials and methods

2.1. Sample description

Three samples denoted Nemrut1 (N1), Nemrut2 (N2) and Nemrut3 (N3) and indicating the changes in eruption styles were selected. Samples were taken from the very proximal location, the interior side of the caldera rim. Unvesiculated and rounded particles with hydration cracks are common in sample Nemrut1 which was collected from a base surge deposit. Few vesicles on Nemrut1 are filled with adhering dust. Particle morphologies of this sample exhibit the water effect. Sample Nemrut2 is highly vesiculated. The tubular vesicles are prevalent indicating the effects of a magmatic origin. Nemrut3 is also highly vesiculated, and exhibits tubular vesicles. It is not easy to separate the phreatoplinian samples Nemrut2 and Nemrut3 with naked eye. In the field, the arrangement of deposits from base to top is Nemrut3, Nemrut2 and Nemrut1 indicating the progressive increase in amount of water interacting with magma.

In addition, 160 samples were collected from the Nemrut Volcano (Turkey) for ash details determination. The samples from Nemrut show differences in bed structures, grain sizes, xenolith contents, density and vesiculation indicating the continuous changes in the eruption style (for details see Ersoy et al., in preparation). The grain size analysis includes drying, sieving and weighting of the different grain-size classes in phi scale. Percentage of tephra finer than 1 mm and median diameter (Md) were used to show the finer grain sizes related to high explosion energies due to abundant water. Particles of the 2–4 and 4–8 mm size classes were hand-picked under a binocular stereoscope for particle analysis. The different components were weighed and the weight percentage was calculated. The components are juvenile vesicular grains, unvesicular juvenile clasts and brecciated country-rocks (xenoliths). The dense rock equivalent (DRE) density has been determined on non-vesicular, dense grains, while the average clast density is that of the most vesiculated fragments. The density of juvenile fragments was measured with a pycnometer after coating fragments with a silicon-based aerosol which has negligible mass. About 10 measurements per sample were carried out in the 4-8 mm grain classes. The mean values were then considered. The vesicularity index (V%) was calculated using the method of Houghton and Wilson (1989). The results for three samples N1, N2 and N3 are given in Fig. 2. The percentages of material finer than 1 mm in samples show the decreasing grain size through the explosion produced the last sample (N1) with abundant water interacted with magma. The decreasing median diameters also point the increasing water interaction through the eruption. The increasing xenolith contents through the last sample (N1) also exhibits increasing fragmentation of country rocks with increasing energies due to the abundant water (vapour). The increasing densities and decreasing vesicularities of particles demonstrate the increasing role of external water versus magmatic volatiles in driving explosive eruption.

2.2. Sample preparation and image acquisition

The samples from the three eruption types were washed to remove any organic, loosely adhered and cementing material. Depending upon the freshness of the grains, washing included soaking in hot, dilute HCl and acetone or cleaning in acetone using ultrasound for not more than 4 min to preserve grain edges (Heiken and Wohletz, 1985). The samples were mounted on stainless-steel stubs using double stick tape and coated with carbon in order to counteract grain surface charging while scanning with the electron beam.

A CAMECA SU-30 operating at secondary electron mode with 17 KeV was used at Hacettepe University (Turkey) to take the whole grain and detailed surface photographs. The grain size interval of 250–355 μm was selected for comparing the textures with other studies (Wohletz, 1983; Heiken and Wohletz, 1985). Ten scanning electron images were acquired from each sample.

2.3. Image processing and analysis

Image processing and analysis of the secondary electron images (SEI) were performed using the ImageJ program (Rasband, 2004). The SurfCharJ plugin (Chinga et al., 2003) was used for surface

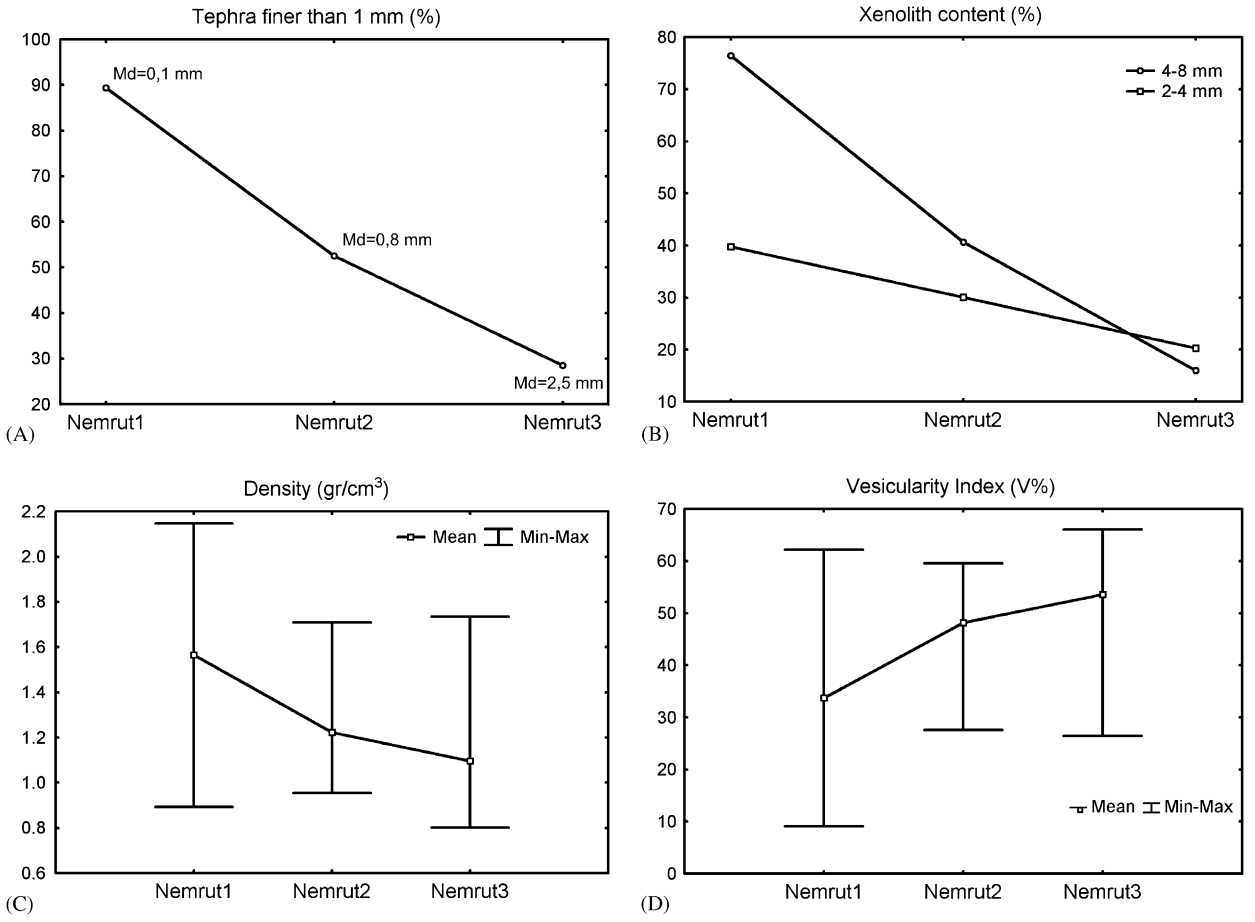

Fig. 2. Determination of volcanic ash details. (A) Percentage of tephra finer than 1 mm; (B) xenolith ratio; (C) density; (D) vesicularity index.

assessment and gradient analysis. The SurfCharJ plugin describes surface representations by calculating surface statistics like the standard deviation, the skewness, the kurtosis, mean greylevel (mGL) and standard deviation of greylevel values (sGL). The statistics were calculated for all the images. The standard deviation is given by

$$\text{Standard deviation} = \left(\frac{1}{wh} \sum_{x=1}^{w} \sum_{y=1}^{h} (\bar{z} - z_{xy})^2 \right)^{1/2}, \quad (1)$$

where w and h are the image dimensions, $\bar{z}$ the mean greylevel and z_{xy} local greylevel at local position x,y. For details about the surface descriptors yielded by the SurfCharJ plugin see Chinga et al. (2003).

A gradient analysis based on Sobel operators was performed. The computation of the gradient of an image is based on obtaining the partial derivatives at every pixel. Derivatives may be implemented in several ways, however, the Sobel operators have the advantage of providing both differencing and a smoothing effect (Gonzalez and Woods, 1993). This smoothing effect of Sobel operators is particularly attractive due to the noise enhancing effect of derivatives. Derivatives based on Sobel operator masks are

$$G_x = (z_7 + 2z_8 + z_9) - (z_1 + 2z_2 + z_3) \quad (2)$$

and

$$G_y = (z_3 + 2z_6 + z_9) - (z_1 + 2z_4 + z_7), \quad (3)$$

where the z's represent the greylevels overlapped by the 3×3 mask at any location in an image. The numbering of the z-values corresponds to the sequence from left to right, top to bottom in a 3×3 mask. The direction at the location of the

centre of the masks is given by

$$\alpha(x,y) = \tan^{-1}\left(\frac{G_y}{G_x}\right), \quad (4)$$

where the angle is measured with respect to the x-axis (for details see Gonzalez and Woods, 1993).

The images, filtered with Sobel operators, yield azimuthal images with gradients having values in radians, which are converted to angles between -180° and 180° relative to the x-axis (Fig. 3B). The frequency of the gradients is plotted in polar coordinates to form a polar plot indicating the preferred orientation of the structure.

The polar plot was analysed with the Shape descriptor plugin (available at http://home.online.no/~gary.c) for assessing the shape of the generated plot. Different shape descriptors like the aspect ratio, compactness, roundness and form factor were calculated according to Russ (1999). The form factor seems suitable for describing the polar plot shape (Eq. (5)).

$$\text{Form factor} = \frac{4\pi A}{P^2}, \quad (5)$$

where A represented the area and P the perimeter of a given polar plot (Fig. 3C). A circular polar plot has a form factor equal to 1 and indicates a structure having gradients oriented in all directions. Lower form factor values indicate flattened polar plots and a higher degree of structure orientation in specific directions as indicating in Fig. 3C.

A quadtree decomposition routine interfaced to the ImageJ program was used for texture characterization (Chinga, 2005). The quadtree decomposition was performed by assessing the local greylevel standard deviation. A greylevel standard deviation (sGL) of 25 was used for the decomposition. If the image has a sGL value of 25, the image is divided into four sub-images or blocks. Each sub-image is evaluated again using the same criteria. Each sub-image having a sGL value larger than 25 is decomposed into four new sub-images. This is done iteratively until the local area (sub-image) has a sGL value lower than the given threshold. The variables yielded by the current decomposition are the number of blocks (nQT), the mean block size (mQT) and the standard deviation of block sizes (sQT).

SPSS (SPSS Inc, Release 9.0) was used for statistical analysis.

3. Results

The percentage of tephra finer than 1 mm, median diameters, xenolith ratios, density and vesicularity index show the increasing amount of water interacting with magma (Fig. 2). In addition to confirming the transition to a wetter explosion, the obtained results exemplify the necessity of suitable parameters for discriminating between different explosion mechanisms.

Three quadtree decomposition, two greylevel parameters and seven shape descriptors were calculated on images and polar plots of images. An analysis of variance (ANOVA) was performed on the potential surface descriptors for verifying their suitability for differentiating among the samples. A variable is accepted when the variance between groups (samples) is significantly larger than

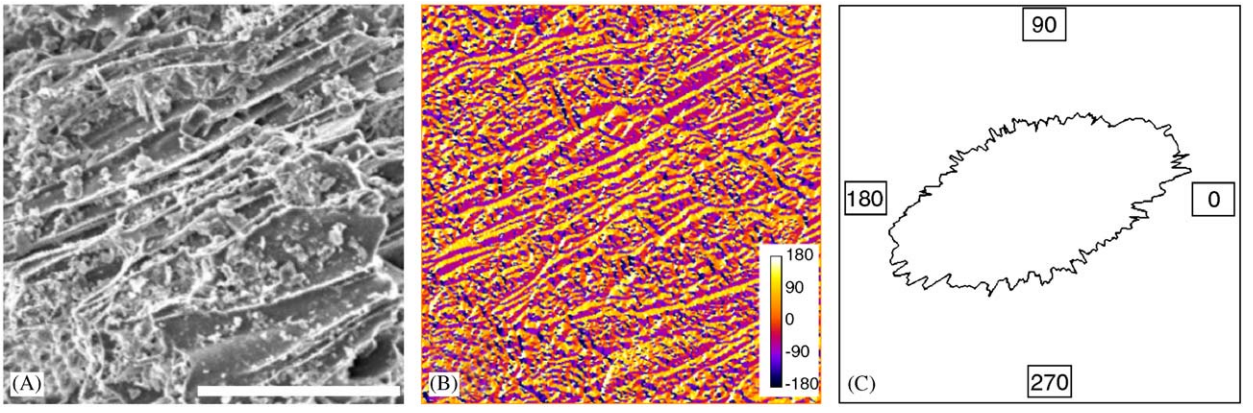

Fig. 3. Structure orientation analysis. (A) Original greylevel image; (B) azimuthal image; (C) polar plot based on frequency of gradients. Bar in $A = 100\,\mu m$.

the variances within the groups (replicates). The ANOVA tests for the accepted variables are given in Figs. 4–6. The greylevel standard deviation (sGL), the form factor (FF) and the number of quadtree blocks (nQT) seem suitable for differentiating between samples, having p-values well below 0.05 with a 95% confidence interval (CI).

Among all the evaluated surface texture descriptors, the greylevel standard deviation seems to give the best differentiation between the samples. However, this parameter alone is insufficient to describe the structure in detail. The greylevel and greylevel variation may vary significantly depending on the settings used for image acquisition. Besides, two different structures may have the same greylevel variation, but different texture. This is exemplified in Fig. 7. A gradient analysis revealed significant differences between the structures (Fig. 8). Fig. 7A has a texture with clear orientation compared to Fig 7B.

Though both images have the same global sGL, there are also clear differences with respect to the local greylevel standard deviation. This is exemplified in Fig. 9 where Fig. 9B has larger areas with lower greylevel variation, thus having larger and fewer blocks after the corresponding quadtree decomposition.

All the presented texture descriptors (sGL, nQT and FF) seem to model the transition from a drier explosion to a wetter explosion. In addition, a data reduction method, R-mode factor analysis was performed on the three variables. The term factor analysis was first introduced by Thurstone, 1931.

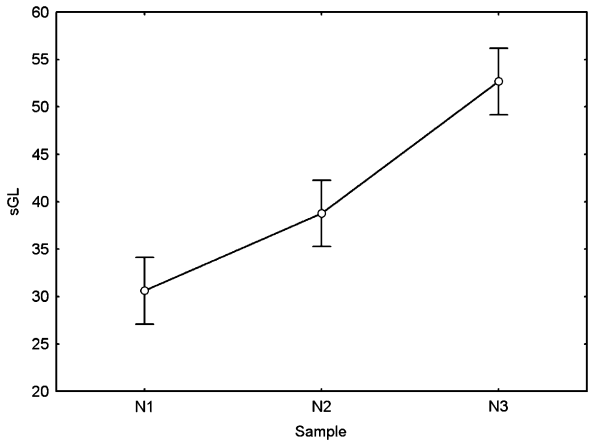

Fig. 4. ANOVA of greylevel standard deviation of (sGL) variable. Samples Nemrut1 (N1), Nemrut2 (N2) and Nemrut3 (N3) are included in analysis. Mean values are given with corresponding 95% CI.

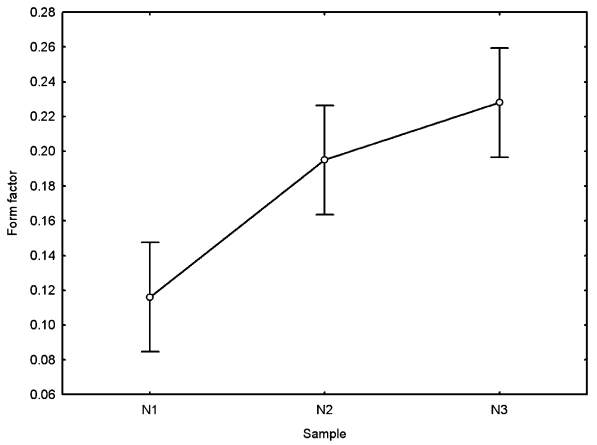

Fig. 5. ANOVA of form factor (FF) variable. Samples Nemrut1 (N1), Nemrut2 (N2) and Nemrut3 (N3) are included in analysis. Mean values are given with corresponding 95% CI.

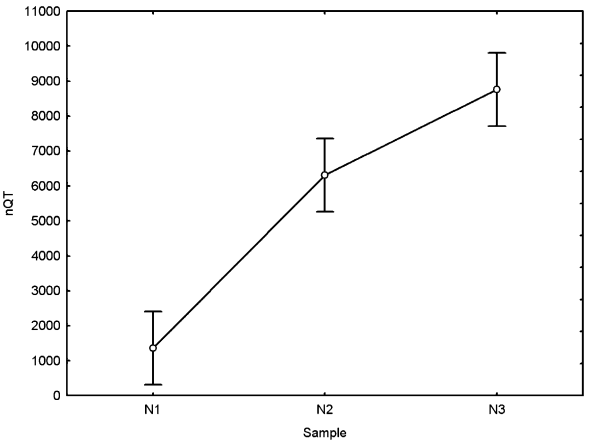

Fig. 6. ANOVA of number of quadtree block sizes (nQT) variable. Samples Nemrut1 (N1), Nemrut2 (N2) and Nemrut3 (N3) are included in analysis. Mean values are given with corresponding 95% CI.

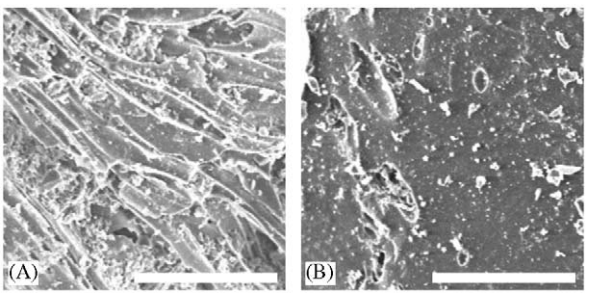

Fig. 7. Two images having same greylevel standard deviation, i.e., 36. (A) Image from N2 sample showing a clear texture orientation; (B) image from N3 sample. Bar = 100 μm.

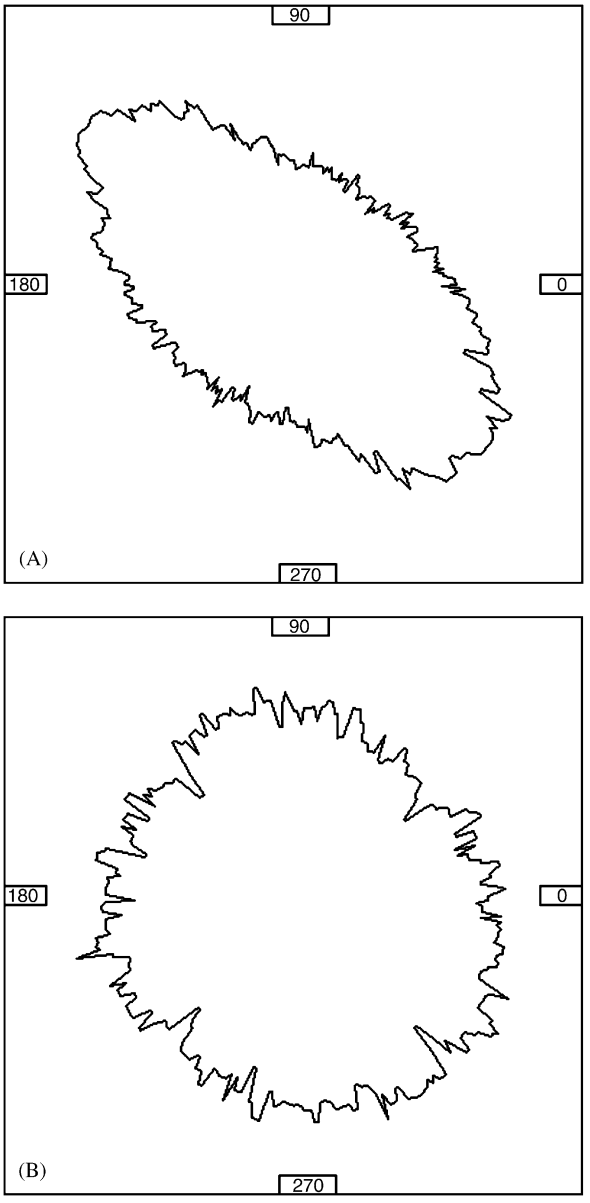

Fig. 8. Polar plots of corresponding images depicted in Fig. 7.

The main applications of factor analytic techniques are: (1) to reduce the number of variables and (2) to detect structure in the relationships between variables, that is to classify variables. Therefore, factor analysis is applied as a data reduction or structure detection method. A hands-on how-to approach about factor analysis can be found in Stevens (1986). The utility of factor analysis is plotting the singular samples on a factor diagram as factor scores [Fr]. The numbers of extracted factors, 2 were determined by the scree test. The scree test is a

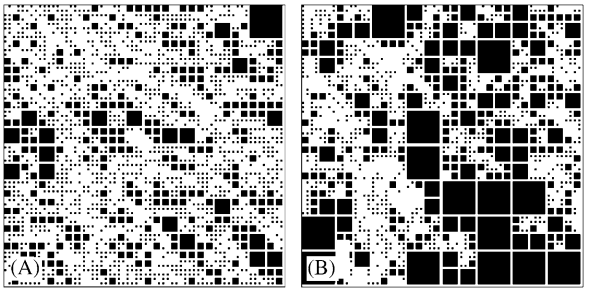

Fig. 9. Quadtree decomposition of corresponding images depicted in Fig. 7.

graphical method first proposed by Cattell (1966). Cattell (1966) suggests finding place where smooth decreases of eigenvalues appears to level off to the right of the plot. To the right of this point, presumably, one finds only "factorial scree". "Scree" is the geological term referring to the debris which collects on the lower part of a rocky slope. According to this criterion, we retain 2 factors in our study (Fig. 10). The discriminating diagram is generated by using the factors as axes and the surface descriptor values as data points. In this case two factors could explain the 98% of the variance. The discriminating diagram including the three proposed variables (sGL, nQT and FF) is depicted in Fig. 10. For comparison, the particle outline parameters such as elongation, roundness, compactness and rectangularity used in Dellino and La Volpe (1996) were calculated on Nemrut samples. A discriminating diagram based on the particle outline parameters is depicted in Fig. 11. The different samples overlapped on the diagram, thus indicating the poor suitability of shape parameters for discriminating between different ash samples.

4. Discussion and conclusion

Volcanic ash particles from different fragmentation mechanisms have different surface textures and morphologies (Wohletz, 1983; Heiken and Wohletz, 1985). The success in the discrimination of volcanic ashes from SEM images depends on the experience of microscopist (Sheridan and Marshall, 1983). Thus the analysis of the volcanic clast shape remained largely qualitative (Marshall, 1987). Volcanologists have a beneficial book with huge data about volcanic ash by the agency of Heiken and Wohletz (1985). The qualitative data of volcanic ash needs to be expressed in quantitative ways. This provides the use of supplementary methods, e.g.

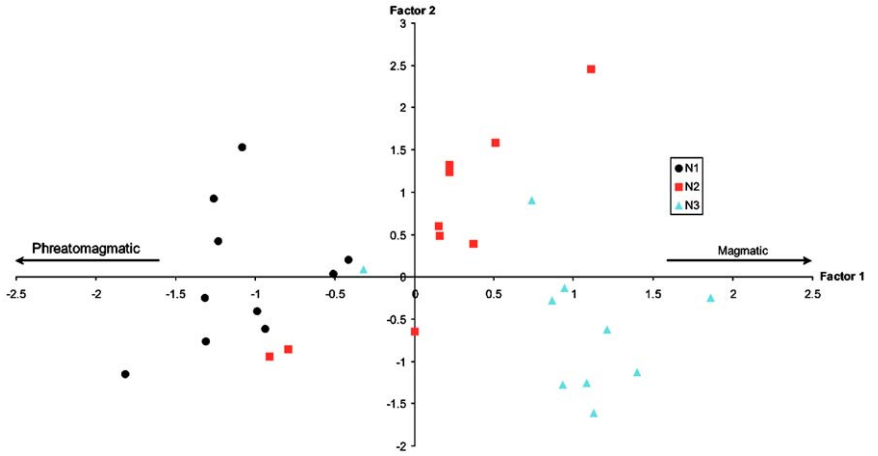

Fig. 10. Discriminating diagram based on texture classification. Diagram shows a clear transition between wetter and drier stages. Samples from Nemrut1 (N1), Nemrut2 (N2) and Nemrut3 (N3) are included in diagram.

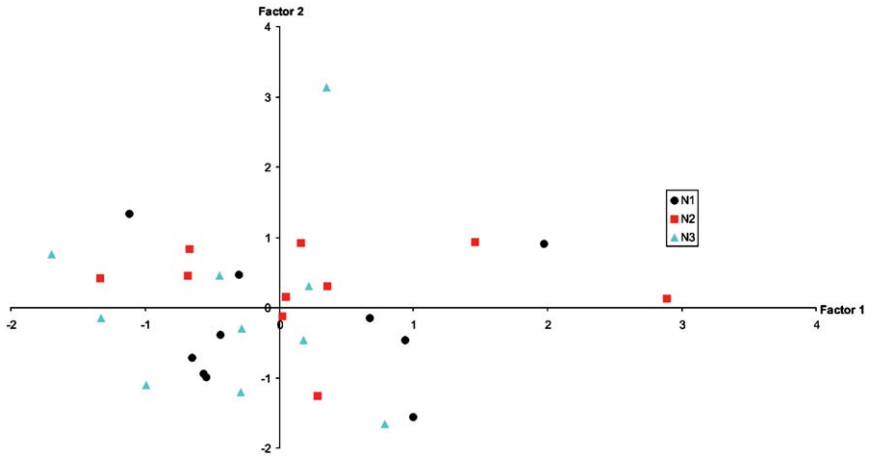

Fig. 11. Discriminating diagram based on particle outlines. No differentiation between three given stages is observed. Samples from Nemrut1 (N1), Nemrut2 (N2) and Nemrut3 (N3) are included in diagram.

statistical analysis, artificial intelligence and study on high dimensional data.

Simple and well-defined surface descriptors have been presented in this study. Parameters derived from a quadtree decomposition approach seem to be suitable for describing ash texture. Complementary information is obtained by performing a gradient analysis. The proposed image processing and analysis is simple to implement and requires little subjective intervention.

Although, the common shapes of glass pyroclasts in phreatomagmatic explosions such as blocky-equant, moss-like, plate-like and drop or spherical may be used as ''key'' structures, they are uncommon, indefinable or absent in some products related to the varying energies, modes of contact of water and chemistry of magma. Multicondition-driven mechanisms may produce pyroclastic deposits varying in fundamental properties such as dispersal, grain size, vesicularity and morphology of juvenile clasts, and the abundance of lithic or ''wall rock'' ejecta (xenoliths).

The products under the influence of modifying conditions can be discriminated from each other by using the properties mentioned above. Among the criteria used to distinguish the products of ''dry'' magmatic eruptions from ''wet'' phreatomagmatic eruptions, the vesicularity of the juvenile clasts is generally considered to be high in the former and lower in the latter case (Walker and Croasdale,

1972; Houghton and Wilson, 1989). Even though it is necessary to take all fundamental properties into consideration in such variable mechanisms, the quadtree decomposition variables as well as surface descriptors derived from gradient analysis, which may be directly related to vesicularity, clustered the ash particles between two end member mechanisms.

The most effective and most hazardous volcanic mechanism of conversion of thermal into kinetic energy is by phreatomagmatic explosion (Lorenz et al., 1991; Wohletz, 1986; Wohletz and Sheridan, 1983; Wohletz and Brown, 1995; Zimanovski et al., 1997). The fluctuations in the vesicularity of ash particles may permit the anticipation of volcanic hazards. Textural analysis performed during the course of eruption may enable the prediction of some important changes in the eruptive style (Gourgaud et al., 2000). Complementary details may be obtained by assessing the ash surface topography, thus yielding valuable information about, e.g. vesicularity of the ash particles. This may enrich our capabilities for effective discrimination between magmatic and phreatomagmatic pyroclastics. The activities of volcanoes in heavily populated areas need to be monitored by various methods to detect precursory signs to enable scientists to issue advisories and warnings to the public and authorities in the area. This may also enrich our capabilities for effective prediction for the basis of planning to overcome the impending danger of eruptions.

Acknowledgements

This work benefited from a research grant of Hacettepe University Research Foundation (Project no. 01 01 602 020). The research activities of the first author in France were supported by French Government. Pierre Boivin and Jean-Luc Le Pennec are thanked for constructive suggestions to improve the paper. The improvements of anonymous reviewers and editor-in-chief G. F. Bonham-Carter on the manuscript are greatly appreciated.

References

Aydar, E., Gourgaud, A., Ulusoy, I., Digonnet, F., Labazuy, P., Sen, E., Bayhan, H., Kurttas, T., Tolluoglu, A.U., 2003. Morphological analysis of active Mount Nemrut stratovolcano, eastern Turkey: evidences and possible impact areas of future eruption. Journal of Volcanology and Geothermal Research 2571, 1–12.

Cattell, R.B., 1966. The scree test for the number of factors. Multivariate Behavioral Research 1, 245–276.

Chinga, G., 2004. Detailed characterisation of paper surface structure for gloss assessment. Journal Pulp Paper Science 30 (8), 222–227.

Chinga, G., 2005. A quadtree decomposition approach for surface assessment. Pattern Analysis and Applications, in press.

Chinga, G., Gregersen, Ø., Dougherty, R., 2003. Paper surface characterisation by laser profilometry and image analysis. Journal of Microscopy and Analysis 84, 5–7.

Costa, M.A., 2000. Fractal description of rough surfaces for haptic display. Ph.D. Dissertation, Stanford University, Stanford, CA, 119pp.

Dellino, P., La Volpe, L., 1996. Image processing analysis in reconstructing fragmentation and transportation mechanisms of pyroclastic deposits. The case of Monte Pilato-Rocche Rosse eruptions, Lipari (Aeolian islands, Italy). Journal of Volcanology and Geothermal Research 71, 13–29.

Fisher, R.V., Schminke, H.V., 1984. Pyroclastic Rocks. Springer, Berlin 472pp.

Gadala-Maria, F., Parsi, F., 1993. Measurement of fiber orientation in short-fiber composites using digital image processing. Polymer Composites 14 (2), 126–131.

Gonzalez, R., Woods, R.E., 1993. Digital Image Processing. Addison-Wesley Publishing Company, Reading, MA 716pp.

Gourgaud, A., Thouret, J.-C., Bourdier, J.-L., 2000. Stratigraphy and textural characteristics of the 1982–83 tephra of Galunggung volcano (Indonesia): implications for volcanic hazards. Journal of Volcanology and Geothermal Research 104, 169–186.

Heiken, G., 1972. Morphology and petrography of volcanic ashes. Geological Society of America Bulletin 83, 1961–1988.

Heiken, G., 1974. An atlas of volcanic ash. Smithsonian Contributions to Earth Science, vol. 12, 101pp.

Heiken, G., Wohletz, K.H., 1985. Volcanic Ash. University of California Press, Berkeley, CA 245pp.

Hjaltason, G.R., Samet, H., 1999. Speeding up construction of quadtrees for spatial indexing. Computer Science Department, TR-4033, University of Maryland, College Park, MD. Available from http://www.cs.umd.edu/~hjs/pubs/bulkload.pdf.

Houghton, B.F., Wilson, C.J.N., 1989. A vesicularity index for pyroclastic deposits. Bulletin of Volcanology 51, 451–462.

Lee, P.S., Piehler, H.R., Adams, B.L., Jarvis, G., Hampel, H., Rollett, A.D., 1998. Influence of surface texture on orange peel in aluminum. Journal of Materials Processing Technology 80–81, 315–319.

Lorenz, V., Zimanowski, B., Fröhlich, G., 1991. Experiments on explosive basic and ultrabasic, ultramafic, and carbonatitic volcanism. CPRM-Special Publication 2/91, Brasilia, pp. 245–247.

Macdonald, G.A., 1972. Volcanoes. Prentice-Hall, Englewood Cliffs, NJ 510pp.

Marshall, J.R., 1987. Shape analysis. In: Marshall, J.R. (Ed.), Clastic Particles. Van Nostrand Reinhold, New York, NY, 255pp.

Panozzo Heilbronner, R., 1992. The autocorrelation function: an image-processing tool for fabric analysis. Tectonophysics 212, 351–370.

Rao, C., Pan, T., Tutumluer, E., 2003. Determination of coarse aggregate surface texture using image analysis. 16th ASCE

Engineering Mechanics Conference, University of Washington, Seattle.
Rasband, W.S., 1997–2004. ImageJ. National Institutes of Health, Bethesda, Maryland, USA, http://rsb.info.nih.gov/ij
Russ, J.C., 1999. The Image Processing Handbook, third ed. CRC Press, Boca Raton, FL 771pp.
Samet, H., 1984. The quadtree and related hierarchical data structures. Computing Surveys 16 (2), 187–260.
Samet, H., 1990. Applications of Spatial Data Structures. Addison Wesley, Reading, MA 507pp.
Self, S., Sparks, R.S.J., 1978. Characteristics of widespread pyroclastic deposits formed by interaction of silicic magma and water. Bulletin Volcanologique 41 (3), 197–212.
Sheridan, M.F., Marshall, J.R., 1983. Interpretation of pyroclast surface features using SEM images. Journal of Volcanology and Geothermal Research 16, 153–159.
Sheridan, M.F., Wohletz, K.H., 1981. Hydrovolcanic explosions: the systematics of water-tephra equilibration. Science 212, 1387–1389.
Stachowiak, G.W., 1998. Numerical characterization of wear particles morphology and angularity of particles and surfaces. Tribology International 31, 139–157.
Stearns, H.T., MacDonald, G.A., 1946. Geology and groundwater resources of the island of Hawaii. Hawaii Division of Hydrology Bulletin 67, 13–49.
Stevens, J., 1986. Applied Multivariate Statistics for the Social Sciences, first ed. Lawrence Erlbaum Associates, Mahwah, NJ 712pp.
Thurstone, L.L., 1931. Multiple factor analysis. Psychological Review 38, 406–427.
Walker, G.P.L., Croasdale, R., 1972. Characteristics of some basaltic pyroclastics. Bulletin of Volcanology 35, 303–317.
Wang, S., Armstrong, M.P., 2003. A quadtree approach to domain decomposition for spatial interpolation in Grid computing environments. Parallel Computing 29, 1481–1504.
Wohletz, K.H., 1983. Mechanisms of hydrovolcanic pyroclast formation: size, scanning electron microscopy, and experimental studies. In: Sheridan, M.F., Barberi, F. (Eds.), Explosive Volcanism. Journal of Volcanology and Geothermal Research 17, 31–63.
Wohletz, K.H., 1986. Explosive magma–water interactions: thermodynamics, explosion mechanisms, and field studies. Bulletin of Volcanology 48, 245–264.
Wohletz, K.H., Brown, W., 1995. Particulate size distributions and sequential fragmentation/transport theory. In: Theofanous, T.G., Akiyama, M. (Eds.), Intense Multiphase Interactions. Proceedings of US (NSF) Japan (JSPS) Joint Seminar, Santa Barbara, CA, June 8–13, pp. 235–241.
Wohletz, K.H., Krinsley, D., 1982. Scanning electron microscopy of basaltic hydromagmatic ash. Los Alamos National Laboratory Report, LA-UR 82-1433, 43pp.
Wohletz, K.H., Sheridan, M.F., 1983. Hydrovolcanic explosions II. Evolution of basaltic tuff rings and tuff cones. American Journal of Science 283, 385–413.
Yoshigi, M., Clark, E.B., Yost, H.J., 2003. Quantification of stretch-induced cytoskeletal remodeling in vascular endothelial cells by image processing. Cytometry Part A 55A, 109–118.
Zimanowski, B., Büttner, R., Lorenz, V., Häfele, H.-G., 1997. Fragmentation of basaltic melt in the course of explosive volcanism. Journal of Geophysical Research 102, 803–814.
Zimanowski, B., Wohletz, K., Dellino, P., Büttner, R., 2002. The volcanic ash problem. Journal of Volcanology and Geothermal Research 2557, 1–5.

4.2. Clustering of volcanic ash arising from different fragmentation mechanisms using Kohonen self-organizing maps

ELSEVIER

Computers & Geosciences 33 (2007) 821–828

COMPUTERS & GEOSCIENCES

www.elsevier.com/locate/cageo

Clustering of volcanic ash arising from different fragmentation mechanisms using Kohonen self-organizing maps

Orkun Ersoy[a,b,*], Erkan Aydar[a], Alain Gourgaud[b], Harun Artuner[c], Hasan Bayhan[a]

[a]*Department of Geological Engineering, Hacettepe University, 06532, Beytepe-Ankara, Turkey*
[b]*Universitè Blaise Pascal, UMR-CNRS 6524, 5 rue Kessler, 63038 Clermont-Ferrand, France*
[c]*Department of Computer Science & Engineering, Hacettepe University, 06532, Beytepe-Ankara, Turkey*

Received 31 October 2005; received in revised form 17 October 2006; accepted 25 October 2006

Abstract

In this study, we present the visualization and clustering capabilities of self-organizing maps (SOM) for analyzing high-dimensional data. We used SOM because they implement an orderly mapping of a high-dimensional distribution onto a regular low-dimensional grid. We used surface texture parameters of volcanic ash that arose from different fragmentation mechanisms as input data. We found that SOM cluster 13-dimensional data more accurately than conventional statistical classifiers. The component planes constructed by SOM are more successful than statistical tests in determining the distinctive parameters.

Keywords: Neural networks; Kohonen self-organizing maps; Volcanic ash; Nemrut

1. Introduction

Fragmentation of magma may occur due to exsolution of gas phases as a result of decompression (magmatic) or by an interaction between external water and magma (phreatomagmatic) (Cashman et al., 2000). These two fragmentation processes produce ash particles with end-members displaying characteristic morphology and surface features (Wohletz, 1983; Heiken and Wohletz, 1985). Scanning electron microscopy (SEM) provides a suitable method for classifying volcanic ash based on surface morphology and texture (Wohletz and Krinsley, 1982; Büttner et al., 1999; Ersoy et al., 2006), with the most extensive SEM studies of pyroclast shapes having been presented by Heiken (1972, 1974), Wohletz (1983) and Heiken and Wohletz (1985). A study of explosive fragmentation dynamics by examination of the morphological features of natural and experimental ash particles has demonstrated the significance of morphological microfeatures on ash grains (Wohletz, 1983). However, the lack of analogue particles produced by scaled experiments at that time allowed only a qualitative assessment. Although a study of natural pyroclastic sequences combined with scaled laboratory experiments identified the different fragmentation

*Corresponding author. Department of Geological Engineering, Hacettepe University, 06532, Beytepe-Ankara, Turkey.
Fax: +90 312 2992034.
E-mail address: oersoy@hacettepe.edu.tr (O. Ersoy).

0098-3004/$ - see front matter © 2007 Elsevier Ltd. All rights reserved.
doi:10.1016/j.cageo.2006.10.008

mechanisms related to the water/magma mass ratios during their interaction (Büttner et al., 1999), the surface features of the ash were not quantified. Classification of volcanic ash surfaces is still limited to descriptive terms such as stepped, planar, crack patterns, and hydration skin. The qualitative data of volcanic ash need to be expressed in quantitative ways, supported by supplementary methods such as statistical analysis and artificial intelligence.

Ersoy et al. (2006) introduced a new method of ash particle characterization based on a quadtree decomposition approach and gradient analysis of SEM micrographs of volcanic ash particles from Mount Nemrut, eastern Turkey. They calculated 13 different surface parameters for volcanic ash particles to assess the fragmentation mechanisms operating during eruption. The calculated quadtree variables, such as the number of blocks (nQT), mean block size (mQT), and standard deviation of block sizes (sQT), as well as surface descriptors derived from gradient analysis, are suitable for quantifying structural changes of the ash surface associated with variable explosion conditions. Ersoy et al. (2006) presented these parameters in volcanology as key parameters for identifying different eruption types. In the present paper, we use the data of the 13 surface parameters with 10 replicates from each of three different samples analyzed by Ersoy et al. (2006).

Visualizing multi-dimensional data are critical to understanding complex relationships in natural systems; consequently, earth scientists are faced with increasingly large amounts of data. As the dimensionality of the data increases, the complexity of visualizing relationships also increases. To understand natural systems, data from diverse sources must be integrated in a manner that is comprehensible to human interpretation (Penn, 2005). Several approaches have been presented to convey high-dimensional data (e.g., Tukey, 1977; Levoy, 1988; Wegman and Solka, 2002). Methods, which preserve certain properties of the structure of the data set as faithfully as possible, are called 'projection methods' (Ripley, 1996).

A projection method that categorizes or groups similar data items is termed 'clustering'. Clustering methods (Anderberg, 1973; Hartigan, 1975; Jain and Dubes, 1988; Jardine and Sibson, 1971; Sneath and Sokal, 1973; Tryon and Bailey, 1973) can be divided into two basic types: hierarchical and partitional clustering (Kaski, 1997).

Ersoy et al. (2006) performed the data reduction method (linear projection method) factor analysis (principal component analysis) on their data to visualize different types volcanic ash. The utility of factor analysis is plotting the singular samples on a factor diagram as factor scores ([Fr]). In this case, two factors explained 98% of the variance. The authors used the three most suitable parameters for differentiating between samples, with resulting p-values well below 0.05 at a 95% confidence interval (CI) in analysis of variance (ANOVA).

For the present paper, we used the data of Ersoy et al. (2006) to cluster the different types of volcanic ash particles via self-organizing maps (SOM), which classify data more accurately than conventional statistical classifiers (Moline and Bahr, 1995; Dolmatova et al., 1997; Kocjancic and Zupan, 1997). Although the data-mining tools described above are divided into two categories, projection and clustering methods, SOM are special cases where data are simultaneously reduced and projected onto a lower-dimension.

2. Artificial neural networks

Artificial neural networks (ANN) are relatively crude electronic models based on the neural structure of the brain. ANN attempt to mirror the brain functions in a computerized way by resorting to the learning mechanism as the basis of human behavior (Lipman, 1987; Anderson and McNeil, 1992; Hagan et al., 1996; Kartalopoulos, 1995).

ANN can generally be defined as a structure composed of a number of interconnected units (Skapura, 1996). Each unit has an input/output (I/O) characteristic and implements a local computation or function. The output of each unit is determined by its I/O characteristic, its interconnection to other units and (possibly) external inputs, and its internal function. The network usually develops an overall functionality through one or more forms of training. The fundamental unit or building block of the ANN is the artificial neuron (termed neuron from here on). The neuron has a set of inputs (X_i) weighted before reaching the main body of the processing element. In addition, it has a bias term, a threshold value that has to be reached or exceeded for the neuron to produce a signal, a non-linearity function (f_i) that acts on the produced signal (R_i), and an output (O_i) (Lipman, 1987; Haykin, 1994; Hagan et al., 1996; Kartalopoulos, 1995). The basic model of a neuron is illustrated in Fig. 1.

ANN are classified into two major types on the basis of learning modes: supervised and unsupervised. In supervised mode, the actual output of a neural network is compared to the desired output. The network then adjusts weights, which are usually initially randomly set, so that the next iteration or cycle produces a closer match between the desired and actual output. The learning method seeks to minimize the current errors of all processing elements. This global error reduction is created over time by continuously modifying the input weights until acceptable network accuracy is achieved. With supervised learning, someone should train the network before it becomes useful. Training consists of presenting input and output data to the network. This training is considered complete when the neural network reaches a user-defined performance level. This level signifies that the network has achieved the desired statistical accuracy as it produces the required outputs for a given sequence of inputs. When no further learning is necessary, the weights are typically frozen for the application. Some network types allow continual training while in operation, although at a much slower rate. This helps the network to adapt to gradually changing conditions.

Unsupervised learning holds great promise for the future, with the possibility that computers could some day learn by themselves. These networks use no external influences to adjust their weights; instead, they monitor their performance internally. These networks search for regularities or trends in the input signals and make adaptations according to the function of the network. Even without being told whether it is right or wrong, the network still requires some information concerning how to organize itself. This information is built into the network topology and learning rules. An unsupervised learning algorithm might emphasize cooperation among clusters of processing elements; in such a scheme, the clusters work together. If an external input activated any node in the cluster, the cluster's activity as a whole is increased. Likewise, a decrease in the external input to nodes in the cluster has an inhibitory effect on the entire cluster. Competition between processing elements also forms a basis for learning. Training of competitive clusters amplifies the responses of specific groups to specific stimuli. As such, it associates these groups with each other and with a specific appropriate response. Generally, when competition for learning is in effect, only the weights belonging to the winning processing element are updated.

Because all ANN are based on the concept of neurons, connections, and transfer functions, there is a similarity between the different structures or architectures of neural networks. The majority of the variations stem from the various learning rules and the way in which these rules modify a network's typical topology (Aleksander and Morton, 1990; Anderson and McNeil, 1992; Fausett, 1994; Schalkoff, 1997). Because of the advantages and accuracy of Kohonen SOM for clustering problems of geological materials (Chang et al., 2002), in the present study we used SOM for our clustering problem.

2.1. Kohonen SOM

Kohonen SOM are unsupervised ANN developed by Kohonen (1982). They represent the result of a vector quantization algorithm that places a number of reference or codebook vectors into a high-dimensional input data space to approximate its data sets in an ordered fashion. When local-order relations are defined between the reference vectors, the relative values of the latter are made to depend on each other as if their neighboring values lie along an 'elastic surface'. By means of the self-organizing algorithm, this 'surface' becomes defined as a kind of nonlinear regression of the reference vectors through the data points. Mapping from a high-dimensional data space R^n onto, for example, a two-dimensional lattice of points, is thereby also defined.

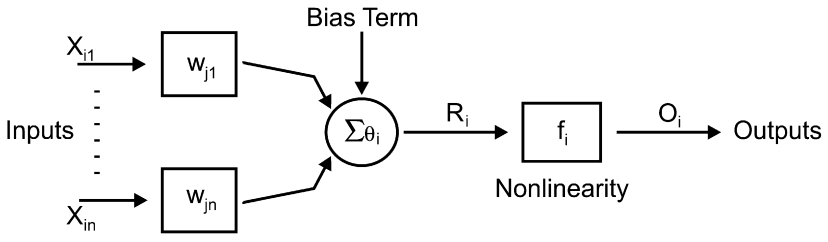

Fig. 1. Basic model of artificial neuron.

Such mapping can be used to effectively visualize metric ordering relations of input samples. In practice, mapping is obtained as an asymptotic state in a learning process (Kohonen et al., 1996a).

3. Source of data

The data include calculated quadtree variables such as the number of blocks (nQT), the mean block size (mQT), the standard deviation of block sizes (sQT), and the surface descriptors derived from gradient analysis of SEM micrographs of volcanic ash particles. Ten replicates were acquired from three samples: N1, N2, and N3. These three samples are volcanic ash particles derived from different fragmentation mechanisms (for details, see Ersoy et al., 2006). ANOVA was performed on the data to test hypotheses concerning differences between means. ANOVA is used to test the significance of differences among several means without increasing the Type I error rate. The successful parameters for discrimination were determined previously by Ersoy et al. (2006); however, here all parameters are considered to document the limits of SOM in visualizing and clustering high-dimensional data. The number of variables is 13, which is also the codebook vector dimension. All values in the input data are numeric and stored in ASCII form.

4. Architecture and learning algorithm of SOM

4.1. Map construction

There are many versions of the SOM. Here SOM define mapping from the input data space R^n onto a regular two-dimensional array of nodes, which can be visualized as a sheet-like neural-network array. We preferred a hexagonal lattice. The x-coordinates of the map (column numbers) range from 0 to $n-1$ where n is the x-dimension of the map, while the y-coordinates (row numbers) vary from 0 to $m-1$, where m is the y-dimension of the map (Fig. 2). Our map dimension is 30×20 in the x- and y-directions, respectively. We used the Self-Organizing Map Program Package (SOM_PAK) (Kohonen et al., 1996a) for the correct application of the SOM algorithm.

A parametric reference vector $m_i \in R^n$ is associated with every node i. An input vector $x \in R^n$ is compared with the m_i, and the best match is defined as 'response'; the input is thus mapped onto this location. SOM is a nonlinear projection of the

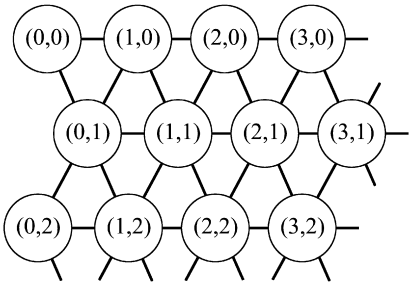

Fig. 2. Locations of units in hexagonal topological structure. The distance between two units in map is computed as a Euclidean distance in (two-dimensional) map topology. Reproduced from Kohonen et al. (1996a).

probability density function of the high-dimensional input data onto the two-dimensional display (Kohonen, 1989). The smallest of the Euclidean distances $\|x-m_i\|$ usually define the best-matching node (c):

$$\|x-m_c\| = \min_i\{\|x-m_i\|\} \quad \text{or,}$$
$$c = \underset{i}{\operatorname{argmin}}\{\|x-m_i\|\}. \tag{1}$$

Thus, x is mapped on the c relative to the parameter values m_i. During learning, the nodes that are topographically close in the array, up to a certain distance, activate each other to learn from the same input. The useful values of m_i can be found as convergence limits of the following learning process, whereby the initial values of the $m_i(0)$ are random in our map:

$$m_i(t+1) = m_i(t) + h_{ci}(t)[x(t) - m_i(t)], \tag{2}$$

where t is an integer, the discrete-time coordinate, and $h_{ci}(t)$ is the so-called neighborhood kernel, which is a function defined over the lattice points. Usually, $h_{ci}(t) = h(\|r_c - r_i\|, t)$, where $r_c \in R^2$ and $r_i \in R^2$are the radius vectors of the nodes c and i, respectively, within the array. With increasing $\|r_c - r_i\|, h_{ci} \to 0$. The average width and form of h_{ci} define the 'stiffness' of the 'elastic surface' to be fitted to the data points. For the definition of h_{ci}, we used a neighborhood set of array points around node c. When we denote this set as N_c, $h_{ci} = \alpha(t)$ if i N_c and $h_{ci} = 0$ if $i \notin N_c$, where $\alpha(t)$ is some monotonically decreasing function of time ($0 < \alpha(t) > 1$). This type of kernel is nicknamed 'bubble' because it relates to certain activity 'bubbles' in laterally connected neural networks (Kohonen, 1989; Kohonen et al., 1996a).

4.2. Training of the map

We trained the map in two phases. In the first phase, we ordered the reference vectors of the map units. It was a rough training for ordering with a large neighborhood radius. The neighborhood radius was five for this phase, and it decreased to one during training. Therefore, in the end only the nearest neighbors were trained. The learning rate for the first phase was 0.07, decreasing to zero, while the training time was 200 000. The learning rate, $\alpha(t)$ is some monotonically decreasing function of time as described above. The training time is the number of steps in training. During the second phase, the reference vectors were fine-tuned and for each unit they converged to their 'correct' values. For the second phase, the training time was longer and the learning rate and neighborhood radius smaller, as described in Kohonen et al. (1996a). Values used for training time, learning rate, and neighborhood radius in the last phase were 400 000, 0.02, and 2, respectively. Therefore, in the beginning the units up to a distance of two were covered. In our map, the training time of the second phase was 2 times longer than in the first phase.

4.3. Quality of learning

Strongly contrasting learning processes can be defined by starting with different initial values $m_i(0)$ and applying different sequences of the training vectors $x(t)$ and different learning parameters. It is clear that an optimal map must exist for certain input data (Kohonen et al., 1996a), but the best map must have a minimum quantization error. The average quantization error (mean of $\|x - m_c\|$) is a useful performance index because it defines the map that best fits the data. In our map, 500 random initializations of the $m_i(0)$ were undertaken, and the map with the minimum quantization error (0.003956) was selected.

5. Results and discussion

We generated a list of coordinates that correspond to the best-matching unit in the map for each data sample. The SOM successfully discriminated the N1 sample from others (Fig. 3). There are two ash particles from each sample, N2 and N3, which fall into the other sample's fields. These ash particles appear to be negatively affecting the success of the clustering. 'A' and 'B' in particular are almost

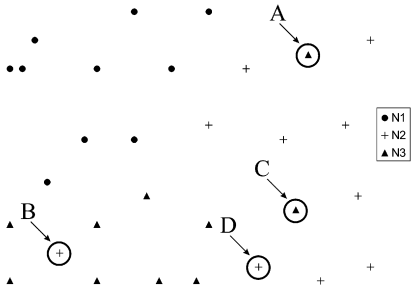

Fig. 3. Best-matching units in map for each data sample. The diagram is constructed from the parameters sGL, nQT, and FF, which were determined as most successful distinctive parameters from statistical analysis (e.g., ANOVA). A, B, C, and D correspond to ash particles with similar surface textures to those of other groups.

members of other groups. The positioning of 'C' and 'D' may reflect the effect of transition between groups, and consequently fragmentation mechanisms; however, this scattering is not the fault of clustering. These ash particles have similar surface textures to other samples. In addition, they are in other sample fields on the discrimination diagram (Fig. 4) of Ersoy et al. (2006).

We also constructed the component planes of our map. These planes visualize the values of the components using gray levels. Each component plane shows the values of one variable in each map unit. From component planes, we can observe the discriminate performance of each variable, namely parameters. Planes of the gray-level standard deviation (sGL), the number of quadtree blocks (nQT), and the mean block size (mQT) appear to be most suitable for visualizing the discrimination (Fig. 5). The gray-level standard deviation (sGL) and the number of quadtree blocks (nQT) were also the most successful parameters for distinguishing fragmentation process in Ersoy et al. (2006), however, the form factor (FF) is not as suitable for discrimination (Fig. 6). We propose the mean block size (mQT) instead of the FF as a parameter for distinguishing fragmentation process by keeping with the component planes of ANN.

We construct the discrimination diagram from factor analysis of three variables: sGL, nQT, and mQT (Fig. 7). The factors are the diagram axes, and the single analyzed surfaces are data points on the diagram. In this case, two factors explain 97% of the variance. We achieve a better-organized diagram by sticking to component planes. Only the ash particle labeled 'A' plotted in the field of a different group.

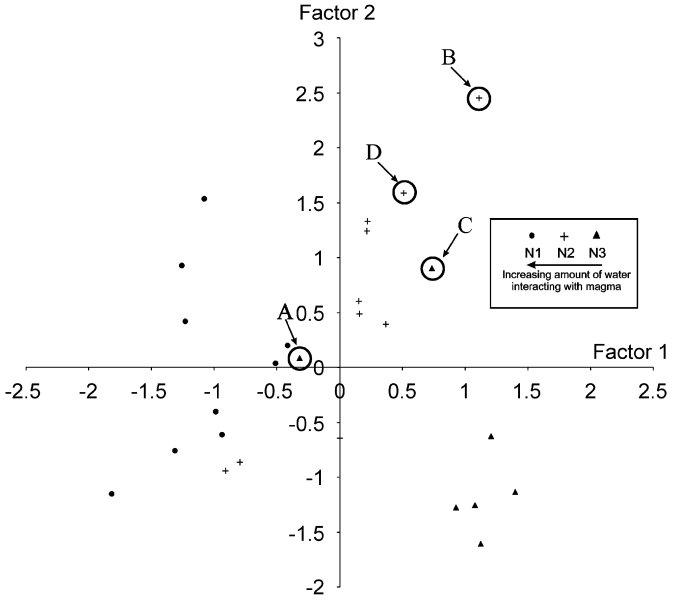

Fig. 4. Discrimination diagram from Ersoy et al. (2006). The diagram is constructed from parameters sGL, nQT, and FF, which were determined as most successful distinctive parameters from statistical analysis (e.g., ANOVA). A, B, C, and D correspond to particles shown in Fig. 3. The inset figure details sample numbers and different fragmentation mechanisms related to amount of water that interacted with magma.

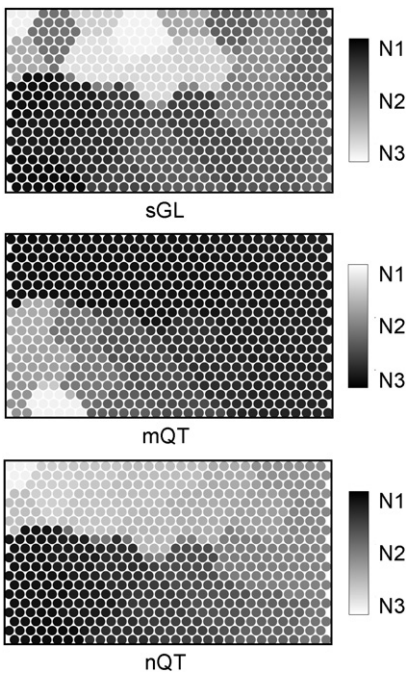

Fig. 5. Component planes of gray-level standard deviation (sGL), number of quadtree blocks (nQT), and mean block size (mQT). The mQT parameter appears as a distinctive parameter instead of form factor parameter, as determined from component planes of self-organizing maps.

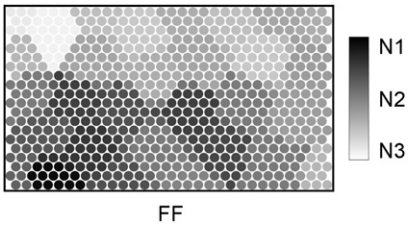

Fig. 6. Component plane of form factor (FF). Form factor parameter is unsatisfactory as a distinctive parameter.

We constructed a new map with the new three-dimensional data, using sGL, nQT, and mQT parameters as variables; the size of the new map was 20×10. We used the settings of the first map for training. After 500 trials, we used the map with the smallest quantization error (0.004572) for visualization. The new distinctive parameters determined by the component planes optimized the new discrimination (Fig. 8).

6. Conclusions

In this study, we present the visualization and clustering capabilities of self-organizing maps (SOM) for analyzing high-dimensional data. SOM

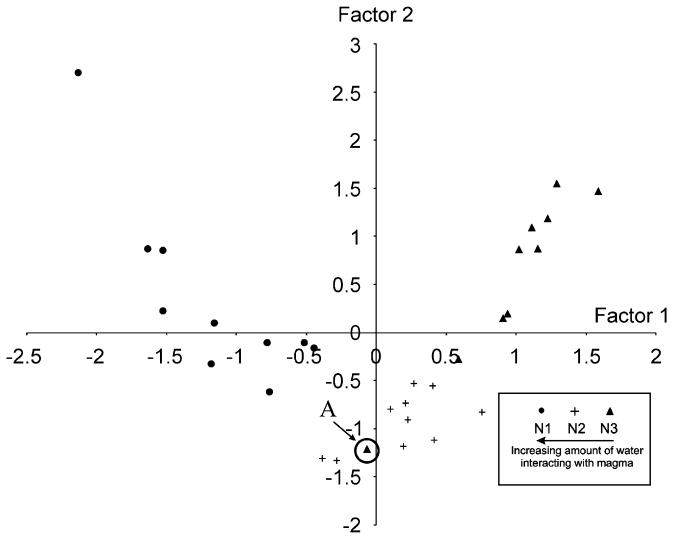

Fig. 7. Discrimination diagram using new parameters derived from component planes of SOM. Scattering of particles is tidier and well organized than that in Fig. 4. Ash particle labeled 'A' is only point that plotted in another group's field.

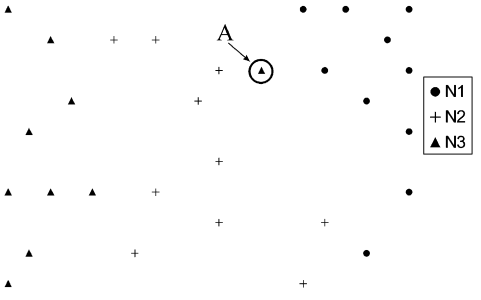

Fig. 8. Best-matching units in new map for each data set. Diagram is constructed from parameters sGL, nQT, and mQT, which were determined as most successful distinctive parameters from component planes of SOM. Only ash particle labeled 'A' is positioned in wrong field, due to its similarity in surface texture with this group. Note optimization as compared with that in Fig. 3.

were used because they implement the orderly mapping of a high-dimensional distribution onto a regular low-dimensional grid and are thereby able to convert complex nonlinear statistical relationships between high-dimensional data items into simple geometric relationships on a low-dimensional display.

We used surface texture parameters of volcanic ash that arose from different fragmentation mechanisms as input data. The component planes constructed by SOM were more successful than statistical tests in determining parameters for distinguishing the different fragmentation mechanisms. Component planes helped to determine the discriminate performance of each variable. Based on these planes, we modified the parameters to attain the absolute discrimination.

The SOM solves difficult high-dimensional and nonlinear problems such as feature extraction and classification of images and acoustic patterns, adaptive control of robots, and the equalization, demodulation, and error-tolerant transmission of signals in telecommunications. A new area of application is the organization of very large document collections (Kohonen, 2001).

In many applications, sensor failures, recording errors, and resource limitations may prevent data collection from completing each input vector; however, such incomplete training examples still contain useful information. For example, partial data can still be used to determine the distribution statistics of the available vector components. For incomplete input data vectors, the distance calculations and reference vector modification steps using the available data components would be undertaken by a supervised learning algorithm; for example, the learning vector quantization (LVQ), which is related to the SOM (Kohonen et al., 1996b). Finally, we note that the SOM are one of the most realistic models of biological brain function (Kohonen, 2001).

Acknowledgments

This work benefited from a research grant from the Hacettepe University Research Foundation

(Project No. 01 01 602 020). The French Government supported the research activities of the first author in France. Pierre Boivin and anonymous reviewers are thanked for constructive suggestions that helped to improve the paper. International Science Editing improved the English of paper.

References

Aleksander, I., Morton, H., 1990. An Introduction to Neural Computing, Second ed. Chapman & Hall, New York, NY, 240pp.

Anderberg, M.R., 1973. Cluster Analysis for Applications. Academic Press, Inc., New York, NY, 359pp.

Anderson, D., McNeil, G., 1992. Artificial Neural Network Technology. Data & Analysis Center for Software, Rome, 83pp.

Büttner, R., Dellino, P., Zimanowski, B., 1999. Identifying modes of magma/water interaction from the surface features of ash particles. Nature 401, 688–690.

Cashman, K.V., Sturtevant, B., Papale, P., Navon, O., 2000. Magmatic fragmentation. In: Sigurdsson, H., Houghton, B.F., McNutt, S.R., Rymer, H., Stix, J. (Eds.), Encyclopedia of Volcanoes. Academic Press, San Diego, pp. 412–430.

Chang, H-C., Kopaska-Merkel, D.C., Chen, H-C., 2002. Identification of lithofacies using Kohonen self-organizing maps. Computers & Geosciences 28, 223–229.

Dolmatova, L., Ruckebusch, C., Dupuy, N., Huvenne, J.P., Legrand, P., 1997. Quantitative analysis of paper coatings using artificial neural networks. Chemometrics and Intelligent Laboratory Systems 36 (2), 125–140.

Ersoy, O., Chinga, G., Aydar, E., Gourgaud, A., Cubukcu, H.E., Ulusoy, I., 2006. Texture discrimination of volcanic ashes from different fragmentation mechanisms: a case study, Mount Nemrut stratovolcano, eastern Turkey. Computers and Geosciences 32, 936–946.

Fausett, L.V., 1994. Fundamentals of Neural Networks, US ed. Prentice Hall, NJ, 461pp.

Hagan, M.T., Demuth, H.B., Beale, M., 1996. Neural Network Design. PWS Publishing Company, Boston, MA, 730pp.

Hartigan, J.A., 1975. Clustering Algorithms. Wiley, New York, NY, 351pp.

Haykin, S., 1994. Neural Networks: A Compherensive Foundation. New York, Macmillan.

Heiken, G., 1972. Morphology and petrography of volcanic ashes. Geological Society of America Bulletin 83, 1961–1988.

Heiken, G., 1974. An atlas of volcanic ash. Smithsonian Contributions to the Earth Sciences 12, 1–101.

Heiken, G., Wohletz, K.H., 1985. Volcanic Ash. University of California Press, Berkeley, California, 245pp.

Jain, A.K., Dubes, R.C., 1988. Algorithms for Clustering Data. Prentice-Hall, Englewood Cliffs, NJ, 320pp.

Jardine, N., Sibson, R., 1971. Mathematical Taxonomy. Wiley, London, 304pp.

Kartalopoulos, S.V., 1995. Understanding neural networks and fuzzy logic: basic concepts and applications. Wiley, IEEE Press, New York, 232pp.

Kaski, S., 1997. Data exploration using self-organizing maps. Ph.D. Dissertation, Acta Polytechnica Scandinavica, Mathematics, Computing and Management in Engineering Series No. 82, Espoo. Published by the Finnish Academy of Technology, 57pp.

Kocjancic, R., Zupan, J., 1997. Application of a feed-forward artificial neural network as a mapping device. Journal of Chemical Information and Computer Sciences 37 (6), 985–989.

Kohonen, T., 1982. Self-organized formation of topologically correct feature maps. Biological Cybernetics 43, 59–69.

Kohonen, T., 1989. Self-Organization and Associative Memory, third ed. Springer, New York Inc, NY, 312pp.

Kohonen, T., 2001. Self-organizing maps, third ed. Springer, Berlin, 501pp.

Kohonen, T., Hynninen, J., Kangas, J., Laaksonen, J., 1996a. SOM_PAK: the self-organizing map program package. Technical Report A31, Helsinki University of Technology, Laboratory of Computer and Information Science, FIN-02150 Espoo, Finland, 27pp.

Kohonen, T., Hynninen, J., Kangas, J., Laaksonen, J., Torkkola, K., 1996b. LVQ_PAK: the learning vector quantization program package. Technical Report A30, Helsinki University of Technology, Laboratory of Computer and Information Science, FIN-02150 Espoo, Finland, 30pp.

Levoy, M., 1988. Display of surfaces from volume data. IEEE Computer Graphics & Applications 8 (5), 29–37.

Lipman, R.P., 1987. An Introduction to Computing with Neural Nets. IEEE ASSP Magazine, April, 4–22.

Moline, G.R., Bahr, J.M., 1995. Estimating spatial distributions of heterogeneous subsurface characteristics by regionalized classification of electrofacies. Mathematical Geology 27, 3–22.

Penn, B.S., 2005. Using self-organizing maps to visualize high-dimensional data. Computers and Geosciences 31, 531–544.

Ripley, B.D., 1996. Pattern Recognition and Neural Networks. Cambridge University Press, Cambridge, Great Britain, 415pp.

Schalkoff, R.J., 1997. Artificial Neural Networks. McGraw-Hill, New York, 448pp.

Skapura, D., 1996. Building Neural Networks. ACM Press, Addison-Wesley, NY, 282pp.

Sneath, P.H.A., Sokal, R.R., 1973. Numerical Taxonomy. Freeman, San Francisco, CA, 573pp.

Tryon, R.C., Bailey, D.E., 1973. Cluster Analysis. McGraw-Hill, New York, NY, 347pp.

Tukey, J.W., 1977. Exploratory Data Analysis. Addison-Wesley, Reading, MA, 688pp.

Wegman, E.J., Solka, J.L., 2002. On some mathematics for visualizing high dimensional data. The Indian Journal of Statistics 64 (A-2), 429–452.

Wohletz, K.H., 1983. Mechanisms of hydrovolcanic pyroclast formation: size, scanning electron microscopy, and experimental studies. In: Sheridan, M.F., Barberi, F. (Eds.), Explosive Volcanism, Journal of Volcanology and Geothermal Research, vol. 17, pp. 31–63.

Wohletz, K.H., Krinsley, D., 1982. Scanning electron microscopy of basaltic hydromagmatic ash. Los Alamos National Laboratory Report, LA-UR 82-1433, 43pp.

4.3. Quantitative scanning-electron microscope analysis of volcanic ash surfaces: Application to the 1982–1983 Galunggung eruption (Indonesia)

Quantitative scanning-electron microscope analysis of volcanic ash surfaces: Application to the 1982–1983 Galunggung eruption (Indonesia)

Orkun Ersoy†
Department of Geological Engineering, Hacettepe University, 06532, Beytepe-Ankara, Turkey, and Université Blaise Pascal, 5 rue Kessler, 63038 Clermont-Ferrand, France

Alain Gourgaud
Observatoire de Physique du Globe de Clermont-Ferrand and Institut de Recherche pour le Développement, Université Blaise Pascal, UMR-CNRS 6524, 5 rue Kessler, 63038 Clermont-Ferrand, France

Erkan Aydar
Department of Geological Engineering, Hacettepe University, 06532, Beytepe-Ankara, Turkey

Gary Chinga
GCSCA, Trondheim, Norway

Jean-Claude Thouret
OPGC and IRD, Université Blaise Pascal, UMR-CNRS 6524, 5 rue Kessler, 63038 Clermont-Ferrand, France

ABSTRACT

Qualitative analyses of volcanic ash are time-consuming and subjective, whereas quantitative analyses are methodical and automated. Not only volcanic ash particles, but also many natural particles have been widely described and quantified by their outlines. The qualitative data of volcanic ash surfaces need to be expressed quantitatively, supported by supplementary methods such as statistical analysis and artificial intelligence. Well-defined surface descriptors can be applied to volcanic ash particles. In this study, roughness and texture descriptors of pyroclastic material from the 1982–1983 eruption of Galunggung (Java, Indonesia) were used to describe the vesicle surfaces of the particles, alteration intensity, and/or fine particle abundance. These parameters are important for distinguishing the products of magmatic eruptions from those of phreatomagmatic eruptions. Further application of this method may allow these descriptors to be easily converted to alteration grade, vesicularity index, intensity of the fragmentation mechanism, and relative proportions of the pyroclast types. Hence, discrimination between products of different fragmentation mechanisms may permit forecasting of volcanic hazards.

†E-mail: oersoy@hacettepe.edu.tr.

Keywords: volcanic ash, roughness, gradient analysis, texture descriptors, Galunggung.

INTRODUCTION

Microscopy Analysis of Volcanic Ash

Qualitative analyses of volcanic ash are time-consuming and may be affected by the human operator, whereas quantitative analyses are methodical and automated. Multiple samples can be analyzed quantitatively over a short period of time with limited intervention, allowing quantitative analyses to produce reliable results. Diverse efficient methods have been developed to describe and quantify natural objects in geosciences, such as gastropod shells (Dommergues et al., 2003) and detrital sediments (Drolon et al., 2003). Qualitative data describing volcanic ash also need to be expressed quantitatively, which requires supplementary methods including statistical analysis and artificial intelligence. Scanning electron microscopy (SEM) provides classification of volcanic ash based on surface morphology and texture (Wohletz and Krinsley, 1982; Büttner et al., 1999; Ersoy et al., 2006), and the most extensive SEM studies of pyroclast shapes to date have been presented by Heiken (1972, 1974), Wohletz (1983), and Heiken and Wohletz (1985). A study of explosive fragmentation dynamics by examination of the morphological features of natural and experimental ash particles has demonstrated the significance of morphological microfeatures on ash grains (Wohletz, 1983). The lack of analogue particles produced by scaled experiments at that time, however, allowed only a qualitative assessment. Although a study of natural pyroclastic sequences combined with scaled laboratory experiments identified the different fragmentation mechanisms related to the water/magma mass ratios during their interaction (Büttner et al., 1999), the surface features of the ash were not quantified. Bayhurst et al. (1994) developed an automated program for the characterization of volcanic ash particles of Redoubt volcano (Alaska) based on size, density, shape, and mineralogy using a SEM with an energy-dispersive X-ray detector (EDS); however, classification of volcanic ash surfaces is still limited to descriptive terms such as stepped, planar, crack patterns, and hydration skin.

Surface Measurements

Several texture descriptors have been developed to characterize the detailed surface structure of aluminum (Lee et al., 1998), aggregate (Rao et al., 2003), wear particles (Stachowiak, 1998), and paper surfaces (Chinga et al., 2003; Chinga, 2004). Fractal dimension, autocorrelation, gradient analysis, band-pass filtering, wavelet analysis, roughness statistics, and quadtree decomposition have been applied to assess complex surface structures (Panozzo, 1992; Costa, 2000; Chinga et al., 2003; Chinga, 2006). Analysis

GSA Bulletin; May/June 2007; v. 119; no. 5/6; p. 743–752; doi: 10.1130/B26048.1; 7 figures; 4 tables.

of surfaces of volcanic ash particles has been commonly limited to their outlines (Dellino and LaVolpe, 1996; Dellino and Liotino, 2002, Riley et al., 2003). Durant et al. (2004) and Horwell et al. (2003) measured the surface area of volcanic ash particles to investigate the ice-nucleating ability and to measure the production of radicals on the surfaces, respectively. Ersoy et al. (2006) calculated quadtree decomposition parameters and the surface descriptors derived from gradient analysis in order to quantify the structural changes of the ash surfaces due to variable explosion conditions in the phreatoplinian eruption of Nemrut volcano. The quadtree decomposition was performed by assessing the local gray-level standard deviation. The computation of the gradient of the presumed height data in the presumed topographical image was based on the partial derivatives at every pixel in the image.

The 1982–1983 Eruption of Galunggung

During the last eruption of Galunggung, Java, in 1982–1983, the composition of the erupted magma evolved from andesite (58% SiO_2) to Mg-rich basalt (47% SiO_2) (Gerbe et al., 1992), while the style of the eruption changed markedly through time (Katili and Sudradjat, 1984; Sudradjat and Tilling, 1984; Gourgaud et al., 1989). Observers from the Volcanological Survey of Indonesia (Katili and Sudradjat, 1984) recognized three distinct phases with three different eruptive styles: an initial Vulcanian phase 1, a phreatomagmatic phase 2, and a Strombolian phase 3. Gourgaud et al. (1989, 2000) emphasized the increase in explosivity (expressed as volcanic explosivity index; Newhall and Self, 1982) from the Vulcanian phase 1 to the phreatomagmatic phase 2, including higher plume height, larger volume of deposits, and great changes in crater morphology. In particular, Gourgaud et al. (2000) identified the transition between the phases with systematic variations of clast vesicularity and xenolith proportions and aimed to issue a volcanic-hazard forecast. Phase 1 was Vulcanian, but according to the limited involvement of groundwater in Vulcanian eruptions and Schmincke's proposal (Schmincke, 1977), the dynamism of phase 1 was already phreatomagmatic, and phase 2 represented an increase in phreatomagmatic activity (Gourgaud et al., 2000). The grain-size analysis did not reflect the transition from phase 1 to phase 2 (Gourgaud et al., 2000). The slight but continuous decrease in the vesicularity index of juvenile clasts and progressive increase in the ratio of xenolith versus juvenile lava clasts showed evidence of the increasing efficiency of groundwater-magma interaction during eruption (Gourgaud et al., 2000). Irrespective of the grade of phreatomagmatic activity, we use the term "Vulcanian" herein for phase 1 to suggest that less water was interacting with magma than during phase 2.

Types of Pyroclasts in 1982–1983 Tephra

Three main sequences of tephra properties during the 1982–1983 eruption are related to the three distinct eruptive phases. The variations in xenolith proportions and vesicularity in pyroclastic-flow deposits record an increase in magma-water interaction through the transition from Vulcanian phase 1 to phreatomagmatic phase 2 (Gourgaud et al., 2000). Here, we have available only xenolith and vesicularity data for pyroclasts from the pyroclastic flows of Vulcanian phase 1 and phreatomagmatic phase 2 (Gourgaud et al., 2000) to make a comparison with our quantitative results. Thus, we deal with pyroclastic-flow deposits of phase 1 and phase 2 from the Hot River and Cibanjaran valley sections (Fig. 1). The detailed stratigraphy includes four sections (Hot River, Cikunir, Cipanas, Cibanjaran), and all units can be found in Gourgaud et al. (2000). The grain-size interval of 250–500 μm was selected to enable comparison of the textures with those recorded in other studies (Wohletz, 1983; Heiken and Wohletz, 1985). Furthermore, the fine ash fractions often show shapes or textures that are distinct from coarser fractions, and they may be more definitive of explosive fragmentation (e.g., Zimanowski et al., 2003). Micrographs of whole grains and detailed surface configurations were obtained with JEOL JSM-5910 and CAMECA SU-30 operating at secondary electron modes with 5–15 keV at Laboratoire Magmas et Volcans (Clermont-Ferrand, France) and Hacettepe University (Ankara, Turkey), respectively.

In this study, two dominant juvenile pyroclast types were distinguished on 220 SEM micrographs. Their shapes correspond to type 1 and type 2 recognized by Wohletz (1983). The surfaces of particles show the influence of water-magma interaction, a form of "fuel-coolant interaction (FCI)" (e.g., Sheridan and Wohletz, 1983). FCI involves the contact of two fluids, where the fuel has a temperature above the boiling point of the coolant (Board et al., 1974; Buchanan, 1974; Board and Hall, 1975; Frölich et al., 1976; Drumheller, 1979; Corradini, 1981). The interaction generally results in vaporization of the coolant and chilling or quenching of the fuel. The fragmentation-vaporization process can be a cyclic process of vapor film generation and collapse. The energy of this collapse is partially cycled back into the system, generating new contact surfaces so that the system is self-sustaining. The collapse of a superheated vapor film or the explosive expansion of the film produces stress waves in the melt. If these exceed the bulk modulus of the melt and if it fractures in a brittle fashion, blocky type 1 or type 2 pyroclasts may form (see Figure 19 in Wohletz, 1983). Type 1 pyroclasts are found in compositions ranging from basaltic to rhyolitic. Type 2 pyroclasts were only found in basaltic compositions, especially in Surtsey tephra, by Wohletz (1983).

Pyroclasts of different types have unique shapes and textures and can therefore be distinguished visually on 220 SEM micrographs by an operator. Type 1 pyroclasts have blocky, equant morphology. Typically, vesicular surfaces are rare and cut by curviplanar fracture surfaces. The irregularities on surfaces of type 1 pyroclasts belong to alteration products and adhering dust or vesicle embayment. Type 2 pyroclasts have surfaces controlled by vesicle walls. Vesicle edges are rounded and smoothed, and overall grain shape is irregular. The smooth curved surfaces between vesicles are lumpy and appear to be fused and fluid-formed. Quenching and solidification during and after brittle fracture probably preserved the blocky shapes with curviplanar surfaces (type 1). Solidification and formation of a quenched crust was probably incomplete after fracture, and subsequent movement of fragments out of the zone of interaction formed smooth, fluid-like surfaces on fragments (type 2) (Wohletz, 1983).

Definitive Characteristics of 1982–1983 Tephra

The first sequence of the 1982–1983 erupted tephra, including initial, high-energy pyroclastic surges at the onset of eruption, lithic-rich pyroclastic flows, scoriaceous block-and-ash flows and, brief pulses of surges interspersed with brief and small-volume tephra fallouts, is related to the Vulcanian phase 1 of 5 April to 13 May 1982. Samples from pyroclastic flows of the Vulcanian phase have free crystals or crystals with vesicular glass. Some crystals have stepped fractures on their surfaces, characteristic of brittle breakage. Fine adhering dust (maximum 10 μm) on the surfaces of crystals is common. Several juvenile glass fragments are nonvesicular and have equant, blocky surfaces (type 1) (Fig. 2). In particular, surfaces have irregularities caused by poorly developed vesicles. Many of these vesicles are cut by curviplanar fractures, possibly as a result of hydrovolcanic fragmentation of the melt (Wohletz, 1983; Heiken and Wohletz, 1985). The surfaces are covered by aggregates of fine ash and alteration products, probably clay minerals. Vesicular

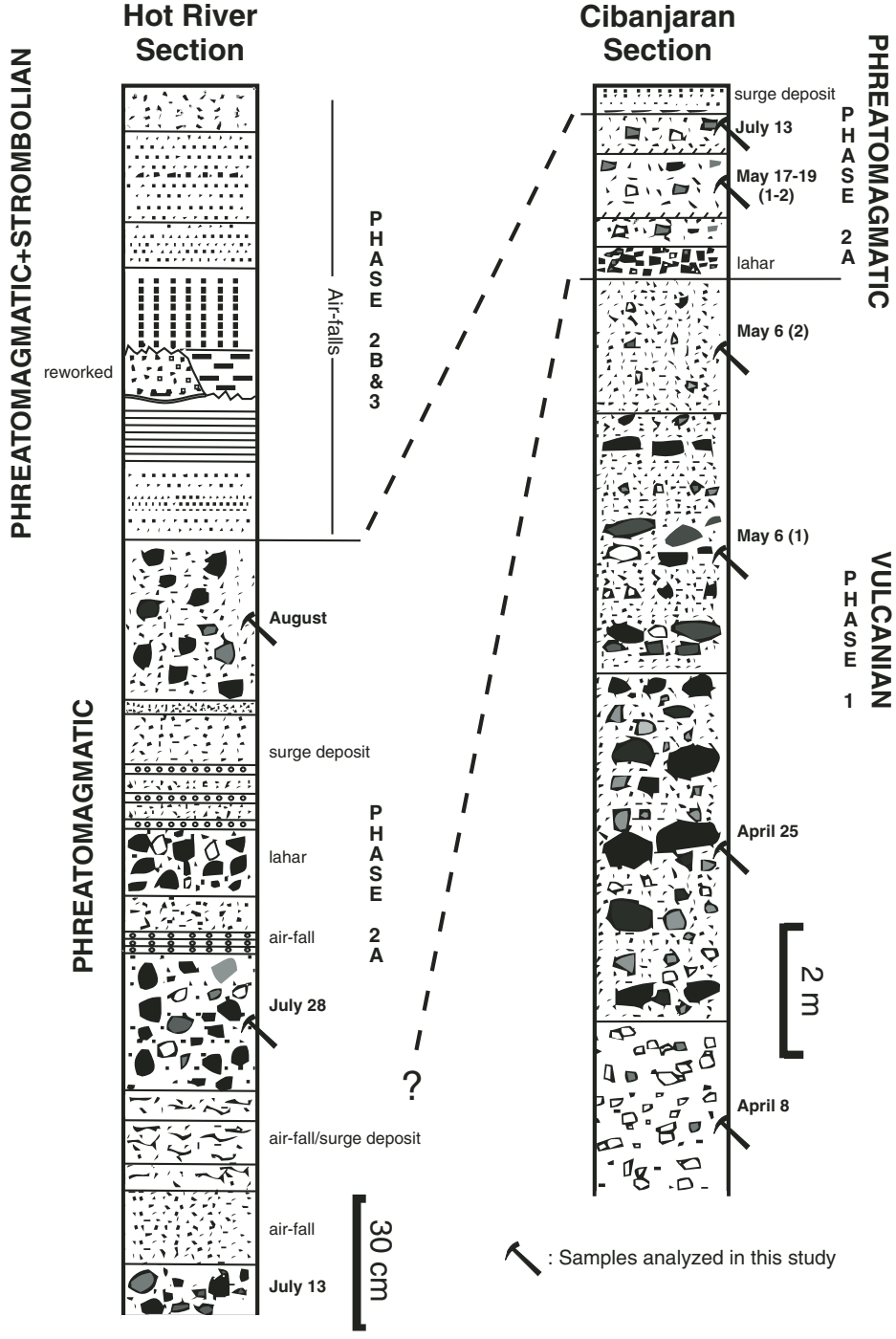

Figure 1. Stratigraphic sections of the 1982 erupted deposits from Hot River area and Cibanjaran valley after Gourgaud et al. (2000). The samples analyzed in this study are labeled with a hammer symbol.

glass fragments have frosted, smooth, fluidal surfaces (type 2) (Fig. 2). The vesicles are filled with fine ash and alteration products. Vesicle edges are rounded and chipped by transport abrasion or the fragmentation mechanism. Glass fragments from the Vulcanian phase have elongated particles with a width:length ratio of up to 0.25. Some show large crystal molds. Hydration cracks are absent in samples from the first phase of the eruption. Nonjuvenile particles of the Vulcanian phase are more altered and rounded than the juvenile ones.

Following a major break in the eruptive activity, several pulses of energetic base surges deposited dune-like, cross-bedded deposits on the crater slopes. This suggests a sudden increase in magma-water interaction in the phreatomagmatic phase (Gourgaud et al., 2000). Repeated tephra-fall deposits of small volume and a few lithic-rich pyroclastic flows were emplaced in the first part of the phreatomagmatic phase. Moreover, a new crater that largely intersected the 1918 dome was opened on 17–19 May and 13–17 July. It has been interpreted as a maar crater, and it removed 80% of the 1918 dome (Gourgaud et al., 2000). The crystals of the phreatomagmatic phase have the same characteristics as those of the Vulcanian phase. Juvenile blocky pyroclasts (type 1) are more common than smooth fluidal ones (type 2). The vesicles are filled with adhering dust, and vesicle edges have been smoothed by chipping (Fig. 3). The juvenile particles are rounded and altered. The dusty appearance is attributable to clay-like debris in hollows. Hydration cracks and pitting are present on the surfaces of the juvenile particles (Fig. 3). The nonjuvenile particles show extreme alteration with rounded outlines. The adhering dust completely covers the surface of particles. Uncharred wood fragments are present within samples from the phreatomagmatic phase. The aggregation of small particles, strong surface alteration, and uncharred wood fragments indicate low-temperature emplacement during the phreatomagmatic phase. Gourgaud et al. (2000) also proposed these characteristics as evidence for the phreatomagmatic phase.

The products of eruptions on 17–19 May and 13 July, when new maars formed (Gourgaud et al., 2000), show the highest proportions of blocky type 1 pyroclasts (Fig. 4; Table 1). Despite the washing procedure, small particles still adhered to the analyzed surfaces. To understand the sensitivity of our quantitative descriptors to altered surfaces, an operator labeled all particles as altered or fresh (Fig. 4; Table 1). Samples from the first maar formation were completely altered. At the end of the phreatomagmatic phase, the phreatomagmatic fall deposits preceded the transition to the late Strombolian activity. The activity clearly shifted to the long-lasting Strombolian phase (3) of November 1982–January 1983, which emplaced a thick pile of lapilli and ash-fall deposits (Gourgaud et al., 2000).

METHODOLOGY

Image Processing and Analysis

The roughness of a surface can be measured in different ways. Figure 5 depicts a schematic representation of a surface and the applied terms used to describe it. Roughness amplitude

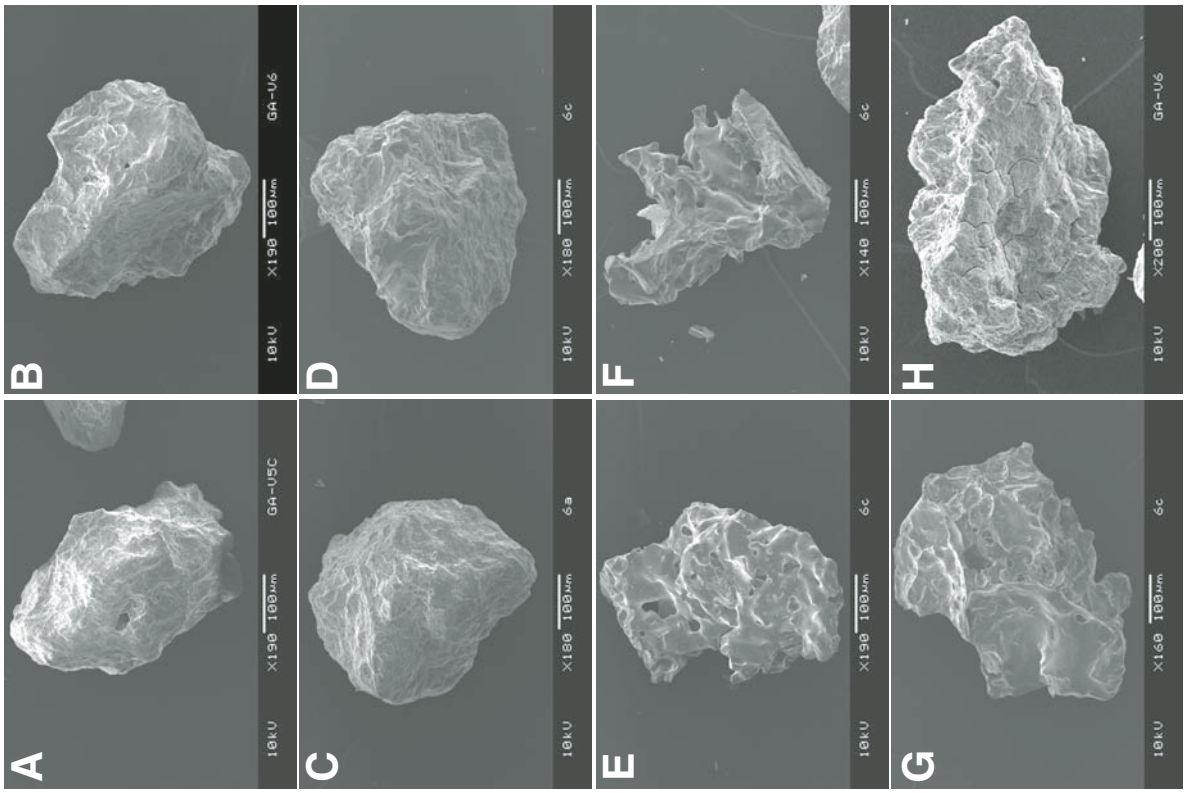

Figure 2. Type 1 (A, B, C, and D) and type 2 (E, F, G, and H) pyroclasts from Vulcanian phase (1). Type 1 pyroclasts are nonvesicular and have equant, blocky shapes. Type 2 pyroclasts are vesicular and have frosted, smooth, fluidal-surfaces.

Figure 3. Type 1 (A, B, C, and D) and type 2 (E, F, and G) pyroclasts from phreatomagmatic phase (2). Hydration cracks and pitting are present on surfaces of some pyroclasts from phase 2 (H).

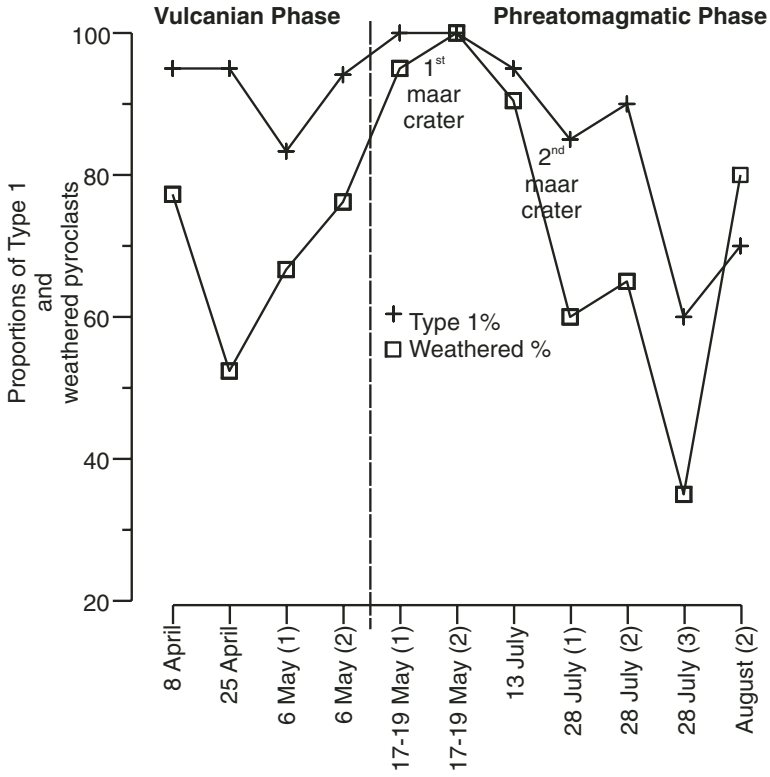

Figure 4. Proportions of type 1 and altered pyroclasts through time in the pyroclastic-flow deposits of 1982 eruption.

TABLE 1. PROPORTIONS OF TYPE 1, TYPE 2, ALTERED, AND FRESH PYROCLASTS THROUGH TIME IN PYROCLASTIC-FLOW DEPOSITS OF 1982 ERUPTION

	Eruption date	Type 1 (%)	Type 2 (%)	Altered (%)	Fresh (%)
Vulcanian phase	8 April	77,27	22,73	95	5
	25 April	52,38	47,62	95	5
	6 May (1)	66,67	33,33	83,33	16,67
	6 May (2)	76,19	23,81	94,12	5,88
Phreatomagmatic phase	17–19 May (1)	95	5	100	0
	17–19 May (2)	100	0	100	0
	13 July	90,48	9,52	95	5
	28 July (1)	60	40	85	15
	28 July (2)	65	35	90	10
	28 July (3)	35	65	60	40
	August (2)	80	20	70	30

descriptors give an average measurement of the surface height. Some amplitude descriptors include the average roughness (R_a) and the root-mean-square roughness (R_q). Statistical descriptors are skewness (R_{sk}) and kurtosis (R_{ku}) of the amplitude distribution function (ADF), which gives the probability that the profile of the surface has a certain height, z, at any position x. Extreme value descriptors depend on isolated events, e.g., the maximum peak height (R_p), the maximum valley depth (R_v), and the maximum peak to valley height (R_t). Roughness amplitude descriptors are still used extensively in science and industry to characterize a surface and can be applied to volcanic ash particles. Detailed information about the roughness parameters and an application on paper surfaces can be found in Chinga et al. (2003).

Gradient analysis has also proven to be suitable for describing surface texture orientation. Similar methods have been used to detect the orientation of short-fiber composites (Gadala-Maria and Parsi, 1993), actin fibers in cytoskeletal structures (Yoshigi et al., 2003), and features on volcanic ash surfaces (Ersoy et al., 2006). It may be a valuable tool for differentiating between textures that have the same gray-level variation. The gradient analysis is based on Sobel operators as described by Gonzalez and Woods (1993) and implemented by Chinga et al. (2003). For more details on the current application of gradient analysis for surface structure quantification, see Chinga and Dougherty (2006).

Four samples from phase 1 and seven samples from phase 2 were analyzed. Twenty replicates were acquired from each sample for texture analysis. Image processing and analysis were performed on 220 SEM micrographs using the ImageJ program (Rasband, 2004). ImageJ is a public-domain image-processing program based on Java and was designed with an open architecture that provides extensibility via Java plugins (available at http://rsb.info.nih.gov/ij/).

The micrographs taken by SEM were cropped to 300 × 300 pixel images to include only surfaces without background. All images were converted to a sequential stack. A band-pass filter was used to filter out large structures (shading correction) and small structures (smoothing) of the specified size from the images. Seven roughness descriptors were calculated for each grain (Chinga et al., 2003; Table 2). The SurfCharJ plugin (Chinga et al., 2003, available at http://www.gcsca.net) was used for surface roughness and gradient analysis. The processing algorithm produces a polar plot image that represents the magnitude of the gradients relative to the surface (Fig. 6). A detailed application and technical explanation of gradient analysis on volcanic ash can be found in Ersoy et al. (2006). The polar plot was analyzed with the Shape Descriptor plugin (available at http://www.gcsca.net). Different shape descriptors such as the aspect ratio, compactness, roundness, and form factor were calculated according to Russ (1999) (Table 3).

Statistical Analysis

We identified grains by type (type 1 and Type 2) and labeled all pyroclasts as altered or fresh to determine the correlation of qualitative and quantitative descriptors. Furthermore, we compared our results with xenolith proportions and the vesicularity index calculated by Gourgaud et al. (2000), who used the method of Houghton and Wilson (1989). These variables were subjected to correlation analysis using Pearson's correlation coefficient, which is a measure of linear association. Our calculations of Pearson correlation coefficients used Statistical Package for the Social Sciences (SPSS Inc, Release 9.0) and the bivariate correlations procedure.

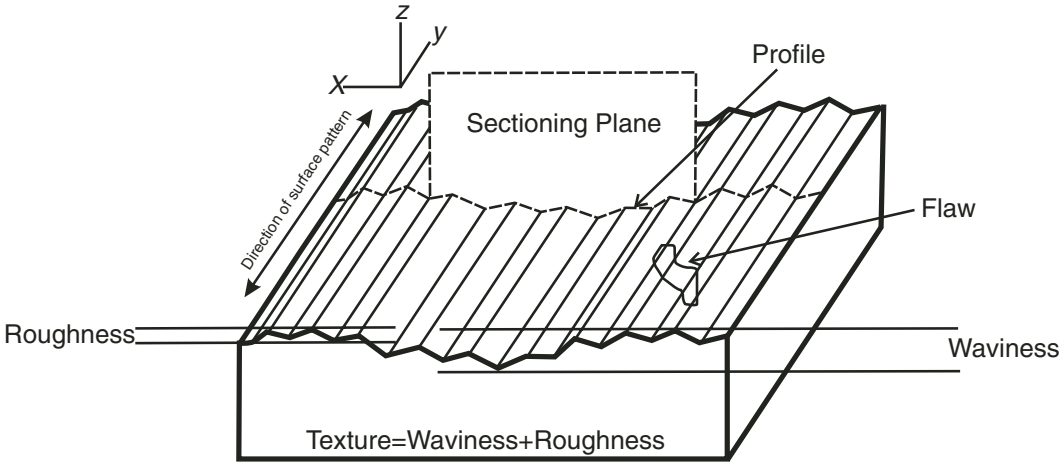

Figure 5. Surface profile (reproduced from TS 6956, 2004).

RESULTS

The roughness amplitude descriptors, R_a and R_q, are similarly related to other parameters (Table 4). Their strongest correlations are with R_{ku}, R_p, R_t, form factor, and alteration. The correlations of R_a and R_q with the proportion of altered surfaces are significant (0.82 and 0.83, respectively). These parameters seem sensitive to alteration or to adhering particles on surfaces. There is no correlation with vesicularity (–0.09 and –0.07), and their correlations with pyroclast type are insignificant (0.58 and 0.57).

The statistical descriptors, R_{sk} and R_{ku}, are strongly correlated with each other. R_{sk} is strongly correlated with vesicularity (0.96) and is sensitive to pyroclast types (–0.82). The correlation of R_{sk} to these two parameters points to the internal correlation of pyroclastic types and vesicularity. The vesicularity index of pyroclasts and their types show a strong correlation (–0.90), indicating that the proportions of pyroclastic types affect vesicularity index. R_{ku} has an important correlation with form factors of polar plots of surfaces (–0.91). Details are not given here for extreme value descriptors since they are similar to other prevalent parameters. R_p and R_t are similar to R_a and R_q and are sensitive to adhering dust and alteration on surfaces.

The strong correlations of form factor with almost all roughness descriptors and alteration are noteworthy. The other texture descriptors, roundness, compactness and aspect ratio, do not show any correlation with roughness of surfaces but only internal correlations among themselves. There is no strong correlation between the proportions of type 1 pyroclasts and pyroclasts with altered surfaces (0.65). Not all type 1 pyroclasts are altered; likewise, not all type 2 pyroclasts are fresh.

Gourgaud et al. (2000) defined the transition between Vulcanian phase 1 and phreatomagmatic phase 2 through systematic variations of clast vesicularity and xenolith proportions. Here, our parameters show the transition from Vulcanian phase to phreatomagmatic phase through different trends (Fig. 7). Furthermore, fluctuations in the calculated parameters give information about the fragmentation mechanisms, abundance of water accessible to the vent and alteration conditions. R_a and R_q values increase during the transition between Vulcanian phase and phreatomagmatic phase and decrease toward the Strombolian phase, whereas R_{sk} and R_{ku} values show a decreasing trend in the transition to the phreatomagmatic phase and an increase toward the Strombolian phase. The increasing trends of R_a and R_q indicate an increasing abundance of fine ash and alteration through the transition from Vulcanian phase to phreatomagmatic phase. It is probable that intense fragmentation mechanisms occurred through the phreatomagmatic eruption of Galunggung in 1982–1983. Evidence such as aggregation of small particles, strong surface alteration, and uncharred wood pieces in the phreatomagmatic phase also points to steam-rich eruptions producing fine-grained tephra. The decreasing trends of R_a and R_q toward the Strombolian phase are signs of a decreasing amount of water interacting with magma. Restricted access of water to the vent probably resulted in drier eruptions and dispersion of coarser particles with fresh surfaces. The form factor of polar plots shows trends similar to those of R_a and R_q. These parameters are also

TABLE 2. PROFILE PARAMETERS ACCORDING TO BS EN ISO 4287 (2000). THE CORRESPONDING DIGITAL ROUTINE IS ALSO GIVEN

R parameter	Line profile	Digital routine	Description
R_a	$=\frac{1}{l}\int_0^L \lvert z(x)\rvert dx$	$=\frac{1}{mn}\sum_{i=1}^{m}\sum_{j=1}^{n}\lvert zij\rvert$	Arithmetical mean deviation
R_q	$=\sqrt{\frac{1}{l}\int_0^L z^2(x)dx}$	$=\left(\frac{1}{mn}\sum_{i=1}^{m}\sum_{j=1}^{n}zij^2\right)^{1/2}$	Root-mean-square deviation
R_{sk}	$=\frac{1}{R_q^3}\left[\frac{1}{l}\int_0^L z^3(x)dx\right]$	$=\frac{1}{R_q^3}\frac{1}{mn}\sum_{i=1}^{m}\sum_{j=1}^{n}zij^3$	Skewness of the assessed profile
R_{ku}	$=\frac{1}{R_q^4}\left[\frac{1}{l}\int_0^L z^4(x)dx\right]$	$=\frac{1}{R_q^4}\frac{1}{mn}\sum_{i=1}^{m}\sum_{j=1}^{n}zij^4$	Kurtosis of the assessed profile
R_v			Largest profile valley depth
R_p			Largest profile peak height
R_t	$=R_v+R_p$		Sum of largest profile valley depth and peak height within the evaluation length

Note: Table data were taken from Chinga et al. (2003).

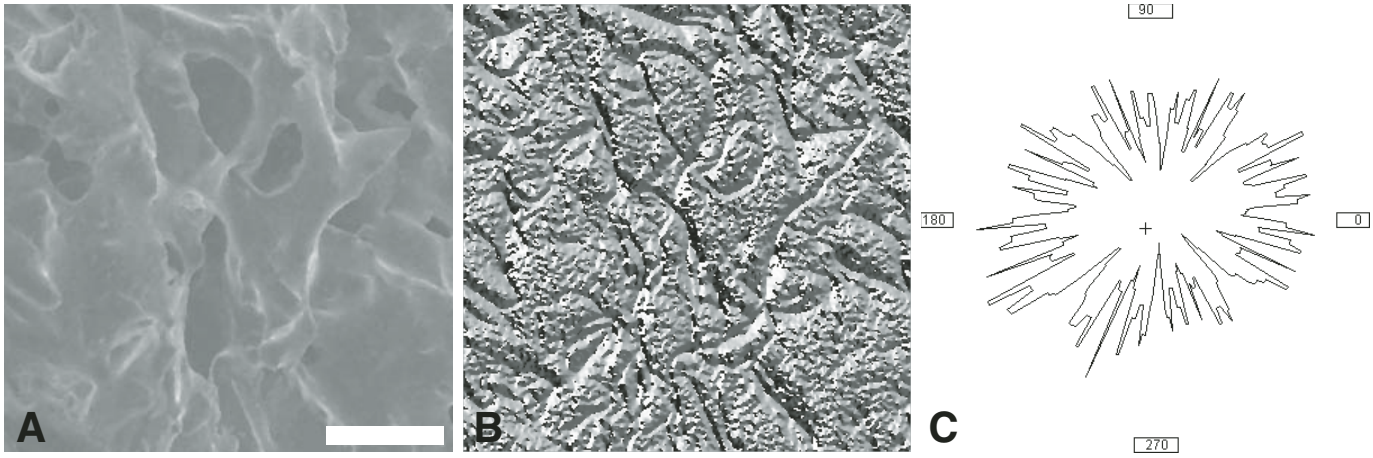

Figure 6. Original gray-level image (A), azimuthal image (B), and polar plot based on frequency of gradients (C). Bar in A = 30 µm.

sensitive to alteration, and they indicate finer materials and intense alteration in the phreatomagmatic phase and fresh coarse particles toward the Strombolian phase.

R_{sk} and R_{ku} trends are very similar to the vesicularity index trends of Gourgaud et al. (2000). The higher correlations of R_{sk} and R_{ku} with pyroclast type indicate the abundance of type 1 pyroclasts through the transition from Vulcanian phase to phreatomagmatic phase and their reduction toward the Strombolian phase.

DISCUSSION

The simplicity of this method has its advantages and disadvantages.

Advantages

In addition to the variations in the vesicularity and abundance of xenoliths, the quantitative surface descriptors show the increased water-magma interaction and intensity of the fragmentation mechanism between phases. Multicondition-driven mechanisms may produce pyroclastic deposits that vary in fundamental properties such as dispersal, grain size, vesicularity and morphology of juvenile clasts, and the abundance of lithic or "wall rock" ejecta (xenoliths). Among the criteria used to distinguish the products of magmatic eruptions from phreatomagmatic eruptions, the vesicularity of the juvenile clasts is generally considered to be higher in the former and lower in the latter (Walker and Croasdale, 1972; Houghton and Wilson, 1989). The statistical descriptors, R_{sk} and R_{ku}, are sensitive to vesicles on ash surfaces. These two parameters of surface roughness may be suitable for describing the vesicularity of the particles. They demonstrate the decreasing vesiculation through the transition from Vulcanian to phreatomagmatic phase. Fragmentation by explosive interaction with water takes the place of magma disruption by expansion of magmatic gases during the transition between these phases. Toward the Strombolian phase, exsolution of magmatic gas tends to inhibit an efficient magma-water interaction (Zimanowski et al., 1991). The abundance of fine ash and alteration may also give clues about the intensity of fragmentation. Fine, adhering dust is the evidence of high degrees of fragmentation, which tends to produce abundant fine ash. Steam-rich eruptions produce relatively fine-grained tephra, which may be emplaced with steam that condenses on ash surfaces. Ash grains are subjected to hot fluids from the time of their formation until they finally cool to ambient temperatures within the deposit. Under these circumstances, alteration may progress quickly, and it is more rapid for the finest grain sizes (Heiken and Wohletz, 1985). R_a, R_q, and form factor are sensitive to adherence of particles that result from intense fragmentation and/or alteration. Form factor also shows strong correlations with almost all roughness descriptors and alteration. Form factor is therefore an ideal parameter to use in tephra studies. All informative surface roughness parameters can be reduced to this parameter.

Quantitative analyses are methodical and automated. Furthermore, they allow the use of supplementary methods. We used ImageJ and its plugins for image analysis in this study. They are freely available, and the codes are in the public domain. Quantitative functions on digital images give the microscopist an unprecedented degree of flexibility and convenience in using the output of the SEM (Goldstein et al., 2003). ImageJ displays a "stack" of related images in a single window and processes an entire stack using a single command. This ensures the analysis of multiple images in a short time period. The macros can be written to combine several commands; therefore, the process becomes faster, automated, and unbiased. The most powerful property of this quantitative method is that it is methodical and automated, and there is limited intervention of the operator.

TABLE 3. CALCULATED SHAPE DESCRIPTORS ACCORDING TO RUSS (1999)

Shape descriptor	Formula
Form factor	$= \frac{4\pi \times Area}{Perimeter^2}$
Roundness	$= \frac{4 \times Area}{\pi \times Major\ axis^2}$
Compactness	$= \frac{\left(\left[4/\pi\right] Area\right)^2}{Major\ axis}$
Aspect ratio	$= Major\ axis / Minor\ axis$

Disadvantages and Suggestions

Carbon coating is a demanding process. Coating of the specimen is essential in order to conduct charge away from the area being analyzed. Poor carbon coating may give rise to charging on surfaces and misleading results. One of the most important recent developments is the variable-pressure SEM. A differential pumping system is used to maintain the electron gun at high vacuum while the specimen is under a much higher pressure. This instrument can be used to study insulating, uncoated, wet, and generally untreated specimens (Goldstein et al., 2003). Gold coating or the variable-pressure mode of SEM may solve the charging problems.

TABLE 4. PEARSON CORRELATION COEFFICIENTS CALCULATED FOR ROUGHNESS AMPLITUDE, STATISTICAL, EXTREME VALUE, AND TEXTURE DESCRIPTORS, PERCENTAGE OF TYPE 1 AND ALTERED PYROCLASTS, AND VESICULARITY INDEX

	Roughness amplitude descriptor		Statistical descriptor		Extreme value descriptor			Texture descriptors			Type 1	Altered	Vesicularity
	R_a	R_q	R_{sk}	R_{ku}	R_p	R_v	R_t	Form factor	Roundness	Compactness	Aspect ratio			
R_a	1	1.000††	−0.667†	−0.774††	0.928††	−0.061	0.793††	0.927††	0.630†	0.632†	−0.623†	0.583	0.823††	−0.094
R_q	1.000††	1	−0.651†	−0.763††	0.928††	−0.065	0.793††	0.925††	0.636†	0.638†	−0.629†	0.571	0.825††	−0.074
R_{sk}	−0.667†	−0.651†	1	0.968††	−0.679†	−0.247	−0.665†	−0.800††	−0.086	−0.085	0.081	−0.818††	−0.645†	0.963††
R_{ku}	−0.774††	−0.763††	0.968††	1	−0.791††	−0.22	−0.755††	−0.908††	−0.167	−0.165	0.164	−0.794††	−0.787††	0.783†
R_p	0.928††	0.928††	−0.679†	−0.791††	1	0.302	0.961††	0.955††	0.57	0.565	−0.575	0.535	0.909††	−0.228
R_v	−0.061	−0.065	−0.247	−0.22	0.302	1	0.553	0.185	−0.11	−0.126	0.08	0.019	0.281	−0.219
R_t	0.793††	0.793††	−0.665†	−0.755††	0.961††	0.553	1	0.888††	0.467	0.458	−0.48	0.473	0.876††	−0.524
Form factor	0.927††	0.925††	−0.800††	−0.908††	0.955††	0.185	0.888††	1	0.433	0.431	−0.434	0.685†	0.929††	−0.239
Roundness	0.630†	0.636†	−0.086	−0.167	0.57	−0.11	0.467	0.433	1	0.997††	−0.998††	0.066	0.384	−0.142
Compactness	0.632†	0.638†	−0.085	−0.165	0.565	−0.126	0.458	0.431	0.997††	1	−0.997††	0.07	0.387	−0.136
Aspect ratio	−0.623†	−0.629†	0.081	0.164	−0.575	0.08	−0.48	−0.434	−0.998††	−.997††	1	−0.062	−0.397	0.15
Type 1	0.583	0.571	−0.818††	−0.794††	0.535	0.019	0.473	0.685†	0.066	0.07	−0.062	1	0.654†	−0.904††
Altered	0.823††	0.825††	−0.645†	−0.787††	0.909††	0.281	0.876††	0.929††	0.384	0.387	−0.397	0.654†	1	−0.307
Vesicularity	−0.094	−0.074	0.963††	0.783†	−0.228	−0.219	−0.524	−0.239	−0.142	−0.136	0.15	−.904††	−0.307	1

†Correlation is significant at the 0.01 level.
††Correlation is significant at the 0.05 level.

Figure 7. Evolution of surface parameters on volcanic ash particles through time in 1982 eruption of Galunggung volcano.

It is also important to keep in mind that the surface descriptors are used for describing the three-dimensional (3-D) structure of surfaces. The images used in the present study are SEM two-dimensional images. The popularity of the SEM stems from its capability of obtaining three-dimensional–like images of surfaces of a very wide range of materials (Goldstein et al., 2003). Although the SEM images give a 3-D impression of the ash surfaces, they do not give real topographical representations with local height values. Despite this fact, it is assumed that the gray-level variation is related to the real roughness variation of the surface. The three-dimensional appearance of the images is due to the large depth of field of the SEM as well as to the shadow relief effect of the secondary and backscattered electron contrast (Goldstein et al., 2003). Rough surfaces emit more low-energy secondary electrons from the surface edges, which creates the measured gray-level variation. Topographic contrast arises because the number of secondary electrons depends on the angle of incidence between the beam and the specimen surface. The angle of incidence between the beam and the local surface will vary only because of the local inclination of the specimen (Goldstein et al., 2003). In addition, SEM stereo pairs can be used for generating height maps, thus making it possible to assess the real topography of ash particles. The large depth of field available in the SEM makes it possible to observe 3-D objects by the use of stereoscopy. Three-dimensional images allow different morphological features to be correctly interpreted and definitively measured (Goldstein et al., 2003). Surface descriptors such as fractal dimension may be used on 3-D surfaces of ash particles.

The fragmentation mechanisms of volcanic ash particles have been discriminated by their shapes and supported by eruptive observations, textures of deposition, componentry, and grain-size analyses. For the case of phreatomagmatic eruptions, surface chemistry of individual grains can be acquired by an energy-dispersive X-ray detector (EDS) on a SEM. Such data can also reveal the origin of volcanic ash particles, and it may be a complementary parameter for this study.

CONCLUSIONS

Many natural particles other than volcanic ash have been widely described and quantified by their outlines. In addition to their outlines, the volcanic ash surfaces also need to be expressed in quantitative ways. Consequently, we can use supplementary methods, e.g., statistical analysis, to classify surfaces that have different properties. In this study, easy and well-defined surface descriptors were introduced. R_a, R_q, and form factor provided information about the alteration intensity and/or fine particle abundance; these can be interpreted as evidence of steam in eruption and/or intense fragmentation. R_{sk} and R_{ku} are suitable for describing the vesicularity of the particles to distinguish the products of magmatic and phreatomagmatic eruptions. Furthermore, R_{sk} and R_{ku} are sensitive to pyroclast type, which results from different fragmentation mechanisms. Quenching and solidification during and after brittle fracture probably preserved blocky shapes with curviplanar surfaces, and type 1 pyroclasts were formed. Solidification and formation of a quenched crust were not complete after fracture, and subsequent movement of fragments out of the zone of interaction formed smooth, fluid-like surfaces on type 2 pyroclasts. Steam and fine particle abundance and the presence of blocky, equant and poorly or nonvesicular altered pyroclasts (type 1) suggest water-magma interaction, an effective and hazardous mechanism of conversion of thermal into kinetic energy (Wohletz and Sheridan, 1983; Wohletz, 1986; Lorenz et al., 1991; Wohletz and Brown, 1995; Zimanowski et al., 1997). Wide application of this method in the future may allow these descriptors to be easily converted to alteration grade, vesicularity index, intensity of fragmentation mechanism and amount of fine particles, and different types of pyroclasts with the ultimate aim of issuing a volcanic hazard forecast.

Apart from volcanology, this method can be utilized in numerous geological applications. Because of the increasing interest in surface properties of natural materials, surface descriptors proposed in this study can be applied to surfaces of various natural materials. Roughness and texture descriptors can be calculated on bulk rock samples to observe the relation among roughness and alteration, hydromechanical properties (Sausse, 2002; Pot and Genty, 2007), slake durability index (Kolay and Kayabali, 2006), classification of the stylolites (Brouste et al., 2007), etc.

ACKNOWLEDGMENTS

The research activities of the first author in France were supported by a scholarship granted by the French government. Thanks are due to Laboratoire Magmas et Volcans (France) for technical assistance. A. Çiner and E. Cubukcu gave a critical reading of the manuscript and significantly improved the English. We thank Associate Editor Nancy Riggs, and reviewers Sharon Allen and Ken Wohletz for their constructive suggestions. International Science Editing edited the English in the paper.

REFERENCES CITED

Bayhurst, G.K., Wohletz, K.H., and Mason, A.S., 1994, A method for characterizing volcanic ash from the December 15, 1989, eruption of Redoubt volcano, Alaska, *in* Casadevall, T., ed., Volcanic Ash and Aviation Safety: U.S. Geological Survey Bulletin 2047, p. 13–18.

Board, S.J., and Hall, R.W., 1975, Thermal explosions at molten tin/water interfaces, *in* Okendon, J.R., et al., eds., Moving Boundary Problems in Heat Flow Diffusion: Oxford, Clarendon Press, p. 259–269.

Board, S.J., Farmer, C.L., and Poole, D.H., 1974, Fragmentation in thermal explosions: International Journal of Heat and Mass Transfer, v. 17, p. 331–339, doi: 10.1016/0017-9310(74)90094-5.

Brouste, A., Renard, F., Gratier, J.-P., and Schmittbuhl, J., 2007, Variety of stylolites' morphologies and statistical characterization of the amount of heterogeneities in the rock: Journal of Structural Geology (in press).

Buchanan, D.S., 1974, A model for fuel-coolant interactions: Journal of Physics, ser. D, Applied Physics, v. 7, p. 1441–1457, doi: 10.1088/0022-3727/7/10/318.

Büttner, R., Dellino, P., and Zimanowski, B., 1999, Identifying modes of magma/water interaction from the surface features of ash particles: Nature, v. 401, p. 688–690, doi: 10.1038/44364.

Chinga, G., 2004, Detailed characterization of paper surface structure for gloss assessment: Journal of Pulp and Paper Science, v. 30, no. 8, p. 222–227.

Chinga, G., 2006, A quadtree decomposition approach for surface assessment: Pattern Analysis & Applications, v. 9, no. 4, p. 94–101.

Chinga, G., and Dougherty, R., 2006, Quantification of surface structures, *in* Jahren, A., and Moll, C., eds., Proceedings of the 1st Image J User and Developer Conference: Luxembourg, Centre de Recherche Public Henri Tudor, Luxembourg, p. 117–122.

Chinga, G., Gregersen, Ø., and Dougherty, R., 2003, Paper surface characterization by laser profilometry and image analysis: Journal of Microscopy and Analysis, v. 84, p. 5–7.

Corradini, M.L., 1981, Analysis and modeling of steam explosion experiments: Sandia National Laboratory Report SAND80–2131, NUREG/CR-2072, 114 p.

Costa, M.A., 2000, Fractal description of rough surfaces for haptic display [Ph.D. thesis]: Stanford, Stanford University, 119 p.

Dellino, P., and La Volpe, L., 1996, Image processing analysis in reconstructing fragmentation and transportation mechanisms of pyroclastic deposits. The case of Monte Pilato–Rocche Rosse eruptions, Lipari (Aeolian Islands, Italy): Journal of Volcanology and Geothermal Research, v. 71, p. 13–29, doi: 10.1016/0377-0273(95)00062-3.

Dellino, P., and Liotino, G., 2002, The fractal and multifractal dimension of volcanic ash particles contour: A test study on the utility and volcanological relevance: Journal of Volcanology and Geothermal Research, v. 113, p. 1–18, doi: 10.1016/S0377-0273(01)00247-5.

Dommergues, E., Dommergues, J.-L., Magniez, F., Neige, P., and Verrecchia, E.P., 2003, Geometric measurement analysis versus Fourier series analysis for shape characterization using the gastropod shell (*Trivia*) as an example: Mathematical Geology, v. 35, no. 7, p. 887–894, doi: 10.1023/B:MATG.0000007785.96748.62.

Drolon, H., Hoyez, B., Druaux, F., and Faure, A., 2003, Multiscale roughness analysis of particles: Application to the classification of detrital sediments: Mathematical Geology, v. 35, no. 7, p. 805–817, doi: 10.1023/B:MATG.0000007780.52861.57.

Drumheller, D.S., 1979, The initiation of melt fragmentation in fuel-coolant interactions: Nuclear Science and Engineering, v. 72, p. 347–356.

Durant, A.J., Mi, Y., Shaw, R.A., Ernst, G.G.J., and Rose, W.I., 2004, Ice nucleation by volcanic ash: Influence of composition and morphology, *in* Proceedings of the International Association of Volcanology and Chemistry of the Earth's Interior General Assembly: Pucon, Chile, www.geo.mtu.edu/~ajdurant/ice_nucleation_experiments/objects/durant_etal_IAVCEI_2005.pdf.

Ersoy, O., Chinga, G., Aydar, E., Gourgaud, A., Cubukcu, H.E., and Ulusoy, I., 2006, Texture discrimination of volcanic ashes from different fragmentation mechanisms: A case study, Mount Nemrut stratovolcano, eastern Turkey: Computers & Geosciences, v. 32, p. 936–946, doi: 10.1016/j.cageo.2005.10.013.

Frölich, G., Müller, G., and Unger, G., 1976, Experiments with water and hot melts of lead: Journal of Non-Equilibrium Thermodynamics, v. 1, p. 91–103.

Gadala-Maria, F., and Parsi, F., 1993, Measurement of fiber orientation in short-fiber composites using digital image processing: Polymer Composites, v. 14, no. 2, p. 126–131, doi: 10.1002/pc.750140206.

Gerbe, M.C., Gourgaud, A., Sigmarsson, O., Harmon, R.S., Joron, J.L., and Provost, A., 1992, Mineralogical and geochemical evolution of the 1982–1983 Galunggung eruption (Indonesia): Bulletin of Volcanology, v. 54, p. 284–298, doi: 10.1007/BF00301483.

Goldstein, J., Newbury, D., Joy, D., Lyman, C., Echlin, P., Lifshin, E., Sawyer, L., and Michael, J., 2003, Scanning electron microscopy and X-ray microanalysis: New York, Springer Press, 687 p.

Gonzalez, R., and Woods, R.E., 1993, Digital Image Processing: Reading, Massachusetts, Addison-Wesley Publishing Company, 716 p.

Gourgaud, A., Camus, G., Gerbe, M.C., Morel, J.M., Sudradjat, A., and Vincent, P.M., 1989, 1982–83 eruption of Galunggung (Indonesia): A case study of volcanic hazards with particular relevance to air navigation, *in* Latter, J.H., ed., International Association of Volcanology and Chemistry of the Earth's Interior Proceedings in Volcanology 1. Volcanic Hazards: Berlin, Springer, p. 151–162.

Gourgaud, A., Thouret, J.C., and Bourdier, J.L., 2000, Stratigraphy and textural characteristics of the 1982–83 tephra of Galunggung volcano (Indonesia): Implications for volcanic hazards: Journal of Volcanology and Geothermal Research, v. 104, p. 169–186, doi: 10.1016/S0377-0273(00)00205-5.

Heiken, G., 1972, Morphology and petrography of volcanic ashes: Geological Society of America Bulletin, v. 83, p. 1961–1988, doi: 10.1130/0016-7606(1972)83[1961:MAPOVA]2.0.CO;2.

Heiken, G., 1974, An atlas of volcanic ash: Smithsonian Contributions to the Earth Sciences, v. 12, p. 1–101.

Heiken, G., and Wohletz, K.H., 1985, Volcanic Ash: Berkeley, California, University of California Press, 245 p.

Horwell, C.J., Fenoglio, I., Ragnarsdottir, K.V., Sparks, R.S.J., and Fubini, B., 2003, Surface reactivity of volcanic ash from the eruption of Soufrière Hills volcano, Montserrat, with implications for health hazards: Environmental Research, v. 93, p. 202–215, doi: 10.1016/S0013-9351(03)00044-6.

Houghton, B.F., and Wilson, C.J.N., 1989, A vesicularity index for pyroclastic deposits: Bulletin of Volcanology, v. 51, p. 451–462, doi: 10.1007/BF01078811.

BS EN ISO 4287, 2000, Surface texture: Profile method—terms, definitions and surface texture parameters, *in* Geometrical Product Specifications (GPS): British Standards Institution, p. 1–40.

Katili, J.A., and Sudradjat, A., 1984, Galunggung: The 1982–83 Eruption: Bandung, Volcanological Survey of Indonesia, p. 1–102.

Kolay, E., and Kayabali, K., 2006, Investigation of the effect of aggregate shape and surface roughness on the slake durability index using the fractal dimension approach: Engineering Geology, v. 86, no. 4, p. 271–284, doi: 10.1016/j.enggeo.2006.05.007.

Lee, P.S., Piehler, H.R., Adams, B.L., Jarvis, G., Hampel, H., and Rollett, A.D., 1998, Influence of surface texture on orange peel in aluminum: Journal of Materials Processing Technology, v. 80–81, p. 315–319, doi: 10.1016/S0924-0136(98)00189-7.

Lorenz, V., Zimanowski, B., and Fröhlich, G., 1991, Experiments on explosive basic and ultrabasic, ultramafic, and carbonatitic volcanism: Brasilia, Companhia de Pesquisa de Recursos Minerais Special Publication 2/91, p. 245–247.

Newhall, C.G., and Self, S., 1982, The volcanic explosivity index (VEI): An estimate of explosive magnitude for historical volcanism: Journal of Geophysical Research, v. 87, p. 1231–1238.

Panozzo-Heilbronner, R., 1992, The autocorrelation function: An image-processing tool for fabric analysis: Tectonophysics, v. 212, p. 351–370, doi: 10.1016/0040-1951(92)90300-U.

Pot, V., and Genty, A., 2007, Dispersion dependence on retardation in a real fracture geometry using lattice-gas cellular automaton: Advances in Water Resources, v. 30, no. 2, p. 273–283, doi: 10.1016/j.advwatres.2005.08.011.

Rao, C., Pan, T., and Tutumluer, E., 2003, Determination of coarse aggregate surface texture using image analysis, *in* Proceedings of the Pavement Mechanics Symposium at the 16th ASCE Engineering Mechanics Conference: Seattle, University of Washington, www.ce.washington.edu/em03/proceedings/papers/820.pdf.

Rasband, W.S., 1997–2006, ImageJ: Bethesda, Maryland, USA, National Institutes of Health: http://rsb.info.nih.gov/ij (January 2005).

Riley, C.M., Rose, W.I., and Bluth, G.J.S., 2003, Quantitative shape measurements of distal volcanic ash: Journal of Geophysical Research, v. 108, no. B10, p. ECV8.1–ECV8.15 (1 P.1/4).

Russ, J.C., 1999, The Image Processing Handbook (4th edition): Boca Raton, Florida, CRC Press, 732 p.

Sausse, J., 2002, Hydromechanical properties and alteration of natural fracture surfaces in the Soultz granite (Bas-Rhin, France): Tectonophysics, v. 348, no. 1–3, p. 169–185, doi: 10.1016/S0040-1951(01)00255-4.

Schmincke, H.U., 1977, Phreatomagmatische phasen in quartären vulkanen der Osteifel: Geologisches Jahrbuch Reihe, v. A39, p. 3–45.

Sheridan, M.F., and Wohletz, K.H., 1983, Hydrovolcanism: Basic considerations and review: Journal of Volcanology and Geothermal Research, v. 17, p. 1–29, doi: 10.1016/0377-0273(83)90060-4.

Stachowiak, G.W., 1998, Numerical characterization of wear particles morphology and angularity of particles and surfaces: Tribology International, v. 31, p. 139–157, doi: 10.1016/S0301-679X(98)00016-4.

Sudradjat, A., and Tilling, R., 1984, Volcanic hazards in Indonesia: The 1982–83 eruption of Galunggung: Episodes, v. 7, p. 13–19.

TS 6956, 2004, Surface texture: Profile method—terms, definitions and surface texture parameters, *in* Geometrical Product Specification (GPS): Ankara, Turkish Standards Institution, p. 1–22 (in Turkish).

Walker, G.P.L., and Croasdale, R., 1972, Characteristics of some basaltic pyroclastics: Bulletin of Volcanology, v. 35, p. 303–317.

Wohletz, K.H., 1983, Mechanisms of hydrovolcanic pyroclast formation: Size, scanning electron microscopy, and experimental studies, *in* Sheridan, M.F., et al., eds., Explosive Volcanism: Journal of Volcanology and Geothermal Research, v. 17, p. 31–63.

Wohletz, K.H., 1986, Explosive magma-water interactions: Thermodynamics, explosion mechanisms, and field studies: Bulletin of Volcanology, v. 48, p. 245–264, doi: 10.1007/BF01081754.

Wohletz, K.H., and Brown, W., 1995, Particulate size distributions and sequential fragmentation/transport theory, *in* Theofanous, T.G., and Akiyama, M., eds., Proceedings of the US (NSF) Japan (JSPS) Joint Seminar: Santa Barbara, California, Wohletz and Brown, p. 235–241.

Wohletz, K.H., and Krinsley, D., 1982, Scanning electron microscopy of basaltic hydromagmatic ash: Los Alamos National Laboratory Report LA-UR 82–1433, 43 p.

Wohletz, K.H., and Sheridan, M.F., 1983, Hydrovolcanic explosions: II. Evolution of basaltic tuff rings and tuff cones: American Journal of Science, v. 283, p. 385–413.

Yoshigi, M., Clark, E.B., and Yost, H.J., 2003, Quantification of stretch-induced cytoskeletal remodeling in vascular endothelial cells by image processing: Cytometry, part A, v. 55A, p. 109–118, doi: 10.1002/cyto.a.10076.

Zimanowski, B., Frölich, G., and Volker, L., 1991, Quantitative experiments in phreatomagmatic explosions: Journal of Volcanology and Geothermal Research, v. 48, no. 3–4, p. 341–358, doi: 10.1016/0377-0273(91)90050-A.

Zimanowski, B., Büttner, R., Lorenz, V., and Häfele, H.G., 1997, Fragmentation of basaltic melt in the course of explosive volcanism: Journal of Geophysical Research, v. 102, p. 803–814, doi: 10.1029/96JB02935.

Zimanowski, B., Wohletz, K., Dellino, P., and Büttner, R., 2003, The volcanic ash problem: Journal of Volcanology and Geothermal Research, v. 122, p. 1–5, doi: 10.1016/S0377-0273(02)00471-7.

Manuscript Received 29 May 2006
Revised Manuscript Received 20 December 2006
Manuscript Accepted 11 January 2007

Printed in the USA

4.4. Contrasting fragmentation and transportation dynamics during emplacement of a rhyodacitic dome: Dikkartin Dağ, Erciyes stratovolcano, Central Anatolia, Turkey

4.4.1. Introduction

Tuff rings and tuff cones are the most common landforms created by explosive hydromagmatic (phreatomagmatic) volcanism. Tuff rings commonly have numerous bed-form transitions per vertical meter indicating rapidly changing depositional characteristics. A varying supply of water at vents for tuff rings results in sporadic eruptions of variable strength. Thinly bedded deposits of tuff rings are dominantly composed of pyroclastic surge deposits with subordinate ash-fall beds (Wohletz and Sheridan, 1983) however, phreatomagmatic and phreatoplinian eruptions may form tuff rings consisting surge deposits interstratified with coarser grained (lapilli sized) fall deposits (e.g. Obsidian Dome, California (Heiken and Wohletz, 1985)). In fluidization-deflation model of surge deposition (Wohletz and Sheridan, 1979), sandwave, massive, and planar bed forms are deposited respectively from surges of decreasing steam to pyroclast volume ratios (degree of inflation). Fall deposits result from little or no steam generation during eruptions. For this reason, the deposits record information about the intensity of fragmentation and quantity of water that partakes in the fragmentation process. Sandwave beds deposited from highly inflated surges require the greatest amount of explosive water interaction and fall beds the least (Wohletz and Sheridan, 1983).

Three rhyodacitic domes on flanks of Mt. Erciyes stratovolcano in Central Anatolia (Turkey) (Fig. 22), Dikkartın, Karagüllü and Perikartın emplaced after pyroclastic sequences characterized by an alternation of layers related to contrasting fragmentation and transportation dynamics (Şen et al., 2002). In the framework of this thesis, the evolution of Dikkartın Dağ was studied, where the eruption begins as purely magmatic and continues as phreatomagmatic with interlayered phretoplinian fall and surge deposits with different bed forms related to the amount of water interacted with vesiculating magma. These eruption phases were followed by a sub-Plinian eruption and passive lava extrusion. The phreatomagmatism created an explosion crater surrounded by a tuff ring rampart, and final extrusions filled the explosion crater with a lava dome.

Here, stratigraphic, granulometric, morphometric and textural variations were documented to gain quantitative physical volcanological insight and interpret eruption and emplacement mechanisms in Dikkartın. In order to better characterize the samples with respect to their size-distribution and highlight possible changes in the fragmentation processes occurred during eruptions, Sequential Fragmentation/Transport theory (SFT, Wohletz et al., 1989) has been applied on tephra. Owing to the fact that every single ash particle may convey information about its own formation environment and conditions, quantitative surface descriptors on volcanic ash surfaces were calculated. The suitability of surface descriptors in characterizing complex volcanic ash surfaces from different fragmentation mechanisms was confirmed in previous studies (e.g. Ersoy et al., 2006-Section 4.1; Ersoy et al., 2007b-Section 4.3). By way of addition, the surface texture of ash particles was defined by qualitative descriptive terms frequently used in volcanology community to measure the quantification capability of calculated surface descriptors.

4.4.2. Stratigraphy

Dikkartın sequence exhibits non-welded fallout, massive pumiceous flow deposit, planar, massive to wavy pyroclastic density current deposits (surges) interlayered with fallouts, lithic-rich fallout and a later stage dome extrusion (Fig. 22). Here, the term pyroclastic surge deposit has been used to designate thin (maximum 30 cm) planar-massive-wavy ash-rich beds

produced from pyroclastic density currents. According to the distribution, bedforms and eruptive style, four eruptive phases for Dikkartın were suggested.

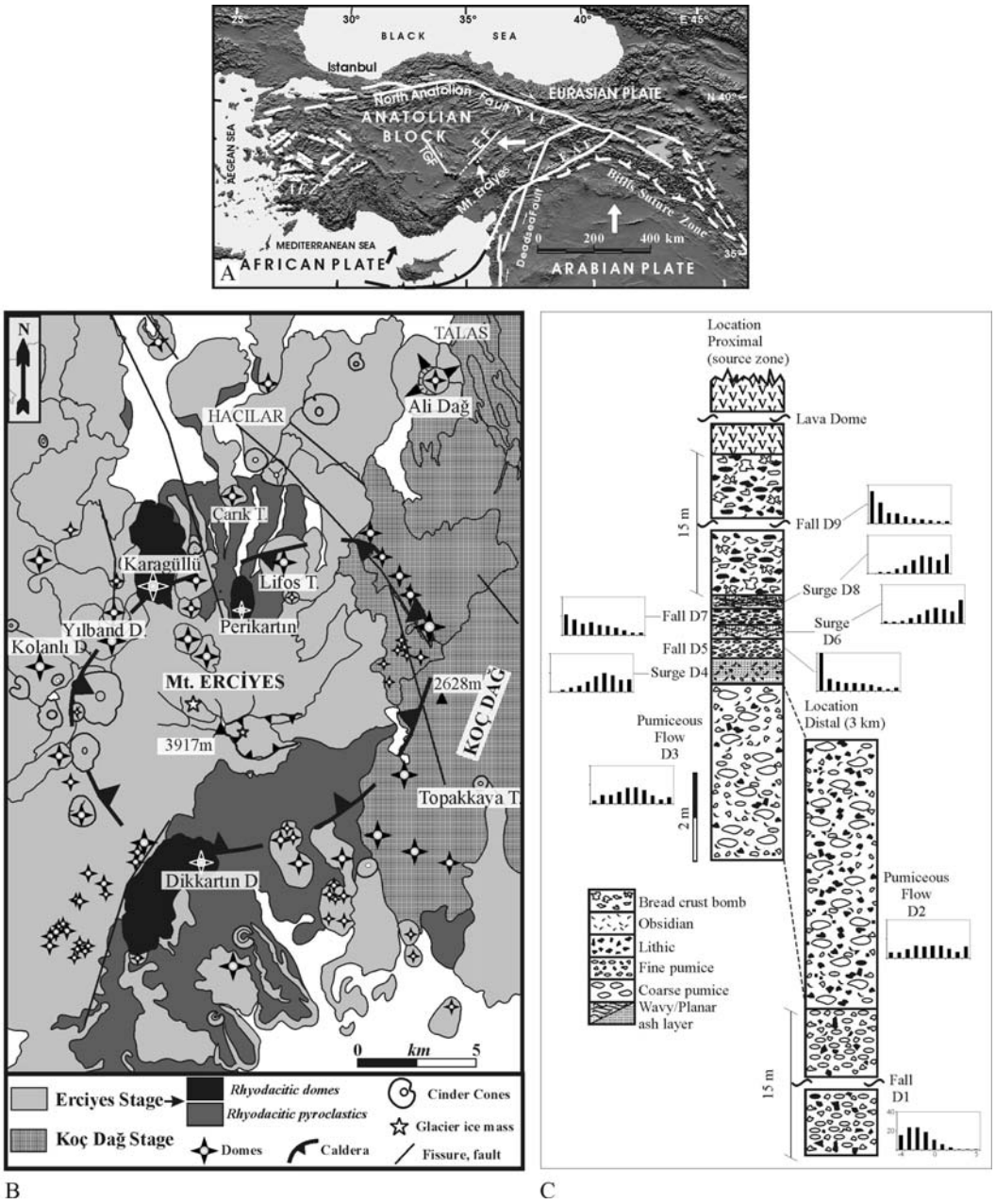

Figure 22: (A) Geodynamical sketch map of Anatolian block, locations of major faults and study area (Mt. Erciyes) placed on Digital Elevation Model (DEM) of Anatolia. (AEZ: Aegean Extension Zone; NAF: North Anatolian Fault; EAF: East Anatolian Fault; EF: Ecemis Fault; TGF: Tuz Gölü Fault. White and black arrows indicate the sense of plate motion; white half arrow show the relative motion direction on the faults), (B) Simplified geological sketching map of Mt. Erciyes after Şen et al. (2002), (C) Generalized stratigraphic section of Dikkartın products. Grain-size distributions were given as histograms.

4.4.2.1. Phase 1

Phase 1 deposits include the initial Plinian fall and pyroclastic-flow deposits. They are more widespread and exposed 15 km from source. The wider distribution, magmatic character, and coarse particles of Plinian fall deposits indicate the higher eruption column in the beginning of the eruption. Applying the method of Carey and Sparks (1986), the height of the climactic eruption column was estimated as 25 km. The opening phase (1) generated two stratigraphic units; D1 fallout and D2 pumiceous flow deposits (Fig. 23). The fallout deposits and flow deposits are separated with a thin ash layer (2 cm). The column deposited D1 fallout including grey, vesicular, moderately angular pumices with maximum 58 cm diameters (Şen et al., 2002). The unit has 15 m thickness on the outcrop 6 km from the inferred source. This fall unit is overlained by a pyroclastic flow (D2) with ash matrix. At 3 km southeast from Dikkartın, it exhibits normal grading having oversized pumices (60 cm in diameter) at the bottom of the deposit (Fig. 23). In distal zones (8,5 km from source), it shows reverse grading. Pumices in the flow deposit are pink, white, grey in color and rounded. Pyroclastic flow deposit has 3 m thickness while the upper surface is eroded in the relatively distal zone, 3 km southeast from the inferred source.

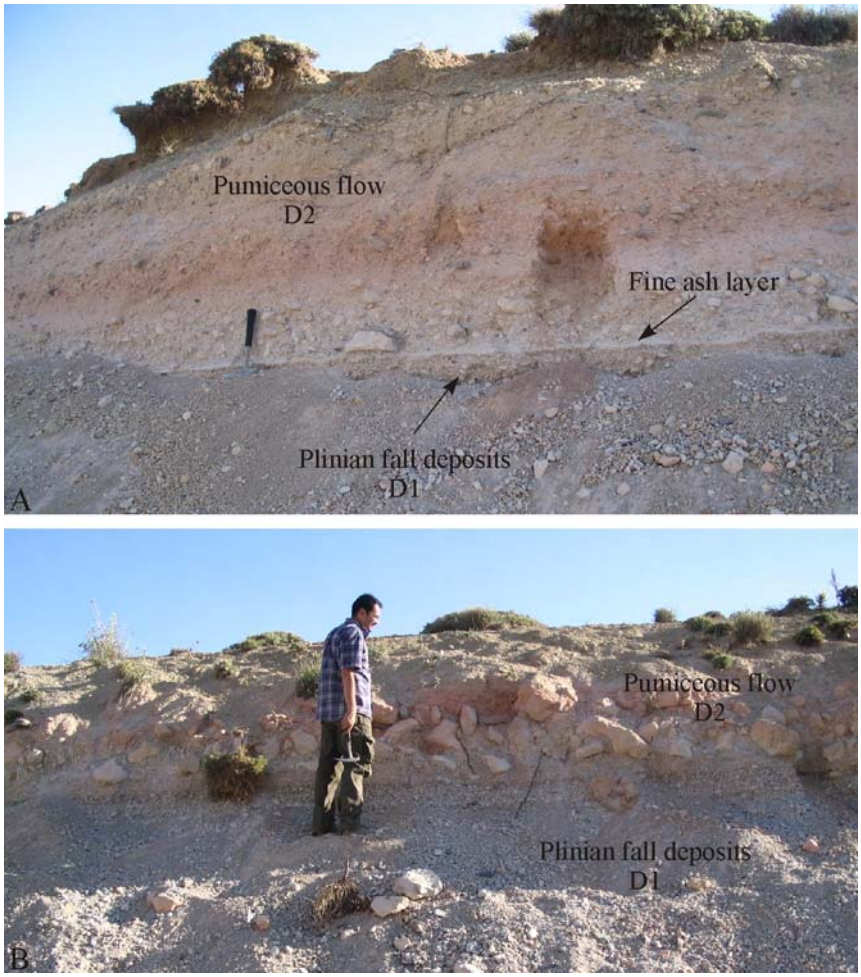

Figure 23: Plinian fall and pumiceous flow deposits (phase) at 3 km southeast from the source zone. The thin ash layer separating the deposits is more pronounced in A. Pink-colored coarse pumices exist in the lower parts of the flow deposists.

In the proximal location (1,5 km northwest from the source area), a pumiceous flow deposit (D3) with pink, white and grey pumices outcrops (Fig. 24). The pumices in this deposit are moderately rounded. The lower part of the flow is buried by debris and the observed thickness is 2 m. D3 is believed to be the upper zone of the D2. Şen et al. (2002) also deal with one pyroclastic-flow deposit in south and east of the dome.

Figure 24: Deposits related to Dikkartın eruption at 1,5 km northwest from the source area (relatively proximal zone).

4.4.2.2. Phase 2

Phase 2 is related to the opening of an explosion crater. The deposits of phase 2 are not widely dispersed and outcrop around the dome. Phase 2 starts with a planar finely stratified layer (D4-surge) with 30 cm thickness in the proximal zone (Fig. 24). Planar stratification is defined by fine pumice lapilli. D5 is a fall deposit with pink, vesicular and moderately rounded pumices. The maximum pumice size (Mp) is 6 cm. Deposit has 20 cm thickness. Fall deposit D5 is overlained by a structureless (massive) ash layer (D6-surge) with 7 cm thickness and exhibit bomb sags (Fig. 24). D7 is a fall deposit with maximum 6 cm sized pink and grey

pumices. The deposit has 15 cm thickness. D8 is wavy-stratified surge deposit with 15 cm. thickness. It exhibits antidune features and bomb sags. The lack of underlying explosion breccia in Phase 2 deposits at 1,5 km away from the source is explicable in terms of being buried by dome itself in very proximal zone and grading laterally into finer grained fall and surge deposits (Wohletz and Sheridan, 1983).

4.4.2.3. Phase 3

Products of this phase outcrop in the north and northeastern part of the lava dome. D9 is a thick (15 m) sub-Plinian fall deposit overlying all deposits in the proximal zone (Fig. 24 and 25). The deposit is rich in lithics (62,9 wt %) and glass (19,15 wt %) and exhibits bread crust bombs with 60 cm diameters. Some bombs have radial cracks (Fig. 25). Contact relationships suggest that the eruption was continuous and there are no significant clues about the time break between phases.

Figure 25: Lithic-rich fall deposits related to phase 3 of Dikkartın eruption at 1 km north from the source. (A) Coarse bombs (60 cm diameters) exist in this deposit. (B) Bomb with radial cracks.

4.4.2.4. Phase 4

Phase 4 is an extrusive phase where a lava dome emplaced. Rhyodacitic dome of Dikkartın represents occasionally banded obsidiennic facies. It buries the previous explosion crater and reaches to 2 760 m from its base, situated at 2 350 m (Fig. 26). The extruded lava flowed down about 5 km toward the south and represents blocky surface due to its high viscosity. This dome-flow covers an area of 11,7 km^2 and corresponds to 0,82 km^3 of erupted magma (Şen et al., 2002).

Figure 26: View of the explosive deposits and lava dome from northeast through southwest.

4.4.3. Componentry

The relative abundance of components in the size -2φ (4 mm) was determined (Table 3). Components have been divided into the following groups: (1) poorly vesicular pumices (lithics); (2) pumices with moderate vesicularity; (3) highly vesicular pumices; (4) juvenile glass (obsidians); (5) xenoliths (accessory lithics). Component analysis included hand picking under a binocular microscope and weighting. Although free crystals were observed on SEM micrographs of particles in the size 4 φ (63 μm) and 2 φ (250 μm), they were lacking in the size -2φ (4 mm). The qualitative observations on samples noted during hand picking were given in Table 4.

All products, explosive and extrusive, exhibit similar mineralogical composition: plagioclase (An40-82 in pumices, An39-83 in lava dome), orthopyroxene (En60-66 in pumices, En59-66 in lava dome), amphiboles (tchermakitic hornblende and magnesio-hornblende in pumices and lava dome), glass (74-75 % SiO_2 in pumices 76-77 % SiO_2 in lava dome) (Şen et al., 2002). Microprobe analysis in the framework of this thesis give the same results as Şen et al. (2002) however, minor amount of clinopyroxene (En 39-44) was determined in pumices but no analysis on lava dome samples were performed. Microprobe analyses on phenocrysts and glass have been carried out on Zeiss EVO50 with Bruker-Axs XFlash 3001 SDD EDS in Hacettepe University, Department of Geological Engineering, Ankara, Turkey. The representative microprobe analyses on pumices were given in Table 5.

Dikkartın samples include grey, white and pink phenocryst-rich pumices. Characteristically, the color shifts from white to gray while the pumices get denser. The obsidian particles are

vesicular or non-vesicular and their color gets darker while they get denser. Here, the term 'xenolith' for accessory components and 'lithic' for juvenile denser particles was used. The xenolith types include light-dark gray lava and reddish hydrothermally altered lava.
The density of juvenile fragments was measured with a pycnometer after coating fragments with a thin impermeable film using a silicon-based spray. About ten measurements per sample were carried out in the -2φ (4 mm) grain size. The mean values were considered. The vesicularity index (V%) was calculated using the method of Houghton and Wilson (1989):

$$V(\%)=100\ (\text{DRE density}-\text{clast density})\ /\ \text{DRE density} \quad (12)$$

The DRE density was determined on non-vesicular, dense grains, while the average clast density is that of the most vesiculated fragments.
The particles are generally vesicular regardless of the eruption types and bed-forms indicating effect of magmatic volatiles during fragmentation or subsequent contact of water in conduit with already vesiculated and/or fragmented magma (Fig. 27). However, there is a general decreasing trend through time in the eruption sequence indicating loss of initial gas content during eruption, which was also proposed by Şen et al. (2002).

Table 3 Components in samples (%)

Sample	Nature	MVP	HVP	Lithics	Xenoliths†	Obsidian
D1	Fall	71,4	-	10,6	14,0	4,0
D2	Flow	27,1	4,2	36,0	11,5	21,3
D3	Flow	42,8	12,7	7,6	9,5	27,4
D4	Surge	46,8	3,3	24,6	5,4	19,9
D5	Fall	59,2	12,3	1,4	5,0	22,2
D6	Surge	51,6	4,7	10,0	0,9	32,8
D7	Fall	61,8	2,4	9,2	9,2	17,3
D8	Surge	25,5	-	31,1	18,5	24,9
D9	Fall	7,9	-	62,9	-	29,1

MVP: Moderately vesicular pumices

HVP: Highly vesicular pumices

†: Accessory lithics

4.4.4. Grain size characteristics of Dikkartın

Grain size analyses were performed by dry sieving at full-φ intervals up to 4φ. Log-normal sorting, median and skewness parameters were calculated after Inman (1952). The plots of samples on median diameter (Md_φ) versus sorting (σ_φ) diagram were compared with fields of deposits from well-studied eruptions (Fig. 28A). Surge deposits have median grain sizes (Md_φ) between 1,55φ and 2,05 φ (medium-fine grained ash) and poor sorting (σ_φ=2,13-2,35). Pyroclastic flow deposits have median grain sizes (Md_φ) between 0 φ and 0,25 φ (coarse ash) and poor sorting (σ_φ=2,45-3). Fall deposits have median grain sizes (Md_φ) between -2,05 φ and -3,35 φ (medium to fine lapilli). Sorting is moderate in first Plinian fall (D1) (σ_φ=1,65) but the phreatoplinian fall deposits and last sub-Plinian fall deposit (D9) are poorly sorted (σ_φ=2,35-2,73). The deposits relating to phase 1 have harmonic trends of Md_φ and σ_φ (Fig. 28B) indicating better sorting with increasing median grain sizes. However, the other deposits have opposite trends for these parameters that show better sorting with decreasing median

grain sizes. The skewness of the size distribution (Inman, 1952) distinguishes fall samples from others (Fig. 29A). All pumice-rich fall samples are positively skewed, however, ash-rich surge samples and pumiceous flow deposits lack noticeable skewness. Positive skewness of fall samples (implying a fine secondary mode) is partly due to artificial break-up during sieving. However, some natural processes also lead to positive skewness. One cause is impact breakage and another is premature fallout of small clasts from the eruption column (Self and Sparks, 1978). However, this can be interpreted as mixing of two populations of grain-size with different origins. These two size populations reflect breakage of the magma by two different mechanisms, initial explosive expansion of magmatic gases and after explosive interaction with water (Self and Sparks, 1978).

Table 4 Observation notes during hand picking

Samples	Vesicularity	Roundness	Color	Glassy
D1	Moderate	Moderately angular	Gray	-
D2	Moderate	Moderately rounded	Gray,pinky white	Very glassy
D3	Moderate	Moderately rounded	Gray,pinky white	Very glassy
D4	Moderate	Moderately angular	Gray,pinky white	-
D5	High	Moderately rounded	Pinky	-
D6	Low	Moderately angular	Gray,pinky white	-
D7	Moderate	Moderately angular	Gray,pinky white	-
D8	Ext. Low	Moderately angular	Pinky	Very glassy
D9	Ext. Low	Angular	Gray	-

Within the fall deposits, the first Plinian fall deposit (D1) is closer to the zero value of skewness indicating a more homogeneous fragmentation mechanism relative to others. The surge and flow deposits with inconsiderable skewness designate the lack of an extended coarse tail. The lack of negative skewness, chiefly in surge deposits, also evidences the lack of contamination by erosion from underlying fall beds. F1 (< 1mm) versus F2 (< 63 μm) diagram also distinguishes fall, flow and surge deposits (Fig. 29B). The ranges for F1 values are narrow for flow and surge deposits but wider for fall deposits. In contrast, flow and surge deposits have wider ranges of F2 values than those of fall deposits. Fall deposits are uniform in F2 values. Within all surge deposits, the first surge deposit (D4) overlying the pumiceous flow deposits are closer to flow deposits, chiefly in terms of F2 values. Surge deposit D6 seems to be produced from the most intensive fragmentation mechanism according to its fine ash (< 63 μm) abundance (Zimanowski et al., 2003).

4.4.4.1. Modeling of granulometric data and sequential fragmentation transport theory

In order to better characterize the samples with respect to their size-distribution, and highlight possible changes in the fragmentation processes occurred during eruptions, the SFT (Sequential Fragmentation/Transport) theory (Wohletz et al., 1989) has been applied to Dikkartın tephra. The detailed explanation about the theory was given in Section 3.1. The grain size distributions were analyzed using the Windows-based software SFT (a new version of SEQUEN from Wohletz et al. (1989)), which allows user-interactive discrimination of the subpopulations present in the distribution, and their characterization in terms of three parameters: mode, dispersion and weight fraction.
Four distinct subpopulations were determined in all samples in varying degrees of prominence (Fig. 30). There are several possible causes for existence of the designated subpopulations.

These include (1) size populations inherited from the initial fragmentation of the magma and country rock; (2) size populations related to clast type and density (e.g., crystals, lithics, pumice and glass); and (3) size populations related to transport and deposition processes.

Table 5 Representative microprobe analyses of phenocryts and glass

	Plag	Plag		Orho Prx	Ortho Prx	Clino Prx	Clino Prx		Tscher-Horn	Mg-Horn	Glass	Glass
Na_2O	5,7	2,0		0,1	0,0	0,2	0,2		1,8	1,5	2,5	2,1
MgO	0,0	0,0		22,6	22,8	14,8	17,2		14,1	15,2	0,3	0,3
Al_2O_3	26,5	32,4		0,6	0,9	1,8	1,7		9,6	7,7	13,4	12,8
SiO_2	57,6	48,8		52,4	52,8	54,0	54,5		43,5	47,0	74,4	75,1
K2O	0,6	0,3		0,0	0,0	0,0	0,0		0,4	0,2	3,5	3,6
CaO	8,5	15,4		1,2	0,9	19,8	20,8		10,6	9,7	1,5	1,5
TiO_2	0,0	0,0		0,5	0,2	0,0	0,1		2,0	1,3	0,0	0,2
MnO	0,0	0,0		0,6	0,6	0,0	0,0		0,3	0,3	0,0	0,1
FeO	0,1	0,3		21,4	22,5	8,1	6,5		14,3	14,0	1,5	1,8
Total	99,0	99,2		99,5	100,7	98,7	101,0		96,7	96,7	97,0	97,5
Ab %	52,9	19,0	Fs%	31,9	33,5	15,7	11,5	Si	6,2	6,7		
An %	43,4	79,4	En%	60,6	60,4	39,1	43,7	Mg/ $(Mg+Fe^{2+})$	1,0	0,9		
Or %	3,7	1,6	Wo%	7,4	6,1	45,1	44,8					

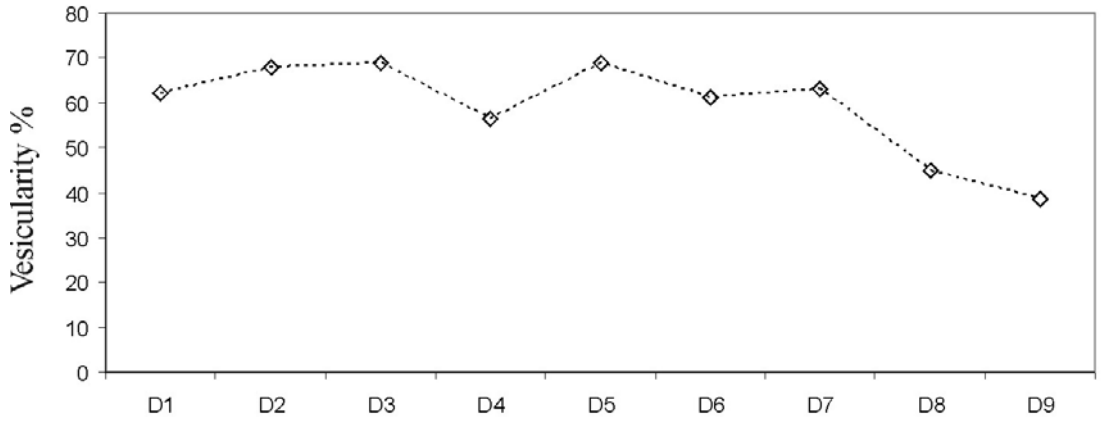

Figure 27: Evolution of vesicularity index (V%) through time in Dikkartın deposits.

4.4.4.1.1. Fragmentation

Best-fit polynomial curve on subpopulation fraction versus subpopulation mode (φ_m) define two groupings of subpopulations: coarser mode subpopulations A and B can be separated from those of fine subpopulations C and D by a line drawn at -0,5 φ (Fig. 31A). These groupings are assigned to magmatic and phreatomagmatic origins (Wohletz et al., 1995). There is a distinct separation between two groups assigned to different fragmentation mechanisms in Dikkartın tephra.

Subpopulation dispersion (or sorting, γ) is very sensitive to fragmentation mechanism. Subpopulations can be distinguished by their mode in Figure 31B in which a fragmentation factor is plotted versus mode. The fragmentation factor chosen (expressed as $\varphi_m/\ \gamma$) discriminates the relative contribution of magmatic and phreatomagmatic fragmentation mechanisms in development of the size distribution of each sample (Wohletz et al., 1995).

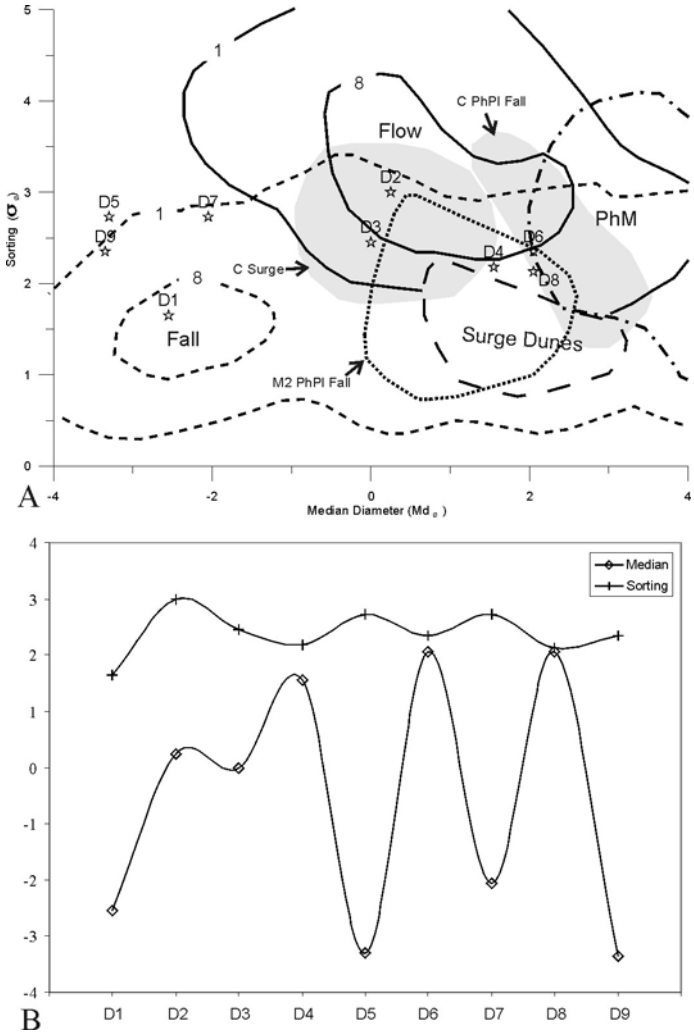

Figure 28: Plots of sorting (σ) and median diameter (Md). (A) Walker diagram showing the 1% and 8% fields of pyroclastic flows (enclosed by solid lines) (Walker, 1971) and falls (enclosed by dashed lines) and that of pyroclastic surge dunes (enclosed by dotted line) (Fisher and Schmincke, 1984). Labeled fields cover silisic phreatomagmatic deposits: Askja layer C base surge and phreatoplinian fall deposits (Sparks et al., 1981), Wairekei (Oruanui) Formation Member 2 phreatoplinian fall deposits (Self, 1983), distinct phreatomagmatic character described by Sheridan and Wohletz (1983). (B) Md and σ vs. stratigraphic position.

The variation in these parameters is uniform except the extreme coarse and fine tails. The anomalous dispersion values may be resulted from particle aggregation despite sample disaggregation. The coarse modes have positive values of fragmentation factor while fine modes have negative values. This discrimination separates magmatic from phreatomagmatic subpopulations and is supported by field, laboratory and theoretical observations described by Sheridan and Wohletz (1983), Wohletz (1983) and Wohletz et al. (1995), which show that magmatic tephra have coarser grain sizes and more negative γ values than do phreatomagmatic tephra.

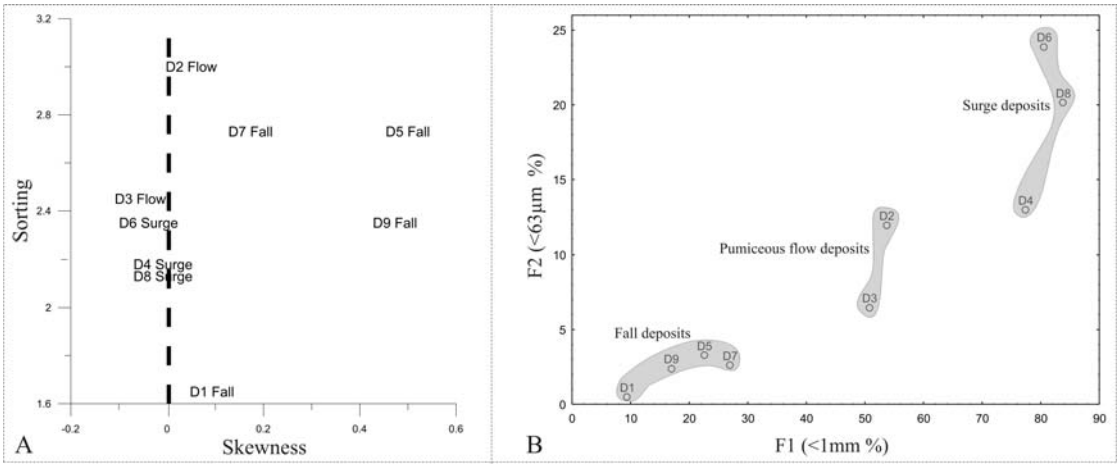

Figure 29: (A) Skewness versus sorting. (B) F1 (<1mm) versus F2 (<63 µm).

The distinct character of fragmentation factor was shown on an histogram of average values of each four subpopulations (Fig. 32A). Subpopulations A and B are dominantly formed by magmatic fragmentation and subpopulations C and D are formed by phreatomagmatic fragmentation. Magmatic and phreatomagmatic components for each stratigraphic position that can be related to progressive changes in eruptive dynamics were shown on Fig 32B. The widely dispersed fallout layer (D1) is mostly magmatic with only magmatic subpopulations A and B. The pumiceous flow (D2) overlying D1 varies between magmatic and phreatomagmatic. The pumiceous flow shows an increasing phreatomagmatic component from bottom (D2) to top (D3). In the phase 2 products, the surge deposits have small amounts of magmatic character. The fall deposits have important amounts of magmatic component while they include phreatomagmatic subpopulations. The reason of bimodality may be first disruption by expansion of magmatic gases to produce the coarse mode and then further fragmentation by explosive interaction with water (Self and Sparks, 1978). The relative contribution of magmatic and phreatomagmatic components to Dikkartın were shown on Figure 33A. Dikkartın has an important phreatomagmatic character (53,22 %). In order to find how the water/magma mass ratio (R) varied during the course of the Dikkartın eruption, the fraction of phreatomagmatic constituents was assumed as a measure of water abundance and that for magmatic constituents as a measure of magma abundance (Wohletz et al., 1995). Their ratio was normalized to 1 where all fragmentation is phreatomagmatic. The estimated R values with stratigraphic positions in Dikkartın are given by Figure 33B. The pyroclastic bed types were also plotted on samples. These data support field interpretations that Dikkartın varied between magmatic and phreatoplinian. The fall deposit underlying the pumiceous flow deposit is purely magmatic. The phreatomagmatic character in pumiceous flow increases through time and the deposit type changes to interlayered surge and fallouts. The sub-plinian fall deposit has also significant amount of magmatic components.

4.4.4.1.2. Transport

Dikkartın shows a variety of depositional textures suggestive of multiple modes of tephra dispersal and emplacement. Fallout layers are characterized by the coarsest modes (subpopulations A and B) while flow/surge layers show a range for particle sizes including subpopulations C and D (Fig. 32B). Fine grained surge beds D6 and D8 are dominated by subpopulation C but have an important content of subpopulation D. The massive forms and wavy stratification in these surges can be explained by modes of appropriate size for saltation

transport. The first surge deposit D4 involves lesser amount of subpopulation D but higher subpopulation C and substantial amount of coarser subpopulation B. Thus, coarse-medium grained surge bed (D4) show bedding texture suggestive of emplacement in a traction carpet (planar stratification beds).

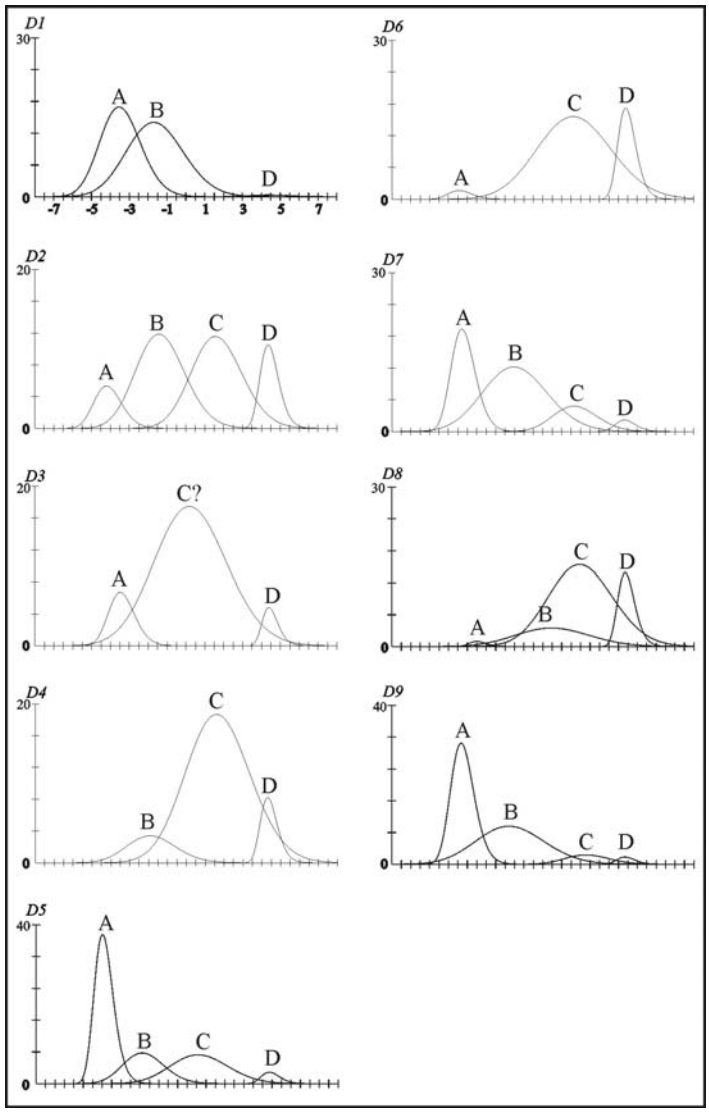

Figure 30: Subpopulations determined from analysis of grain-size distributions of deposits.

The thickness and distribution of pumiceous flow deposits, chiefly for D2, suggest that the current had a moderate-high particle concentration and was relatively sustained, enabling continued transport of 60 cm sized pumices to some 8,5 km from the source. The pyroclastic density current, which produced the pumiceous flow deposits, had features transitional between those of conventional pyroclastic surges and pyroclastic flows, chiefly for D3 which has a significant amount of phreatomagmatic components (Fig. 32B and 33B). Probably, water influx caused an unsteady pyroclastic current characterized by variable transport processes, both suspension and traction. In the terms of textural features and origin, pumiceous flow deposits show similarities to the B pyroclastic density current deposit in Kos Plateau Tuff (Allen and Cas, 1998). The moderate-high particle concentration (rather than dilute) of the current commonly suppressed turbulence and the development of tractional bedforms within the most proximal areas, favouring rapid suspension sedimentation that

formed massive beds. The fall deposits involving substantial amount of coarser subpopulations was likely transported by ballistic fallout (Wohletz et al., 1989).

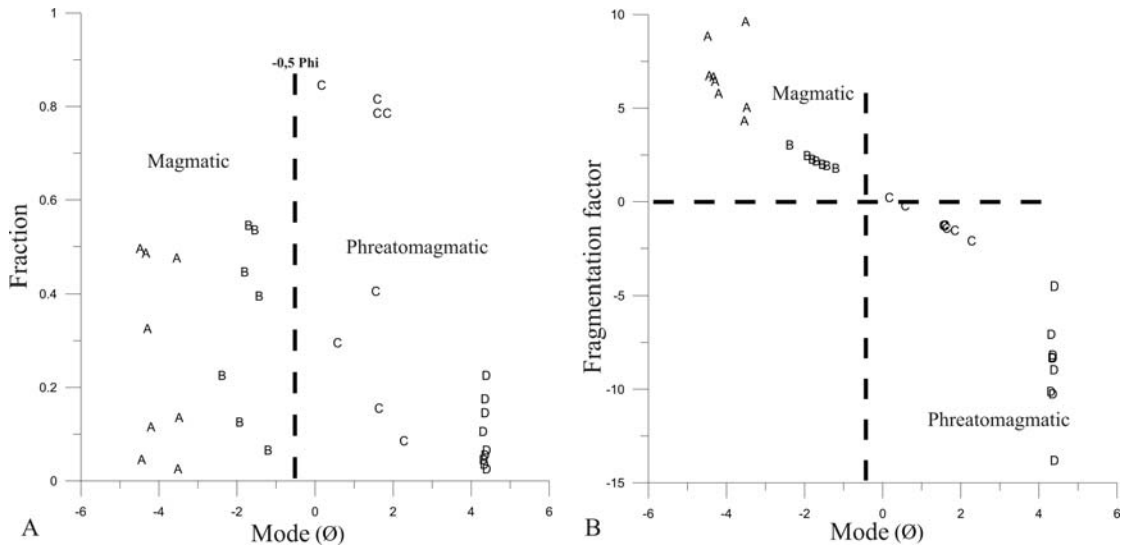

Figure 31: (A) Subpopulation fraction versus subpopulation mode (φ_m) indicate two main groupings of sub-populations. (B) Fragmentation factor (φ_m/γ) versus subpopulation mode.

4.4.5. Qualitative and quantitative descriptions of volcanic ash surfaces

4.4.5.1. Sample preparation and image acquisition

Samples in the 2 φ (250 μm) grain size were steeped in acetone not more than 5 minutes so as to remove dust adhered on particles during sieving process or transportation of samples from field to laboratory. Not to detach adherent alteration products or shards holding clues about steam abundance and energy in eruption, respectively was expected. Samples were dried in drying oven at 110 ˚C overnight. Volcanic ash particles were sprinkled on carbon adhesive tabs placed on an aluminum stub and coated with carbon in order to counteract grain surface charging while scanning with the electron beam. The SEM instrument used for microprobe analysis was also used to take the whole grain and detailed surface micrographs. Ten scanning electron images were acquired from each sample.

4.4.5.2. Qualitative description of surface textures

Here, surface textures from SEM micrographs were defined by using the confirmed descriptive terms widely used in volcanology community and mostly derived from a glorious reference book about volcanic ash thanks to Heiken and Wohletz (1985).
In Plinian fall deposit (D1) highly vesicular and slightly vesicular pyroclasts coexist together. Vesicles show variety of forms including elongated, tubular and ovoidal cavities (Fig. 34). The slightly vesicular pyroclasts are common and more angular with large ovoid vesicles and thick vesicle walls. Large pockets compose coalesced vesicles and small vesicles surround these pockets. Septae that remain from collapsed walls between coalesced vesicles are visible within the vesicles. Many of the vesicles are not only elongate but also flattened. The vesicle walls between elongated vesicles in vesicular pyroclast are thin (~5 μm) while they are thick (~60 μm) between ovoid vesicles in slightly vesicular pyroclasts. Some pyroclasts exhibit

crystals embedded in the glass. Fine-grained particles adhering to grain surfaces are present. The outlines of particles are angular in general.

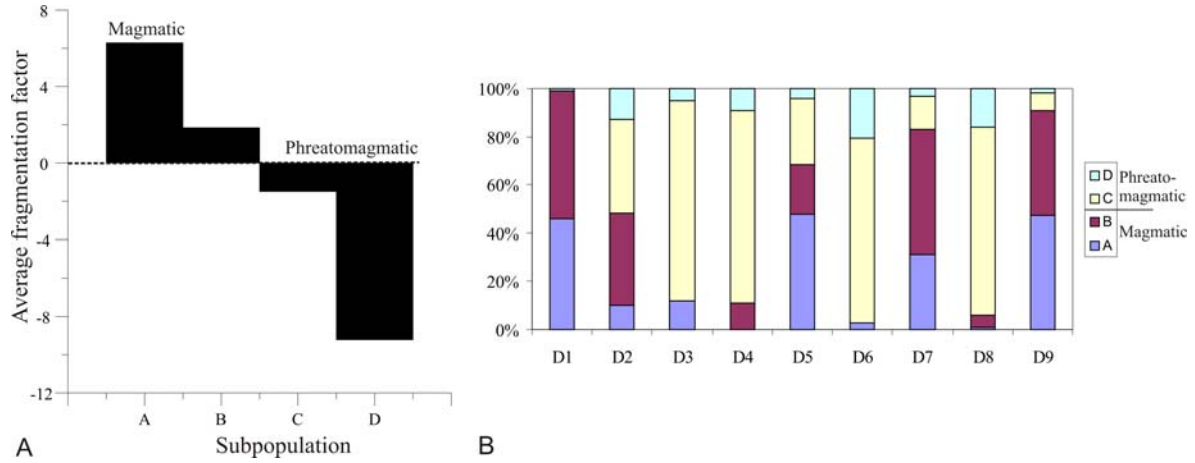

Figure 32: (A) Histogram of average φ_m/γ values as a function of subpopulation. (B) Magmatic and phreatomagmatic components for each stratigraphic position.

Pumiceous flow deposit (D2 and D3) has equant, subequant blocky pyroclasts with mostly ovoid vesicles (Fig. 34). Moderately thick vesicle walls (~20 μm) separate the vesicles. The pyroclasts also have slightly elongated vesicles and many of these vesicles are also flattened. Most of the ovoid vesicles show collapse of mutual vesicle walls and coalescence to form larger composite vesicles. Fine-particles adhering to grain surfaces are abundant chiefly in D2 indicating higher fragmentation intensities for fine material formation and steam abundance for adhesion in the eruption. Generally, the particles in pyroclastic flow deposit are rounded.

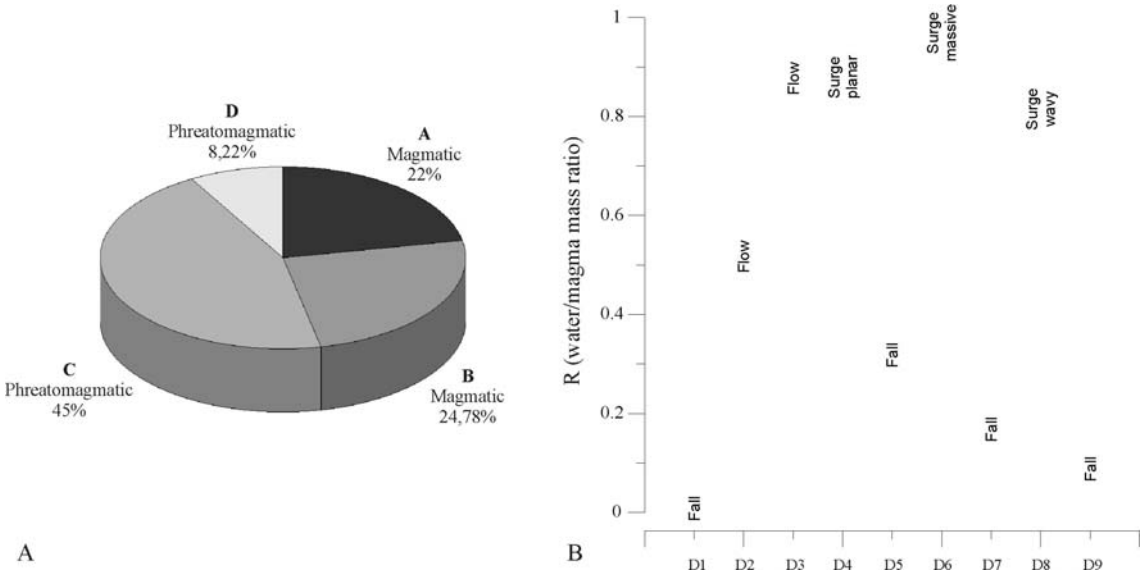

Figure 33: (A) Pie diagram shows an abundant phreatomagmatic character (53,22 %) for Dikkartın eruption. (B) Plot of R (water/magma mass ratios) vs. stratigraphic position.

Fine adhering particles is also present on pyroclasts from D4 surge deposit (Fig. 34). Three different types of pyroclasts are present in this surge deposit; 1) vesicular pyroclasts with elongated vesicles and thin vesicle walls, 2) vesicular pyroclasts with ovoid and coalesced

vesicles, 3) slightly vesicular equant, subequant subrounded pyroclasts with few ovoid vesicles. The pyroclasts from surge deposit D4 are subrounded.

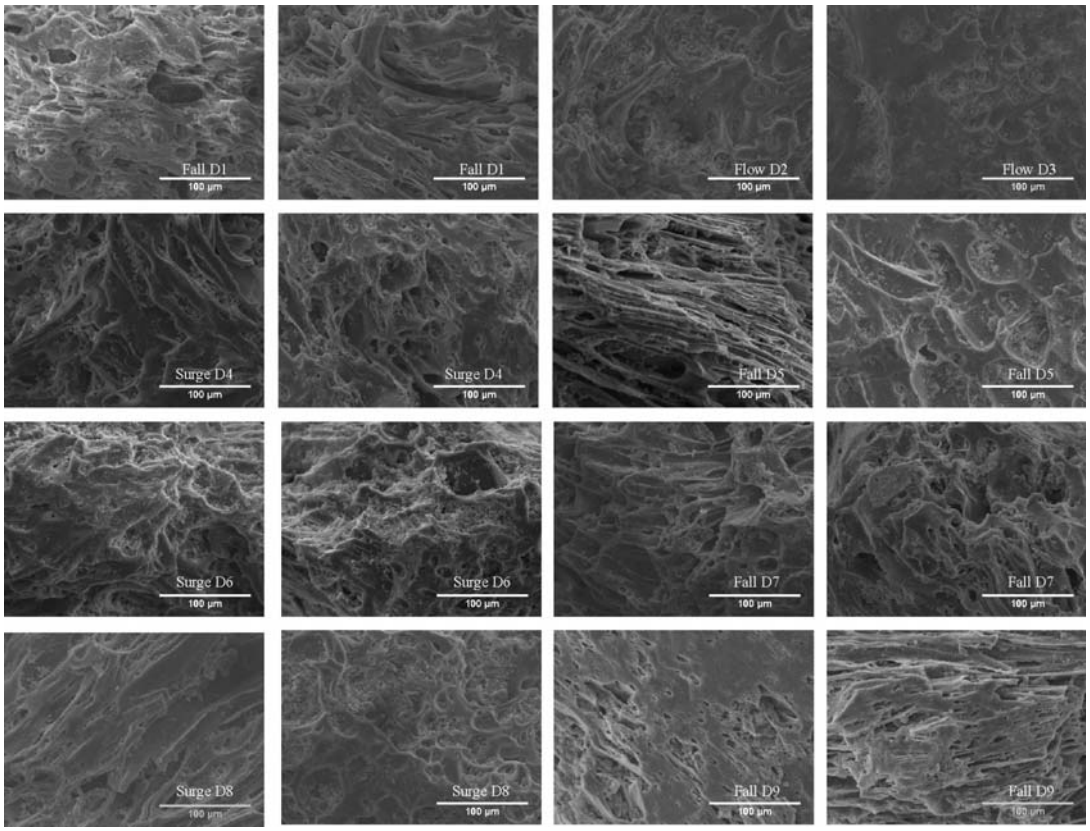

Figure 34: Representative SEM micrographs of ash surfaces from Dikkartın eruption.

Fall deposit D5 has vesicular pyroclasts with abundant ovoid vesicles (Fig. 34). Elongated vesicles are also present but minor. Large pockets composed of coalesced vesicles and small, elongate vesicles surrounding the pockets are present. Fine particles adhere to surfaces but not abundant as flow deposit D2. Fall deposit D5 has angular pyroclasts.

Surge deposit D6 involves pyroclasts with fine material on their surfaces similar to D4 (Fig. 34). Ovoid vesicles in immature form are as nicks on surfaces. They have minor depths and seem shallow. Slightly elongated vesicles unusually exist but they are also shallow with minor depths. Particles of surge deposit D6 are rounded.

In fall deposit D7, heterogeneous nature of the vesicles is obvious: there are large pockets composed of coalesced vesicles, spherical-ovoid vesicles, and slightly elongated vesicles (Fig. 34). In general, all vesicles are shallow with minor depths. Vesicular pyroclast are rich in spherical-ovoid vesicles. Fine adhering material is present but minor. Pyroclasts are angular.

Abundance of fine adhering particles and hollows filled by fine material are characteristic in surge deposit D8 (Fig. 34). Pockets are present with ovoid and elongated vesicles. The vesicle walls have thicknesses in a wide range (5-20 µm). Pyroclasts of D8 surge are angular.

Fall deposit D9 has moderately vesicular pyroclasts with ovoid and slightly elongated vesicles and non-vesicular pyroclasts (Fig. 34). The vesicle walls are thick up to 100 µm. Fine material on particle surfaces is in limited scale. Pyroclasts of D9 fall deposit are highly angular.

4.4.5.3. Quantitative analysis on volcanic ash surfaces

The geometrical characterization of rough profiles or surfaces is a widespread problem in various geological examples such as erosion patterns, multiphase fluid percolation in porous rocks, fractures, or stylolites (Brouste et al., 2007 and references therein). Several texture descriptors have been used to characterize the detailed surface structure of volcanic ash surfaces (Ersoy et al., 2006-Section 4.1; Ersoy et al., 2007b-Section 4.3). The roughness of volcanic ash surfaces is associated with key features such as the vesicularity, type of vesicles and alteration products on surfaces that are mainly affected by water/magma interaction during eruptions. Here, we calculated some statistical roughness parameters on volcanic ash surfaces in order to assess the micro-geometrical deviation related to different fragmentation mechanisms. The image processing side is based on assuming that the gray level variation is related to the roughness variation of the surface. Namely, we use two-dimensional SEM micrographs and the shadow relief effect for estimation of real topographical representations. The advantages and disadvantages of the method here applied were discussed in Ersoy et al. (2007b) (Section 4.3).

Image processing and analysis were performed using the *ImageJ* program (Rasband, 2007). All images were converted to a sequential stack. Median filter was carried out which is the nonlinear filter more used to remove the impulsive noise from an image (Yin et al., 1996). Bandpass filter was used to filter out large structures (shading correction) and small structures (smoothing) of the specified size from the images. The suitability of bandpass filtering for assessing the surface structure size was also confirmed in previous studies (Chinga et al., 2007). *SurfCharJ* plugin (Chinga et al., 2003, available at http://www.gcsca.net) was used for roughness analysis.

Detailed information about roughness approach can be found in Section 2.3. Here, we only dwelled upon two widely used statistical roughness descriptors (average roughness R_a and the skewness $R_{sk)}$ which were used in previous applications on volcanic ash surfaces and provided information about vesicularity, types of pyroclasts (Wohletz, 1983), alteration intensity and/or fine particle abundance.

Ersoy et al. (2007b) (Section 4.3) demonstrated the sensitivity of R_a parameters on fine adhered particles on volcanic ash surfaces, namely on the micro-roughness of the surfaces. The adhering dust on surfaces or in vesicle hollows of volcanic ash particles is common especially in phreatomagmatic eruptions. However, these fine materials may grow out from alteration of glass or fine-sized fraction of the eruption products. Both may be the results of steam in the eruption column causing alteration and adhesion of fine material to surfaces, respectively. Fine-sized juvenile material may form besides as an effect of intensive fragmentation mechanism (Zimanowski et al., 2003). Here, the surge deposits related to phase 2 and flow deposits from phase 1, chiefly D2 have higher R_a values indicating higher micro-roughness (Fig. 35A). The adhered fine material on surfaces forms a rough surface in micro-scale. Moreover, the quantitative micro-roughness descriptions associated with adhered fine material overlaps the qualitative descriptions of surface textures cited above. The Plinian fall deposit (D1) despite its purely magmatic character (R=0,01) involves substantial amount of adhered fine material on pyroclast surfaces indicating a steam-rich highly energetic fragmentation and eruption mechanism (Zimanowski et al., 2003). The probable causes for abundant fine material on ash surfaces from a Plinian eruption will be discussed later. In larger scales, adhering fine material covers the surface, fills some hollows and masks the vesicularity and tapered edges resulting in a smoothing effect on surface. R_{sk} is more descriptive on larger features such as cavities (vesicles) (Fig. 35B). It has been proposed as a parameter that describes vesicularity and distinguishes pyroclasts from different fragmentation mechanisms on the basis of different type and sized cavities on the ash surfaces

(Ersoy et al., 2007b-Section 4.3). Here, it has a considerable correlation with vesicularity values of samples indicating its sensibility on cavities (Fig. 36).

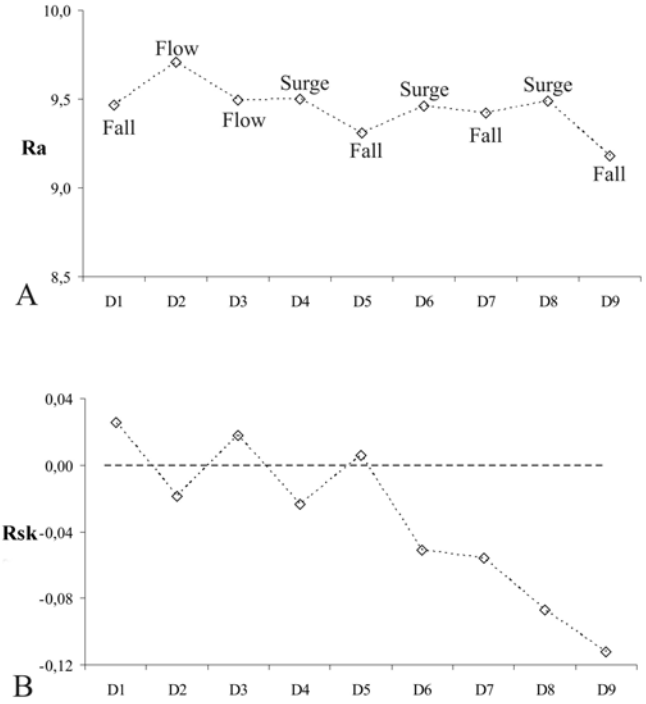

Figure 35: Evolution of (A) average roughness (R_a) and (B) skewness (R_{sk}) through time in Dikkartın deposits.

4.4.6. Discussion

Stratigraphic, granulometric, morphometric and textural variations were given to gain quantitative physical volcanological insight and interpret eruption and emplacement mechanisms in Dikkartın. The fallout deposit in the beginning phase is purely magmatic and relatively widespread. However, despite its purely magmatic character (R=0,01), Plinian fall deposit involves substantial amount of adhered fine material on pyroclast surfaces indicating a steam-rich highly energetic fragmentation and eruption mechanism (Zimanowski et al., 2003). Nevermore, the fine material on ash surfaces is believed to represent the minor amount of fine ash (<63 μm) in the deposits (F2=0,5 %) and/or in the overlying fine ash layer that existed in the eruption but deposited subsequently (Fig. 23A). Formation of a tuff ring shortly after this eruption indicates a shallow explosion, namely interaction of magma with a surface or near-surface water (Wohletz and Sheridan, 1983). Limited infiltration of water into the conduit above the fragmentation level may permit the occurrence of steam in the eruption column. Furthermore, water vapour is one of the main components of gaseous volcanic emissions both for steady degassing and during explosive events. A Plinian eruption column involves substantial amount of hydrometeors without interaction of external water (Textor et al., 2006). Ambient atmospheric water vapor is entrained into eruption plumes by turbulent motions and is responsible for most of the water in the eruption column. The fine materials on pyroclast surfaces are juvenile chips and flakes other than alteration products indicating relatively dry emplacement of deposits (superheated steam media) beside the little vapor condensation on pyroclasts.

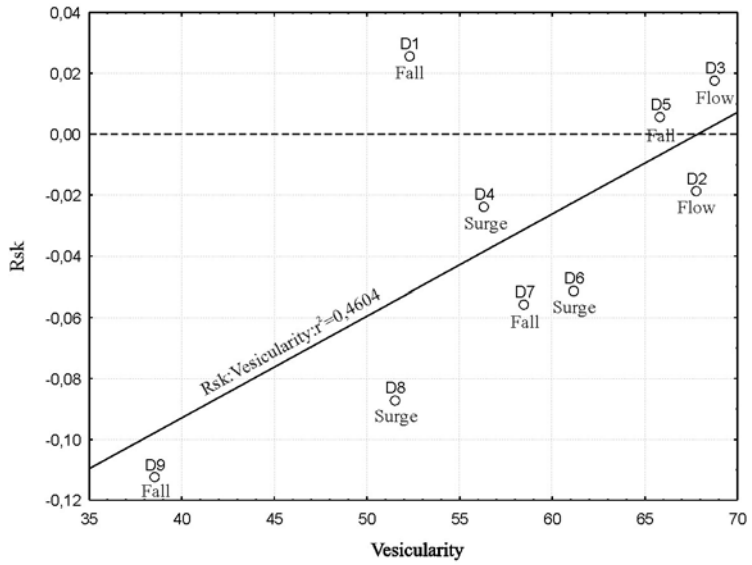

Figure 36: The correlation between skewness (R_{sk}) values of ash surfaces and vesicularity index (V%).

The pumiceous flow deposits overlying the Plinian deposit have components with magmatic and phreatomagmatic origin indicating operation of both magmatic and phreatomagmatic fragmentation mechanisms during the eruption. The phreatomagmatic character increases in the top of the pumiceous flow and transits to a surge deposit that belongs to Phase 2. For the first phase in Dikkartın, a shift from an early convective to a transitional and partly collapsing regime is suggested. Eventually also due to intense fragmentation and/or higher discharge rates the vent widened or the eruption column became greatly overloaded with fine particles, and the partial column collapse began (Sparks and Wilson, 1976; Sparks et al., 1978; Wilson et al., 1981). The relatively higher proportion of xenolith contents in Plinian fall and pumiceous flow deposits refers to a probable vent enlargement (Table 3). The enlargement of vent probably allowed water access to the vent. Moreover, water interacting with the magma probably acted as a heat sink, further reducing the ability of the column to convect (Wilson et al., 1978; Sheridan et al., 1981). Lower rate of heat release decreased the height of column (Woods and Wohletz, 1991) and transformed it into a phreatoplinian column relating to the fallouts and surge deposits in Phase 2. The scale of phenomena was small but similar in comparison with the eruption and deposition styles in the eruption of Kos Plateau Tuff (Allen and Cas, 1998). Furthermore, initiation of phreatoplinian eruption after widening of the vent allowing water access to the magma resembles the case in the eruption of Bishop Tuff, California (Heiken and Wohletz, 1985). The phreatomagmatic origin of both fall and surge deposits in phase 2 and their dispersions connotes that they were derived from the same column and/or surges originated from lateral explosions derived from the same vent. Although the deposits of Phase 2 involve phreatomagmatic components, vesiculation is observed in all samples. Water-magma interaction was evidently restricted to shallow levels in the conduit, and largely above the level of vesiculation and probably in patches above the level of volatile driven fragmentation, chiefly for phreatoplinian fall deposits. Magma was disrupted first by expansion of magmatic gases to produce the coarse mode and then further fragmentation occured by explosive interaction with water (Self and Sparks, 1978). Although, the generation of dilute currents that form base-surge deposits from Plinian eruption columns seems problematic (Dellino et al, 2004), the lateral or partial collapses of the phreatoplinian column generated laterally moving base surges (Self, 1983).

Xenolith fragments within the deposits are inferred to have been derived from the shallowest levels in the stratigraphy intersected at the vent and conduit. However, there is not a clear distinction between the xenolith contents of relatively dry fall deposits and wetter surge deposits (Table 3). Namely, there is not any relation between water/magma mass ratios (R) during eruptions and the xenolith abundance of deposits (R^2=0). Probably, the conduit wall stability was also important for xenolith abundance beside the water amount accessed to the vent and magma discharge rate. Proportions of juvenile lithic content do not distinguish fallout deposits from surge deposits. There is not any correlation (R^2=0,03) between the water/magma mass ratios (R) values and lithic content. However, the inverse correlation between the lithic proportions and vesicularity values (R^2=0,46) indicates the volatile content as the dominant factor rather than magma/water interaction on lithic occurrence. The insignificant correlation (R^2=0,17) between the water/magma mass ratios (R) and vesicularity values already designates interaction of water after vesiculation of the rhyodacitic magma. The obsidian content has correlation with water/magma mass ratios (R^2=0,33). Probably, the water interaction in the late stage of vesiculation had a quench effect on pyroclasts forming vesicular and unvesicular obsidian particles in deposits.

The external water in eruption sequences of Dikkartın is believed only to be responsible from the intense fragmentation of already vesiculated magma thereby in determination of grain size distribution and bed forms. Parallel cases were observed on other eruptions where the ground or surface water interacted with magma after vesiculation (eg. St. Helens, 1980 eruption, Taupo eruption (Heiken and Wohletz, 1985)). Magma-water interaction causes intense fragmentation of the magma (Peckover et al., 1973; Wohletz, 1983; Wohletz and McQueen, 1984; Zimanowski et al., 1991), produces a fine-grained assemblage of clasts in the eruption column (Walker and Croasdale, 1972; Wohletz, 1983) and thus varying ratios of magma to water change the grain-size characteristics of the resulting deposits (Self, 1983). During the eruptions that deposited fallouts, mass flux rates of magma was probably high that water-magma interaction was less efficient yielding a large coarse component to the grain size distribution. The increase in median grain size is interpreted as a decrease in the explosive energy of eruptions. Experimental studies demonstrate that exsolution of magmatic gas tends to inhibit an efficient magma/water interaction (Zimanowski et al., 1991). Furthermore, vesicles developed before water magma interaction facilitated intense fragmentation producing finer materials. The presence of tubular vesicles instead of ovoidal pores in vesicular magma generated finer fragments (Martel et al., 2000), which also explains existence of tubular vesicles in surge deposits.

The subsequent interaction of water after vesiculation mainly prevented the occurrence of key features on pyroclast surfaces indicating phreatomagmatism. The viscous behaviour of magma also prevented viscous deformation of the melt if any turbulent mixing of the melt and water occurred after fracture. Presumably, R_{sk} specified the abundance of vesicles regardless of whether or not the water interaction prevailed in determination of vesicularity. The vesiculation was heterogeneous in samples; elongated, tubular and ovoidal cavities coexist in the same pyroclast as pockets. Differences in vesicle types can be explained by heterogeneous vesicle development. It is possible for vesicle growth to begin at depths of 2 or 3 km in rhyodacitic or rhyolitic melts with a water content of 3% or more (Sparks, 1978; Heiken and Wohletz, 1985). Probably, early vesicle growth began at phenocryst surfaces, when those surfaces acted as bubble nuclei. The larger pockets with thin internal vesicle walls had a higher bulk viscosity than the surrounding melt and resisted deformation by flow (Heiken and Wohletz, 1985). However, as magma rose, vesiculation began around the pockets. Closer to the surface, later stage vesicles were sheared into highly elongate, tube-like forms. At or near the surface, this heterogeneous, vesicular mass was fragmented, perhaps by an early pressure wave passed down into the vent and subsequently by water/magma interaction. Due to

heterogeneous vesicle types, classification of pyroclast surfaces according to their vesicle shapes was difficult. However, beside the cavities on surfaces, the cavity masking side of dust covering the surfaces was also highlighted by R_{sk} parameter. The surfaces having positive Rsk values probably have tapered ends of vesicles and these ends were perceived as peaks on surfaces. Furthermore, surfaces with masked vesicles or few vesicle surfaces caused negative R_{sk} values. R_a parameter confirmed adhered fine particle (dust) abundance and ran true to form by assigning micro-roughness on surfaces. However, the later stage water interaction and heterogeneous vesicularity involve detailed surface characterization and analysis on a larger number of micrographs.

4.4.7. Conclusions

Stratigraphic sequence of the Dikkartın eruption is related to the ratio of magma and external water during each phase even each unit of the activity. The vesiculation of the magma occurred earlier than the water interaction and thereby facilitated efficient fragmentation of the melt (Martel et al., 2000). The deposits designate an initial magmatic eruption column with high discharge rates, which widened the vent and allowed water access to the magma (Fig. 37A). Magma-water interaction caused intense fragmentation of the magma thus, the eruption column became greatly overloaded with fine particles and/or water in the column reduced the ability of the column to convect. Partial collapses of the column occurred however, the complete column collapse did not become true just decreasing its height and being transformed into a phreatoplinian column (Fig. 37B). The lateral or partial collapses of the phreatoplinian column generated laterally moving base surges interstratified with fall deposits (Fig. 37C). Depletion of water in the eruption environment and loss of volatiles in the magma terminated the explosion stage with a dry explosion followed by passive lava extrusion (Fig. 37D and 37E). The heterogeneous vesicle shapes and ineffectiveness of water interaction on vesicle development make classification of pyroclasts difficult on the surface quantification basis. However, pyroclast surfaces were quantified according to their micro- and macro-roughness. The unaltered surfaces with only adherent fine juvenile material suggest that most of the phreatomagmatic eruptions producing the tuff ring were dry with superheated steam but little vapour condensation occurred allowing adhesion of fine material on surfaces.

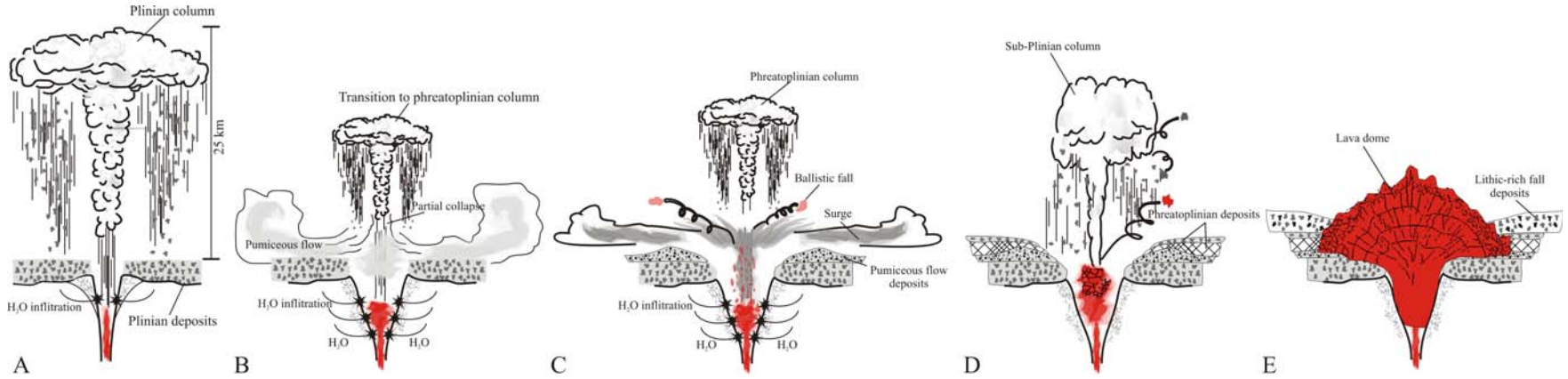

Figure 37: Qualitative sketch illustrating eruption column behavior during the course of eruption of Dikkartın. (A) Opening eruption of Dikkartın involved Plinian column and widespread deposits. (B) The following eruption column is shorter and involves phreatomagmatic components due to interaction of water and rhyodacitic magma. The partial collapses occurred from margins of the column generating pumiceous flows with features transitional between those of conventional pyroclastic surges and pyroclastic flows. (C) Phreatoplinian column generates surge and fall deposits indicating amount of water interacting with magma. Depletion of water in the eruption environment and loss of volatiles in the magma terminated the explosion stage with a dry explosion (D) followed by passive lava extrusion (E).

5. Upgrading into three-dimension (3D)

It is important to keep in mind that the surface descriptors are used for describing the three-dimensional (3-D) structure of surfaces. The images used in some applications in the context of this thesis are SEM two-dimensional images. The popularity of the SEM stems from its capability of obtaining three-dimensional-like images of surfaces of a very wide range of materials (Goldstein et al., 2003). Although the SEM images give a 3-D impression of the ash surfaces, they do not give real topographical representations with local height values. Despite this fact, it is assumed that the gray-level variation is related to the real roughness variation of the surface. The three-dimensional appearance of the images is due to the large depth of field of the SEM as well as to the shadow relief effect of the secondary and backscattered electron contrast (Goldstein et al., 2003). Rough surfaces emit more low-energy secondary electrons from the surface edges, which creates the measured gray-level variation. Topographic contrast arises because the number of secondary electrons depends on the angle of incidence between the beam and the specimen surface. The angle of incidence between the beam and the local surface will vary only because of the local inclination of the specimen (Goldstein et al., 2003). In order to better illustrate the 3-D impression of gray level variation, 3-D surface plot of a volcanic ash surface using gray values of 2-D image was created (Fig. 38). *Interactive 3-D surface plot* plugin was used for creating surface plot from gray values (available at http://rsb.info.nih.gov/ij/plugins/surface-plot-3d.html).

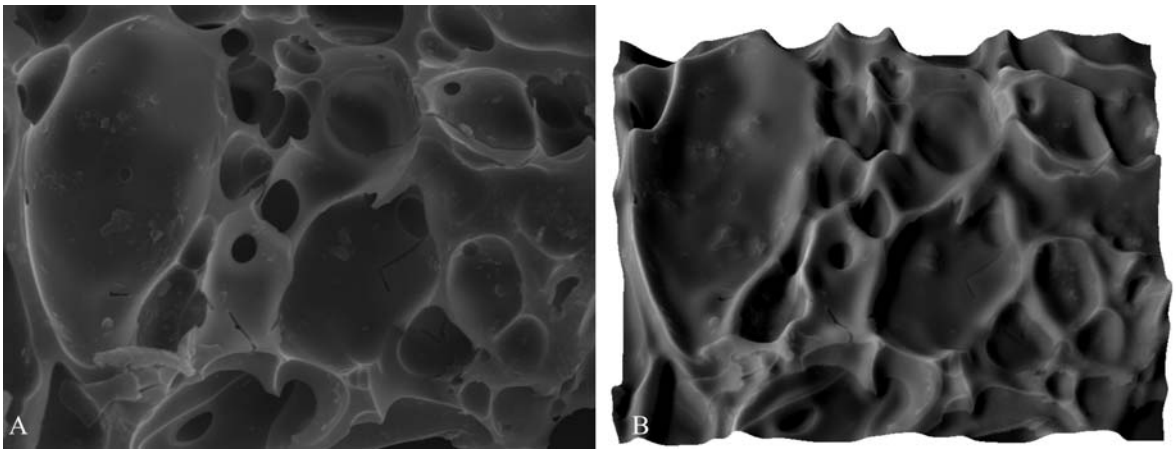

Figure 38: SEM micrograph of a volcanic ash surface (A) and corresponding 3-D surface plot generated from gray level values of A (B). The 3-D surface was tilted for a better representation of 3-D features.

Needless to say that the simplicity of application has advantages along with obvious disadvantages such as the susceptibility of gray value variations to conditions before and during the acquisition of images. After all, an SEM image is the result of sample and electron beam interaction, and it is expressed approximately as a convolution of geometric functions describing the sample and the primary electron beam, respectively (Ishitani et al., 2005). The visual identification of features is influenced by all the variables involved in SEM imaging, including illumination, contrast, filament, vacuum and sample conditions, and magnification etc. For instance, significant differences in the statistics obtained from same microwear surface when photographed under different conditions were reported (Hagen and Walker, 1994 and references therein). Magnification has a particularly profound effect on the number of features that an analyst will identify. “Image quality,” the result of several subjective

decisions by the SEM operator, is another factor that is generally acknowledged as important (Hagen and Walker, 1994). The three dimensionality of a typical SEM micrograph is more subjective than real but there is scope for obtaining topographic information by use of some methods for 3D reconstruction (Castle and Zhdan, 1997).The scanning electron microscope (SEM) offers high resolution and detailed description of structures. In addition to giving a detailed 3-D impression of surfaces, the SEM can be used for calculating 3-D height maps.

Three-dimensional reconstruction often reveals information about the morphology and composition of a system that can otherwise be obscured or misinterpreted by two-dimensional images (Bansal et al., 2006). There are three basic methods for obtaining 3D images using electron microscopy: (1) recording two views of the specimen to form a stereo pair image, (2) recording many views to compute a 3D reconstruction, and (3) imaging serial depth planes to build a 3D volume (Marko, 2005).

The high resolution, high depth-of-field images produced by SEM are ideally suited for stereophotogrammetric analyses. The technique is well known and is based on stereo pair imaging, i.e. images of a given specimen are obtained from two different tilting angles. Hein (2001) gives a good description of stereo pair analysis.

At present, most 3D transmission electron microscopy (TEM) imaging is done using either electron tomography or the "single particle" approach, both of which involve recording many views of a specimen and computing a 3D volume or "map" of an object (Marko, 2005 and references therein). Electron tomography is suited for reconstruction of individual, unique objects, since all views are recorded from the same object. For thin materials science specimens that can tolerate the high electron dose required, depth resolution as high as 1 nm may be achieved. For dose-sensitive "native" (frozen-hydrated) biological specimens, the depth resolution is limited to about 4 nm at present (Marko, 2005).

Many techniques such as microtoming, serial grinding and polishing, X-ray microtomography, focused ion beam (FIB), micromiller have been used for acquiring 3D datasets for reconstruction (Chinga et al., 2004; Marko, 2005). In addition to being suitable for reconstructing the 3-D structure of surfaces, the SEM has been used for obtaining 3-D data series by serial sectioning (Aronsson et al., 2002; Ersoy et al., 2007a-Section 5.1.2.) and a grinding technique (Chinga & Helle, 2003). Having a detailed description of the 3-D structure, the quantification of the structure details becomes highly informative and valuable (Chinga et al., 2007).

5.1. Extended depth-of-field (focus) algorithm and 3D reconstruction of volcanic ash particles

5.1.1.Preface

The study presented in this section purposes to distinguish two different types of ash by assessing their surface textures. The volcanology and geology side of the samples used in this section is in another PhD thesis field. Mentioned samples are from Villarica stratovolcano (Southern Chile) and the detailed information about their formation and occurrence can be found in Lohmar et al. (2007) which also involves a section about the following application on volcanic ash surfaces.

5.1.2. Quantitative analysis on volcanic ash surfaces: Application of extended depth-of-field (focus) algorithm for light and scanning electron microscopy and 3D reconstruction

Available online at www.sciencedirect.com
ScienceDirect
Micron xxx (2007) xxx–xxx
micron
www.elsevier.com/locate/micron

Quantitative analysis on volcanic ash surfaces: Application of extended depth-of-field (focus) algorithm for light and scanning electron microscopy and 3D reconstruction

Orkun Ersoy [a,b,*], Erkan Aydar [a], Alain Gourgaud [b], Hasan Bayhan [a]

[a] Department of Geological Engineering, Hacettepe University, 06532 Beytepe-Ankara, Turkey
[b] Université Blaise Pascal, UMR-CNRS 6524, 5 rue Kessler, 63038 Clermont-Ferrand, France

Received 28 October 2006; accepted 24 November 2006

Abstract

The depth-of-field mainly affects the image quality either in scanning electron microscopy (SEM) or conventional light microscopy. The limited depth-of-field handicap of microscopy imaging can be used for obtaining ''optically sectioned'' specimens by moving the object along the optical axis. In this study, multiple images corresponding to different object planes were taken in order to overcome limited depth-of-field on conventional light microscope and SEM, estimation of an elevation surface and 3D reconstruction of different type volcanic ash surfaces. We used extended depth-of-field, a fusion algorithm that combines those images into one single sharp composite. Because of larger depth-of-field, we got higher-quality results even with image stacks taken by SEM with a fixed aperture in variable pressure mode. We calculated roughness descriptors, quadtree decomposition and greylevel standard deviation (sGL) and analyzed the shape of polar plots based on gradient analysis of constructed depth-maps. Furthermore, we calculated fractal dimensions of surfaces. Correlation analysis was performed to measure how these quantitative variables are related with different type ash surfaces. Roughness descriptors, quadtree decomposition, sGL and fractal dimension discriminate different types of volcanic ash surfaces.

Keywords: Volcanic ash; Quantitative surface analysis; Depth-of-field; 3D reconstruction

1. Introduction

1.1. Surface topography

Surface topography is a topic of significant interest to science, technology and industry (Castle and Zhdan, 1997, and references cited therein). The quantitative three-dimensional characterization of topography has always been important to gain insight and understanding into material systems. Numerical characterization of 3D topography of engineering, biological and natural surfaces is a subject of intense research (Stachowiak, 1998, and references therein). Classification of volcanic ash surfaces is still limited to descriptive terms. Thus, data describing volcanic ash need to be expressed quantitatively (Ersoy et al., 2006, in press). Three-dimensional reconstruction often reveals information about the morphology and composition of a system that can otherwise be obscured or misinterpreted by two-dimensional images (Bansal et al., 2006). Serial sectioning in conjunction with optical or electron microscopy has been shown to provide valuable three-dimensional information (Bansal et al., 2006, and references cited therein). This has traditionally been accomplished using mechanical polishing techniques to remove material, followed by surface imaging using a scanning electron microscopy (SEM) (Mangan et al., 1997) or a reflective optical microscope (Kral and Spanos, 1997). 3D surfaces of volcanic ash particles can be reconstructed from sections that were obtained optically by the help of limited depth-of-field handicap of light and scanning electron microscopy on unpolished rough surfaces.

1.2. Limited depth-of-field (focus) in microscopy

1.2.1. Light microscopy (LM)

Limited depth-of-field is a common problem especially when imaging is carried out with conventional light microscopy. Often,

* Corresponding author at: Department of Geological Engineering, Hacettepe University, 06532 Beytepe-Ankara, Turkey. Fax: +90 312 2992034.
E-mail address: oersoy@hacettepe.edu.tr (O. Ersoy).

0968-4328/$ – see front matter © 2006 Elsevier Ltd. All rights reserved.
doi:10.1016/j.micron.2006.11.010

specimen profile covers more than the attainable depth-of-field. For a sufficiently rough specimen, portions of the object's surface outside the optical plane appear defocused in the acquired image plane (Forster et al., 2004, and references cited therein). This becomes worse as the magnification M increases (Forster et al., 2004). Changing the magnification is not generally an option because the magnification is chosen to fill the image with the specimen features of interest (Goldstein et al., 2003). In light microscopy, when the magnification M increases, the numerical aperture increases, too (see Eqs. (1)–(3) in Forster et al., 2004). Consequently, each acquisition shows certain parts of the specimen in and out of focus.

1.2.2. Scanning electron microscopy

Although the large depth-of-field of the SEM is one of its greatest strengths, we must understand what factors control the depth-of-field to optimize the range of the image that appears in focus (Goldstein et al., 2003). The action of focusing the beam to a crossover (''plane of optimum focus'') in SEM inevitably produces angular divergence of the ray package that constitutes the focused beam (Fig. 1). This divergence causes the beam to broaden above and below the plane of optimum focus. With the objective lens strength selected to bring the beam to a focus at the plane indicated, different beam sizes strike specimen features, depending on their z position relative to the plane of optimum focus. The beam intersecting some features becomes so large that those features of the specimen will not appear in focus (Goldstein et al., 2003). In electron microscopy, the divergence as the adjustable parameter is decreased to obtain greater depth-of-field. The divergence is adjusted by the selection of the final beam-defining aperture. Decreasing radius of the aperture and increasing the working distance (D_W—the distance from the center of the lens to the specimen plane) both increase the depth-of-field in electron microscopy. However, we used SEM in variable-pressure mode (VPSEM) with a fixed aperture (100 μm) to avoid charging on non-conductive surfaces. Moderate magnifications (∼1200×) on rough surfaces with a fixed aperture resulted in limited depth-of-field in VPSEM.

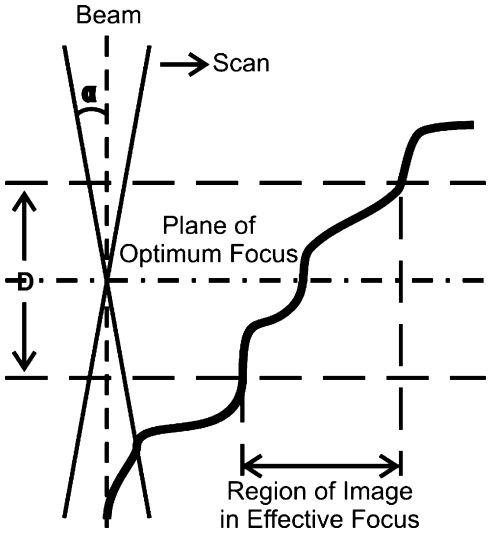

Fig. 1. Schematic illustration of the depth-of-field (focus) in a SEM image. Any portion of the specimen that lies within the range of Z (along the optical axis) defined by the planes located at $\pm D/2$ from the plane of optimum focus will appear to be in focus. Reproduced from Goldstein et al. (2003).

1.3. Limited depth-of-field (focus) as a tool for 3D reconstruction

The limited depth-of-field handicap of microscopy imaging can also be used for obtaining ''optically sectioned'' specimens by moving the object along the optical axis (Forster et al., 2004). Optically sectioning requires different areas in focus in serial images. For estimation of an elevation surface and 3D reconstruction, we need to image the whole specimen in focus by taking multiple images corresponding to different object planes. The challenge then becomes to select from each slice the area that is focused in order to reconstruct an image that is sharp everywhere. In this way, it is possible to extend the depth of focus without the physical limitation of the numerical aperture of the objective lens. Numerous articles have been written on this matter and some solutions have proven to be more efficient than others (Forster et al., 2004, and references cited therein). Extended depth-of-field, a fusion algorithm that combines those images into one single sharp composite (Forster et al., 2004) was used to extend depth-of-focus of microscopic images. Thus, depth-maps, which approximate to the real topography of volcanic ash particles, were generated. Due to the necessity of expressing and classification of volcanic ash surfaces quantitatively, we calculated several surface parameters of volcanic ash surfaces.

2. Materials and methods

2.1. Volcanic ash and sample preparation

Fragmentation of magma may occur due to exsolution of gas phases as a result of decompression or by an interaction between external water and magma (Cashman et al., 2000). These two fragmentation processes produce ash particles with end-members displaying characteristic morphology and surface features (Wohletz, 1983; Heiken and Wohletz, 1985). The quantitative analysis of volcanic ash particles provides insight into the energy release rate of volcanic explosions (Zimanowski et al., 2003). Two volcanic ash (250–500 μm in size) samples (labeled as A and B) were analyzed. Blocky, equant poorly or non-vesicular weathered pyroclasts in sample A suggest water–magma interaction, the result of an effective and hazardous mechanism of conversion of thermal into kinetic energy. (Wohletz and Sheridan, 1983; Wohletz, 1986; Lorenz et al., 1991; Wohletz and Brown, 1995; Zimanowski et al., 1997). Samples were washed to remove any organic, loosely adhered and cementing material. Depending upon the freshness of the grains, washing realized in acetone using ultrasound for not more than 4 min to preserve grain edges (Heiken and Wohletz, 1985). After drying at 105 °C in oven and cooling to room temperature, the samples were mounted on a lamella using double stick tapes.

2.2. Instruments

A digital camera equipped Leica DM2500 M polarized light microscope in reflection mode and Zeiss EVO 50 XVP SEM in variable-pressure mode at Hacettepe University (Ankara, Turkey) were used to take multiple images corresponding to different focal planes on samples for 3D reconstruction. The variable-pressure SEM (VPSEM) instrument allows the examination of surfaces of almost any specimen, wet or dry, because the environment around the specimen no longer has to be at high vacuum (Goldstein et al., 2003). Poor coating may give rise to charging on surfaces and misleading results, so that in this work, the samples were not coated and SEM in variable-pressure mode was used. In VPSEM works, it is necessary to supply sufficient gas to produce a stable image. At gas pressure about 200 Pa (1.5 Torr), the interactions between electrons and the gas resulted in the production of ions, which changed the charge balance at the specimen (Goldstein et al., 2003).

2.3. Image acquisition

The image fusion algorithm relies on two conditions prior to processing (Forster et al., 2004). The first is that the images must be aligned throughout the stack and the second is that at least the in-focus areas must be at the same magnification level.

Both conditions are met if the original images are taken by a traditional light microscope with the specimen being translated along the optical axis z to obtain the slices. First images from particles were taken by focusing the double stick tape at the base of the particles. The fine-gear of the light microscope was moved by the same amount (e.g. interval value of 1 equals to 5 μm) among image acquisition so all images were equally distanced apart. Last images for particles were taken by focusing top of the particles.

For SEM, the working distance (D_W) increases by lowering the specimen stage with the z-control and refocusing the beam on the specimen. Increasing the working distance produces a larger spot size at the specimen and a consequent degradation of the image resolution, although the beam current remains about the same. The convergence angle decreases, giving an improved depth of field (Goldstein et al., 2003). While lowering the specimen stage, to operate at a particular working distance D_W, we set the current in the objective lens to a specific value. The specimen was then moved vertically with the z-control until desirable area came into focus. The magnification was constant for all images. The specimen stage of SEM was also lowered by the same amount (e.g. 10 μm), although the working distance remained the same. Ten replicates (volcanic ash particles) were acquired from each sample. From the sample A, 1105 and 553 micrographs, from B, 1191 and 595 micrographs were taken by light microscope and SEM, respectively.

2.4. Image processing, 3D reconstruction and surface measurements

Image processing, 3D reconstruction and analysis were performed using the ImageJ program (Rasband, 1997–2006). ImageJ is a public domain image processing program based on Java and was designed with an open architecture that provides extensibility via Java plugins (available at: http://rsb.info.nih.gov/ij/). During each session, the brightness and contrast settings for image acquisition must be adjusted and it was difficult to achieve a default setting for all of the slices. Hence, in order to overcome variations that result from various imaging conditions, contrast normalization was performed on every image.

2.4.1. Complex wavelets for extended depth-of-field

For image fusion, it is essential to detect image areas where sharp features and details are present. This can be performed using the wavelet transform, which allows for the decomposition of an image into sub-bands that contain details of various sizes. A short review of the wavelet transform is presented in Forster et al. (2004). In order to overcome the limited depth-of-field, we used the algorithm of Forster et al. (2004) which allows the fusion of a stack of images. This approach computes the discrete complex-valued wavelet transform of each image slice of the object, and builds up the wavelet coefficients of the composite image by a maximum-absolute-value selection rule. The final composite image is obtained after computing the inverse complex wavelet transform. For its successful application into multi-channel images, Forster et al. (2004) proposed an adapted multi-channel conversion and recovery as a pre- and post-processing step. In essence, this method compensates for the increase in dynamic range of the image obtained after fusion and avoids the introduction of false colors (Forster et al., 2004).

The software of the algorithm named ‘‘Extended Depth-of-Field’’ (available at: http://bigwww.epfl.ch/demo/edf/index.html) is an ImageJ plugin and suited for multi-channel data. The software produces a topological and an ‘‘in focus’’ images (Fig. 2).

2.4.2. 3D reconstructions from conventional light microscope and SEM images

The topological and ‘‘in focus’’ images produced by the ‘‘Extended Depth-of-Field’’ plugin, were used as inputs for another ImageJ plugin (*Anaglyph* by Gabriel Landini, available at: http://www.dentistry.bham.ac.uk/landinig/software/software.html). Analglyph creates red-cyan or red-green anaglyphs, crossed view stereo pairs and depth-map from topological and ‘‘in focus’’ images. The depth-map is the mapping of the topological image (i.e. intensity is the depth) into the hue values of the original image (Fig. 2). By this way, the color of the image varies according to the selected range of hues (the default is 25 steps of hue). The depth of hues displayed does not essentially depend on the depth, but on the rescaled range. Thanks to the equally distanced slices, we calibrated the z-scale of the depth-maps by summing the distances and looking at which part of each pixel in depth map corresponds to the image (the same greyscale level represents the same altitude) (Gabriel Landini, pers. comm., 2006).

2.4.3. Surface measurements on volcanic ash

Several texture descriptors have been developed to characterize the detailed surface structure of aluminum (Lee

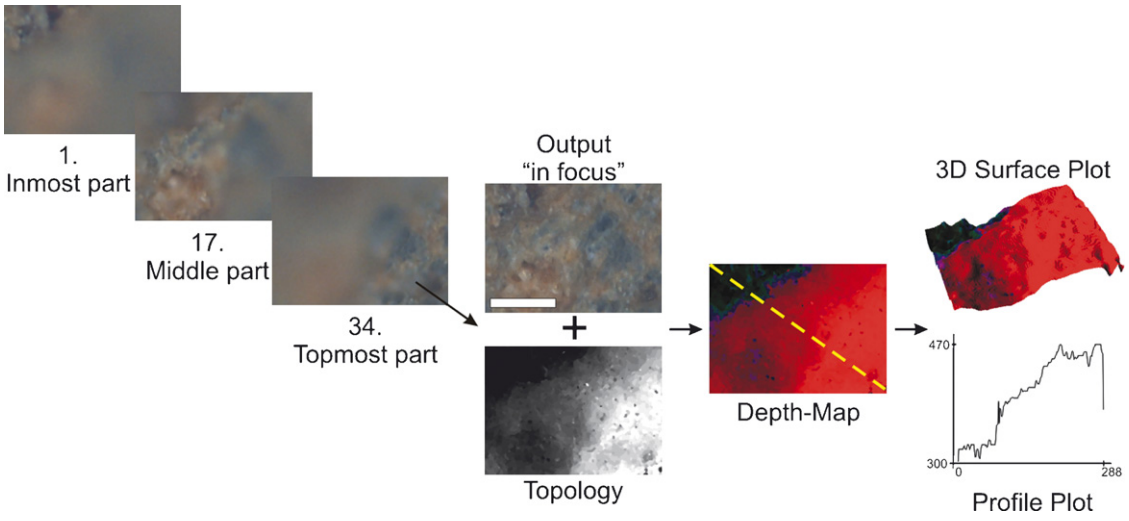

Fig. 2. Output (in focus) and topology images produced from 34 light microscope images corresponding to different object planes. Depth-map is mapping of the topology image (i.e. intensity is the depth) into the hue value of the original image. 3D surface plots were constructed by the plugin SurfacePlot_3D written by Kai Uwe Barthel. Profile plot is the profile of diagonal yellow line on depth-map. Bar in output image is 80 μm. The scale in profile plot is in microns.

et al., 1998), aggregate (Rao et al., 2003), wear particles (Stachowiak, 1998) and paper surfaces (Chinga et al., 2003; Chinga, 2004). Fractal dimension, autocorrelation, gradient analysis, band pass filtering, wavelet analysis, roughness statistics and quadtree decomposition have been applied to assess complex surface structures (Panozzo, 1992; Costa, 2000; Chinga et al., 2003; Chinga, 2005).

2.4.3.1. Roughness. Roughness parameters can be calculated in either two-dimensional (2D) or three-dimensional (3D) forms. 2D profile analysis has been widely used for more than half a century. Recently, there has been an increased need for 3D surface analysis (Gadelmawla et al., 2002). The roughness of a volcanic ash surface can be measured in various ways. Fig. 3 depicts a schematic representation of a surface and the applied terms used to describe it. *Roughness amplitude descriptors* give an average measurement of the surface height. Some *amplitude descriptors* are the average roughness (Ra) and the root-mean-square roughness (Rq). *Statistical descriptors* are skewness (Rsk) and kurtosis (Rku) of the amplitude distribution function (ADF) which give the probability of a profile of the surface having a certain height, z, at any position x. *Extreme value descriptors* depend on isolated events, e.g. the maximum peak height (Rp), the maximum valley depth (Rv), and the maximum peak to valley height (Rt). *Roughness amplitude descriptors* are used extensively in order to characterize a surface and can be also applied to volcanic ash particles. Detailed information about the roughness parameters and an application on paper surfaces can be found at Chinga et al. (2003). The SurfCharJ plugin (Chinga et al., 2003) was used for the analyses of surface roughness (available at: http://www.gcsca.net).

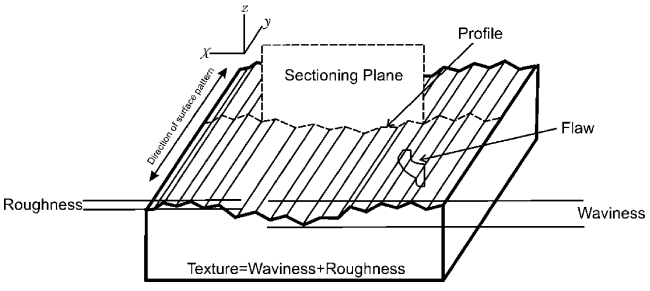

Fig. 3. Surface profile. Reproduced from TS 6956 (2004).

2.4.3.2. Gradient analysis and texture descriptors. Gradient analysis has also proved to be suitable for describing surface texture orientation. Similar methods have been used to detect the orientation of short-fibre composites (Gadala-Maria and Parsi, 1993), actin fibres in cytoskeletal structures (Yoshigi et al., 2003) and features on volcanic ash surfaces (Ersoy et al., 2006). This provides valuable information for differentiating between textures having the same grey level variation. The gradient analysis is based on Sobel operators as described by Gonzalez and Woods (1993) and implemented by Chinga et al. (2003). For more details on the current application of gradient analysis for surface structure quantification, see Chinga and Dougherty (2006). The gradient analysis yielded polar plots giving the preferred orientations of the structures (Fig. 4C). The polar plots were analyzed with the Shape Descriptor plugin (available at: http://www.gcsca.net). Different shape descriptors like the aspect ratio, compactness, roundness and form factor were calculated according to Russ (1999).

2.4.3.3. Fractal dimension. Traditionally, statistical functions and parameters, such as auto-correlation function, correlation length, auto-covariance function, structure function, etc., have been used to characterize the surface topography (Stachowiak, 1998, and references therein). Recently, however fractal methods have also been applied to describe the complexity of surface topography. The physical characteristics of some

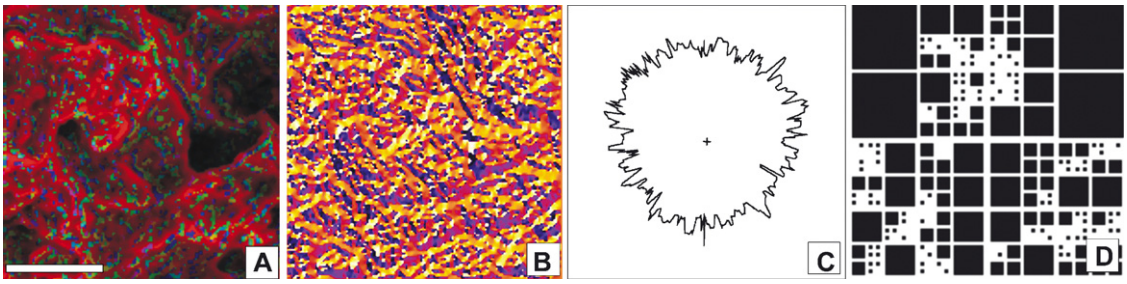

Fig. 4. (A) Depth map, (B) azimuthal image, (C) polar plot based on frequency of gradients and (D) quadtree decomposition. Bar in depth-map image is 70 μm.

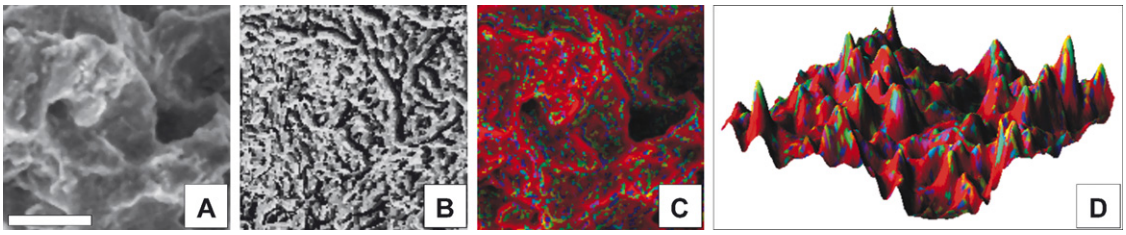

Fig. 5. (A) Output (in focus), (B) topology, (C) depth map and (D) 3D surface plot images constructed from SEM images. Bar in output image is 70 μm.

bodies are related to the fractal dimensions of their surfaces (Ortega et al., 2003). The studies on fractal geometry of volcanic particles were limited with the boundary of a particle that results from an intersection with a plane, i.e. a thin section of a grain, from contours obtained from SEM micrographs or photographs directly taken from drill cores or exposures (Carey et al., 2000; Dellino and Liotino, 2002; Barnett, 2004). There is a fundamental difference between a particle boundary and surface profile. The particle boundary is self-similar while profile is self-affine. Self-affine profiles scale by different amounts in vertical (z) and horizontal (x) directions. Also, the units of the measurements may not be the same, i.e. the profile can be treated as the time series, where the elevation varies with time (Stachowiak, 1998). The fractal dimensions of depth-maps were calculated with the plugin of Fractal Count for Maps 1.36 written by Per Christian Henden (available at: http://www.pvv.org/∼perchrh/imagej/).

2.4.3.4. Quadtree decomposition. Currently, quadtrees are used for indexing point data, regions, curves, surfaces, and volumes (Samet, 1990). Details about the quadtree decomposition analysis on volcanic ash surfaces can be found at Ersoy et al. (2006). A quadtree decomposition routine integrated with ImageJ was used for texture characterization (Chinga, 2005). The quadtree decomposition was performed by assessing the local greylevel standard deviation (sGL). The minimum sGL is obtained from the stack of all images and assigned as the threshold value. If the image has a sGL value equal to or larger than the threshold, the image is divided into four sub-images or blocks. Each sub-image is evaluated again using the same criteria. Each sub-image having a sGL value larger than threshold value is decomposed into four new sub-images. This is done iteratively until the local area (sub-image) has a sGL value lower than the given threshold (Fig. 4D). The variables yielded by the current decomposition are the number of blocks (nQT), the mean block size (mQT) and the standard deviation of block sizes (sQT).

3. Results

In this study, multiple images corresponding to different object planes were taken in order to overcome limited depth-of-field on conventional light microscope and VPSEM, to estimate the elevation surface and thus 3D reconstruction.

Because of larger depth-of-field, we got higher-quality results even with image stacks taken by VPSEM with a fixed aperture. The in-focus and topological images were more

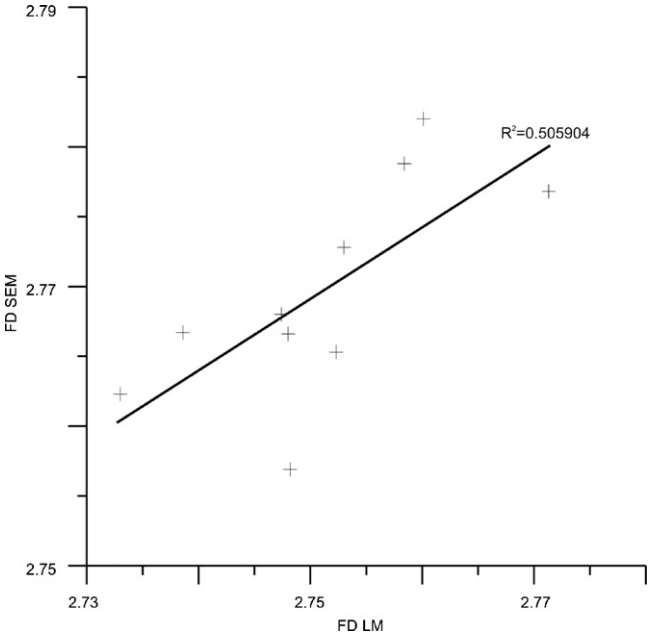

Fig. 6. Fractal dimension values of surfaces calculated on light microscope vs. SEM images.

Table 1
Pearson correlation coefficients for surface parameters calculated on light microscope images

	Type	sGL	nQT	mQT	sQT	Rq	Ra	Rsk	Rku	Rv	Rp	Rt	FD map	Round	Compa	AR	FF
Type	1	−0.994**	0.874**	−0.813**	−0.834**	−0.994**	−0.995**	0.726**	0.860**	0.503*	−0.992**	−0.987**	−0.971**	0.034	0.065	−0.058	0.389
sGL	−0.994**	1	−0.835**	0.800**	0.797**	10.000**	0.999**	−0.751**	−0.856**	−0.537*	0.993**	0.986**	0.964**	0.013	−0.021	0.009	−0.446*
nQT	0.874**	−0.835**	1	−0.896**	−0.956**	−0.835**	−0.832**	0.660**	0.672**	0.456*	−0.834**	−0.828**	−0.816**	0.257	0.284	−0.296	0.144
mQT	−0.813**	0.800**	−0.896**	1	0.941**	0.800**	0.784**	−0.760**	−0.575**	−0.603**	0.782**	0.762**	0.747**	−0.264	−0.297	0.309	−0.11
sQT	−0.834**	0.797**	−0.956**	0.941**	1	0.797**	0.788**	−0.643**	−0.624**	−0.466*	0.798**	0.790**	0.783**	−0.359	−0.372	0.4	−0.095
Rq	−0.994**	10.000**	−0.835**	0.800**	0.797**	1	0.999**	−0.751**	−0.856**	−0.537*	0.993**	0.986**	0.964**	0.013	−0.021	0.009	−0.446*
Ra	−0.995**	0.999**	−0.832**	0.784**	0.788**	0.999**	1	−0.740**	−0.873**	−0.512*	0.993**	0.988**	0.969**	0.011	−0.023	0.011	−0.447*
Rsk	0.726**	−0.751**	0.660**	−0.760**	−0.643**	−0.751**	−0.740**	1	0.665**	0.761**	−0.685**	−0.649**	−0.726**	−0.062	−0.001	0.008	0.451*
Rku	0.860**	−0.856**	0.672**	−0.575**	−0.624**	−0.856**	−0.873**	0.665**	1	0.326	−0.835**	−0.838**	−0.892**	0	0.021	−0.036	0.36
Rv	0.503*	−0.537*	0.456*	−0.603**	−0.466*	−0.537*	−0.512*	0.761**	0.326	1	−0.480*	−0.418	−0.489*	−0.192	−0.111	0.152	0.322
Rp	−0.992**	0.993**	−0.834**	0.782**	0.798**	0.993**	0.993**	−0.685**	−0.835**	−0.480*	1	0.998**	0.961**	−0.014	−0.036	0.03	−0.438
Rt	−0.987**	0.986**	−0.828**	0.762**	0.790**	0.986**	0.988**	−0.649**	−0.838**	−0.418	0.998**	1	0.956**	−0.029	−0.046	0.043	−0.428
FD map	−0.971**	0.964**	−0.816**	0.747**	0.783**	0.964**	0.969**	−0.726**	−0.892**	−0.489*	0.961**	0.956**	1	−0.05	−0.077	0.073	−0.388
Round	0.034	0.013	0.257	−0.264	−0.359	0.013	0.011	−0.062	0	−0.192	−0.014	−0.029	−0.05	1	0.977**	−0.991**	−0.201
Compa	0.065	−0.021	0.284	−0.297	−0.372	−0.021	−0.023	−0.001	0.021	−0.111	−0.036	−0.046	−0.077	0.977**	1	−0.970**	−0.164
AR	−0.058	0.009	−0.296	0.309	0.4	0.009	0.011	0.008	−0.036	0.152	0.03	0.043	0.073	−0.991**	−0.970**	1	0.193
FF	0.389	−0.446*	0.144	−0.11	−0.095	−0.446*	−0.447*	0.451*	0.36	0.322	−0.438	−0.428	−0.388	−0.201	−0.164	0.193	1

* Correlation is significant at the 0.05 level.
** Correlation is significant at the 0.01 level.

Table 2
Pearson correlation coefficients for surface parameters calculated on SEM images

	Type	sGL	nQT	mQT	sQT	Rq	Ra	Rsk	Rku	Rv	Rp	Rt	FD map	Round	Compa	AR	FF
Type	1	−0.933**	0.937**	−0.893**	−0.886**	−0.933**	−0.941**	0.867**	0.922**	0.805**	−0.931**	−0.913**	−0.968**	−0.262	−0.271	0.289	0.209
sGL	−0.933**	1	−0.777**	0.776**	0.742**	1.000**	0.999**	−0.733**	−0.899**	−0.823**	0.955**	0.937**	0.934**	0.116	0.119	−0.137	−0.059
nQT	0.937**	−0.777**	1	−0.933**	−0.950**	−0.777**	−0.789**	0.888**	0.832**	0.750**	−0.788**	−0.758**	−0.880**	−0.301	−0.298	0.332	0.346
mQT	−0.893**	0.776**	−0.933**	1	0.982**	0.776**	0.782**	−0.837**	−0.783**	−0.753**	0.809**	0.782**	0.857**	0.289	0.269	−0.317	−0.223
sQT	−0.886**	0.742**	−0.950**	0.982**	1	0.742**	0.749**	−0.847**	−0.763**	−0.764**	0.800**	0.769**	0.851**	0.292	0.283	−0.325	−0.258
Rq	−0.933**	1.000**	−0.777**	0.776**	0.742**	1	0.999**	−0.733**	−0.899**	−0.823**	0.955**	0.937**	0.934**	0.116	0.119	−0.137	−0.059
Ra	−0.941**	0.999**	−0.789**	0.782**	0.749**	0.999**	1	−0.750**	−0.911**	−0.818**	0.954**	0.938**	0.940**	0.126	0.13	−0.148	−0.067
Rsk	0.867**	−0.733**	0.888**	−0.837**	−0.847**	−0.733**	−0.750**	1	0.899**	0.683**	−0.712**	−0.683**	−0.839**	−0.301	−0.32	0.333	0.151
Rku	0.922**	−0.899**	0.832**	−0.783**	−0.763**	−0.899**	−0.911**	0.899**	1	0.721**	−0.846**	−0.832**	−0.904**	−0.242	−0.259	0.272	0.129
Rv	0.805**	−0.823**	0.750**	−0.753**	−0.764**	−0.823**	−0.818**	0.683**	0.721**	1	−0.819**	−0.738**	−0.821**	−0.12	−0.124	0.16	0.086
Rp	−0.931**	0.955**	−0.788**	0.809**	0.800**	0.955**	0.954**	−0.712**	−0.846**	−0.819**	1	0.992**	0.936**	0.226	0.238	−0.245	−0.074
Rt	−0.913**	0.937**	−0.758**	0.782**	0.769**	0.937**	0.938**	−0.683**	−0.832**	−0.738**	0.992**	1	0.916**	0.238	0.252	−0.252	−0.067
FD map	−0.968**	0.934**	−0.880**	0.857**	0.851**	0.934**	0.940**	−0.839**	−0.904**	−0.821**	0.936**	0.916**	1	0.385	0.389	−0.411	−0.219
Round	−0.262	0.116	−0.301	0.289	0.292	0.116	0.126	−0.301	−0.242	−0.12	0.226	0.238	0.385	1	0.987**	−0.996**	−0.510*
Compa	−0.271	0.119	−0.298	0.269	0.283	0.119	0.13	−0.32	−0.259	−0.124	0.238	0.252	0.389	0.987**	1	−0.987**	−0.512*
AR	0.289	−0.137	0.332	−0.317	−0.325	−0.137	−0.148	0.333	0.272	0.16	−0.245	−0.252	−0.411	−0.996**	−0.987**	1	0.529*
FF	0.209	−0.059	0.346	−0.223	−0.258	−0.059	−0.067	0.151	0.129	0.086	−0.074	−0.067	−0.219	−0.510*	−0.512*	0.529*	1

* Correlation is significant at the 0.05 level.
** Correlation is significant at the 0.01 level.

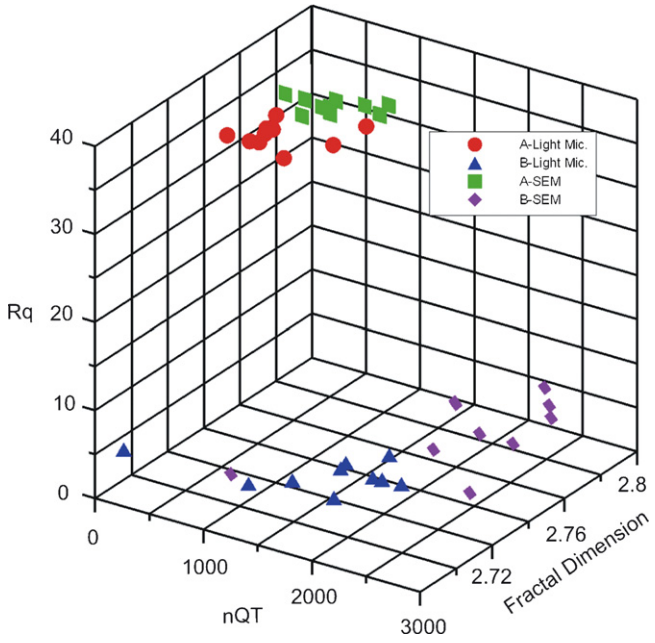

Fig. 7. 3D scatter plot of Rq, nQT and fractal dimension values of surfaces from different type volcanic ashes (A and B).

reliable in VPSEM than the conventional light microscope (Figs. 2 and 5). Despite the better preserved details in fused images of VPSEM, there is significant correlation between textures of surfaces (e.g. fractal dimension) reconstructed from multiple images taken by VPSEM and by conventional light microscope (Fig. 6).

Here, we calculated seven roughness descriptors (Ra, Rq, Rsk, Rku, Rp, Rv, Rt), three quadtree decomposition parameters (nQT, mQT, sQT), greylevel standard deviations (sGL), fractal dimensions on reconstructed 3D surface images (depth-maps), four shape descriptors (form factor, roundness, compactness, aspect ratio) on polar plots of surfaces. All parameters were subjected to correlation analysis. Calculation of Pearson correlation coefficients was realized in SPSS (SPSS Inc., Release 9.0). Pearson's correlation coefficient is a measure of linear association. We carried out bivariate correlations procedure. The surface roughness, quadtree decomposition parameters, sGL and fractal dimensions calculated on depth-maps from both VPSEM and light microscope, effectively discriminate the volcanic ash surfaces, which formed by different fragmentation mechanisms (Tables 1 and 2; Fig. 7). Shape descriptors of polar plots show insignificant correlations with surfaces from different mechanisms.

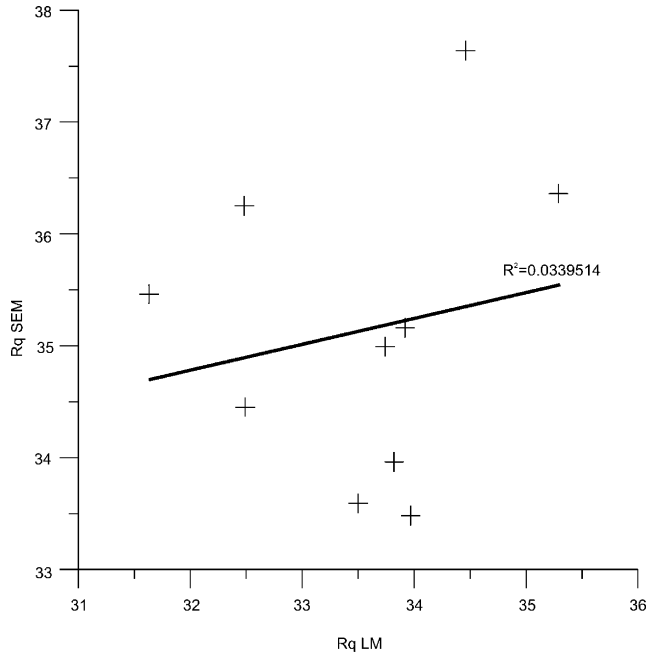

Fig. 8. Rq values of surfaces calculated on light microscope vs. SEM images.

4. Discussion and conclusion

Numerical characterization of 3D topography of surfaces at microscopic scales is of great importance for scientific and industrial research. In volcanology, identification and classification of volcanic ash surface textures are limited to some descriptive terms. Here, we reconstructed 3D surfaces of volcanic ash particles by using the images taken from light and variable pressure scanning electron microscopes. We made quantitative analysis on ash surfaces to characterize textures quantitatively. The strength of the method is its simplicity. However, simplicity brings both advantages and disadvantages. Study on a conventional light microscope is more economical than on SEM. Many laboratories, particularly those for petrographical research have light microscopes. However, the greylevels taken from light microscope or SEM images are strongly affected by some conditions, such as illumination homogeneity, edge highlighting, varying atomic structure of the sample, sample charging, detector orientation, etc. (Stachowiak, 1998, and references therein). It is also important to keep in mind that SEM images give a 3D impression of the ash surfaces but they do not give real topographical representations with local height values. Despite this fact, it is assumed that the grey level variation in light microscope and SEM images is related with the real roughness variation of the surface. The 3D surfaces reconstructed from SEM images seem more reliable due to the higher resolution and larger depth-of-field of SEM. However, this study demonstrates that the depth-maps generated from multiple images taken by these two instruments successfully expose the differences on volcanic ash surfaces. Surface topography is essentially a non-stationary random process for which the variance of height distribution depends on the sampling length. This means that the same surface can exhibit different values of the statistical parameters when a different sampling length or an instrument with a different resolution is used. Thus, conventional surface parameters, such as the root-mean-square roughness (Rq), strongly depend on the scan length and the measurement technique and hence are not adequate for a particular surface. In order to characterize a surface at all scales, scale-independent parameters must be developed and used (Stachowiak, 1998, and references therein). Here, we determined an important correlation between scale-independent parameter e.g. fractal dimensions of depth-maps constructed from light microscope and SEM (see Fig. 6). Thus,

a conventional light microscope overcomes estimation of an elevation surface as well as a SEM. The correlations between scale-dependent parameters (e.g. roughness parameters) on depth-maps constructed from different instruments are weak (Fig. 8). However, some of scale-dependent parameters are adequate to discriminate various surfaces from different types of volcanic ashes. The capabilities of ash surface texture discrimination of some of these parameters were also denoted in previous studies (Ersoy et al., 2006, in press). Roughness parameter-Rq, quadtree decomposition parameter-nQT and texture parameter-Fractal dimension cluster two different types of ash surfaces as demonstrated in Fig. 7. The roughness parameter-Rq has higher values for on the surface of sample A indicating water–magma interaction during fragmentation. The higher Rq values reflect alteration and/or fine particle abundance on surfaces (Ersoy et al., 2006); these can be interpreted as evidence of steam in eruption and/or intense fragmentation due to water–magma interaction. The smaller nQT values for sample A also indicate water–magma interaction and limited vesiculation on surface due to rapid quenching (Ersoy et al., 2006). However, the fractal dimensions of surfaces those interacted with water (sample A) are higher than the surfaces formed in dry conditions. Surface fractal dimension is between two for a smooth, regular surface and three for an infinitely porous medium. Thus, it is textural fractal dimension, representing surface irregularity/roughness and textural complexity (Huang et al., 2001, and references therein). Although we expect lower complexity of the surfaces from sample A due to water interaction and limited vesiculation, they have higher fractal dimensions. The higher fractal dimensions on sample B could be attributed to fine textures as a result of alteration and/or fine particle abundance on its surface. On account of the reason that Ra–Rq parameters are higher for fine textures such as alteration products and/or fine adhered particles on surfaces (Ersoy et al., 2006), the correlation between these parameters and fractal dimension demonstrates higher complexities on surfaces of sample A. The shape descriptors calculated on polar plots of surfaces neither have strong correlations between results of different instruments on same surfaces nor are capable of discriminating different surface types.

Acknowledgements

The research activities of the first author in France were supported scholarship granted by the French Government. H.E. Cubukcu gave a critical reading of the manuscript and significantly improved the English. Thanks to anonymous reviewers for their constructive suggestions. This study was funded by Hacettepe University Scientific research Unit (Project No: 04A602010).

References

Barnett, W., 2004. Subsidence breccias in kimberlite pipes—an application of fractal analysis. Lithos 76 (1–4), 299–316.

Bansal, R.K., Kubis, A., Hull, R., Fitz-Gerald, J.M., 2006. High-resolution three-dimensional reconstruction: a combined scanning electron microscope and focused ion-beam approach. J. Vac. Sci. Technol. B: Microelectron. Nanometer Struct. 24 (2), 554–561.

Cashman, K.V., Sturtevant, B., Papale, P., Navon, O., 2000. Magmatic fragmentation. In: Sigurdsson, H., Houghton, B.F., McNutt, S.R., Rymer, H., Stix, J. (Eds.), Encyclopedia of Volcanoes. Academic Press, pp. 412–430.

Castle, J.E., Zhdan, P.A., 1997. Characterization of surface topography by SEM and SFM: problems and solutions. J. Phys. D: Appl. Phys. 30, 722–740.

Carey, S., Maria, A., Sigurdsson, H., 2000. Use of fractal analysis for discrimination of particles from primary and reworked jokulhlaup deposits in SE Iceland. J. Volcanology Geother. Res. 104, 65–80.

Chinga, G., 2004. Detailed characterization of paper surface structure for gloss assessment. J. Pulp Paper Sci. 30 (8), 222–227.

Chinga, G., 2005. A quadtree decomposition approach for surface assessment. Pattern Anal. Appl. 9 (1), 94–101.

Chinga, G., Dougherty, R., 2006. Quantification of surface structures. In: Proceedings, Image J User and Developer Conference, 1st, Luxembourg, pp. 117–122.

Chinga, G., Gregersen, Ø., Dougherty, R., 2003. Paper surface characterisation by laser profilometry and image analysis. J. Microsc. Anal. 84, 5–7.

Costa, M.A., 2000. Fractal description of rough surfaces for haptic display. Ph.D. Thesis. Stanford University, Stanford, 119 pp.

Dellino, P., Liotino, G., 2002. The fractal and multifractal dimension of volcanic ash particles contour: a test study on the utility and volcanological relevance. J. Volcanology Geother. Res. 113, 1–18.

Ersoy, O., Chinga, G., Aydar, E., Gourgaud, A., Cubukcu, H.E., Ulusoy, I., 2006. Texture discrimination of volcanic ashes from different fragmentation mechanisms: A case study, Mount Nemrut stratovolcano, eastern Turkey. Comput. Geosci. 32, 936–946.

Ersoy, O., Aydar, E., Gourgaud, A., Artuner, H., Bayhan, H. Clustering of volcanic ashes arising from different fragmentation mechanisms using Kohonen self-organizing maps. Comput. Geosci., in press.

Forster, B., Van de Ville, D., Berent, J., Sage, D., Unser, M., 2004. Complex wavelets for extended depth-of-field: a new method for the fusion of multichannel microscopy images. Microsc. Res. Tech. 65, 33–42.

Gadala-Maria, F., Parsi, F., 1993. Measurement of fiber orientation in short-fiber composites using digital image processing. Polym. Compos. 14 (2), 126–131.

Gadelmawla, E.S., Koura, M.M., Maksoud, T.M., Elewa, I.M., Soliman, H.H., 2002. Roughness parameters. J. Mater. Process. Technol. 123, 133–145.

Goldstein, J., Newbury, D., David, J., Lyman, C., Echlin, P., Lifshin, E., Sawyer, L., Michael, J., 2003. Scanning Electron Microscopy and X-Ray Microanalysis, third ed. Springer, New York.

Gonzalez, R., Woods, R.E., 1993. Digital Image Processing. Addison-Wesley Publishing Company, Reading, MA.

Heiken, G., Wohletz, K.H., 1985. Volcanic Ash. University of California Press, Berkeley.

Huang, W.L., Shi, H.C., Kai, M.L., Shou, R.G., 2001. Influence of calcining temperature on the mesopore structures and surface fractal dimensions of $MgO–Al_2O_3–SiO_2$ xerogels. J. Phys. Chem. Solids 62 (7), 1205–1211.

Kral, M.V., Spanos, G., 1997. Three-dimensional analysis of proeutectoid cementite precipitates. Acta Mater. 47, 711–724.

Lee, P.S., Piehler, H.R., Adams, B.L., Jarvis, G., Hampel, H., Rollett, A.D., 1998. Influence of surface texture on orange peel in aluminum. J. Mater. Process. Technol. 80–81, 315–319.

Lorenz, V., Zimanowski, B., Fröhlich, G., 1991. Experiments on Explosive Basic and Ultrabasic, Ultramafic and Carbonatitic Volcanism. CPRM-Special Publ. 2/91, Brasilia, pp. 245–247.

Mangan, M.A., Lauren, P.D., Shiflet, G.J., 1997. Three-dimensional reconstruction of Widmanstatten Plates in Fe–12.3Mn–0.8C. J. Microsc. 188 (1), 36–41.

Ortega, A., Dalhoum, A.A., Alfonseca, M., 2003. Grammatical evolution to design fractal curves with a given dimension. IBM J. Res. Dev. 47 (4), 483–493.

Panozzo, H.R., 1992. The autocorrelation function: an image-processing tool for fabric analysis. Tectonophysics 212, 351–370.

Rao, C., Pan, T., Tutumluer, E., 2003. Determination of coarse aggregate surface texture using image analysis. In: Proceedings Pavement Mechanics

Symposium at the 16th ASCE Engineering Mechanics Conference. University of Washington, Seattle.

Rasband, W.S., 1997–2006. ImageJ. National Institutes of Health, Bethesda, Maryland, USA, http://rsb.info.nih.gov/ij.

Russ, J.C., 1999. The Image Processing Handbook, third ed. CRC Press, Boca Raton, FL, ISBN: 3-540-64747-3.

Samet, H., 1990. Applications of Spatial Data Structures. Addison Wesley, Readings, MA.

Stachowiak, G.W., 1998. Numerical characterization of wear particles morphology and angularity of particles and surfaces. Tribology Int. 31, 139–157.

TS 6956, 2004. Geometrical product specification (GPS)–surface texture: profile method-terms, definitions and surface texture parameters. Turk. Standard 1–22 (in Turkish).

Wohletz, K.H., 1983. Mechanisms of hydrovolcanic pyroclast formation: size, scanning electron microscopy, and experimental studies. In: Sheridan, M.F., Barberi, F. (Eds.), Explosive Volcanism. J. Volcanology Geother. Res. 17, 31–63.

Wohletz, K.H., 1986. Explosive magma–water interactions: thermodynamics, explosion mechanisms, and field studies. Bull. Volcanology 48, 245–264.

Wohletz, K.H., Brown, W., 1995. Particulate size distributions and sequential fragmentation/transport theory. In: Theofanous, T.G., et al. (Eds.), Proceedings of US (NSF) Japan (JSPS) Joint Seminar, Santa Barbara, CA.

Wohletz, K.H., Sheridan, M.F., 1983. Hydrovolcanic explosions II. Evolution of basaltic tuff rings and tuff cones. Am. J. Sci. 283, 385–413.

Yoshigi, M., Clark, E.B., Yost, H.J., 2003. Quantification of stretch-induced cytoskeletal remodeling in vascular endothelial cells by image processing. Cytometry, Part A 55A, 109–118.

Zimanowski, B., Büttner, R., Lorenz, V., Häfele, H.G., 1997. Fragmentation of basaltic melt in the course of explosive volcanism. J. Geophys. Res. 102, 803–814.

Zimanowski, B., Wohletz, K., Dellino, P., Büttner, R., 2003. The volcanic ash problem. J. Volcanology Geother. Res. 122, 1–5.

5.2. Stereoscopy

In the low-scale region (typically fields smaller than ~ 100 μm and elevations below ~ 10 μm), atomic force microscopy (AFM) is a very appropriate technique. In the high-scale region (field size from ~ 100 μm to ~ 1 cm) laser confocal microscopy is widely used. In a wide intermediate range, i.e. for fields from ~ 10 μm to ~ 1 mm (corersponding to magnifications from ~ 10000 to ~ 100), stereo imaging by scanning electron microscopy (SEM) could be very powerful, provided that a sufficiently fast and robust procedure of 3D surface reconstruction could be available (Pouchou et al., 2002).

3D reconstruction from stereosopic images (acquired at varying specimen tilt angles) is based on the measurement of the disparity, which is the shift (in pixels) of the specimen features from one image to the other (Pouchou et al., 2002). There is a long list of experiments performed with the aim of realizing stereo-vision by electron microscopy (Huang et al., 2004 and references therein). An advantage of this method is that it only requires access to a standard SEM, which can be found on almost every university campus, an appropriate software package, and a desktop computer. In practice, the SEM must possess a high-quality stage so that the specimen can be rotated accurately and eucentrically (i.e., the midpoint of the specimen surface being imaged must be positioned so that it is centered on the axis of rotation); it should also be able to output digital image files (Hagen and Walker, 1994 and references therein). The resolution of this model is the same as the resolution of the SEM images. However, Castle and Zhdan (1997) show the practical difficulty of obtaining good contrast from low-level surface topography, even before the necessary stereo pairs can be obtained.

The parallax method for elevation measurement from stereo pairs is well known and accepted. The method consists of imaging the same object from two viewpoints at the same plane, so the parallax, or the object point displacement along an axis parallel to the straight line through these viewpoints contained on the viewer's plane is proportional to the distance between the selected point and the viewer's plane, i.e. the local elevation is proportional to the local parallax.

In a scanning electron microscope (SEM), the object, rather than the viewpoint, is tilted to image the stereo projections. In this case, the specimen holder stage is the most important SEM component for defining the elevation map accuracy. If the specimen can be freely tilted along a eucentric trajectory, it will be possible to get a reconstruction plane normal to the electron beam axis by tilting the stage at opposite angles as shown in Figure 39A. For this condition, the elevation, z, will be related to parallax (x_{left} - x_{right}), magnification (M), and to the overall tilting difference ($\Delta\theta$) by the expression (Hein, 2001):

$$z = \frac{x_{left} - x_{right}}{2M \sin\left(\frac{\Delta\theta}{2}\right)} \qquad (13)$$

The other possible configuration is shown in Figure 39B, when the specimen holder can only be tilted on both positive angles, producing an elevation map with an inclination relative to the normal to beam axis. It implies distortion in parallax measurements, which can be corrected by (Boyde, 1973):

$$z_{0^\circ} = \frac{x_{left} \cos\Delta\theta - x_{right}}{M \sin\Delta\theta} \qquad (14)$$

Another way is to correct the distortion by taking the position on right, or high angle, projection, resulting in the equation:

$$z_{0^\circ} = \frac{x_{left} - x_{right}\cos\Delta\theta}{M\tan\Delta\theta} \tag{15}$$

In the context of the stereoscopy section of this thesis, a scanning electron microscope (Zeiss EVO50) was used in Hacettepe University, Ankara, Turkey. The holder stage of the SEM instrument can only be tilted on positive angles, thus the elevation calculation concerns Equations 14 and 15. ImageJ plugin named *StereoJ* which is an ongoing software was used for creating anaglyph and height maps from stereo pairs. Although the software performs anaglyph side, it still needs to be developed in height map construction. Nevermore, an essay for 3D construction was presented (Fig. 40). The corresponding anaglyph is presented in Figure 41. Anaglyph samples of different ash particles are given in Figure 42.

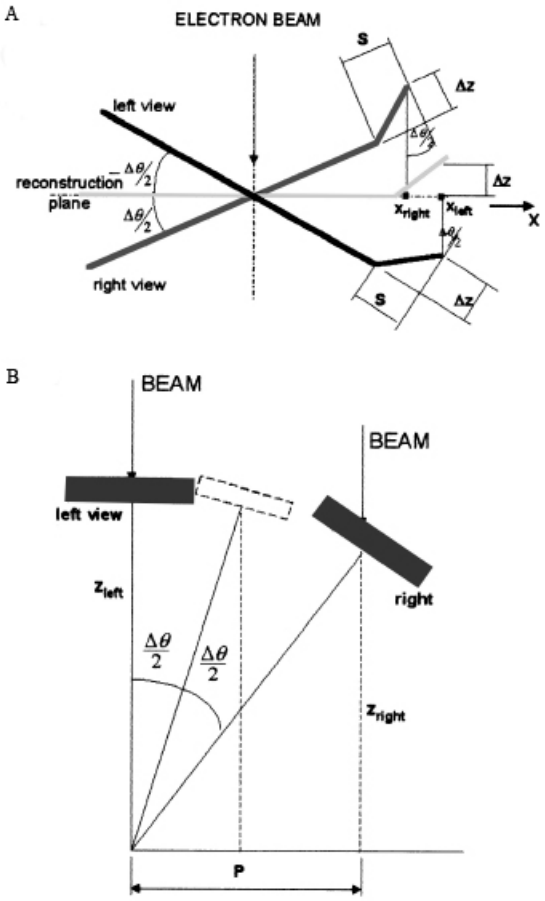

Figure 39: Configurations for stereo pair imaging in a SEM: (A) Reconstruction plane at 90˚ from electron beam; (B) tilted reconstruction plane. Left view position of specimen holder stage corresponds to the lower or negative tilting angle. Right view is related to the higher or positive tilting angle (from Hein, 2001).

5.3. Controlled serial grinding for three-dimensional reconstruction of volcanic ash surface

5.3.1. Preface

Despite reported disadvantages of serial grinding and polishing such as its being destructive, labour-intensive and difficulty in producing cross-sections of constant thickness, previous studies on paper surfaces claimed that its combination with SEM imaging offers a unique way of acquiring images from microstructures (Chinga et al., 2004). Serial depth images may be recorded in the SEM by cutting away a thin layer of the specimen, recording an image, and then cutting away another layer. Chinga et al. (2004) reported an improved preparation procedure for acquiring SEM images for high-resolution 3D reconstruction. They acquired images consecutively after serial grinding and polishing and ingeniously used monodisperse polymer particles (Ugelstad beads) as landmarks for registration purposes and for determining the thickness of the abraded section. In the context of this thesis, poly HEMA-EGDMA (2-hydroxyethyl methacrylate-ethylene glycol dimethacrylate) beads (<63 µm) were used for the same purpose and the largest cross-sectional local diameters of beads were accepted as the real bead radius. The smallest beads which were completely sectioned were used for thickness estimation while larger beads were participated in registration process together with small ones. The grinding, polishing and image acquisition processes were repeated for 27 times. The thickness of the removed layers was approximately 2.2-2.8 µm. Filtering, registration and volume rendering was performed in a public domain program; Image J. Examples of 3D reconstructed volcanic ash surfaces are presented.

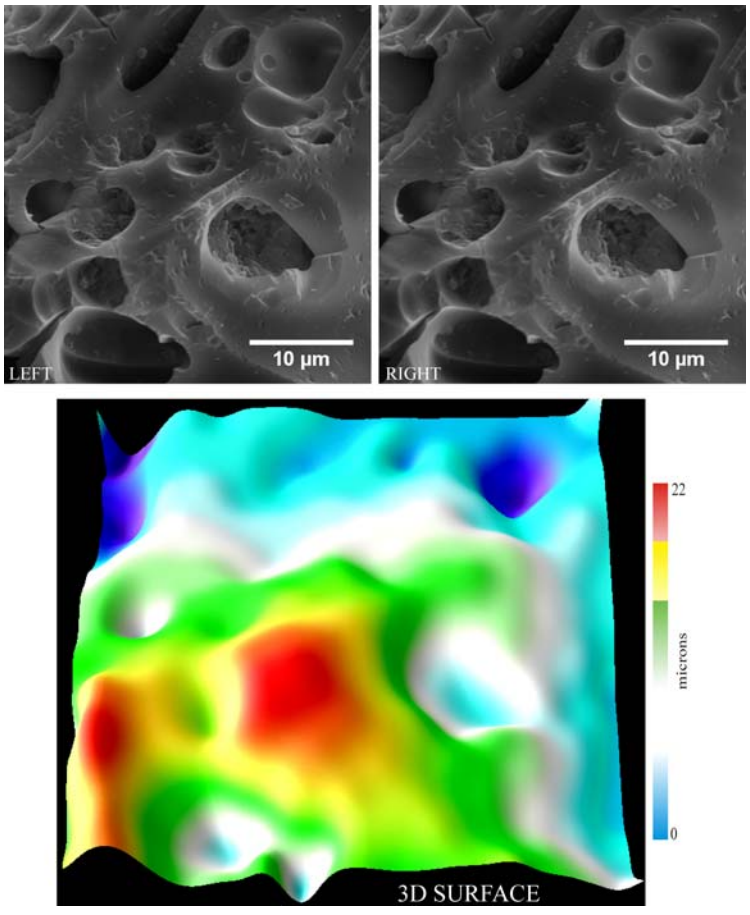

Figure 40: Left and right images used as stereo pairs and the corresponding reconstructed 3D surface of volcanic ash. The 3-D surface was tilted for a better representation of 3-D features.

5.3.2. Materials and methods

Volcanic ash particles in 250-500 μm grain size were cleaned in acetone using ultrasound for not more than 4 minutes to preserve grain edges (Heiken and Wohletz, 1985) and dried in drying oven at 110 ˚C overnight. Dried particles were sprinkled on a double sided carbon adhesive disk placed on a cylindrical aluminum stub. The poly HEMA-EGDMA beads were added into the epoxy resin. The mixture was warmed up to 50 ˚C and mixed until the mixture has very closely spaced beads. The amount of beads to be added was determined by straight eye but advisedly that the acquisition area (approximately 1,5 mm^2) for one particle needs to involve not a few beads for accurate registration and thickness estimation. The aluminum stub and samples were placed in a mold and embedded in mixture involving epoxy resin and beads. Samples were allowed to cure for 24 hours. Cured blocks were ground by hand, using 320-grid abrasive paper with water as a lubricant, removing block surface until approximating ash particles embedded in mixture. A LaboPol-5 and LaboForce-3 (Struers A/S) were used for grinding and polishing using abrasive disc (MD-Largo) and cloth (MD-Dur, Struers A/S) with 9- and 3-μm diamond particles (DP-Suspension M, Struers A/S), respectively at Hacettepe University (Turkey). DP-Lubricant Green (Struers A/S) was used as lubricant. Force and speed were 15 N and 150 r.p.m., respectively. The blocks were washed with distilled water between the grinding and polishing processes. Before each acquisition, they were cleaned in distilled water using ultrasound for 5 minutes and air-dried by a portable dry air compressor system.

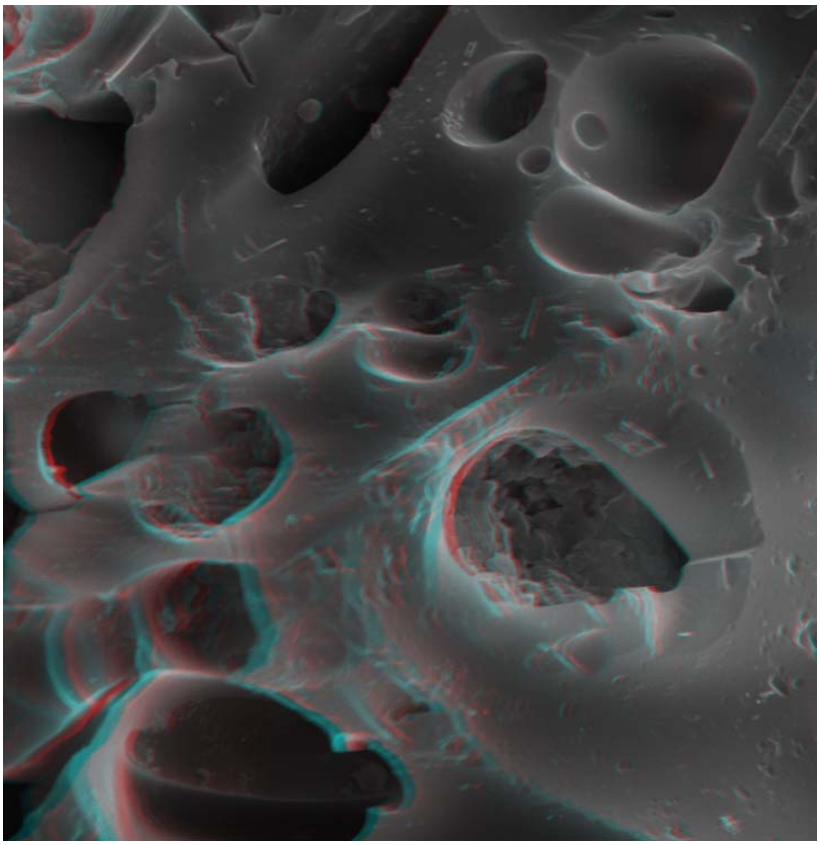

Figure 41: Corresponding anaglyph of surface in Figure 39. Red/green stereo glasses should be used for best visualization.

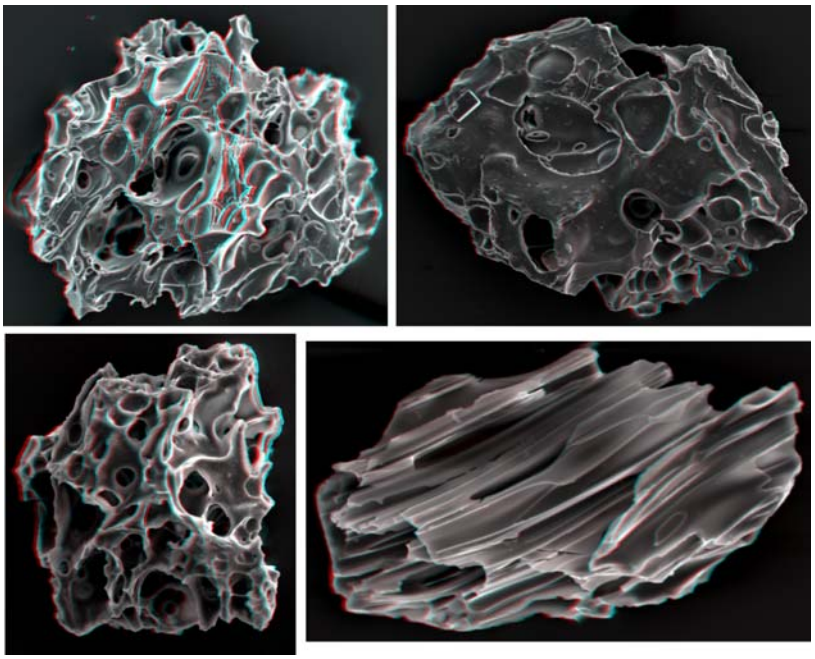

Figure 42: Anaglyph samples of volcanic ash particles. Red/green stereo glasses should be used for best visualization.

The images of volcanic ash particles were acquired consecutively after serial grinding and polishing by a Zeiss EVO50 XVP SEM equipped with silicon drift detector (SDD) operating at BSE mode and 15 KeV at Hacettepe University (Turkey). SEM was used in low vacuum mode (100 Pa) to avoid coating samples with carbon, thus reducing the time required for preparation and image acquisition. Working distance of 11.5 mm and 250x magnification was used. The size of the digital images was 1024x768 pixels using 256 grey levels. The corresponding resolution was 0.7 µm pixel^{-1}. The grinding, polishing and acquisition procedures were repeated for 27 times.
Stacks consisting of acquired images for one particle were created using ImageJ program (Rasband, 2004). We applied median filter on images which is a simple and very effective noise removal filtering process to enhance object-background contrast. The images in stack were aligned (registered) using *StackReg* plugin (Thévenaz et al., 1998) (available at http://bigwww.epfl.ch/thevenaz/stackreg/). The beads were used as landmarks for registration. The local diameters of beads were determined by fitting a bounding rectangle to the local bead cross-section. The thickness of the removed layer was thus calculated according to Eq. 16 (see Fig. 43):

$$d_i = \sqrt{(r^2 - r_i^2)}\,, \tag{16}$$

where r is the bead radius, r_i is the radius of the local cross-section and d_i is the estimated distance between consecutive cross-sections. The bead radius was estimated as the largest cross-sectional local diameter for a completely sectioned bead. Estimation of the bead sizes necessary for suitable thickness quantification at the corresponding spatial resolution and uncertainties were discussed in Chinga et al. (2004). Volume rendering was performed by the *VolumeJ* plugin (Abrámoff and Viergever, 2002). Raytrace rendering algoritm was used with a trilinear interpolation.

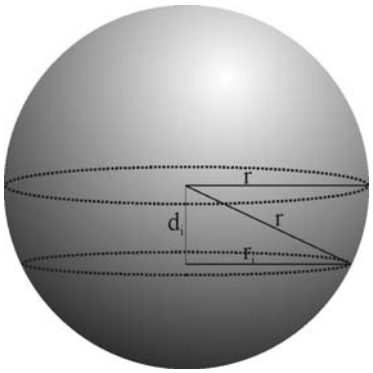

Figure 43: Estimation of the distance between cross-sections (d_i).

5.3.3. Results

The data set for the 3D reconstruction contains images with varying intermediate thicknesses. The procedure described for grinding and polishing removes approximately 2.6 µm for each grinding cycle (95% confidence interval 2.6 ± 0.13 µm). A thickness of approximately 70 µm was calculated for the reconstructed volcanic ash surfaces. The plugin *VolumeJ* has an option for creating two images for left and right eye (stereo pairs). These stereo pairs were combined to give stereo images of the reconstructed surfaces (Fig. 44).
The procedure permits the acquisition of several images for every grinding and polishing step. This is a major improvement compared with microtoming. The backscatter electron imaging allowed discernment of volcanic ash from epoxy. The method seems to be applicable for obtaining datasets for high-resolution 3D reconstruction.

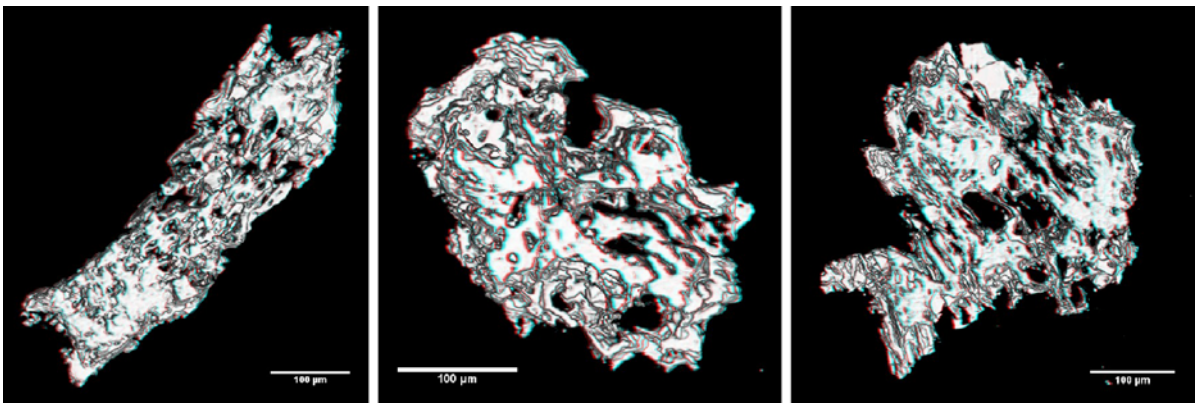

Figure 44: Three-dimensional reconstructions of volcanic ash particles (stereo images). Red/green stereo glasses should be used for best visualization.

6. Discussion

6.1. Preface

Simple and well-defined surface descriptors were presented in this study. These descriptors were calculated on many ash particle surfaces from different volcanoes. Despite the handicap of using two-dimensional SEM micrographs, the shadow relief effect used for estimation of real topographical representations allowed measurement of surface textures. In section 5.1., the method was applied on reconstructed 3D surfaces and consequent sections involved different three-dimensional reconstruction methods. However, as indicated in previous sections, two-dimensional applications which cover the substantial portion of this study have advantages along with obvious disadvantages such as the susceptibility of gray value variations to conditions before and during the acquisition of images. In this section, micrographs of five sample groups from different volcanoes were acquired with the possible identical settings in order to eliminate the defects which take root from different acquiring conditions of SEM (due to different settings of instrument, different vacuum and filament conditions and condition of sample during the coating process). Here, the optimum acquiring conditions were tried to be achieved for calculation of surface descriptors by carrying out some methods. This also gave the opportunity to plot each ash particle from different eruptions on one diagram (abacus) according to their surface textures assessed by quantitative surface descriptors. The advantages and disadvantages of methods were discussed by collating the applications in the previous sections.

6.2. Application of quantitative surface descriptors on images acquired with the possible identical settings

Qualitatively clustered surfaces and water/magma mass ratios (R) were used for measuring the quantification capability of calculated surface descriptors for classifying volcanic ash surfaces formed during different fragmentation mechanisms and eruption environments. Surface textures of volcanic ash particles were described on 439 SEM micrographs using qualitative descriptors. They were labeled with numerical values corresponding to the degree of observed textures. According to labels of textures, all particles were subjected to K-means clustering and three different ash types were distinguished. Samples from five volcanoes with different eruption styles were selected for analysis (Table 6). The eruption styles are known from earlier studies and published data on related volcanoes (Gourgaud et al., 2000; Geshi et al., 2002; Şen et al., 2002; Aydar et al., 2003; Nakada et al., 2005; Ersoy et al., 2006; Lohmar et al., 2007) or field observations. Seven roughness descriptors (Rq, Ra, Rsk, Rku, Rv, Rp, Rt), three quadtree parameters (nQT, mQT, sQT) and fractal dimensions (FDs) were calculated on ash surfaces. A gradient analysis based on Sobel operators was performed and polar plots were generated based on frequency of gradients. Different shape descriptors such as form factor, compactness, roundness, aspect ratio, solidity, convexity and the fractal dimensions (FD_PP) were calculated on polar plots. In order to better characterize the samples with respect to their size-distribution, and highlight possible changes in the fragmentation processes occurred during eruptions, the SFT (Sequential Fragmentation/Transport) theory (Wohletz et al., 1989) has been applied to Mt Nemrut stratovolcano (Eastern Turkey) tephra, beside tephra from Mt Erciyes stratovolcano (Central Anatolia, Turkey). In order to understand the effect of adhering dust on surface descriptors and to distinguish primary and alteration morphologies, some portions of samples from Mount Nemrut were washed in ultrasonic cleaner before analysis while the other portions were analyzed after steeping in acetone not more than 5 minutes. Effects of filters applied in

pre-processing step were discussed on unfiltered and different filtered images. The quantitative surface descriptors having abilities to classify different type surfaces were determined by analysis of variance (ANOVA) and used as distinguishing parameters in principal component and classification analysis.

Table 6 Samples used for analysis

Sample ID	Eruption	Composition	Estimated fragmentation type	Nature
GaV5b	Galunggung 1982-83 (Indonesia) Gourgaud et al., 2000	Basaltic andesite	Phreatomagmatic	Flow
Gav6a		Basaltic andesite	Phreatomagmatic	Flow
July14And	Miyajejima 2000 (Japan) Geshi et al., 2002 Nakada et al., 2005	Basaltic andesite	Phreatomagmatic	Fall
Aug18EP		Basaltic	Vulcanian/Subplinian	Fall
Aug18LS		Basaltic	Vulcanian/Subplinian	Fall
VR05-01	Villarica 13,800 BP (Chile) Lohmar et al., 2007	Basaltic andesite	Phreatomagmatic	Flow
VR05-03		Basaltic andesite	Magmatic	Flow
Dik-1	Erciyes-Dikkartın Dağı (Turkey) 0.14 ± 0.02 to 0.11 ± 0.03 Ma Şen et al., 2002	Rhyodacite	Magmatic	Fall
Dik0		Rhyodacite	Phreatomagmatic?	Flow
Dik4		Rhyodacite	Phreatomagmatic	Surge
N25-10	Nemrut (Turkey) 0.02 ± 0.01 Ma to <10 ka Aydar et al., 2003 Ersoy et al., 2006	Rhyolite	Magmatic	Fall
N25-13		Rhyolite	Phreatoplinian	Fall
N25-18		Rhyolite	Phreatomagmatic	Surge

Different magma compositions, eruption styles and bed forms make samples adequate for classification of ash surfaces from different fragmentation mechanisms. Although a portion of samples were used in previous applications and the eruption styles were explained in the corresponding sections, here in order to prevent the confusion and to preserve the flow in the text they were defined shortly. Because, for instance, in section 4.3 related to Galunggung eruption, the eruption dates were used to label samples but here original sample labels were used.

During the 1982-83 eruption of Galunggung volcano in western Java (Indonesia), the explosivity increased considerably with concomitant jet plane incidents. This drastic change in the style of the eruption is explained by an increase in the efficiency of groundwater-magma interaction (Gourgaud et al., 2000). Observers from the Volcanological Survey of Indonesia (Katili and Sudradjat, 1984) recognized three distinct phases with three different eruptive styles: an initial Vulcanian phase, a phreatomagmatic phase, and a Strombolian phase (Fig. 45A). Gourgaud et al. (1989, 2000) emphasized the increase in explosivity (expressed as volcanic explosivity index; Newhall and Self, 1982) from the Vulcanian phase to the phreatomagmatic phase, including higher plume height, larger volume of deposits, and great changes in crater morphology. From phreatomagmatic phase of 1982-83 eruption of

Galunggung volcano, we used two pyroclastic flow samples Ga5b and Ga6a which are basaltic andesite in composition (Fig. 45A). Sample Ga5b corresponds to May 17-19 dated eruption when first maar crater was opened. Sample Ga6a is related to July 28 dated large eruption. This eruption continued until August 1 and a new vent was observed inside the previous one. Pyroclastic flow corresponding to sample Ga5b is composed of yellowish scoriaceous lapilli, yellow and red, oxidized and angular, unvesicular lapilli and crystals (plagioclase, pyroxene). Some juvenile lapilli show a typical caulifower shape. Xenolith content in the size class 2.8-4 mm is 35% wt in sample Ga5b. Sample Ga6a is related to a block-and-ash and scoria-rich pyroclastic-flow deposit where scoriaceous lapilli are dominant and black in color. The xenolith content is 27% wt. for sample Ga6a.

Three fall samples (July14And, Aug18EP and Aug18LS) from 2000 eruption of Miyakejima volcano (Japan) were investigated (Fig. 45B). The eruption started as a small subaqueous eruption occurred in the sea on the western flank in late June 2000, and was followed by summit phreatic and phreatomagmatic explosions in July and August, during which a caldera formed at the summit (Geshi et al., 2002; Nakada et al., 2005). The 2000 activity of Miyakejima is divided into four stages based on surface phenomena; magma intrusion, summit subsidence, explosion, and degassing stages (Nakada et al., 2005). Sample July14And corresponds to the summit subsidence stage of the activity (Fig. 45B). In July 14, phreatomagmatic explosions occurred and a cauliflower-shaped eruption column rose up to 2,600-3,100 m a.s.l.. Eruption products consisted of gray-colored fine ash derived from old volcanic rocks and a small amount of juvenile material. The other two samples (Aug18EP and Aug18LS) are related to explosion stage of the activity. The largest explosion occurred in 18 August and an eruption column ascended to about 16 km a.s.l. Samples Aug18EP and Aug18LS correspond to the early phase and later stage of the 18 August event, respectively, which was defined as vulcanian to subplinian in type by Nakada et al. (2005). Sample July14And is basaltic andesite in composition, less vesiculated and crystallized than the basaltic samples of eruptions in August (Aug18EP and Aug18LS).

Samples VR05-01 and VR05-03 correspond to the top and bottom of a massive ash and scoria flow deposit from major explosive eruption of Villarica stratovolcano (Southern Chile) about 13,800 BP, respectively (Lohmar et al., 2007) (Fig. 45C). The deposits of this eruption mainly consist of massive pyroclastic flows, stratified pyroclastic surges and known as the “Licán ignimbrite”. Sample VR05-01 is rich in xenoliths (59,2% wt.) and holds the distinction of having more signs of phreatomagmatism such as less vesicularity and finer grain-size relative to sample VR05-03 (xenolith content 22% wt.) (Lohmar et al., 2007). Two samples are basaltic andesite in composition.

Samples from Mt Erciyes is relating to Dikkartın Dağı which is one of the three rhyodacitic domes on flanks of the volcano. Dikkartın emplaced after pyroclastic sequences characterized by an alternation of layers related to contrasting fragmentation and transportation dynamics (Şen et al., 2002). The eruption begins as purely magmatic and continues as phreatomagmatic with interlayered phretoplinian fall and surge deposits related to the amount of water interacted with vesiculating magma (Fig. 46A). The phreatomagmatism forms an explosion crater and a tuff ring. The eruptive style changes from explosive to effusive, thus a rhyodacitic dome emplaces and it buries the previous explosion crater. Samples Dik1, Dik2 and Dik6 correspond to plinian fall, pyroclastic flow and surge deposits, respectively. According to distributions, bed-forms and eruptive styles, four eruptive phases were suggested for Dikkartın Dağı. Samples Dik1 and Dik2 are related to phase 1 while Dik6 to phase 2. Phase 1 deposits are more widespread and exposed 15 km from source. The wider distribution, magmatic character and coarse particles of sample D1 in phase 1 deposits indicate the higher eruption column in the beginning of the eruption. Applying the method of Carey and Sparks (1986); the climactic eruption column was estimated 25 km high. Sample

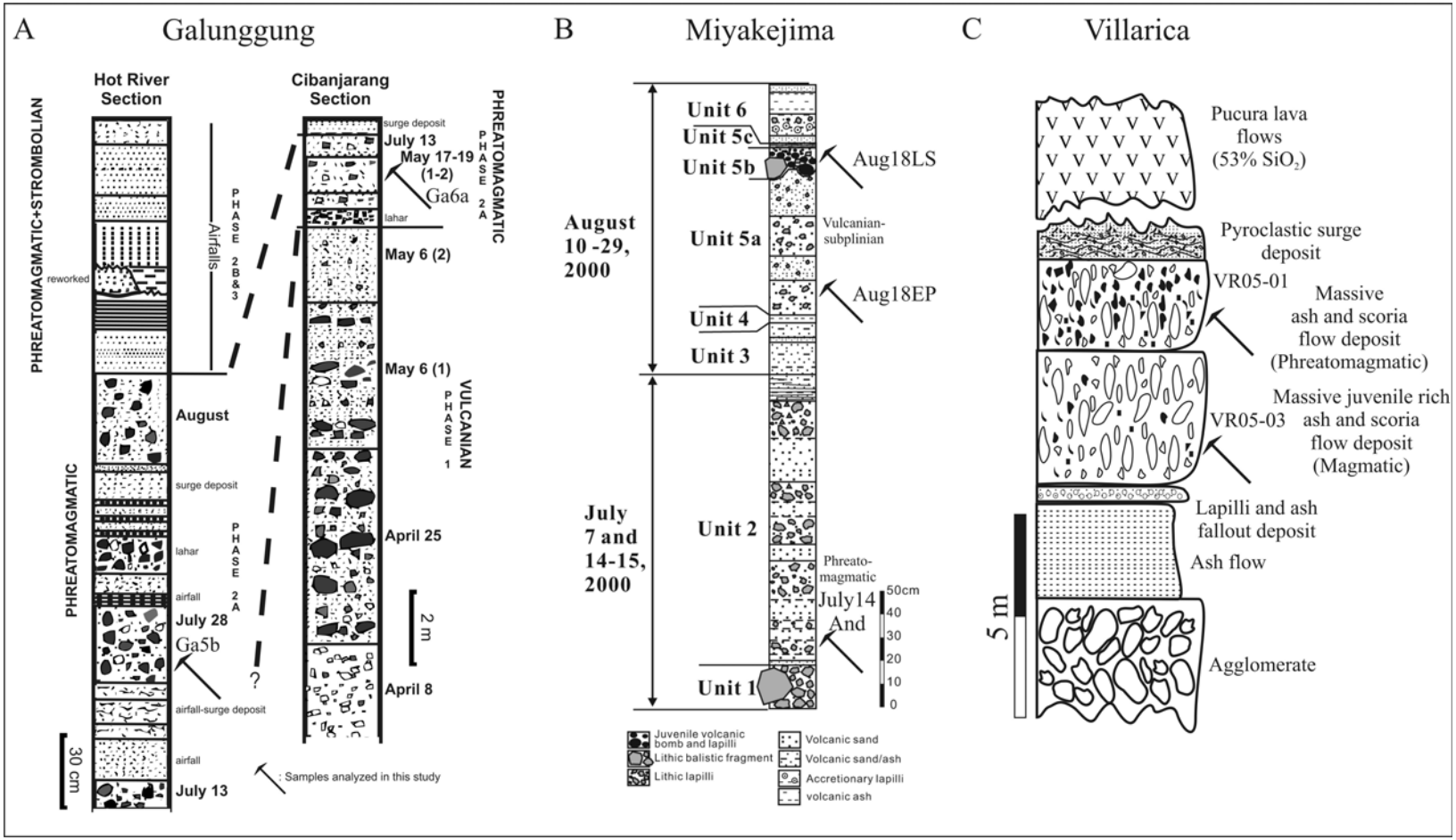

Figure 45: (A) Stratigraphic sections of the 1982 erupted deposits in Hot River area and Cibanjaran valley from Galunggung volcano (Indonesia) after Gourgaud et al. (2000). (B) Stratigraphic section of deposits related to 2000 eruption of Miyakejima volcano (Japan) after personal communication with Nobuo Geshi. (C) Deposits of eruption 13,800 B.P. concerning Villarica volcano after Lohmar et al. (2007). Layers labeled with pick symbol correspond to Licán ignimbrite and analyzed samples in this study.

D2 corresponds to the pyroclastic flow overlying D1 plinian deposits and harbors clues about water interaction which probably caused partial collapse of the plinian column in lower parts and generated the concerning pyroclastic flow deposits. While the plinian deposit (D1) is in purely magmatic character, D2 show signs of phreatomagmatism in its grain-size analysis and particle morphologies. Phase 2 is related to the opening of an explosion crater where sample Dik6 is a massive surge deposit exhibiting bomb sags and defined as purely phreatomagmatic. Mt Nemrut exhibits a summit caldera having a surface area of of 8.5 km x 7 km. The eastern half of the caldera is filled by pyroclastic deposits related to maar-like explosion craters, lava domes and flows. The western half is filled by a freshwater lake covering a surface area of 5.3 km x 3 km and a small lake with hot springs. The fumaroles activity is also present over a dome situated at the northern part of the caldera (Aydar et al., 2003). On the post-caldera stage of the volcano, related to the alternating mass ratio of interacting water and magma, sub-plinian dispersal of pumice and air falls, base surge deposits with dune and anti-dune structures, cross-beddings, bread-crust bombs are observed (Ersoy et al., 2006). Samples N25-10, N25-13 and N25-18 from Mt. Nemrut correspond to plinian fall, phreatoplinian fall and surge deposits of post-caldera eruption in Nemrut, respectively (Fig. 46B). The grain size analysis and field observations indicate fluctuating amount of water contained in the eruption environment. The composition is rhyolite for all samples.

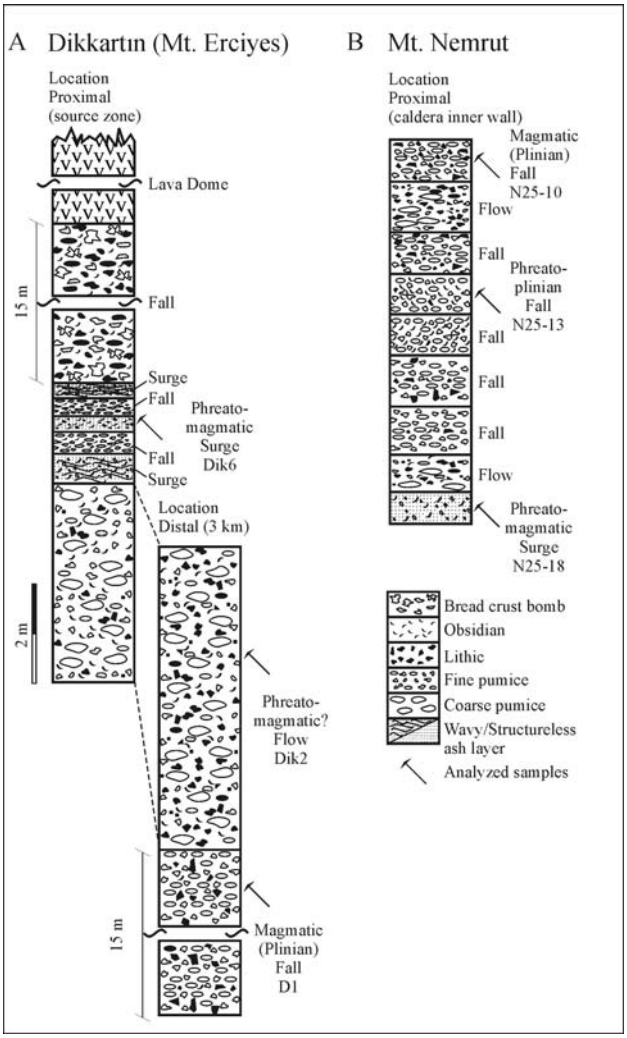

Figure 46: Stratigraphic sections of deposits from (A) Dikkartın Dağı and (B) Nemrut volcano. The samples analyzed in this study are labeled with a pick symbol.

SFT (Sequential Fragmentation/Transport) theory (Wohletz et al., 1989) has been applied on Mt. Nemrut samples. The data mentioned in section 4.4. was used here again for Dikkartın tephra. Fraction vs subpopulation mode (φ_m) defined two groupings of subpopulations: coarser modes can be separated from those of fine subpopulations (Fig. 47A). These groupings are assigned to magmatic and phreatomagmatic origins (Wohletz et al., 1995). The estimated R values for samples of Mt Nemrut and Mt Erciyes are given in Figure 47B (please see section 4.4. for detailed information for R calculation). The nature of deposits and fragmentation types were also plotted on samples. These data support field interpretations of samples. The plinian fall (D1 and N25-10) deposits are purely magmatic. The phreatoplinian fall (N25-13), pyroclastic flow (D2) and surge (N25-18) samples show an increment in water content during their eruption while the surge sample (D6) has a pure phreatomagmatic character.

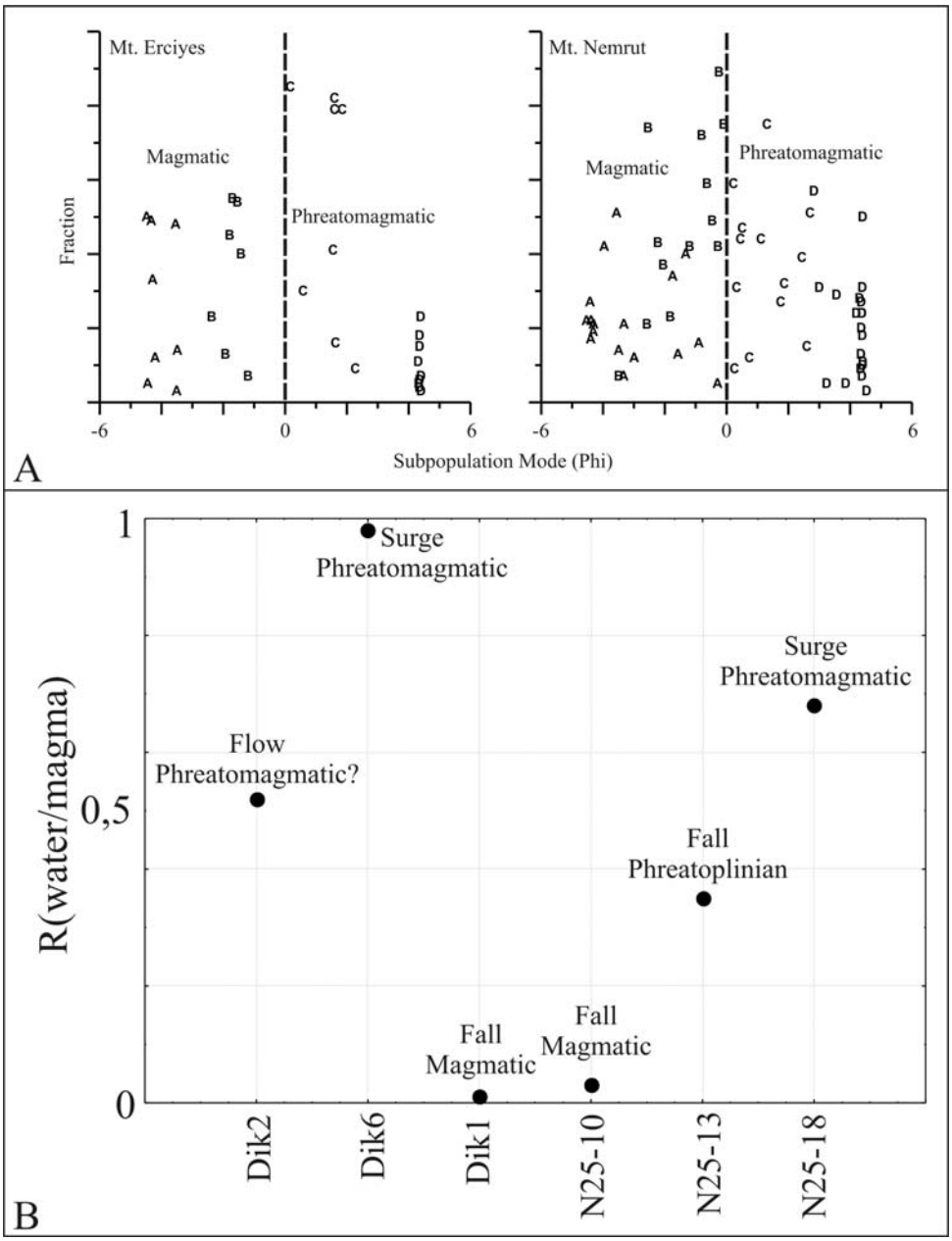

Figure 47: (A) Two groupings of subpopulations discriminated by SFT in Mt. Erciyes and Mt. Nemrut tephra. (B) Calculated water/magma mass ratio for Mt. Erciyes and Mt. Nemrut tephra.

SEM micrographs including volcanic ash particle surfaces from five different eruptions were examined one by one and labeled according to five features (roughness, alteration, vesicularity, vesicle shape and development of vesicles). The features were labeled as indicated in Table 7. The roughness label was determined from the general view of the surface. Completely irregular surfaces due to cavities or aggregates were labeled as “rough” while non-vesicular, regular surfaces as smooth. The alteration was designated according to intensity of alteration or abundance of adhering dust on surfaces. The lower values correspond to clean surfaces while higher values define altered ones. The lower vesicularity or lack of vesicles was expressed by lower label values while the degree of vesicularity increases with increasing values. Three main observed vesicle shapes were labeled with numbers (see Table 7). The development of vesicles represents the depth of cavities while deep cavities having value of “1” and poorly developed vesicles “2”. The numeric data was subjected to K-means clustering. Three clusters were generated according to different levels of features on surfaces. Roughly, “Cluster 1” includes the highly altered non-vesicular pyroclasts, “Cluster 3” cover the highly vesicular lesser altered pyroclasts. “Cluster 2” has the transition types between “Cluster 1” and “Cluster 2”. “Cluster 1” was read as phreatomagmatic, “Cluster 3” as magmatic and “Cluster 2” as the transition fragmentation mechanism between two end-members, possibly phreatoplinian. Statistical analysis used commercial software Statistica (StatSoft, Inc, v6).

Table 7 Qualitative descriptions and corresponding labels for surfaces

Label	Roughness	Alteration	Vesicularity	Shape of vesicles	Development of vesicles
1	Smooth	Unaltered	Nonvesicular	Irregular	Developed (deep vesicles)
2	Smooth/Rough	Low	Low	Tubular	Poorly developed
3	Rough	Moderate	Moderate	Spherical/Ovoidal	-
4	-	High	High	-	-

Seven roughness parameters, three quadtree decomposition parameters and fractal dimensions were calculated on volcanic ash surfaces. Seven shape descriptors and fractal dimensions were calculated on polar plots generated from gradient analysis. Qualitative descriptions were quantified by labeling and clustered in three distinct groups representing different fragmentation mechanisms: (1) phreatomagmatic, (2) phreatoplinian and (3) magmatic. The calculated water/magma mass ratios (R) support the laboratory and field observations on samples (Fig. 47B). They also verify the accuracy of clusters of volcanic ash surfaces according to their qualitative surface descriptions (Fig. 48A). The phreatomagmatic ash surfaces are abundant in products of eruptions having high water/magma mass ratios (R). The surfaces in second cluster (2) which are defined as phreatoplinian are characterized by eruption environments where equal amounts of magma and water interacted. The surfaces involving features in magmatic character seem to be formed in a dry environment where interaction with water did not occur.

Surface descriptors and clusters were subjected to analysis of variance (ANOVA) to measure the discrimination ability of quantitative surface descriptors on clusters. In ANOVA analysis, a variable is accepted when the variance between clusters (groups) is significantly larger than the variances within the groups. In many areas of research, the p-level of 0,05 is customarily treated as a "border-line acceptable" error level. For instance, p-level of 0,05 indicates that there is a 5% probability that the relation between the variables found in our sample is a "fluke". However, this level of significance still involves a pretty high probability of error (5%). Here, we used the p-level of 0,001 which is statistically called “highly” significant to

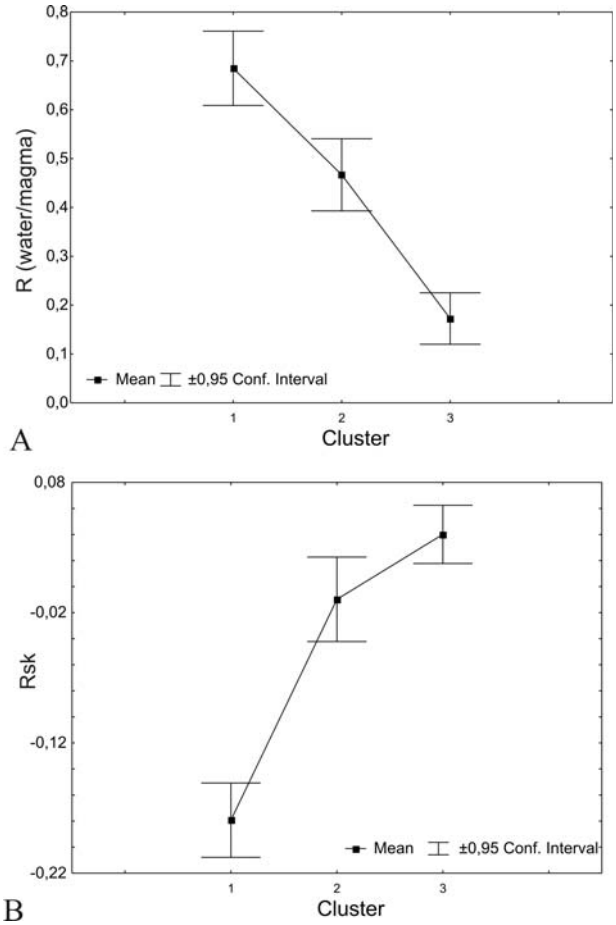

Figure 48: (A) Water/magma mass ratios (R) evidence the achievement of K-means clustering of volcanic ash surfaces. For instance, phreatomagmatic ash surfaces (cluster 1) produced in an environment involving abundant water. (B) Rsk as the leading parameter in discrimination of different type ash surfaces.

consider the optimum quantitative descriptors for classification of different ash surface features. Variable involving the cluster names was assigned as independent variable (categorical predictor) and results of variance analysis were given in Table 8. In order to facilitate to imagine, surface descriptors were grouped as roughness descriptors (Ra, Rq, Rsk, Rku, Rv, Rp, Rt), quadtree decomposition descriptors (nQT, mQT, sQT), fractal dimension of surfaces (FDs) and shape descriptors (form factor, roundness, compactness, aspect ratio, solidity, convexity and fractal dimension of polar plots). Rsk is the leading parameter for distinguishing surfaces with lower p value and higher F value (Table 8, Fig. 48B). Possible reasons for achievement or failure of descriptors will be discussed later. The descriptors having lowest p values (Rsk, mQT, FDs, solidity) from each descriptor group were subjected to principal component analysis in order to show discrimination ability of these variables on a binary plot (Fig. 49A). Two axes (components) explain the 95% of the variance. Apart from some overlapping exceptions, surface descriptors overcome the classification of surfaces from different fragmentation mechanisms. However, one eruption unit may involve different types of ash particles in different amounts. This kind of complexity is faced chiefly in deposits generated by eruptions where external water interacted with the magma. The magma-water interaction can occur at a variety of points along the vesiculation and degassing, thus fragmentation may generate a clast population with heterogeneous vesicularity values. For instance, although sample Dik6 was characterized as purely phreatomagmatic considering the

field observations and grain-size analysis, it involves a substantial amount of ash particles which were recognized as magmatic (17% cluster 3). Variety in ash type content yields wide ranges of quantitative surface descriptor values for each eruption unit (sample), notably for phreatomagmatic eruptions. On this account, in order to represent classification in eruption unit terms, we used the average values of factor coordinates for each eruption unit considering mean values represent the sample as a whole (Fig. 49B). The proportions of each ash surface type (clusters) in the samples were also plotted on the figure as pie diagrams.

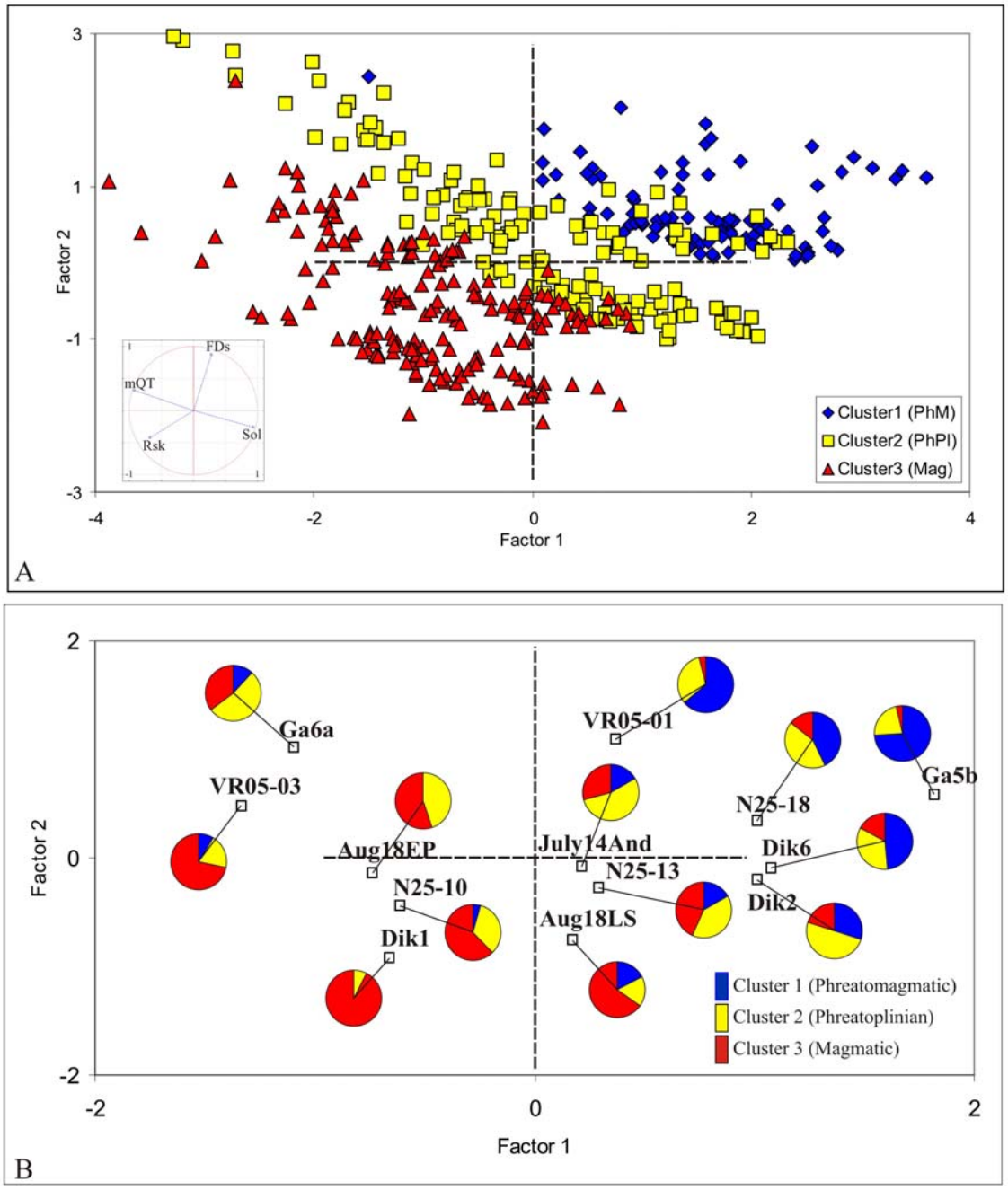

Figure 49: (A) Binary plot of ash surfaces produced by quantitative surface descriptors and principal component analysis. Inset figures the projection of the variables on the factor-plane. (B) Classification in eruption unit (sample) terms. The pie diagrams include proportions of different type surfaces in samples.

Table 8 Analysis of variance (ANOVA) results

	Roughness descriptors							Quadtree decomposition descriptors			Shape descriptors							Fractal Dimension
	Rq	Ra	Rsk†	Rku†	Rv	Rp	Rt	nQT†	mQT†	sQT	FDpp†	FF†	Round†	Compact†	AR†	Solidity†	Convexity	FDs†
F*	0,2	1,9	56,4	9,3	5,2	2,2	6,3	10,4	13,3	5,8	7,6	9,6	7,6	8,8	10,4	10,7	3,9	13,2
p	0,8	0,1	0,0	0,0	0,0	0,1	0,0	0,0	0,0	0,0	0,0	0,0	0,0	0,0	0,0	0,0	0,0	0,0

* Measurement of distance between individual distributions. As F goes up, p goes down (i.e., more confidence in there being a difference between two means)
† Descriptors having p-level well below 0,001

6.3. Methods applied to prevent artificial and technical defects and discussions by collating the applications in the previous sections

6.3.1. Filtering

Here, in order to achieve the optimum operating conditions and to prevent the defects, some methods were carried out. An important approach in surface characterization may be the detection of specific structure sizes affecting a given property (Chinga et al., 2007). Some filters were applied on images for revealing the structure size affecting roughness and surface properties and also for overcoming the artificial or technical defects. For instance, undesirable information defects of stripes arising from charging on surfaces were suppressed by bandpass filter (available at http://rsb.info.nih.gov/ij/plugins/fft-filter.html) which is an absorbing filter and allows a known range of wavelengths to pass, blocking those of lower or higher frequency. In other words, it filters out large structures (shading correction) and small structures (smoothing) of the specified size by gaussian filtering in fourier space.
The stochastic nature of electron microscopy means that the signal to noise ratio (SNR) for unprocessed high resolution secondary electron images is often very low. There are two primary forms of noise in a SEM: noise due to the statistical nature of electron collision and emission, and noise due to the SEM detector and signal processing electronics. Various forms of noise reduction can be used to increase this signal to noise ratio. Frame averaging is the most common type of noise reduction and most modern SEMs implement some form of hardware frame averaging. Pixel averaging (scan rate) is another solution for noise reduction. However, frame averaging or pixel averaging is time consuming and the operator normally desires to obtain maximum number of images within the shortest possible time. In addition to frame and pixel averaging, which are usually implemented in hardware, there is the potential for noise reduction pre-processing in software. This alternative has become more feasible with the drastic performance increases in general purpose microprocessors (Batten, 2000). Here, median filter was used which is a simple and very effective noise removal filtering process. Furthermore, it is a more robust method than the traditional linear filtering, because it preserves the sharp edges. It reduces noise in the active image by replacing each pixel with the median of the neighbouring pixel values. There is no doubt about the advantages of applied filters on obtaining quality information from micrographs. Nevermore filtering may also give rise to data loss in images and has an influence on analysis. Applying the same filters to stacks with same parameters, relative evaluation and interpretation of the results provides omitting the effect of filters over against their advantages. In order to see the effects of filtering on analysis, we calculated the same surface descriptors on unfiltered, median filtered and bandpass filtered images of Mt. Nemrut samples. Standard deviation of gray values (sGL-Rq) figures effects of filters on images (Fig. 50). Median filtering does not have a significant effect but bandpass cuts down and narrows the ranges of values. Beside its narrowing side, the suitability of bandpass filtering for assessing the surface structure size was confirmed in previous studies (Chinga et al., 2007). In the course of interpretation of results, the applied filters must be taken into account and the operator must be aware of the effects of filters on surface parameters. The selection of parameters for filters, particularly for bandpass filter is a demanding procedure due to its giving rise to misinterpretations.

6.3.2. Sample preparation

Sample preparation procedure also needs attention in order to avoid the defects before image acquisition. The adhering dust on surfaces or in vesicle hollows of volcanic ash particles is common especially in phreatomagmatic eruptions. However, these fine materials may grow

out from alteration of glass or fine-sized fraction of the eruption products. Small aggregates form a rough surface which is problematic in coating process of sample. Optimum result is obtained by removing this material from the surface because the sample should be as free from moisture and other contaminants as possible. Washing procedure above cited suffices for removing most of adhering particles from surfaces. However, in the case of persistence of analysis on this material for a variety of reasons, some coating techniques are needed to be considering in optimizing coating process. Using rotating stage with tilt facility will provide surfaces with complete exposure to coating. Here, the carbon-metal-carbon evaporation method was applied which provides an absolute conductive surface. Carbon-metal-carbon "sandwich" coatings prevent "island" formation on surfaces which result from high surface diffusion of sputtered gold or silver films. Moreover, even the samples are exposed to atmospheric conditions for several days; a second carbon film serves as a "preservative" for the sputtered metal film. If charging is still extant during acquisition, using SEM at a low accelerating voltage and beam current minimizes the problem.

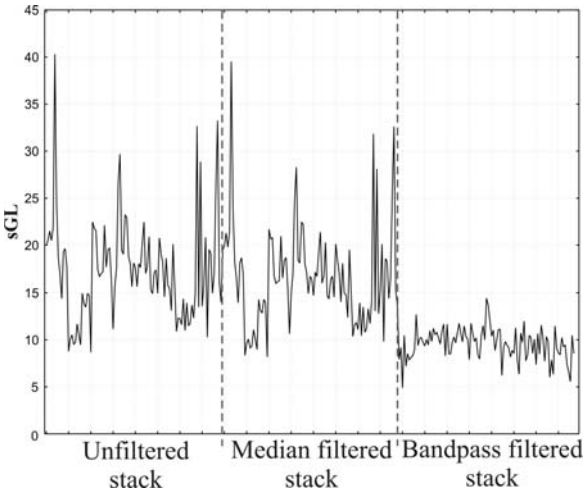

Figure 50: Effect of filtering on standard deviation of gray values (sGL).

6.3.3. Discussions on results obtained in section 6.2.

After achieving the optimum operating conditions, the topographic contrast arising from the angle between the beam and the specimen surface generates the gray value variation practicable for texture analysis. The alteration and vesicularity characteristics were used in labeling ash surfaces and qualitative classification. In previous studies, the sensitivity of R_q and R_a parameters on alteration and the harmony of R_{sk} values with vesicularity index of pyroclastic material were designated (Ersoy et al, 2007b). In this study, R_{sk} is the leading parameter for classification with highest F and lowest p values (Table 8, Fig. 48B). The values of R_{sk} and R_{ku} may give information about the surface features (see Figure 19 in section 2.3.). The tapered ends of vesicles on magmatic ash may be perceived as peaks on surfaces. Furthermore, the features on smooth, irregular surfaces indicating the actual physical mixing of particles with water during fragmentation or few vesicle surfaces showing curviplanar fractures caused negative R_{sk} values of phreatomagmatic tephra. R_{ku} is another descriptor widely used in manufacturing processes in industry similar to R_{sk} and we are also informed about its responses to features on machined surfaces (see Figure 19 in section 2.3.). R_{ku} values of magmatic and phreatoplinian tephra (>3) may indicate their rough, complicated surfaces (Fig. 51). The phreatomagmatic ash surfaces have a mean R_{ku} value of 3 through their smooth, irregular (random) surfaces. In order to understand the effect of adhering dust

and alteration products on surface descriptors, chiefly on R_q and R_a, some portions of samples from Mount Nemrut were washed in ultrasonic cleaner before analysis while the other portions were analyzed after steeping in acetone not more than 5 minutes. Although R_q and R_a seem satisfactory for designating alteration (Fig. 52A and B), plainly, the lack of their correlation with vesicularity and vesicle shapes makes them ordinary classifiers (Fig. 52C and D). The roughness of surfaces increases through alteration products on surfaces. R_a and R_q are suppose to be sensitive to micro-features such as adhering dust or alteration products on surfaces other than larger scale features such as vesicles. R_{sk} and R_{ku} are more descriptive on vesicularity and vesicle shapes. The alteration products covering surfaces roughen the surface in micro-scale however covering has a smoothing effect in larger scales by masking the tapered edges (Fig. 53). Washing procedure exposes the cavities and ragged sharp edges which give rise to higher R_{sk} and R_{ku} values.

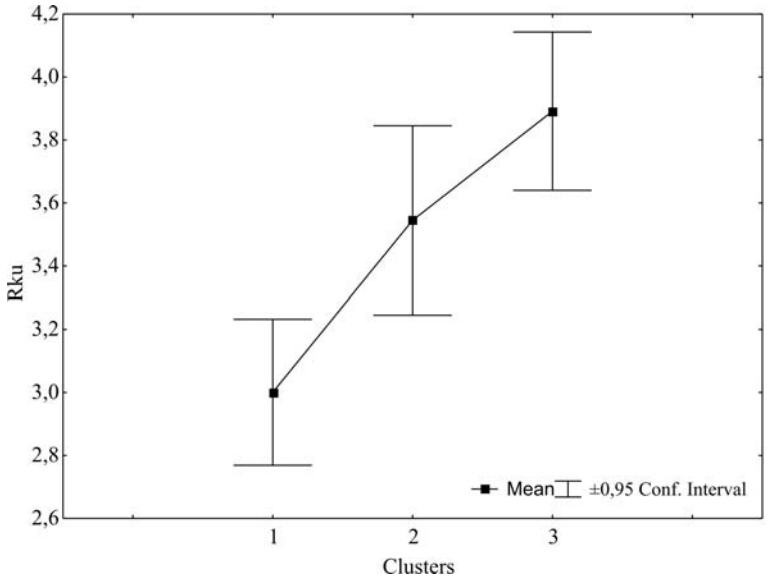

Figure 51: Rku in discrimination of different ash surfaces.

The author of this thesis was inspired by a study in paper research assessing surface structures of paper before and after calendering (Chinga, 2006) to apply the quadtree decomposition approach on volcanic ash surfaces. Heavy calendered paper surfaces have lesser nQT but higher mQT and sQT values. Chinga (2006) uses the same parameter (sGL or R_q) as threshold for quadtree decomposition approach and heavy calendered paper surfaces have lesser Rq (sGL) values indicating the smoothing effect of calendering. The quadtree decomposition parameters are sensitive to micro-features similarly to R_q and R_a. These descriptors together with R_q and R_a have the best performance in characterizing the micro-roughness by reason of adhering dust or alteration aggregates. Upon close examination on two micrographs (N25-10 # 06 and Dik2 # 54) having lowest and higher nQT values, respectively, we explicitly discovered the effects of small scale features on surface descriptors (Fig. 54). Sample N25-10 # 06 is relating to plinian fall deposit (water/magma mass ratio (R)=0,03) of Mt. Nemrut with abundant ovoidal poorly- or well-developed vesicles. The surface has few adhering juvenile fine particles rather than alteration aggregates. Sample Dik2 # 54 is relating to Dikkartın Dağı from Mt Erciyes and corresponds to pyroclastic flow deposit (water/magma mass ratio (R)=0,52). The surface is highly altered and all vesicle hollows are filled by alteration products. Fine material covers the entire surface and masks the vesicles. The qualitative descriptions used in clustering for these two surfaces were also given in Figure 54. Across line profiles of surfaces designate the texture difference between clean vesicular and altered

non-vesicular surfaces (Fig. 54). The fine alteration aggregates on surface constitutes a more irregular and complex profile because of their micro-scale irregularity.

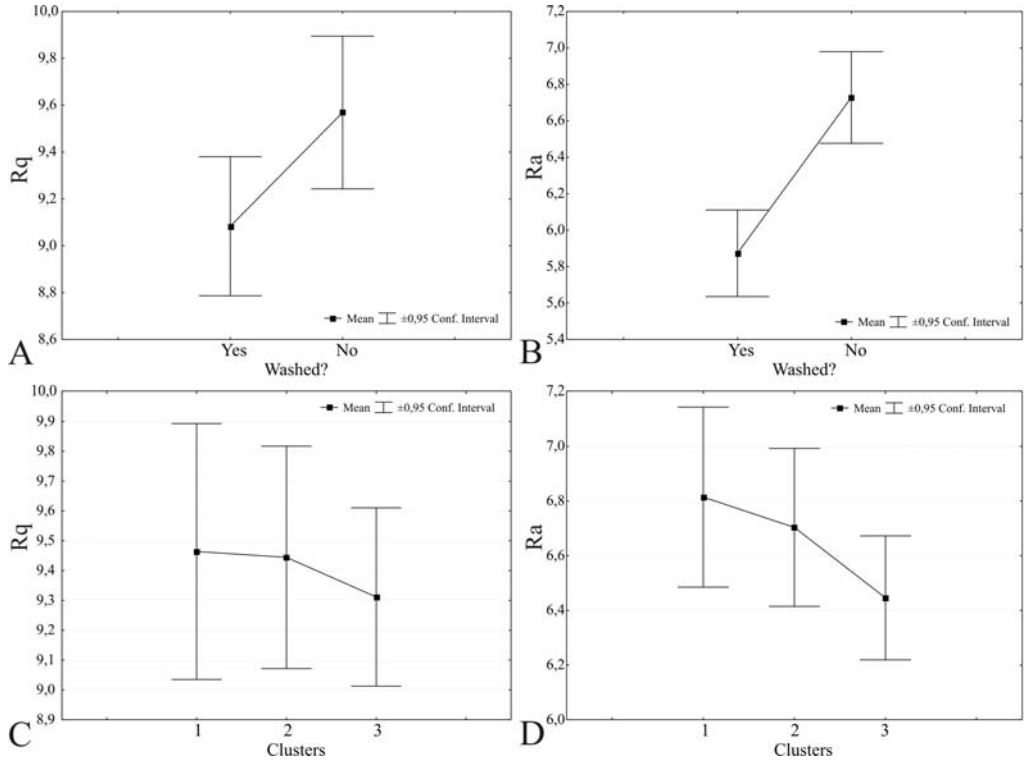

Figure 52: Responses of Rq (A) and Ra (A) on washed and unwashed samples. Rq (C) and Ra (D) in discrimination of different ash surfaces.

The vesicular unaltered surface has lower nQT and Rq values but higher mQT and sQT values than the highly altered surface. Lack of alteration causes smoother surfaces in micro-scale represented as areas composed of fewer but larger black blocks (Fig. 55). As indicated above, R_{sk} and R_{ku} parameters are sensitive to features in larger scales such as vesicles. The vesicular sample surface (N25-10 # 06) relating to plinian fall deposit have higher Rsk (0,24) and Rku (8,48) values than the altered sample surface (Dik2 # 54) relating to pyroclastic fall deposit (Rsk:-0,19, Rku:0,97). Ersoy et al. (2006) applied quadtree decomposition on different samples from Mt. Nemrut and used sGL (R_q), nQT and form factor of polar plots as discriminating descriptors for assessing fragmentation mechanisms operated during eruption.

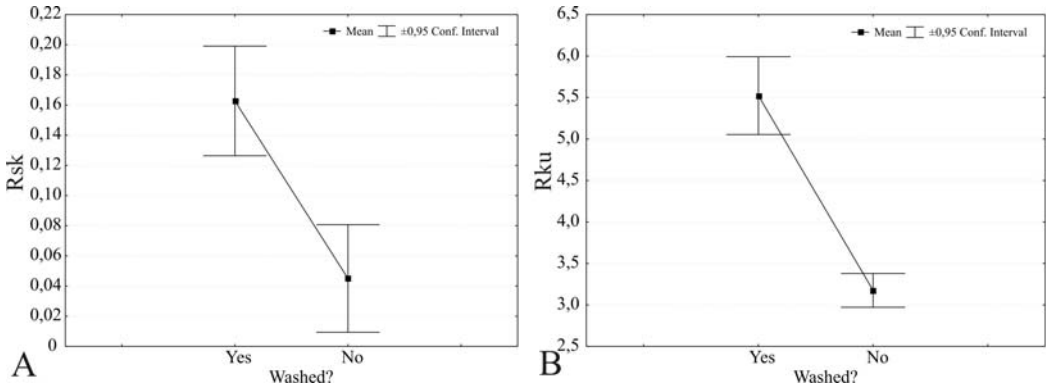

Figure 53: Responses of Rsk (A) and Rku (B) on washed and unwashed samples.

However, they calculated exact opposite values for different types. For instance, they characterize vesicular fall deposits with higher nQT values. As mentioned above, the detection of specific structure sizes affecting a given property is important in surface characterization. Suppressing some features by filters such as bandpass cuts down and narrows the ranges of values. Furthermore, the limit used for bandpass limits the size of perceived features. In all probability, their not using the bandpass filter on images enlarged the size of features participated in calculation of descriptors. For instance, the effects of filtering on nQT values of Mt Nemrut samples were illustrated in Figure 56. While median filter is almost passive, bandpass filter changes the course of the graph.

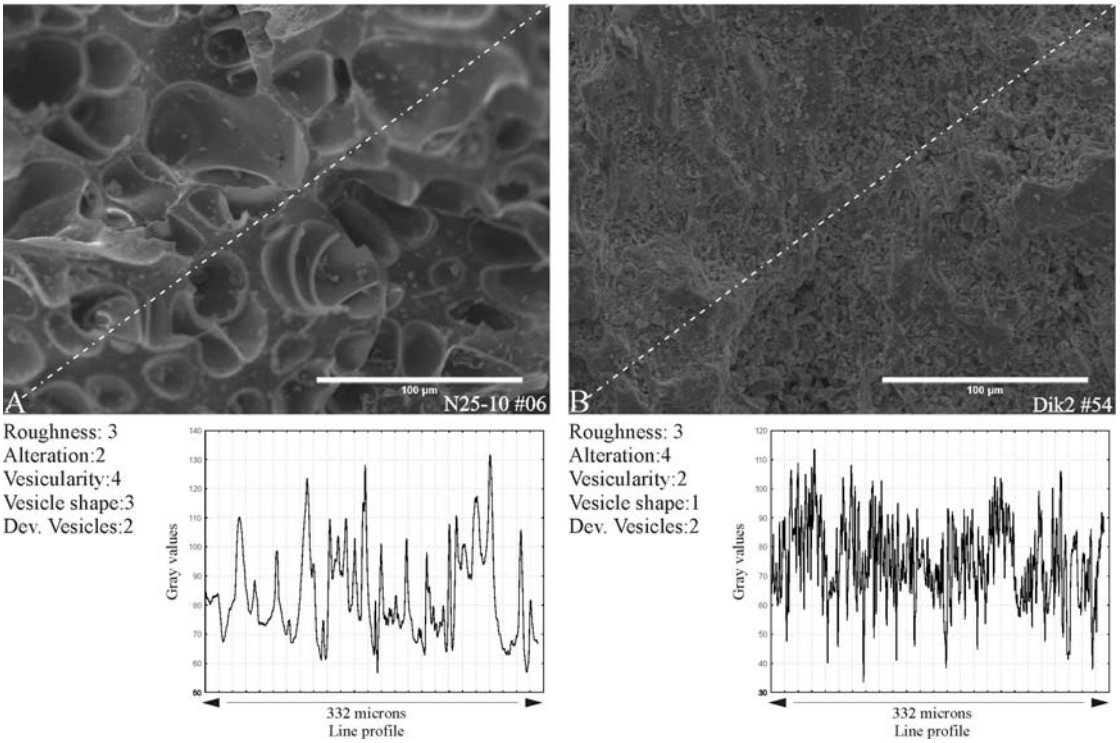

Figure 54: SEM micrographs of surfaces from samples N25-10 # 06 (A) and Dik2 # 54 (B) having lowest and higher nQT values, respectively. The qualitative descriptions and across line profiles were given below the corresponding surface micrograph.

Fractal dimension of surfaces (FDs) are also adequate in discrimination of clusters (Fig. 57). However, alteration has a major effect on FDs similarly to surface descriptors mentioned above (Fig. 57). The higher FDs values connote higher micro-irregularities on surfaces.
Some of descriptors derived from gradient analysis are also adequate for classification (Table 8). The shape descriptors solidity and convexity have the lowest and highest p-values indicating the adequate and inadequate descriptors for classification, respectively. These two parameters are calculated by using the convex hull of a feature and the feature itself. Solidity (area/convex area) quantifies to which extent the feature area covers the convex hull area. Convexity (convex perimeter/perimeter) shrinks as the convex perimeter and feature perimeter depart and has the maximum value for a perfectly convex future (inset on Fig. 58). Despite the strong correlation between two surface descriptors chiefly in medium values, they deviate in two ends, chiefly in higher values (Fig. 58). Although the method of computation for two descriptors seem similar, considered closely it appears that they characterize different features on surfaces. The maximum solidity (area/convex area) value can be obtained by maximum area of the feature (here polar plot) and minimum area of convex through a not

elongated shape and regular outline of plot. The orientation and intensity of gradients need to be homogeneous on entire surface for a not elongated shape. For a regular outline of plot, surface needs to have small features causing small gradient alternations. For the minimum solidity value, more rare but large-scaled gradient alternations result craggy shapes with deeper but rare indents and also smaller plot areas but larger convex areas. Volcanic ash surfaces labeled as N25-10 #06 and Dik2 # 54 have the lowest and highest solidity values within all analyzed surfaces, respectively. These two surfaces have been discussed above due to extreme values of other surface descriptors (Fig. 54 and Fig. 55).

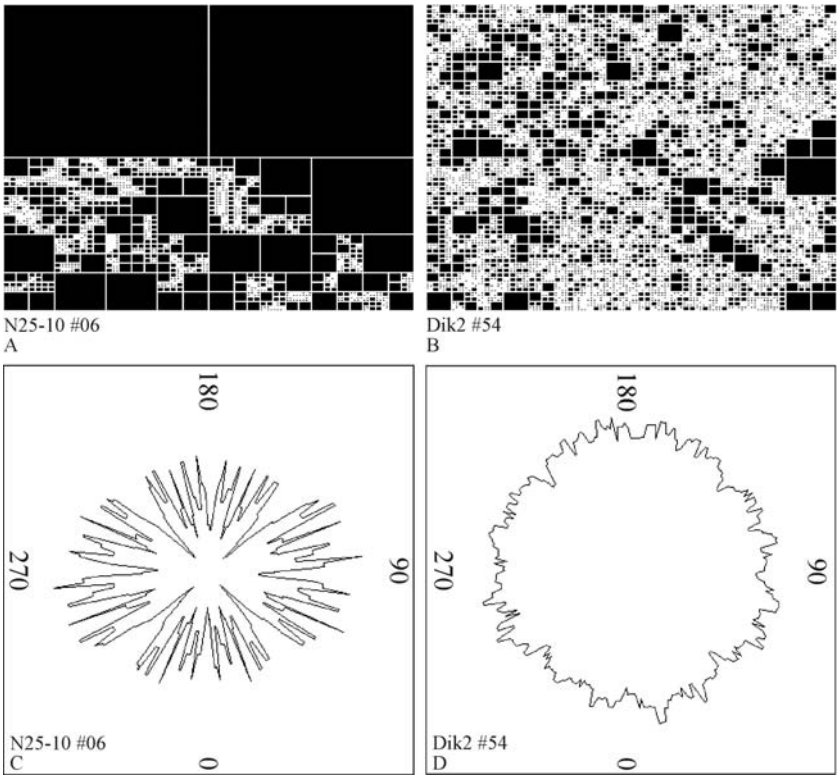

Figure 55: Quadtree decomposition of surfaces relating to N25-10 # 06 (A) and Dik2 # 54 (B). Polar plots of surfaces N25-10 # 06 (C) and Dik2 # 54 (D) having lowest and highest solidity values, respectively.

Fine alternation products cover the surface of Dik2 # 54 and clothe other features on surface resulting small gradient alternations radially and homogeneously directed on entire surface (Fig. 55). Ash particle N25-10 #06 has a surface which was shaped with vesicles and lacking alteration products. The surface involves high gradient alternations easily noticed by blur of higher level planes due to focusing condition of SEM instrument (Fig. 54). The higher gradient variations result deeper indents on polar plot (Fig. 55). Besides, N25-10 #06 has the minimum convexity value through higher plot perimeter, namely, the most irregular possible plot shape. The lower convex perimeters can be achieved by homogeneously directed gradient variations and plots more circular in form. The highest convexity value was calculated on surface labeled as Dik6 # 52 (Fig. 59). Sample is relating to the surge deposit of Mt. Erciyes, however, its surface is composed of tubular elongated vesicles indicating effect of magmatic volatiles during fragmentation or subsequent contact of water in conduit with already vesiculated and/or fragmented magma. Tubular vesicles give rise to small but directed gradient variations on surfaces. Their linear presence and thin bubble walls only form a jagged appearance of polar plots (Fig. 59). However, the elongated polar plots have higher

convex perimeters but small indents cause lower perimeters of plots and finally higher convexity values. Consequently, solidity characterizes highly altered and non-vesicular surfaces with its higher values while clean and vesicular surfaces have lower values. Convexity differently distinguishes tubular highly vesiculated surfaces with its higher values.

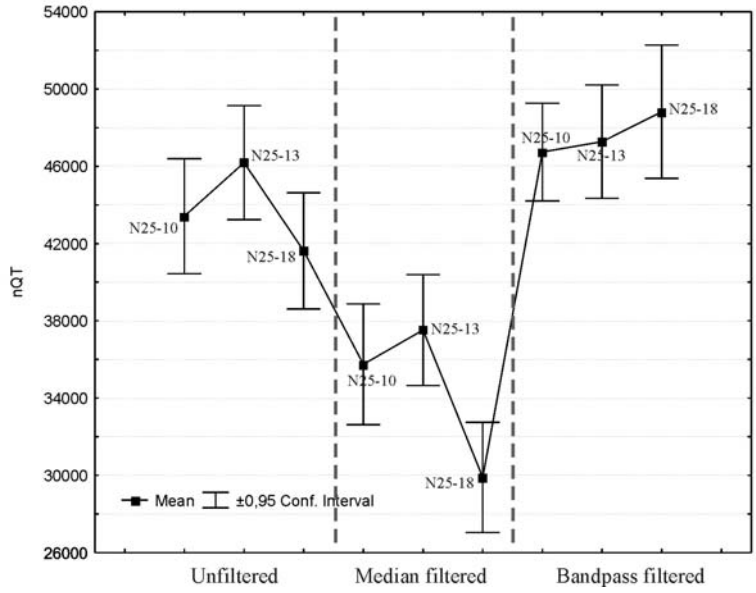

Figure 56: Effect of filtering on nQT. The course of figure is changed by bandpass filter.

Quantitative surface descriptors here presented give important information about the surface texture of volcanic ash surfaces and classify surfaces relating to different fragmentation mechanisms accompanied by field and laboratory observations (Fig. 49). The eruption units (samples) were classified according to proportions of different type ash surfaces. Factor 1 roughly distinguishes magmatic samples from phreatomagmatic samples. According to the projection of the variables (descriptors) on the factor-plane (inset in Fig. 49B), negative Factor 1 values (left side of the diagram) roughly represent magmatic samples whilst positive Factor 1 values (right side of the diagram) represent phreatomagmatic samples. Sample Ga6a from Galunggung volcano was plotted on an unexpected area on the diagram. This sample is related to a phreatomagmatic eruption however classes in the magmatic region of the diagram (negative factor 1 values). Ga6a has volcanic ash particles with surface textures corresponding

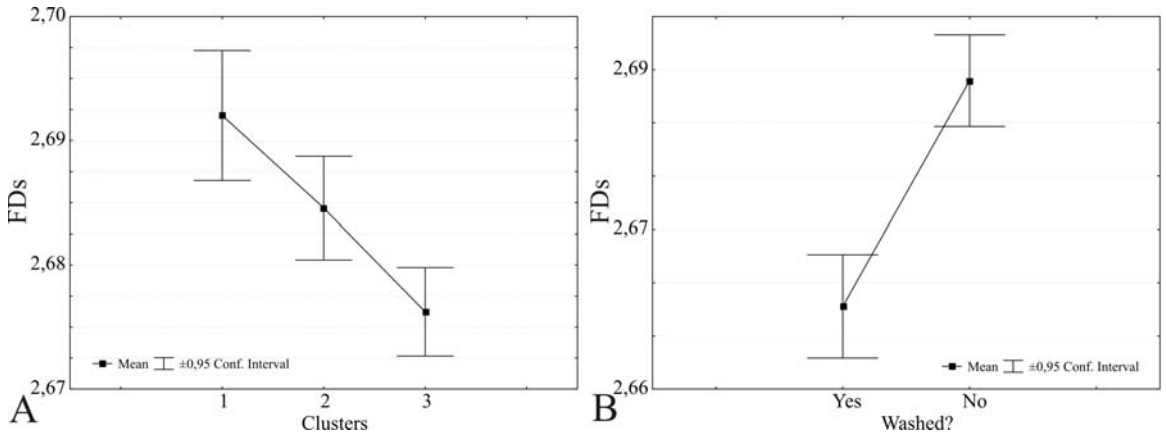

Figure 57: Fractal dimension of surfaces (FDs) in discrimination of different ash surfaces (A) and responses of FDs on washed and unwashed samples.

to Type 2 determined by Wohletz (1983). Surfaces are controlled by vesicle walls. Vesicle edges are rounded and smoothed, and overall grain shape is irregular (Fig. 60). The smooth curved surfaces between vesicles are lumpy and appear to be fused and fluid-formed. The existence of Type 2 pyroclasts (Wohletz, 1983) in 1982-83 eruption deposits of Galunggung volcano was also determined in Ersoy et al. (2007b). Type 2 pyroclasts were only found in phreatomagmatic explosions of basaltic magma (Wohletz, 1983; Ersoy et al., 2007b). Solidification and formation of a quenched crust on the pyroclast surface was probably incomplete after fracture, and subsequent movements of fragments out of the zone of the interaction formed smooth, fluid-like surfaces on fragments (see Figure 10 in section 1.3.).

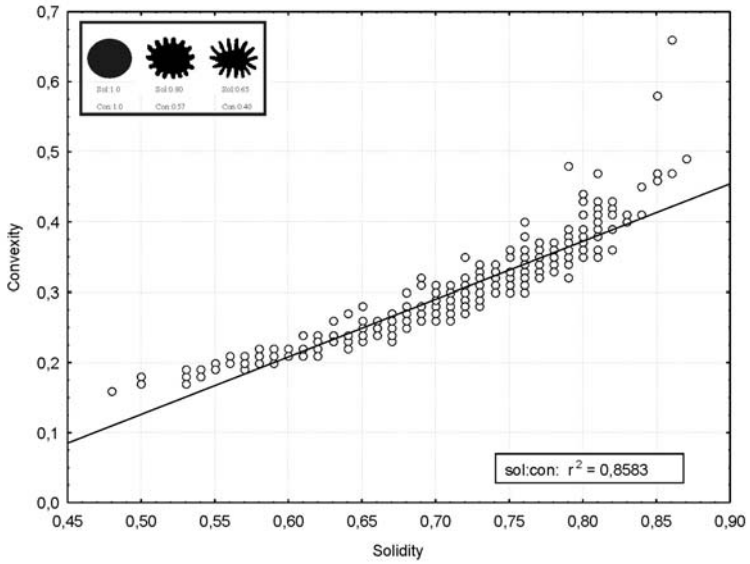

Figure 58: Correlation between solidity and convexity. Inset figures solidity and convexity values of distinctive shapes.

These pyroclasts were distinguished from blocky, non vesicular particles by Rsk parameters calculated on surfaces in Ersoy et al. (2007b). The fresh surfaces and probably unentangled vesicularity due to uncompleted solidification resulted surface forms similar to basaltic magmatic pyroclasts. It is questionable to estimate grade of the action of water on formation of Ga6a because despite its substantial portion of phreatomagmatic components, it involves surfaces indistinguishable because of magma's low viscosity and more ductile behavior during fragmentation. The low viscosity before quenching allows smoothing of pyroclast surfaces also in magmatic eruptions (e.g. intermittent strombolian activity in 1965-1969 eruption of Pacaya (Guatemala) (Heiken and Wohletz, 1985)). Sample VR05-03 is plotted close to the sample Ga6a (Fig. 48B). Two samples are in same composition (basaltic andesite). VR05-03 was denoted as magmatic however it involves phreatomagmatic components similar to Ga6a. VR05-03 has also smooth surfaces result from low viscosities during fragmentation (Fig. 60). The other two samples from the same eruptions (Ga5b and VR05-01) are ploted in the phreatomagmatic side of the diagram (positive factor 1 values). We believe that the samples in question are not the end members in different fragmentation mechanisms. The mechanisms acted in different proportions but that is conclusive that magmatic processes were superior to the role of water in fragmentation in samples Ga6a and VR05-03. However, the quantitative texture discrimination between magmatic and phreatomagmatic smooth surfaces (Type 2) will be examined in detail in a further study. The phreaoplinian sample (N25-13) from Mt. Nemrut is plotted in phreatomagmatic side of the graph but close to zero value of factor 1. Samples from August 2000 eruption of Miyakejima

volcano which were defined as vulcanian-subplinian (Aug18EP-Aug18LS) are separated from each other and were plotted on different zones. The early phase of August eruption (Aug18EP) seems relatively magmatic with no phreatomagmatic content. This sample probably represents the sub-plinian part of the eruption however, the ash particles from the later stage of this eruption (Aug18LS) was characterized as phreatomagmatic and plotted on the right side of diagram but close to zero value of factor 1 indicating a transition type such as phreaoplinian. This sample probably represents the vulcanian side of the eruption. As previously proposed by Schmincke (1977), the vulcanian eruption style may resemble to the phreatomagmatic style and limited involvement of groundwater in vulcanian eruptions is possible (e.g. Gourgaud et al., 2000).

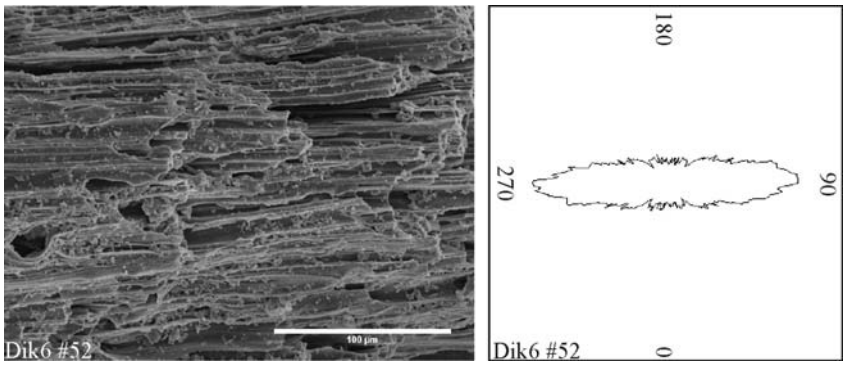

Figure 59: SEM micrograph (A) and polar plot (B) of surface Dik4 # 52 having highest convexity value.

Quantitative analyses are methodical and automated as in the case in this study. There is limited intervention of the operator to the process allowing quantitative analyses to produce reliable results. Besides the destructive methods based on cross-section SEM images, a non-destructive method based on processing SEM images is proposed. It is based on assuming that the gray level variation is related to the roughness variation of the surface. In addition, SEM stereo pairs can be used for generating height maps, thus making it possible to assess the real topography of ash particles. Here, we used gray level values in a form corresponding to vertical z-values on the surface. The disadvantages and advantages of the simplicity of method have been discussed. Three-dimensional images allow different morphological features to be correctly interpreted and definitively measured. Surface image acquisition concurrently with surface chemistry measurements by an energy-dispersive X-ray detector (EDS) on a SEM will be the complementary study seeking answers to smooth surface characterization of basaltic magmatic and phreatomagmatic surfaces in the future.

7. Conclusion

In this study, it is maintained that in the case of achieving the optimum operating conditions, by taking high-resolution scanning electron microscope (SEM) images on volcanic ash surfaces and collecting gray level value information at the location of interest, one can extract considerable and useful measurements or information from the two-dimensional (2D) image fields. Beside the two-dimensional surfaces, simple and well-defined surface descriptors were calculated on three-dimensional surfaces and some methods were explained in order to acquire 3D datasets for reconstruction. The optimum distinctive surface descriptors were determined and used to distinguish volcanic ash surface textures associated with different fragmentation mechanisms. Discrimination between products of different fragmentation mechanisms may permit forecasting of volcanic hazards. Because of increasing interest in

surface properties of natural materials, surface descriptors proposed in this study can be applied to surfaces of various natural materials.

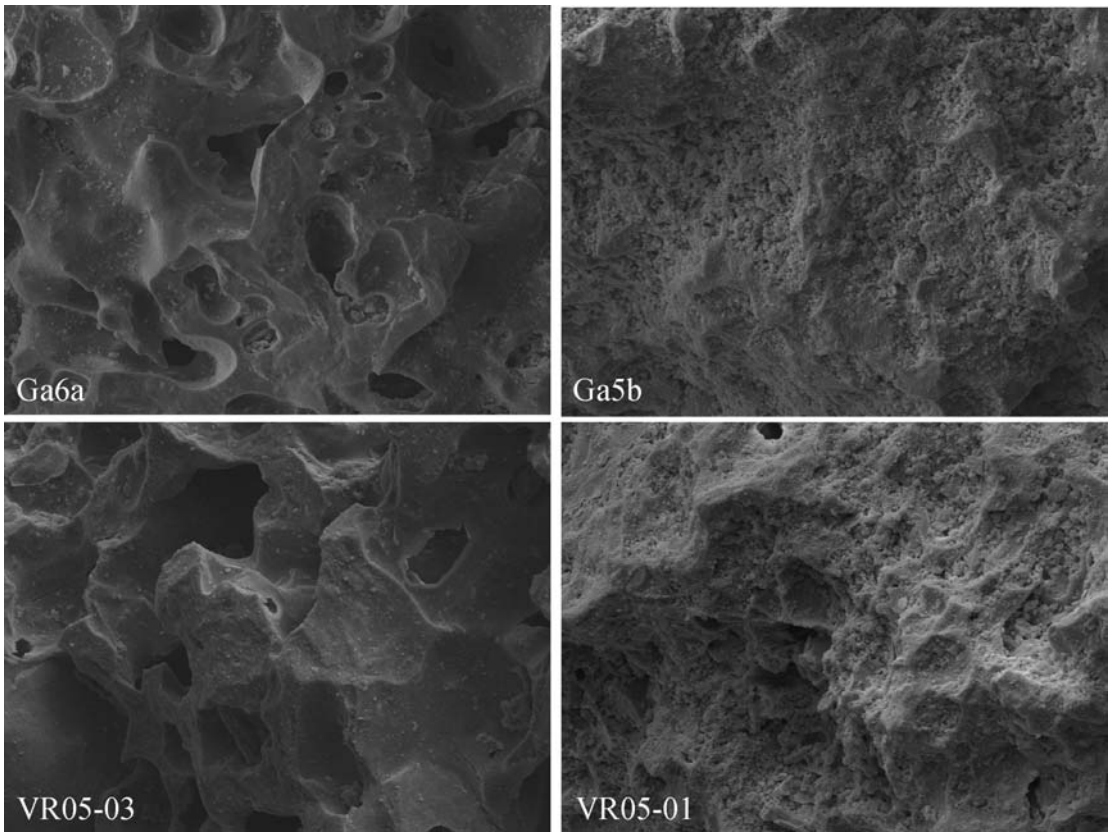

Figure 60: SEM micrographs of basaltic andesite ash surfaces from two different eruptions. Ga6a (Galunggung) and VR05-03 (Villarica) have smooth surfaces and vesicles while Ga5b (Galunggung) and VR05-01 (Villarica) have non vesicular altered surfaces.

The study evidenced the importance of sample preparation and pre-processing image filtering to achieve accurate results. In order to make the relative interpretation on samples, identical pre-processing applications were advised on sample groups. The thesis also involved the infancy stages of the method and consequent inaccuracy. After achieving the optimum conditions for accurate analysis, the reasons for artificial and technical defects for the earlier applications were tried to be explained.

With the possible identical settings for a large sample group, it is agreed that roughness parameters R_a and R_q are sensible to micro-roughness (eg. fine dust) while other roughness parameters R_{sk} and R_{ku} measure the macro-roughness associated with cavities on the surface (vesicles). Furthermore, quadtree parameter nQT, fractal dimension of surfaces and solidity of polar plots also have the same response to micro-roughness similar to R_a and R_q. With the assistance of quantitative surface descriptors, volcanic ash surfaces were characterized and clustered according to their fragmentation mechanisms and eruption styles.

Beside the surface parameters, outline parameters of ash particles were calculated but, no relation was established between these parameters and different eruption styles (see Section 4.1.) which was interpreted as the major effect of transport mechanisms on particle outlines.

8. References

Abràmoff, M.D., Viergever, M.A., 2002. Computation and visualization of three dimensional motion in the orbit. IEEE Transactions on Medical Imaging, 21 (4), 296-304.

Aitkenhead, M.J., Aitkenhead-Petterson, J.A., McDowell, W.H., Smart, R.P., Cresser, M.S., 2007. Modelling DOC export from watersheds in Scotland using neural networks. Computers&Geoscineces, 33(3), 423-436.

Aleksander, I., Morton, H., 1990. An Introduction to Neural Computing, 2nd ed. Chapman and Hall, New York, NY, 240 p.

Alidibirov, M., 1993. Laboratory simulations of highly viscous magma fragmentation during volcanic blasts. EOS, 74, p. 621.

Alidibirov, M., Dingwell, D.B., 1996. Magma fragmentation by rapid decompression. Nature, 380, 146–149.

Alidibirov, M., Dingwell, D.B., 2000. Three fragmentation mechanisms for highly viscous magma under rapid decompression. Journal of Volcanology and Geothermal Research, 100, 413–421.

Allen, S.R., Cas, R.A.F., 1998. Rhyolitic fallout and pyroclastic density current deposits from a phreatoplinian eruption in the eastern Aegean Sea, Greece. Journal of Volcanology and Geothermal Research, 86(1-4), 219-251.

Anderson, D., McNeil, G., 1992. Artificial neural network technology. Data & Analysis Center for Software., Rome, 83 p.

Aronsson, M., Henningsson, O., Sävborg, Ö., 2002. Slice-based digital volume assembly of a small paper sample. Nordic Pulp Paper Research Journal, 17(1), 29-33.

Aydar, E., Gourgaud, A., Ulusoy, I., Digonnet, F., Labazuy, P., Sen, E., Bayhan, H., Kurttas, T., Tolluoglu, A.U., 2003. Morphological analysis of active Mount Nemrut stratovolcano, eastern Turkey: evidences and possible impact areas of future eruption. Journal of Volcanology and Geothermal Research, 2571, 1-12.

Bansal, R. K., Kubis, A., Hull, R., Fitz-Gerald J. M., 2006. High-resolution three-dimensional reconstruction: A combined scanning electron microscope and focused ion-beam approach. The Journal of Vacuum Science and Technology B, 24(2), 554-561.

Barnett, W., 2004. Subsidence breccias in kimberlite pipes-an application of fractal analysis. Lithos, 76 (1-4), 299–316.

Batten, C.F., 2000. Autofocusing and astigmatism correction in the scanning electron microscope. Master's thesis, University of Cambridge, 89 p.

Bayhurst, G.K., Wohletz, K.H., Mason, A.S., 1994. A method for characterizing volcanic ash from the December 15, 1989, eruption of Redoubt Volcano , Alaska, *in* Casadevall, T., eds., Volcanic ash and aviation safety: U.S. Geological Survey Bulletin, 2047, 13-18.

Bérubé, D., Jébrak, M., 1999. High precision boundary fractal analysis for shape characterization. Computers & Geosciences, 25, 1059-1071.

Boyde, A., 1973. Quantitative photogrammetric analysis and qualitative stereoscopic analysis of SEM images. Journal of Microscopy, 98, 452-471.

Brouste, A., Renard, F., Gratier, J-P., Schmittbuhl, J., 2007. Variety of stylolites' morphologies and statistical characterization of the amount of heterogeneities in the rock. Journal of Structural Geology, 29, 422-434.

Brown, C.T., 2001. The fractal dimensions of lithic reduction. Journal of Archaeological Science, 28, 619–631.

Brown, W.K., Wohletz, K.H., 1995. A derivation of the Weibull distribution based on physical principles and its connection to the Rosin-Rammler and the lognormal distributions. Journal of Applied Physics, 78(4), 2758-2763.

Büttner, R., Dellino, P., Zimanowski, B., 1999. Identifying modes of magma/water interaction from the surface features of ash particles. Nature, 401, 688-690.
Capaccioni, B., Sarocchi, D., 1996. Computer-assisted image-analysis on clast shape fabric from the Orvieto-Bagnoregio Ignimbrite (Vulsini District, central Italy): implications on the emplacement mechanisms. Journal of Volcanology and Geothermal Research, 70, 75–90.
Capaccioni, B., Valentini, L., Rocchi, M.B.L., Nappi, G. and Sarocchi, D., 1997. Image analysis and circular statistics for shape-fabric analysis: applications to lithified ignimbrites. Bulletin of Volcanology 58, 501–514.
Carey, S., Maria, A., Sigurdsson, H., 2000. Use of fractal analysis for discrimination of particles from primary and reworked jokulhlaup deposits in SE Iceland. Journal of Volcanology and Geothermal Reserach, 104, 65-80.
Carey, S., Sparks, R.J.S., 1986. Quantitative models of the fallout and dispersal of tephra from volcanic eruption columns. Bulletin of Volcanology, 48, 109-125.
Castle, J.E., Zhdan, P.A., 1997. Characterization of surface topography by SEM and SFM: problems and solutions. Journal pf Physics D: Applied Physics, 30, 722–740.
Chang, H-C., Kopaska-Merkel, D.C., Chen, H-C., 2002. Identification of lithofacies using Kohonen self-organizing maps. Computers and Geosciences, 28, 223-229.
Chinga, G., 2006. A quadtree decomposition approach for surface assessment. Pattern Analysis and Applications, 9, 94-101.
Chinga, G., Helle, T., 2003. 3-Dimensional reconstruction of a coating layer structure. The Journal of Pulp and Paper Science, 29(4), 119-122.
Chinga, G., Johnsen, P.O., Diserud, O., 2004. "Controlled serial grinding for high-resolution 3-D reconstruction". Journal of Microscopy, 214(1): 13-21.
Chinga, G., Gregersen, Ø., Dougherty, R., 2003. Paper surface characterization by laser profilometry and image analysis. Journal of Microscopy and Analysis, 84, 5-7.
Chinga, G., Johnssen, P.O., Dougherty, R, Lunden-Berli, E. and Walter, J., 2007. Quantification of the 3-D micro-structure of SC surfaces. Journal of Microscopy, 227(3), 254-265.
Dellino, P., Isaia, R., La Volpe, L., Orsi, G. 2004. Interaction between particles transported by fallout and surge in the deposits of the Agnano-Monte Spina eruption (Campi Flegrei, Southern Italy). Journal of Volcanology and Geothermal Research, 133(1-4), 193-210.
Dellino, P., La Volpe, L., 1996. Image processing analysis in reconstructing fragmentation and transportation mechanisms of pyroclastic deposits. The case of Monte Pilato-Rocche Rosse eruptions, Lipari (Aeolian Islands, Italy). Journal of Volcanology and Geothermal Research, 71, 13-29.
Dellino, P., Liotino, G., 2002. The fractal and multifractal dimension of volcanic ash particles contour: a test study on the utility and volcanological relevance. Journal of Volcanology and Geothermal Research, 113, 1-18.
Delmelle, P, Lambert, M., Dufrêne, Y., Gerin, P., Óskarsson, N., 2007. Gas/aerosol–ash interaction in volcanic plumes: New insights from surface analyses of fine ash particles. Earth and Planetary Science Letters, 259 (1-2), 159-170.
Durant, A. J., Y. Mi, R. A. Shaw, G. G. J. Ernst, and W. I. Rose, 2004, Ice Nucleation by Volcanic Ash: Influence of Composition and Morphology, *in* Procedings, IAVCEI General Assembly, Pucon, Chile.
Ersoy, O., Chinga, G., Aydar, E., Gourgaud, A., Cubukcu, H.E., Ulusoy, I., 2006, Texture discrimination of volcanic ashes from different fragmentation mechanisms: A case study, Mount Nemrut stratovolcano, eastern Turkey. Computers and Geosciences, 32, 936-946.
Ersoy, O., Aydar, E., Gourgaud, A., Bayhan, H., 2007a. Quantitative analysis on volcanic ash surfaces: Application of extended depth-of-field (focus) algorithm for light and scanning electron microscopy and 3D reconstruction, Micron, in press.

Ersoy, O., Gourgaud, A., Aydar, E., Chinga, G., Thouret, J-C., 2007b, Quantitative SEM analysis of volcanic ash surfaces: application to the 1982-83 Galunggung eruption (Indonesia). Geological Society of America Bulletin 119 (5), 743-752.
Fausett, L.V., 1994. Fundamentals of Neural Networks, US ed. Prentice Hall, NJ, 461 p.
Fisher, R.V., H.U., Schmincke, 1984. Pyroclastic Rocks, Springer-Verlag, Berlin, 472 p.
Freundt, A., Schmincke, H., 1992. Abrasion in pyroclastic flows. Geologische Rundschau, 81(2), 383-389.
Geshi, N., Shimano, T., Chiba, T., Nakada, S., 2002. Caldera collapse during the 2000 eruption of Miyakejima Volcano, Japan. Bulletin of Volcanology, 64. 55-68.
Goldstein, J., Newbury, D., Joy, D., Lyman, C., Echlin, P., Lifshin, E., Sawyer, L., Michael, J., 2003. Scanning electron microscopy and x-ray microanalysis, New York, Springer Press, 687 p.
Gourgaud, A., Camus, G., Gerbe, M.C., Morel, J.M., Sudradjat, A., Vincent, P.M., 1989. 1982-83 eruption of Galunggung (Indonesia): a case study of volcanic hazards with particular relevance to air navigation, in Latter, J.H., ed., IAVCEI Proceedings in Volcanology 1. Volcanic Hazards, Berlin, Springer, 151-162.
Gourgaud, A., Thouret, J.C., Bourdier, J.L., 2000. Stratigraphy and textural characteristics of the 1982-83 tephra of Galunggung volcano (Indonesia): implications for volcanic hazards. Journal of Volcanology and Geothermal Research, 104, 169-186.
Grzesik, W., Brol, S., 2003. Hybrid approach to surface roughness evaluation in multistage machining processes. Journal of Materials Processing Technology, 134, 265–272.
Hagan, M.T., Demuth, H.B., Beale, M., 1996. Neural Network Design, PWS Publishing Company, Boston, MA, 730 p.
Hagen, E.H., Walker, P.L., 1994. A topographical approach to microwear analysis. Unpublished data (available at http://itb.biologie.hu-berlin.de/~hagen/papers.html).
Haykin S., 1994. Neural Networks: A Compherensive Foundation, New York, Macmillan.
Heiken, G., 1972. Morphology and petrography of volcanic ashes. Geological Society of America Bulletin, 83, 1961-1988.
Heiken, G., 1974. An atlas of volcanic ash. Smithsonian Contr. Earth Sci., 12, 101 p.
Heiken, G., 1978. Plinian-type eruptions in the Medicine Lake Highland, California, and the nature of the underlying magma. Journal of Volcanology and Geothermal Research, 4, 375-402.
Heiken, G., Wohletz, K.H., 1985. Volcanic Ash, California, University of California Press, Berkeley, 245 p.
Heiken G., Wohletz, K, 1991. Fragmentation processes in explosive volcanic eruptions. In: Sedimentation in Volcanic Settings (R. V. Fisher and G. Smith Eds), Society of Sedimentary Geology Special Publication, 45,19-26.
Hein, L.R.O., 2001. Quantitative fractography by digital image processing: NIH Image macro tools for stereo pair analysis and 3-D reconstruction. Journal of Microscopy, 204, 17-28.
Hjaltason, G.R., Samet, H., 1999. Speeding up construction of quadtrees for spatial indexing, Computer Science Department, TR-4033, University of Maryland, College Park, MD. Available from http://www.cs.umd.edu/~hjs/pubs/bulkload.pdf.
Honnorez, J, Kirst, P., 1975. Submarine basaltic volcanism: morphometric parameters for discriminating hyaloclastites from hyalotuffs. Bulletin of Volcanology, 34, 1–25.
Horwell, C.J., Fenoglio, I., Ragnarsdottir, K.V., Sparks, R.S.J., Fubini, B., 2003. Surface reactivity of volcanic ash from the eruption of Soufrière Hills volcano, Montserrat, with implications for health hazards. Environmental Research, 93, 202-215.
Houghton, B.F., Wilson, C.J.N., 1989. A vesicularity index for pyroclastic deposits. Bulletin of Volcanology, 51, 451-462.

Huang, Z., Dikin, D., Ding, W., Qiao, Y., Chen, X., Fridman, Y., Ruoff, R. S., 2004. Three-dimensional representation of curved nanowires. Journal of Microscopy, 216, 206-214.
Inman, D.L., 1952. Measures for describing the size distribution of sediments. Journal of Sedimentary Petrology, 22, 125–145.
Ishitani, T., Kamiya, C., Sato, M., 2005. Influence of random noise on the contrast-to-gradient image resolution in scanning electron microscopy. Journal of Electron Microscopy, 54(2), 85-97.
ISO 4287, 2000. Geometrical Product Specifications (GPS)-Surface Texture: profile method-terms, definitions and surface texture parameters, 40 p.
Kartalopoulos, S.V., 1995. Understanding neural networks and fuzzy logic: basic concepts and applications.Wiley IEEE Press, 232 p.
Kaski, S., 1997. Data exploration using self-organizing maps. Acta Polytechnica Scandinavica, Mathematics, Computing and Management in Engineering Series No. 82, Espoo, PhD Thesis, Published by the Finnish Academy of Technology, 57 p.
Katili, J.A., Sudradjat, A., 1984. Galunggung: the 1982-83 Eruption: VSI, Bandung, 102 p.
Kohonen, T., 1982. Self-organized formation of topologically correct feature maps. Biological Cybernetics, 43, 59-69.
Kohonen, T., Hynninen, J., Kangas, J., Laaksonen, J., 1996. SOM_PAK: The Self-Organizing Map Program Package. Technical Report A31, Helsinki University of Technology, Laboratory of Computer and Information Science, FIN-02150 Espoo, Finland, 27 p.
Kueppers, U., 2005. Nature and efficiency of pyroclast generation from porous magma: insights from field investigations and laboratory experiments, PhD dissertation, University (LMU) of Munich, http://edoc.ub.uni-muenchen.de/archive/00004587/.
Kurszlaukis S., Buttner, R., Zimanowski, B., Lorenz, V., 1998. On the first experimental phreatomagmatic explosion of a kimberlite melt. Journal of Volcanology and Geothermal Research, 80(3), 323-326.
Levoy, M., 1988. Display of surfaces from volume data. IEEE Computer Graphics & Applications, 8(5), 29-37.
Lipman, R.P., 1987. An Introduction to Computing with Neural Nets. IEEE ASSP Magazine, April, 4-22.
Lohmar, S., Robin, C., Gourgaud, A., Clavero, J., Parada, M.A., Moreno, H., Ersoy, O., López-Escobar, L., Naranjo, J.A., 2007. Evidence of magma-water interaction during the 13,800 years BP explosive cycle of the Licán ignimbrite, Villarrica volcano (Southern Chile). Revista Geológica de Chile, 34(2), 233-247.
Longley, P.A., Batty, M., 1989. Fractal measurement and line generalization. Computers and Geosciences, 15 (2), 167–183.
Mader, H.M., Phillips, J.C., Sparks, R.S.J., Sturtevant, B., 1996. Dynamics of explosive degassing of magma: observations of fragmenting two-phase flows. Journal of Geophysical Research, 101, 5547–5560.
Mader, H.M., Zhang, Y., Phillips, J.C., Sparks, R.S.J., Sturtevant, B., Stolper, E., 1994. Experimental simulations of explosive degassing of magma. Nature, 372, 85-88.
Mandelbrot, B.B., 1967. How long is the coast of Britain? Statistical self-similarity and fractional dimension. Science, 156, 636-638.
Mandelbrot, B.B., 1982. The fractal geometry of nature, W.H. Freemann and Company, San Francisco. 460 p.
Maria, A., Carey, S., 2007. Quantitative discrimination of magma fragmentation and pyroclastic transport processes using the fractal spectrum technique. Journal of Volcanology and Geothermal Research, 161, 234-246.
Marko, M., 2005. A Survey of Electron Microscopic Methods for 3-D Imaging. Microscopy and Microanalysis, 11 (2), 624-625

Marshall, J.R., 1987. Shape analysis. In: JR Marshall (Editor), Clastic Particles. Van Nostrand Reinhold, New York, NY, 255 p.
Martel, C., Dingwell, D.B., Spieler, O., Pichavant, M., Wilke, M., 2000. Fragmentation of foamed silicic melts: an experimental study. Earth and Planetary Science Letters, 178, 47-58.
McBirney, A.R., Murase, T., 1970. Factors governing the formation of pyroclastic rocks. Bulletin of Volcanology, 34, 372-384.
Moune, S., Faure, F., Gauthier, P.-J., Sims, K.W.W., 2007. Pele's hairs and tears: Natural probe of volcanic plume. Journal of Volcanology and Geothermal Research, 164(4), 244-253..
Mullineaux, D.R., 1996. Pre-1980 tephra-fall deposits erupted from Mount St. Helens, Washington, U. S. Geological Survey Professional Paper 1563, 1-99.
Nakada, S., Nagai, M., Kaneko, T., Nozawa, A., Suzuki-Kamata, K., 2005. Chronology and products of the 2000 eruption of Miyakejima Volcano, Japan. Bulletin of Volcanology, 67, 205-218.
Navon, O., Chekhmir, A., Lyakhovsky, V., 1998. Bubble growth in highly viscous melts: theory, experiments, and autoexplosivity of dome lavas. Earth and Planetary Science Letters 160, 763-776.
Newhall, C.G., Self, S., 1982. The Volcanic Explosivity Index (VEI): an estimate of explosive magnitude for historical volcanism. Journal of Geophysical Research, 87, 1231-1238.
Nowicki, B., 1985. Multiparameter representation of surface roughness. Wear, 102, 161-176.
Ortega, A., Dalhoum, A.A., Alfonseca, M., 2003. Grammatical evolution to design fractal curves with a given dimension. IBM Journal of Research and Development, 47(4), 483-493.
Peckover, R.S., Buchanan, D.J., Ashby, D.E.T.F., 1973. Fuel-coolant interactions in submarine volcanicm. Nature, 245, 307-308.
Penn, B.S., 2005. Using self-organizing maps to visualize high-dimensional data. Computers and Geosciences, 31, 531-544.
Phillips, J.C., Lane, S.J., Lejeune, A.M., Hilton, M., 1995. Gum rosin–acetone system as an analogue to the degassing behavior of hydrated magmas. Bulletin of Volcanology, 57, 263-268.
Pouchou, J.L., Boivin, D., Beauchêne, P., Le Besnerais, G., Vignon, F., 2002. 3D reconstruction of rough surfaces by SEM stereo imaging. Microchimica Acta, 139, 135-144.
Rasband, W.S., 1997-2007. ImageJ: National Institutes of Health, Bethesda, Maryland, USA, http://rsb.info.nih.gov/ij
Riley, C.M., Rose, W.I., Bluth, G.J.S., 2003. Quantitative shape measurements of distal volcanic ash. Journal of Geophysical Research, 108 (B10), 2504, doi:10.1029/2001JB000818.
Ripley, B.D., 1996. Pattern Recognition and Neural Networks. Cambridge University Press, Cambridge, Great Britain, 415 p.
Russ, J.C., 1999. The image processing handbook: 4th ed., Boca Raton, FL., CRC Press, 732 p., ISBN 3-540-64747-3.
Samet, H., 1984. The quadtree and related hierarchical data structures. Computing Surveys, 16(2), 187-260.
Samet, H., 1990. The Design and Analysis of Spatial Data Structures, Addision Wesley Publishing Company, Inc., Reading, 493 p.
Schalkoff, R.J., 1997. Artificial Neural Networks, McGraw-Hill,448 p.
Schmincke, H.U., 1977. Phreatomagmatische phasen in quartären vulkanen der Osteifel. Geologisches Jahrbuch Reihe, A39, 3-45.
Self, S., 1983. Large-scale phreatomagmatic silisic volcanicm: a case study from new Zealand. Journal of Volcanology and Geothermal Research, 17, 433-469.
Self, S., Sparks, R.S.J., 1978. Characteristics of widespread pyroclastic deposits formed from the interaction of silisic magma and water. Bulletin of Volcanology, 41(3), 196-212.

Sheridan, M.F., Barberi, F., Rosi, M., Santacroce, R., 1981. A model for Plinian eruptions of Vesuvius. Nature, 289, 282-285.
Sheridan, M.F., Marshall, J.R., 1983. Interpretation of pyroclast surface features using SEM images. Journal of Volcanology and Geothermal Research, 16, 153-159.
Sheridan, M.F., Wohletz, K.H., 1981. Hydrovolcanic explosions: the systematics of water-tephra equilibration. Science, 212, 1387-1389.
Sheridan, M.F., Wohletz, K.H., 1983. Hydrovolcanism: Basic considerations and review. Journal of Volcanology and Geothermal Research, 17, 1-29.
Skapura, D., 1996. Building Neural Networks, ACM Press, Addison-Wesley, NY, 282 p.
Smith, T.G., Lange, G.D., Marks, W.B., 1996. Fractal Methods and Results in Cellular Morphology. Journal of Neuroscience Methods, 69 (2) 123-136.
Sparks, R.S.J., 1978. The dynamics of bubble formation and growth in magmas: a review and analysis. Journal of Volcanology and Geothermal Research, 3, 1-38.
Sparks, R.S.J., Wilson, L., 1976. A model for the formation of ignimbrite by gravitational column collapse. Journal of Geological Society London, 132, 411-452.
Sparks, R.S.J., Wilson, L., Hulme, G., 1978. Theoretical modeling of the generation, movement and emplacement of pyroclastic flows by column collapse. Journal of Geophysical Research, 83, 1727-1739.
Sparks, R.S.J., Wilson, L., Sigurdsson, H., 1981. The Pyroclastic Deposits of the 1875 Eruption of Askja, Iceland. Philosophical Transactions of the Royal Society of London. Series A, Mathematical and Physical Sciences, 299 (1447), 241-273.
Stachowiak, G.W., 1998. Numerical characterization of wear particles morphology and angularity of particles and surfaces. Tribology International, 31, 139-157.
Sugioka, I., Bursik, M., 1995. Explosive fragmentation of erupting magma. Nature, 373, 689-692.
Suzuki, Y., Gardner, J.E., Larsen, J.F., 2007. Experimental constraints on syneruptive magma ascent related to the phreatomagmatic phase of the 2000 AD eruption of Usu volcano, Japan. Bulletin of Volcanology, 69(4), 423-444.
Şen, E., Aydar, E., Gourgaud, A., Kürkçüoğlu, B., 2002. La phase explosive précédant l'extrusion des domes volcaniques: exemple du dome rhyodacitique de Dikkartin Dag, Erciyes, Anatolie centrale, Turquie (Initial explosive phases during extrusion of volcanic lava domes: example from rhyodacitic dome of Dikkartin Dag, Erciyes stratovolcano, Central Anatolia, Turkey). C. R. Geoscience, 334(1), 27-33.
Textor, C., Graf, H.F., Herzog, M., Oberhuber, J.M., Rose, W.I., Ernst, G.G.J., 2006. Volcanic particle aggregation in explosive eruption columns. Part II: Numerical experiments. Journal of Geophysical Research, 150 (4), 374-394
Thévenaz, P., Ruttimann, U.E., Unser, M., 1998. A pyramid approach to subpixel registration based on intensity. IEEE Transactions on Image Processing, 7(1), 27-41.
Thorarinsson, S., 1944, Tephrochronological studies in Iceland, Geografiska Annaler, 26, 1-217.
Thorarinsson, S., 1954, The tephra-fall from Hekla on March 29, 1947, in The eruption of Hekla 1947-1948, 2(3), Icelandic Scientific Society, 68 p.
Trigila, R., Battaglia, M., Manga, M., 2007. An experimental facility for investigating hydromagmatic eruptions at high-pressure and high-temperature with application to the importance of magma porosity for magma-water interaction. Bulletin of Volcanology, 69(4), 365-372.
TS 6956, 2004. Geometrical product specification (GPS)-Surface texture: profile method-terms, definitions and surface texture parameters (In Turkish): Turkish Standard, 22 p.
Tukey, J.W., 1977. Exploratory Data Analysis, Addison-Wesley, Reading, MA, 688 p.
Unwin, D.J., 1989. Fractals in the geosciences. Computers and Geosciences, 15(2), 163-165.

Verhoogen, J., 1951. Mechanisms of ash formation. American Journal of Science, 249, 29-739.
Verrecchia E.P, 2003. Image analysis and morphometry of geological objects. Mathematical Geology, 35 (7), 759-762.
Walker, G.P.L., Croasdale, R., 1972. Characteristics of some basaltic pyroclastics. Bulletin of Volcanology, 35, 303-317.
Walker, G.P.L., 1971. Grain-size characteristics of pyroclastic deposits. Journal of Geology, 79, 696-714.
Walker, G.P.L., Croasdale, R., 1972. Characteristics of some basaltic pyroclastics. Bulletin of Volcanology, 35, 303-317.
Wang, S., Armstrong, M.P., 2003. A quadtree approach to domain decomposition for spatial interpolation in grid computing environments. Parallel Computing, 29, 1481–1504.
Wegman, E.J., Solka, J.L., 2002. On some mathematics for visualizing high dimensional data. The Indian Journal of Statistics, 64 (A-2), 429-452.
Wen-Shiung, C, Shang-Yuan, Y., Chih-Ming, H., 2003. Two algorithms to estimate fractal dimension of gray level images. Optical Engineering, 42 (8), 2452-2464.
Whalley, W.B., Orford, J.D., 1989. The use of fractals and pseudofractals in the analysis of two-dimensional outlines; review and further exploration. Computers and Geosciences, 15(2), 185-197.
Wilson, L., Sparks, R.S.J., Huang, T.C., Watkins, N.D., 1978. The control of volcanic column heights by eruption energetics and dynamics. Journal of. Geophysical. Research, 83, 1829-1836.
Wilson, L., Sparks, R.S.J., Walker, G.P.L., 1981. Explosive volcanic eruptions-IV. The control of magma properties and conduit geometry on eruption column behavior. Geophysical Journal of the Royal Astronomical Society, 63, 117-148.
Wohletz, K.H., 1983. Mechanisms of hydrovolcanic pyroclast formation: size, scanning electron microscopy, and experimental studies, in Sheridan, M.F. et al., eds., Explosive Volcanism. Journal of Volcanology and Geothermal Research, 17, 31-63.
Wohletz, K., 1987. Chemical and textural surface features of pyroclasts from hydrovolcanic eruption sequences. In: J.R. Marsall, Editor, Clastic Particles, Van Nostrand Reinhold Co, New York, N.Y., 79-97.
Wohletz, K., Heiken, G., 1992. Volcanology and Geothermal Energy. Berkeley. University of California Press, 450 p. ISBN-13: 978-0520079144.
Wohletz, K.H., Krinsley, D., 1982. Scanning electron microscopy of basaltic hydromagmatic ash. Los Alamos National Laboratory Report, LA-UR 82-1433, 43 p.
Wohletz, K.H., McQueen, R.G., 1984. Volcanic and stratospheric dust-like particles produced by experimental water-melt interactions. Geology, 12, 591-594.
Wohletz, K.H., Orsi, G., de Vita, S., 1995. Eruptive mechanisms of the Neapolitan Yellow Tuff interpreted from stratigraphy, chemistry, and granulometry. Journal of Volcanology and Geothermal Research, 67, 263-290.
Wohletz, K.H., Sheridan, M.F., 1979. A model of pyroclastic surge. Geological Society of America Special Paper, 180, 177-193.
Wohletz, K.H., Sheridan, M.F., 1983. Hydrovolcanic explosions II. Evolution of basaltic tuff rings and tuff cones. American Journal of Science, 283, 385-413.
Wohletz, K.H., Sheridan, M.F., Brown, W.K., 1989. Particle size distributions and the sequential fragmentation/transport theory applied to volcanic ash. Journal of. Geophysical. Research, 94, 15,703-15,721.
Woods, A.W., Wohletz, K.H., 1991. Co-ignimbrite eruption columns. Nature, 350, 225-227.
Yin, L., Yang, R., Gabbouj, M., Neuvo, Y., 1996. Weighted Median Filters: A Tutorial. IEEE Trans. on Circuits and Systems, 43(3), 157-192.

Zhang, Y., Sturtevant, B., Stolper, E.M., 1997. Dynamics of gas-driven eruptions: experimental simulations using CO_2–H_2O–polymer system. Journal of. Geophysical. Research, 102, 3077-3096.
Zimanowski, B., Büttner, R., Lorenz, V., 1997. Premixing of magma and water in MFCI experiments. Bulletin of Volcanology, 58, 491–495.
Zimanowski, B., Frölich, G., and Volker, L., 1991. Quantitative experiments in phreatomagmatic explosions. Journal of Volcanology and Geothermal Research, 48 (3-4), 341-358.
Zimanowski, B., Wohletz, K., Dellino, P., Büttner, R., 2003. The volcanic ash problem. Journal of Volcanology and Geothermal Research, 122, 1-5.

"*For after all what is man in nature? A nothing in relation to infinity, all in relation to nothing, a central point between nothing and all and infinitely far from understanding either. The ends of things and their beginnings are impregnably concealed from him in an impenetrable secret. He is equally incapable of seeing the nothingness out of which he was drawn and the infinite in which he is engulfed.*"

Blaise Pascal, Pencées #72

Résume

Les cendres volcaniques issues des différents mécanismes de fragmentation ont diverses textures et morphologies externes. Chaque particule de cendre peut donner des informations sur son propre environnement et sur des mécanismes de formation. On peut définir un régime de fragmentation, l'intensité de la fragmentation et la quantité d'eau qui participe au processus de fragmentation. Actuellement, les cendres volcaniques ont surtout fait l'objet d'approches qualitatives. En effet, la complexité et la variabilité des formes des particules volcaniques rendent l'approche quantitative difficile et la caractérisation numérique des textures de surface des cendres volcaniques, en raison de sa complexité, est encore mal définie. Des descriptions de surface simples et bien définies sont présentées dans cette étude. On se base sur le fait que la variation de niveau de gris est liée à la variation de rugosité de la surface. Ici, des valeurs de niveau de gris ont été employées sous une forme correspondant aux valeurs z vertical sur la surface. Les inconvénients et les avantages de la simplicité de la méthode sont discutés. Sept paramètres de rugosité (Rq, Ra, Rsk, Rku, Rv, Rp, Rt), trois paramètres de quadtree (nQT, mQT, sQT) et dimension de fractale sur des surfaces de cendres sont mesurés. Une analyse de gradient basée sur des opérateurs de Sobel a été exécutée et des parcelles de terrain polaires ont été produites, sur la base de la fréquence des gradients. Différents paramètres de forme, tels que le facteur de forme, la compacité, l'arrondi, l'allongement, la solidité, la convexité et les dimensions de fractale sont calculés sur les parcelles de terrain polaires. Des échantillons provenant de l'activité variée de cinq volcans ont été choisis pour l'analyse 2D: Nemrut, Erciyes (Turquie), Galunggung (Indonésie), Villarica (Chili) et Miyakejima (Japon). Cependant, des images tridimensionnelles permettent à différents dispositifs morphologiques d'être mieux interprétés et mesurés. En conséquence, des coupes de particules, la stéréoscopie et le meulage commandé ont été employés pour acquérir une reconstruction 3D. Des paramètres externes sont calculés sur les surfaces 3D des particules des cendres du volcan Villarica (Chili).
Les paramètres externes sont employés pour regrouper les différents types de particules selon leurs mécanismes de fragmentation et en particulier pour séparer les changements de styles en cours d'éruptions, liés au rapport eau/magma. Les paramètres de morphologie de surface optima ont été déterminés à l'aide des corrélations entre les paramètres de surfaces qualitatif, la porosité, l'abondance des xénolithes, les rapports de masse eau-magma (R) et des paramètres de surfaces quantitatifs. On admet que Ra et Rq sont les paramètres de rugosité sensibles à la micro-rugosité (par exemple la poussière fine) tandis que d'autres paramètres de rugosité, Rsk et Rku, mesurent la macro-rugosité liée aux cavités de surface (vésicules). En effet, le paramètre de quadtree nQT, la dimension de fractale des surfaces et la solidité des parcelles de terrain polaires ont également la même réponse à la micro-rugosité, semblable à Ra et Rq. En raison de l'intérêt croissant pour les propriétés externes de matériaux normaux, les paramètres des surfaces proposés dans cette étude peuvent être appliqués aux surfaces de divers matériaux normaux.

Mots Clés: cendre volcanique, microscopie électronique à balayage, phréatomagmatisme, rugosité, analyse de gradient, texture surface

Quantitative morphological analysis of ashes from pyroclastic deposits of hydrovolcanic and magmatic origin

Abstract

Volcanic ash particles from different fragmentation mechanisms have different surface textures and morphologies. Every single ash particle may convey information about its own formation environment and conditions. Certain features may give a hint about the fragmentation regime, the intensity of fragmentation and quantity of water that partakes in the fragmentation process. However, volcanic ash was characterized widely by qualitative set phrases up to date and the success in the discrimination of ash types depended on the experience of the person who dealt with characterization of particles. Furthermore, the complexity and variability of volcanic particle shapes make quantitative characterization difficult and numerical characterization of volcanic ash surface texture, because of its complexity, still remains largely unresolved. Simple and well-defined surface descriptors were presented in this study. It is based on assuming that the gray level variation is related to the roughness variation of the surface. Here, gray level values were used in a form corresponding to vertical z-values on the surface. The disadvantages and advantages of the simplicity of method have been discussed. Seven roughness descriptors (Rq, Ra, Rsk, Rku, Rv, Rp, Rt), three quadtree parameters (nQT, mQT, sQT) and fractal dimensions (FDs) on ash surfaces were measured. A gradient analysis based on Sobel operators was performed and polar plots were generated based on frequency of gradients. Different shape descriptors such as form factor, compactness, roundness, aspect ratio, solidity, convexity and the fractal dimensions (FD_PP) were calculated on polar plots. Samples from five volcanoes with different eruption styles were selected for 2D analysis (Nemrut, Erciyes (Turkey), Galunggung (Indonesia), Villarica (Chile) and Miyakejima (Japan)). However, three-dimensional images allow different morphological features to be correctly interpreted and definitively measured. Therefore, optically sectioned particles, stereoscopy and controlled grinding were used to acquire 3D datasets for reconstruction. Surface descriptors were calculated on 3D surfaces of ash particles from Villarica volcano (Chile).

The surface descriptors were used to cluster different type of particles according to their fragmentation mechanisms and designated the phase changes in eruptions associated with interacting water/magma ratios. The optimum distinctive surface descriptors were determined with the assistance of correlations between qualitative surface descriptions, vesicularity, xenolith abundance, calculated water/magma mass ratios (R) and quantitative surface descriptors. It is agreed that roughness parameters R_a and R_q are sensible to micro-roughness (eg. fine dust) while other roughness parameters R_{sk} and R_{ku} measure the macro-roughness associated with cavities on the surface (vesicles). Furthermore, quadtree parameter nQT, fractal dimension of surfaces and solidity of polar plots also have the same response to micro-roughness similar to R_a and R_q. Because of increasing interest in surface properties of natural materials, surface descriptors proposed in this study can be applied to surfaces of various natural materials.

Keywords: volcanic ash, scanning electron microscopy, phreatomagmatism, roughness, gradient analysis, surface texture